Ultrafast charge and spin dynamics at solid interfaces

Investigated with femtosecond time-resolved second harmonic spectroscopy

Der Fakultät für Physik
der Universität Duisburg-Essen vorgelegte

Dissertation

zur Erlangung des akademischen Grades eines Doktors der Naturwissenschaft
(Dr. rer. nat.)

Von
Jinghao Chen
aus Quanzhou, China

Erstgutachter:	Prof. Dr. Uwe Bovensiepen
Zweitgutachter:	Prof. Dr. Jens Güdde
Prüfer:	Prof. Dr. Richard Kramer Campen
Vorsitzender:	Prof. Dr. Björn Sothmann
Tag der Disputation:	25. Februar 2021

Abstract

This work investigates the ultrafast charge and spin dynamics on heterogeneous solid interfaces via femtosecond time-resolved second harmonic spectroscopy. With epitaxial Co/Cu(001) films and iron porphyrin molecules adsorbed on Cu(001) two model interface systems for ferro- and paramagnetically ordered overlayers have been studied, respectively. The charge and spin transfer across heterogeneous interfaces are currently areas of interest as being fundamental steps for future spintronic devices. From a technological point of view, one would like to have spin injection with minimal spin dissipation. Investigation of these effects down to fundamental picture in nanometer length scales and femtosecond timescales are of great importance.

In the first part, the present work addresses the length scale of laser induced spin current via systematic thickness dependent studies of epitaxial Co films on a Cu(001) substrate. The spatially inhomogeneous magnetization dynamics is analyzed by time-resolved magnetization-induced second harmonic generation (MSHG), which probes the spin dynamics at vacuum/Co and Co/Cu(001) interfaces. The transient magnetization in-depth profile depends on the Co film thickness. For the Co films less than 3 nm, the vacuum/Co interface is more strongly demagnetized than Co/Cu interface, which is explained by spin transfer with an inelastic mean free paths (MFP) of about 3 nm. While for film thickness larger than 3 nm, a sign change of transient magnetization gradient occurs, which reflects that only spins near Co/Cu interface region can escape into the Cu substrate.

Elementary processes and related timescales at Co/Cu(001) interfaces are further investigated through a combined effort of time-resolved MSHG experiments and *ab initio* time-dependent density functional theory (TDDFT). Based on the agreement between experiment and theory on ultrathin Co/Cu(001) films, spin dependent charge transfer from Co films to Cu substrate has been identified. A spin back transfer can occur due to a resonant optical transition in the Co/Cu(001) interface layers. The spin transfer processes govern the dynamics in the first 35 fs after laser excitation. As a local process competing to spin transfer, spin angular momentum dissipates through spin-orbit coupling on the 100 fs timescale, and eventually flows into the crystal lattice, which serves as a sink for angular momentum.

In addition, photoinduced charge transfer dynamics on *in situ* prepared monolayer Fe-porphyrins (FeOEP) on Cu(001), which serve as a prototype molecule-metal interface, have been studied by time-resolved second harmonic generation (SHG) spectroscopy. Through wavelength and polarization dependent SHG studies, it was found that a SHG enhancement occurs at 2.2 eV photon energy, which can be assigned to interface-assisted charge transfer resonance. In order to verify the resonant excitation, pump-probe SHG experiments are performed at on- and off-resonant photon energies. Distinctive pump effect and SHG relaxation time of 244 ± 22 fs has been observed at 2.2 eV at the FeOEP/Cu(001) interface, which is slower compared to bare Cu(001) with 168 ± 17 fs. Since the electron lifetime in the interface molecular state are expected to be longer than for Cu(001), slower relaxation dynamics observed at 2.2 eV for FeOEP/Cu(001) indicates resonant charge transfer excitation from metal to unoccupied molecular state.

These results give an insight into the fundamental physical interactions at the interfaces, involving charge/spin transfer and dissipation that give rise to many exciting phenomena, which offer a clear potential for future device technology.

Zusammenfassung

Diese Arbeit umfasst die Untersuchung der ultraschnellen Ladungs- und Spin-Dynamik an heterogenen festen Grenzflächen mittels nichtlinearer optischer femtosekunden-zeitaufgelöster-Spektroskopie. Zwei Modellsysteme, nämlich epitakti-sche Co/Cu(001)-Filme und an Cu(001) adsorbierte Eisenporphyrinmoleküle werden untersucht. Der Ladungs- und Spintransfer über heterogene Grenzflächen ist derzeit von Interesse, da er als potenzielle Prozesse für zukünftige Spintronik von Interesse ist. Aus technologischer Sicht zielt man auf eine Spininjektion mit geringer Dissipation. Untersuchung dieser Effekte auf ein grundlegendes Bild in Nanometerlängenskalen und Femtosekunden-Zeitskalen ist von großer Bedeutung.

Im ersten Teil befasst sich die vorliegende Arbeit mit der Längenskala des laser-induzierten Spin-Transport durch systematische dickenabhängige Untersuchungen epitaktischer Co-Filme auf einem Cu(001) Substraten. Die räumlich inhomogene Magnetisierungsdynamik wird durch zeitaufgelöste magnetisierungsinduzierte Erzeugung der zweiten Harmonischen (MSHG) analysiert, die die Spin-Dynamik an den Vakuum/Co und Co/Cu Grenzflächen untersucht. Das transiente Magnetisierungsprofil hängt von der Co-Filmdicke ab. Bei Co-Filmen unter 3 nm ist die Vakuum/Co-Grenzfläche stärker as die Co/Cu-Grenzfläche entmagnetisiert, was durch Spintransfer mit einer inelastischen mittleren freien Weglänge von etwa 3 nm erklärt wird. Ein Vorzeichenwechsel des transienten Magnetisierungsgradienten tritt bei 3 nm Dicke auf. Das bedeutet, dass nur Spins in der Nähe von Co/Cu(001)-Grenzflächen in das Cu-Substrat entweichen können.

Elementare Prozesse und verwandte Zeitskalen an Co/Cu(001)-Grenzflächen werden durch Kombination von zeitaufgelösten MSHG-Experimenten und *ab initio* zeitabhängiger Dichtefunktionaltheorie (TDDFT) weiter untersucht. Basierend auf der Übereinstimmung zwischen Experiment und Theorie an ultradünnen Co/Cu(001)-Filmen wird ein spin-abhängiger Ladungstransfer von Co-Filmen in das Cu-Substrat identifiziert. Eine Rücktransfer des Spins tritt gleichzeitig aufgrund eines resonanten optischen Übergangs an der Co/Cu(001)-Grenzfläche. Auf die Übertragung des Spins dominiert die Dynamik in den ersten 35 fs nach der Laseranregung. Als lokaler Prozess, der Spin-Drehimpuls disspiert durch Spin-Bahn-Kopplung auf der Zeitskala von 100 fs und fließt schließlich in das Gitter-System, das als Senke für den Drehimpuls wirkt.

Zusätzlich wird die photoinduzierte Ladungstransfer-Dynamik auf *in situ* präparierten Fe Porphyrinen (FeOEP) auf Cu(001) untersucht. Durch polarisations- und wellenlängenabhängige SHG wird festgestellt, dass eine SHG-Verstärkung bei 2,2 eV Photonenenergie auftritt, die durch einen resonanten Übergang erklärt werden kann. Um die Resonanz zu verifizieren, werden Pump-Probe SHG unter resonanter und nicht resonanter Photonenenergie durchgeführt. Ein ausgeprägter Pumpeffekt und eine SHG-Relaxationszeit von 244 ± 22 fs wurden bei 2,2 eV an FeOEP/Cu(001) Grenzflächen beobachtet, was langsamer ist als bei Cu (001) mit 168 ± 17 fs. Da eine längere Lebensdauer der Elektronen im molekularen Zustand erwartet wird, weist die langsamere Relaxationsdynamik, die bei 2,2 eV für FeOEP / Cu (001) beobachtet wird, auf eine Resonanzanregung des Ladungstransfers vom Metall in den unbesetzten molekularen Zustand hin.

Diese Ergebnisse geben einen Einblick in die fundamentalen Wechselwirkungen an den Grenzflächen, einschließlich Ladung-/Spin-Transfer und Dissipation, die zu vielen aufregenden Phänomenen führen, die ein klares Potenzial für die zukünftige Gerätetechnologie bieten.

Abbreviations

BBO	β-barium-borate
BS	Beamsplitter
CCD	Charge-coupled device
CM	Chirped mirror
CMOS	Complementary metal-oxide-semiconductor
cw	Continuous wave
DFG	Difference frequency generation
DOS	Density of states
FeOEP	Iron (III) octaethylporphyrin
fs	Femtosecond
FM	Ferromagnetic
FROG	Frequency resolved optical gaining
FWHM	Full width at half maximum
GMR	Giant magnetoresistance
GVD	Group velocity dispersion
HR	High reflection
HOMO	Highest occupied molecular orbital
ITT	Interband transition threshold
LEED	Low energy electron diffraction
LUMO	Lowest unoccupied molecular orbital
M3TM	Microscopic three temperature model
MFP	Mean free path
ML	Monolayer
MOKE	Magneto-optical Kerr effect
MRAM	Magnetoresistive random-access memory
MSHG	Magnetization-induced second harmonic generation
NEQ	Non-equilibrium electron
NM	Non-ferromagnetic
NOPA	Non-collinear Optical Parametric Amplifier
OC	Out coupling
OPA	Optical parametric amplifier
PMT	Photomultiplier
QCM	Quartz crystal microbalance
QMS	Quadrupole mass spectrometer
RegA	Regenerative amplifier

SFG	Sum frequency generation
SPM	Self-phase modulation
SHG	Second harmonic generation
SOC	Spin-orbit coupling
STT	Spin transfer torque
TDDFT	Time dependent density functional theory
TFP	Thin film polarizer
TSP	Titanium sublimation pump
UHV	Ultra high vacuum
UV	Ultraviolet
WL	White light
XC	Cross-correlation
XMCD	X-ray magnetic circular dichroism
2PPE	Two photon-photoemission
2TM	Two temperature model
3TM	Three temperature model

When light encounters magnetism, how many things make people dreamy?

Contents

1 Introduction

Phenomena of ultrafast demagnetization, induced by femtosecond laser pulses in ferromagnetic materials, contain rich physical contents. The underlying microscopic origin involves basic physical issues such as quantum many body interactions in non-equilibrium states between electrons, the crystal lattices and spins. This opens a new area: Ultrafast magnetism. Ultrafast pump-probe spectroscopy provides a way to manipulate and probe spins at the femtosecond time scale, which triggered great interest in academic research and industry. This technology may bring new ideas for future magnetic memory devices.

Looking back on the past, complementary metal-oxide-semiconductors (CMOS) have dominated the semiconductor industry for more than thirty years. It is clear that Moore's law, which states the complexity of integrated circuits regularly doubles every 18 months with minimal component costs, cannot be maintained forever. The exponential increase in density and performance, has reached to a shocking performance plateau, and the problem of data center power are deeply interrelated. Global data centers use 416 terawatts (or about 3% of the total electricity power) in 2016, and this power consumption will double every four years [1]. In the good times of more than ten years ago, the downsizing of semiconductor processes has enabled us to achieve higher performance and lower power consumption at the same time. Now they no longer provide us with faster speeds, nor can they offset the rapidly increasing power consumption in data centers. Both originate from device physics and processor microarchitecture. There is clearly a need for other memory technologies with high speed and low power consumption that could reach this level of complexity.

The memory device in the computer is used for data storage and processing, with the development of computers, it has become more and more important as core of the computer systems. In a certain sense, the magnetic moment of magnetic materials naturally possesses the characteristics of "0" and "1" states by parallel and antiparallel magnetization orientations, which meet the binary requirement, and is thus widely used in magnetic recording and magnetic random access memories (MRAM). In particular, various breakthroughs have been made in the research fields of magnetic nanomaterials, which has greatly improved the performance of magnetic hard disks and MRAM.

Since V. Poulsen developed a magnetic wire recorder in 1988 to storage information [2], the use of magnetic materials as storage media has developed rapidly due to their excellent material properties and broad application prospects. Magnetic recording has become one of the hot topics of research [3]. Magnetic storage has some other incomeparable advantages: high recording density, long lifetime, reusable and repeated erasing, non-volatility etc. For static Random Access Memory (RAM) an electric current hast to be applied to keep the data.

As the thin film growth methods and lithographic patterning technology were applied to magnetic material classes, a numbers of fascinating physical effects were discovered. Especially the finding of giant magneto-resistance (GMR) and tunnel magneto-resistance effect (TMR) [4, 5], which has greatly improved the sensitivity and accuracy of the magnetic read/write head, and significantly increased the storage density of the hard disk. As shown in Figure 1.1, the resistance of the GMR elements strongly depend on the align-

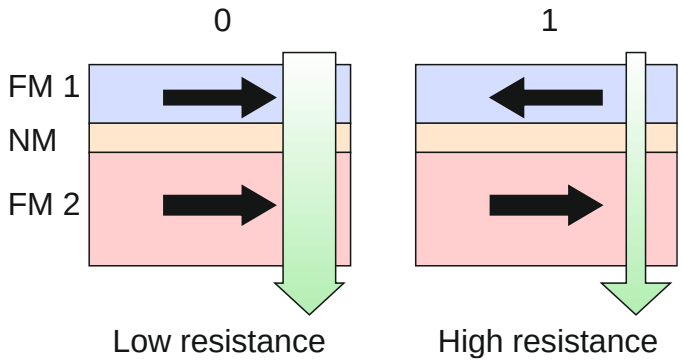

Figure 1.1: Schematic of Giant Magneto Resistance (GMR) effect, the GMR element consists of two ferromagnetic layers (FM1 and FM2) which is spaced by a non-ferromagnetic layer (NM). In a parallel-aligned configuration of magnetization, denoted by black arrow, the resistance is lower than antiparallel alignment. The green arrow indicates the flow of current through the GMR structure.

ment of two ferromagnetic layers, in which the magnetization of one layer being fixed, the other can be switched. The fixed layer (FM2) acts as a spin filter, thus causing the electrons become polarized. Due to the nature of spin dependent scattering, the switch layer (FM1) has lower scattering probability when the magnetizations are parallel.

The goal is to manipulate the magnetization in the GMR elements with faster speed and lower energy consumption. In the conventional picture of thermodynamics magnetism, one applied a magnetic field to reverse the magnetization through precessional dynamics. An extremely high magnetic field is required to increase the magnetization reversal speed. However, the time scale of magnetization precession is fundamentally limited (100 ps – 10 ns) [6], even when a very short pulse of a very high magnetic field is applied, it was shown that if the pulsed magnetic field is shorter than 2 ps [7], no definite magnetization reversal will occur. In order to increase the speed of magnetization reversal, the size of the effective magnetic field needs to be increased. Whether it is to increase the external magnetic field or increase the current density, it means that more energy is required. The idea of using magnetic field to manipulate the magnetic order limits the magnetic reversal time to the nanosecond scale. This is almost not suitable for designing nano devices with high integration and low energy consumption, and it is difficult to further improve it.

One breakthrough came from the spin transfer torque (STT) effect. In 1996, J. Slonczewski and L. Berger theoretically concluded that when a spin-polarized current passes through a nanomagnetic multilayer film, the spin polarized current will affect the electrons near the Fermi surface, resulting in spin angular momentum transfer from spin polarized electrons to magnetic films. The STT effect was experimentally demonstrated in 2000. In 2007, IBM developed STT-MRAM [8, 9]. The importance is that STT provides a way that does not require pulsed magnetic field and uses spin currents to manipulate the magnetic order of the magnetic thin film, which greatly facilitates the integration of spintronic devices and traditional circuits. The spin transfer torque requires low power consumption, and is able to manipulate the magnetization.

Using spin current to manipulate the magnetism is an innovative method, and the idea could be extended into ultrafast timescale. Followed by the study of laser-induced ultrafast magnetization dynamics, which provide evidence that spin current can be generated by an ultrafast laser pulse [11, 12]. As illustrated in Figure 1.2 (a), in 2014, two groups separately demonstrated that an ultrafast spin transfer torque (STT) can be exerted

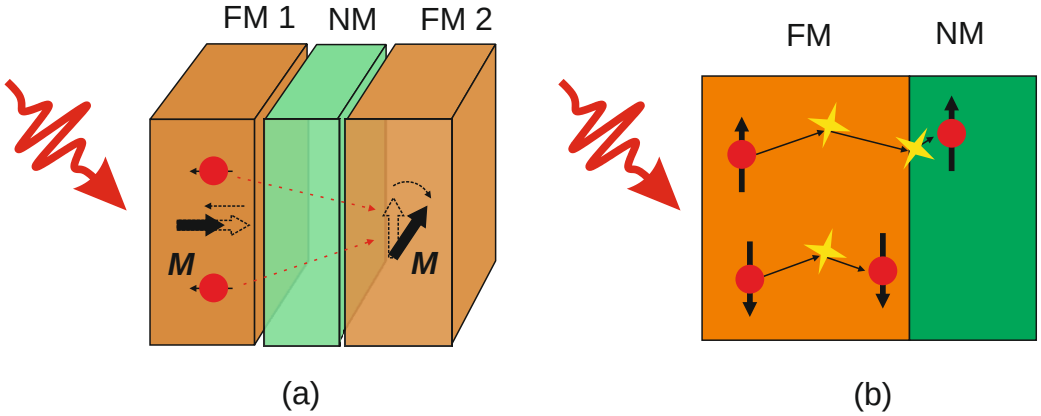

Figure 1.2: (a) Illustration of ultrafast spin-transfer torque. A femtosecond laser pulse drives the first ferromagnetic layer into a highly non-equilibrium state and induces an ultrafast demagnetization, indicated by the dashed black arrow. The laser induced spin-up current flow (red dashed arrows) crosses the first FM/NM interface and travels to the second ferromagnetic layer. The spin current exerts an ultrafast spin-transfer torque (STT), tilts the magnetization of FM2 out of plane and causes a precession, the final magnetization is indicated by the black arrow. Redrawn from [10]. (b) Schematic of laser induced spin-dependent transport cross FM/NM interface. The majority spin (up arrow) can travel over a larger distance than minority spin (down arrow) in FM films. Redrawn from [17].

by the spin current [13, 14]. In this scenario the spin current flows through the spin valve, and crosses the interface between a ferromagnet and a non-ferromagnet.

Discontinuity of interface breaks the inversion symmetry. The material properties are different from bulk, which include structure, electronic properties, diffusion, transport effects and lateral correlations. In bulk, the laser induced spin current can be explained by a superdiffusive model [17]. However, in regard to spin transfer at interfaces, the importance and the role of interfaces in metallic heterostructures has not been addressed completely. In real applications, one would like to have high spin injection efficiency cross the interface i.e. low spin loss due to dissipation in transport or spin-flip scattering at the interface. As illustrated in Figure 1.2 (b), optically excited majority electrons usually have a larger mean free path than minority electrons [60]. Therefore, in order to manipulate the spin degrees of freedom in ultrafast timescales, it is crucial to identify the elementary processes of spin dynamics at interfaces and their corresponding length and time scales.

This thesis reports laser induced ultrafast spin dynamics at ferromagnet/noble-metal interfaces, which is dedicated to a fundamental picture of charge and spin dynamics on a femtosecond time scale (< 100 fs). The investigated model system in this thesis is Co/Cu(001). The experiments are performed with interface-sensitive fs-resolved non-linear magneto-optics, which is also known as magnetization-induced second harmonic generation (MSHG). MSHG has high sensitivity to surfaces and buried interfaces of centrosymmetric materials [15]. Particularly in regard of probing magnetism MSHG offers a strong magnetic contrast in comparison with linear magneto-optics [16].

Femtosecond laser pulses drive the electrons in solids into a non-equilibrium state. In the 3d transition-metal ferromagnets (Fe, Co and Ni), the spin majority and minority are excited and characterized with energy-dependent lifetimes and spin-dependent mean free paths, and generating an effective spin current [17]. Since the laser induced spin current

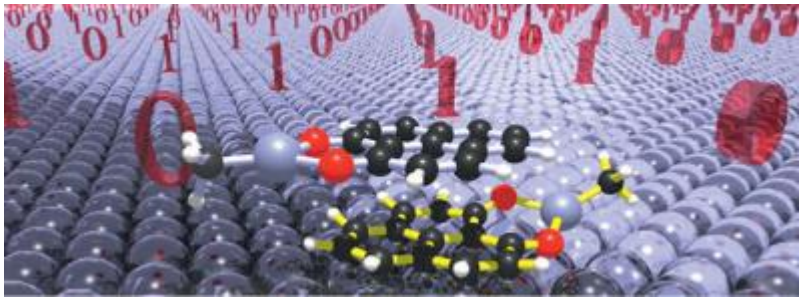

Figure 1.3: Schematic view of using organic molecule/ferromagnet interface to achieve molecular spintronics. As artistically shown here, two Zn methyl phenatenyl planar molecules are placed on a ferromagnet, they can be stored as 0 or 1 data bits dependents on the molecular spin configurations through charge transfer and exchange interaction. [20]

can flow through the ferromagnetic films and across an interface, the starting point of the experiment is to analyze the spin current with increasing thickness of Co films on a Cu(001) substrate. It is demonstrated in this work that MSHG is an interface sensitive method to probe spatially inhomogeneous magnetization dynamics and analyze the spin current mean free path in Co/Cu(001) films [18].

From a fundamental point of view, questions like how fast does the spin transfer process occurs and what limits the spin transfer arise naturally. In order to identify the time scales of elementary processes at interfaces this thesis combines fs nonlinear magneto-optics with *ab initio* time-dependent density functional theory (TDDFT) to study the identical material system, i.e. ultrathin, layer resolved Co/Cu(001) films. Non-equilibrium spin dynamics at interfaces can be described by TDDFT. Interfacial spin transfer differs from bulk based superdiffusive transport. Thus, femtosecond laser excitation prompt spin-dependent charge transfer and spin back transfer between Co and Cu(001). Subsequent to laser excitation in the later timescales >100 fs, spin angular momentum is dissipated through spin-orbit coupling [19].

Another aspect regarding the magnetic memory is to exploit spin of electrons in molecule to realize the binary property. In the field of molecular spintronics single molecules are used as building blocks to extend the limits of Moore's Law, which was based on silicon-integrated circuits. Organic molecules are well defined as they always have the same number of atoms, atomic structure and electronic structure, thus organic molecules are expected to form the smallest possible electronic units. Their properties can be tuned by external stimuli such as electric and magnetic fields, light, pressure. Raman *et al*. [21] had shown that a molecular device can be constructed by using phenalenyl molecules as templates, in which an interfacial spin transfer could be raised due to hybridization and magnetic exchange interaction with the ferromagnetic surface. As a result, the device showed an interface magnetoresistance of more than 20 % near room temperature.

In addition, this work studies charge transfer across the molecule-metal interface. Iron porphyrin molecules (FeOEP) on Cu(001) serve as a model system of paramagnetic porphyrin molecule-metal interfaces [22], this material class is promising as building blocks for molecular electronic devices. The main idea originates from the weak spin-orbital coupling, since organics usually consists of light elements, thus the spin configuration and electron lifetime are expected to be preserved for a longer time than in metal. In this case, the spin can be transferred from metal to molecule, and the spin

information is preserved. Charge transfer excitation from metal to molecule requires resonant pump photon energy corresponding to the difference between the Fermi level and interface assisted molecular state. The FeOEP/Cu(001) interface is then investigated with static and pump-probe surface second harmonic spectroscopy i.e. as a function of photon energy. This work could serve as reference for future nonlinear optical studies at organic molecule metal interfaces.

This thesis is structured as follows: Chapter 2 focuses on introducing the interaction of ultrafast laser pulse with metal, magnetism and molecule-metal interfaces. In chapter 3, basics of nonlinear optics especially nonlinear magneto-optics as well as optical pump-probe methodology are given. Chapter 4 describes the experimental details, sample preparation in ultrahigh vacuum, ultrashort laser sources and detection systems. Chapter 5 reports on two experimental studies on Co/Cu(001), inhomogeneous magnetization dynamics in Co/Cu(001) films and ultrafast spin transfer at ultrathin Co/Cu(001) interfaces. Chapter 6 presents the work of charge transfer dynamics at FeOEP/Cu(001) analyzed by surface second harmonic spectroscopy. Chapter 7 summarize the present work and provides an outlook.

2 Ultrafast phenomena

The interaction between laser light and materials has been an active research topic since the first invention of laser by Maiman 60 years ago. The interaction of intense electromagnetic fields with matter and the material response to light field is a fundamental topic of interest in physics. With the development of ultrafast lasers experiments became able to access the ultrafast time scale, which allows a separation of different elementary processes in the material due to its intrinsic response time [23]. This provides us a deeper understanding of light-matter interaction.

In this chapter, the interaction between light and metals with emphasis of ultrafast laser excitation is introduced i.e. the non-equilibrium electron dynamics in metals. Interaction of ultrashort laser pulses with magnetic material has opened up a new field of magnetism. Subsequently the chapter discusses the state of the art regarding theoretical models and experimental evidence in the ultrafast magnetization dynamics in ferromagnetic films. The third sub chapter presents the laser induced charge transfer dynamics at molecule-metal interfaces.

2.1 Electron dynamics in metals

In this section, the interaction of ultrashort laser pulse with metals is introduced. In the following, excitation and relaxation dynamics of electrons induced by a fs laser pulse are addressed in terms energy redistribution via various elementary processes like electron-electron, electron-phonon, and electron-magnon scattering (Figure 2.1), which contribute as decay channels to energy dissipation.

2.1.1 Absorption of ultrashort light pulses

Light-matter interaction is a fundamental process in nature, it is usually stated that the light is absorbed by the electrons, but this is an oversimplified picture since the energy of light field cannot be absorbed by a free electron because the processes should satisfy both energy and momentum conservation. In many cases, the required momentum is usually provided by the nucleus. Through the recoiled electron, a fraction of the energy is then transferred to the nucleus, yet the energy is small due to smaller mass of electrons in comparison with the nucleus.

In solid-state physics atoms form solids and therefore discrete energy levels of atoms become continuous bands in solids. In metals, the electrons with highest energy E_F occupy partially filled bands. This implies that free carriers in metals can absorb light of "any wavelength" since there is no threshold for excitation of electrons from occupied to unoccupied states. In fact, an incident electric field in metal is screened due to high electron conductivity, at the same time a reflected field is generated. Still, metal can absorb a few percent of the light energy. The optical absorption is usually dominated by free carrier absorption.

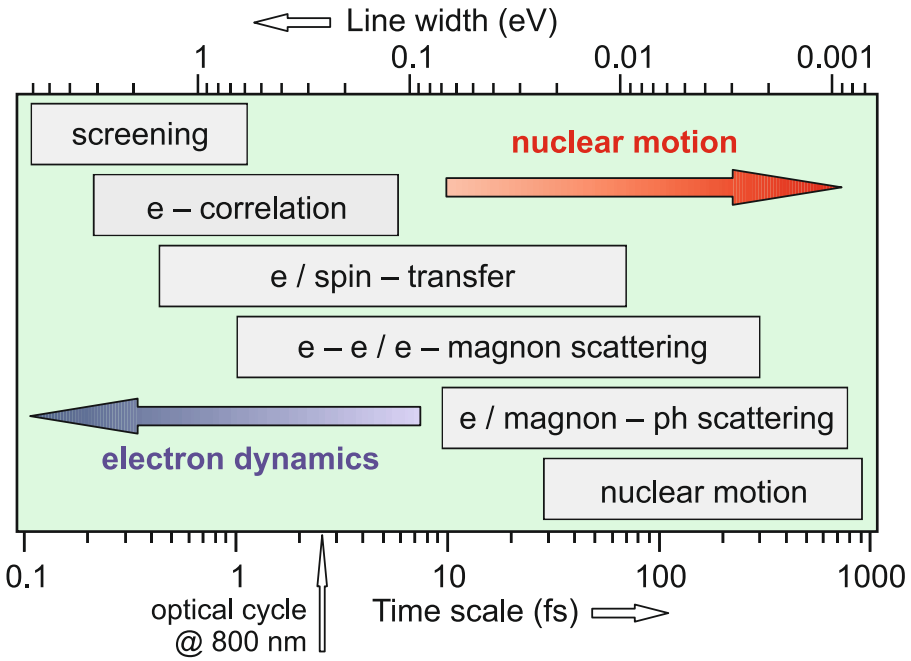

Figure 2.1: The time and energy scales for various elementary processes in metals [23].

In Drude's approach, electrons move in the electric field of laser light (angular frequency of light ω_L) and this leads to a dielectric function [24] of

$$\varepsilon(\omega_L) = \varepsilon_r - \left(\frac{\omega_P}{\omega_L}\right)^2 \frac{1}{1 - \frac{i\nu_D}{\omega_L}}, \tag{2.1}$$

in which ε_r is the unperturbed material dielectric constant and the plasma frequency

$$\omega_P = \sqrt{\frac{n_e e^2}{m_e \varepsilon_0}}, \tag{2.2}$$

determined by free electron density n_e and effective mass m_e. The collision frequency ν_D is the so called Drude frequency and several types of collision can be applied according to Matthiesen's rule. The frequency ν_D is often assumed in 10^{15} Hz and corresponding to a femtosecond collision time [25].

The complex refractive index $\hat{n}$ is defined as the square root of the dielectric function,

$$\hat{n} = n + i\,k = \sqrt{\varepsilon(\omega_L)} \tag{2.3}$$

where the real part n is responsible for refraction of light and the imaginary part k handles the attenuation of an electromagnetic field in the material. The reflectivity R and the absorption coefficient α can be written as

$$R = \frac{|\hat{n} - 1|^2}{|\hat{n} + 1|^2} \tag{2.4}$$

$$\alpha = \frac{2\pi k \omega_L}{c} = \frac{4\pi k}{\lambda} \tag{2.5}$$

with c being the speed velocity of light in vacuum and λ the wavelength of light. In the case of linear absorption, the absorbed energy in solid materials per unit and time is

proportional to the intensity I_0 of incident laser light. The absorption results in an exponential decay of laser intensity in the material, the process is described by the Lambert-Beer's law:

$$I(z,t) = I_0(t)(1-R)\exp(-\mathrm{z}\,\alpha) \tag{2.6}$$

The spatial extension of light in the material is characterized by the optical penetration depth (or optical skin depth) δ and is given by

$$\delta = \frac{1}{\alpha} = \frac{\lambda}{4\pi k} \tag{2.7}$$

The optical penetration depth in metals ranges around $10-30$ nm for visible light excitation. For example δ for copper at wavelength 800 nm is around 13 nm. The spatial decay of absorbed light intensity leads to an inhomogeneous excitation in depth. Particularly for metal films with thickness larger than optical skin depth, laser induced hot electron can be transported out of the excited region [26], due to the spatial gradient of the absorbed energy.

An ultrashort pulsed laser and a continuous wave (cw) laser radiation show a dramatic difference of optical excitation in metals. A laser pulse with 800 nm wavelength, 1 μJ energy and 100 fs duration yields around 4×10^{12} photons per pulse, which is 10^6 times larger than radiation by 1 W cw laser over 100 fs. This has a consequence that stored energy by ultrashort pulse is huge in metal over such a short time, and also the number of excited electrons per atom.

One should note that absorption of light can be affected by interband transition in metals. For example, the absorption in polyvalent metals like aluminum is increased at certain laser wavelength due to nearly parallel bands [27, 28]. It is more complicate for noble metals, where d band electrons can be excited into the s band above the Fermi level with far large enough photon energy to cross the interband transition threshold [26]. Those transitions are out of Drude's picture and more sophisticated approaches should be applied [29]. The strength of absorption is determined by practically using the refractive index of bulk materials, especially for layered structure, multiple reflections should also be taken into account. One note that nonlinear electronic excitation can also play a role [30].

2.1.2 Ultrafast processes in optically excited metals

Collective excitation

As an "instantaneous" response to a femtosecond laser field at the metal surface, a polarization is set by conduction electrons through collective oscillation, in which the optical phase memory of the laser pulse is preserved. The collective excitation of electrons responds at frequency up to plasma frequency. This dynamical screening of external fields can be practically approximated as "instantaneous", but it occurs actually at sub-femtosecond timescale in metals [31]. As fundamental response of electrons, it is also related to linear and nonlinear reflection of light. As shown in Figure 2.2 (a), a collective excitation of electrons can be described by the superposition of states that are coupled to a photoexcited electron and a hole, which induces a coherent polarization. At metal surfaces most of the energy carried by the external field is radiated as coherent reflection and a fraction is absorbed in the surface region.

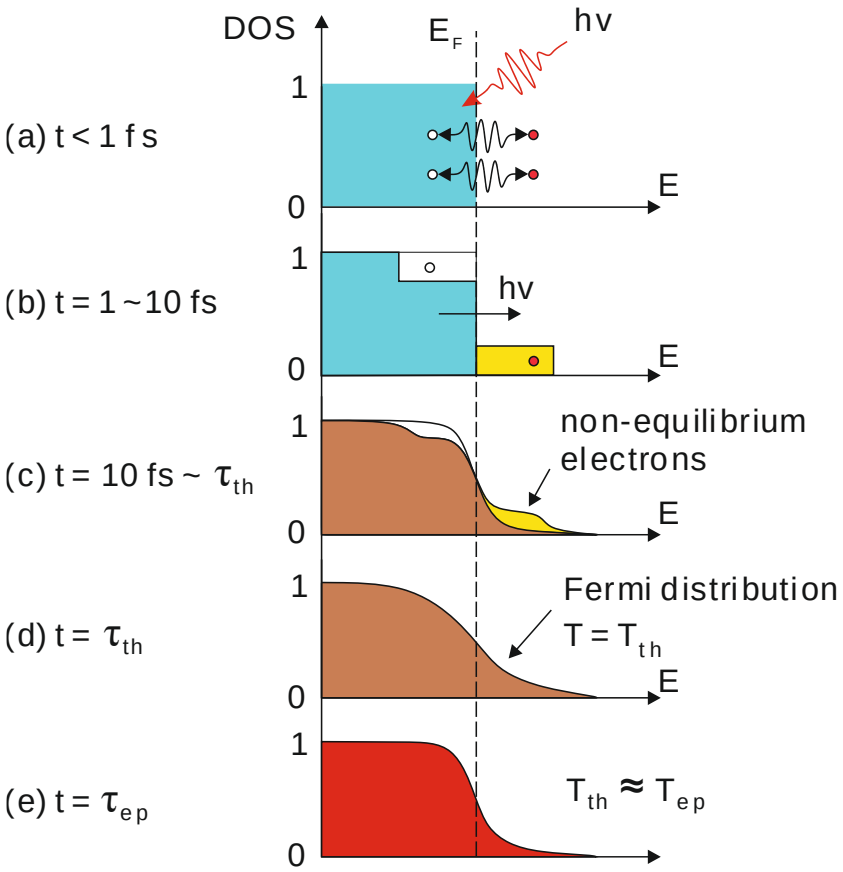

Figure 2.2: Optical excitation and relaxation of electron induced by a fs-laser pulse at a metal surface. Before excitation the metal is in thermal equilibrium. (a) A laser pump pulse with a photon energy *hv* generates a collective coherent polarization. (b) Dephasing of collective excitation leads to absorption of pump energy and creates an incoherent ensemble of electron-hole pairs, which does not obey Fermi statistics. (c) The excited non-equilibrium electrons exchange energy with other electrons via inelastic electron-electron scattering. (d) The electron distribution after electron thermalization can be described by Fermi distribution with electronic temperature T_{th}. (e) Energy carried by hot electrons is transferred to cold lattices through electron-phonon scattering, both systems are thermalized till they have same temperature. Redrawn from [26, 36].

Dephasing of electrons

Charge carrier momentum scattering events lead to decoherence of collective electron motion. According to Drude theory, those processes occur on femtosecond timescales. In other words, shortly after the laser excitation on a timescale 1 fs - 10 fs, through elastic processes such as electron-electron scattering, electron-phonon scattering and impurity scattering [32], phase memory of the collective excitation is lost. In the dephasing processes, the kinetic energy of the electrons remains the same, but the momentum is randomized. At this point it is fair to say that a femtosecond laser pulse is absorbed in metals, in respect to photon energy *hv* electrons are populated above Fermi level. This incoherent population of hot electrons and hot holes is created by scattering of coherently excited electron-hole pairs and do not follow Fermi-Dirac statistics. The density of state after dephasing of collective excitations is displayed in Figure 2.2 (b).

Electron thermalization

So far the pump pulse energy is deposited mainly in the electronic system, and generates non-equilibrium states. The stored energy is then redistributed between non-thermalized and unexcited electrons via inelastic electron-electron scattering. Distribution of non-equilibrium electrons is depicted in Figure 2.2 (b) and (c). Thermalization of the electron system in metals usually takes place within a thermalization time τ_{th} of $200 - 500$ fs [29, 33-35]. Later on the electron energy distribution can be described by Fermi-Dirac distribution with a thermalized electronic temperature T_{th}, see Figure 2.2 (d).

For low excitation density (less than 10^{-3} electrons per atom), the relaxation of an excited single electron at a given energy $E - E_F$ above Fermi energy is usually theoretically treated base on the Landau-Fermi-liquid theory (FLT) [37, 38], in which the excitation is viewed as a quasiparticle. For a free electron gas at $T = 0$ K, the lifetime τ_{e-e} of a quasiparticle located above Fermi level is given by:

$$\tau_{e-e} \propto \frac{1}{(E - E_F)^2} \tag{2.8}$$

The lifetime has an inverse proportionality to $(E - E_F)^2$. It reflects the nature of Pauli-repulsion on the number of available unoccupied states and available amount of final states involved in scattering events, in short words, the available phase space for scattering. The electron-electron and hole-hole scattering rates go to zero when the electron energy is near $E - E_F \to 0$. The free electron model can describe the electron-electron scattering rates in metals such as the energy dependence of e-e scattering near the Fermi surface of noble metals. However, due to possible intraband ($sp \to sp$ electrons) and interband ($d \to sp$ electrons) scattering processes [32], the energy dependence of hot electrons lifetime is quite different for noble and transition metals or even interband transitions in noble metals, because screening of the electron-electron interaction by the *d*-band electrons should be considered [34].

In addition to electron-electron scattering, electron transport is a competing channel of energy relaxation to equilibrate the energy in the excited region. As mentioned earlier, the exponential absorption profile causes an inhomogeneous energy distribution in depth, as a consequence, the energy carried by the non-equilibrium electrons at the surface is then transfered out of the excited region into the bulk. On the time scale <100 fs, this effect is attributed to ballistic electron transport with a Fermi velocity 10^6 m/s (= 1 nm/fs) [39, 40]. For noble metals such as gold, the ballistic electrons can move up to the mean free path $\Lambda_{ball} \approx 100\ nm$ [41]. The mean free path of other *sp* band metals can be calculated, $\Lambda(\mathrm{Cu}) = 70\ nm$, $\Lambda(\mathrm{Ag}) = 70\ nm$ [26, 42]. Owning to larger phase space for electron scattering in *d* band [43], the efficiency of ballistic transport in transition metals is strongly reduced, for example the estimated values are $\Lambda(\mathrm{Ni}) = 11\ nm$, $\Lambda(\mathrm{Cr}) = 14\ nm$, $\Lambda(\mathrm{Mo}) = 20\ nm$ [26]. One notes here that the energy transfer from electron system to lattice can be faster in case of transition metals [26].

Electron phonon scattering

First, high electron temperatures can be reached after the internal thermalization of electrons. But the electron system and phonon system are not well equalized in terms of temperature due to the difference in heat capacity, the lattice is still "cold" while the electrons are "hot" after laser excitation. From the perspective of energy transfer, typical phonon energy in metals is limited by Debye energy of $30-40$ meV, therefore, the decay of a hot electron requires several electron-phonon scattering events. In other words, the

energy transfer between hot electrons and phonon bath cannot be faster than one single phonon oscillation period. Through electron-phonon coupling the electronic and phononic system are thermalized $T_e \approx T_{ph}$ on picosecond timescales $\tau_{e\text{-}ph}$ [44, 45] (see figure 2.2 (e)).

In the time scales where the electron system is internally thermalized but not yet interacting with the phonon system $\tau_{th} < t < \tau_{e-ph}$, the energy carried by hot electrons can be redistributed by hot electron transport [26]. The energy dissipation is driven by the temperature gradient with a slower speed 10^4 m/s than ballistic transport and diffuses into bulk. Noble metals have a longer diffusion length compared to transition metals due to weaker e-ph coupling [46]. The energy transport and dissipation between hot electrons and phonon in time and space can be described by two temperature model (2TM) [47]. After the thermalization between electron and phonon systems $t > \tau_{e-ph}$, temperature gradient proceeds a heat flow in deeper part of the metals in the form of thermal diffusion, which is accomplished in few hundreds of picoseconds.

Electron magnon scattering

In magnetically ordered materials the energy can also be transferred through collective excitation of magnetic moments i.e. magnons. In case of iron the magnon energy is in the order of 100 meV [48], which makes the energy dissipation via electron-magnon coupling more efficient than electron-phonon coupling. In regards to momentum conservation, the spin of electrons in ferromagnetic metals can be flipped through both electron-phonon and electron-magnon couplings. As a decay channel for energy and momentum, magnons can play an important role during the ultrafast time scales [48, 49].

2.2 Ultrafast spin dynamics in ferromagnetic metals

This section aims to provide a basic understanding of laser induced ultrafast phenomena in 3d ferromagnetic transition metals. After laser excitation, the exchange and dissipation of energy and spin angular momentum among different subsystems is introduced. Relevant earlier works of experiments as well as theories are reviewed.

Magnetic order in ferromagnetic materials can be manipulated on different time scales, which originate from different fundamental physical processes, which can be determined by the interaction energy E via Heisenberg's principle $\tau \approx h/E$. The spin dynamics range from nanoseconds to femtoseconds. In Figure 2.3 the characteristic time scales are shown. Pulsed magnetic fields can excite the magnetic order as a precession of magnetization on the intermediate time scales 1 ps $-$100 ps. At this time scales, the electron-phonon, phonon-phonon and spin-lattice couplings play a major role. At the same time, the electronic excitation should be considered. On the slowest timescale 100 ps $-$ 10 ns, the magnetization dynamics are mainly driven by dipolar interactions, external fields and spin-lattice interactions. Switching of magnetization under external magnetic fields is associated with a damped precessional motion. The damping of magnetization can be successfully described by phenomenological Landau-Lifschitz-Gilbert (LLG) theory, without considerations of electronic excitations. On the time scales 1 fs – 1 ps where the magnetism is accessible by ultrashort laser pulses, the magnetic order can be manipulated in the ultrafast time scales via electron-electron, exchange interaction, spin-orbit coupling and electron-phonon coupling [6].

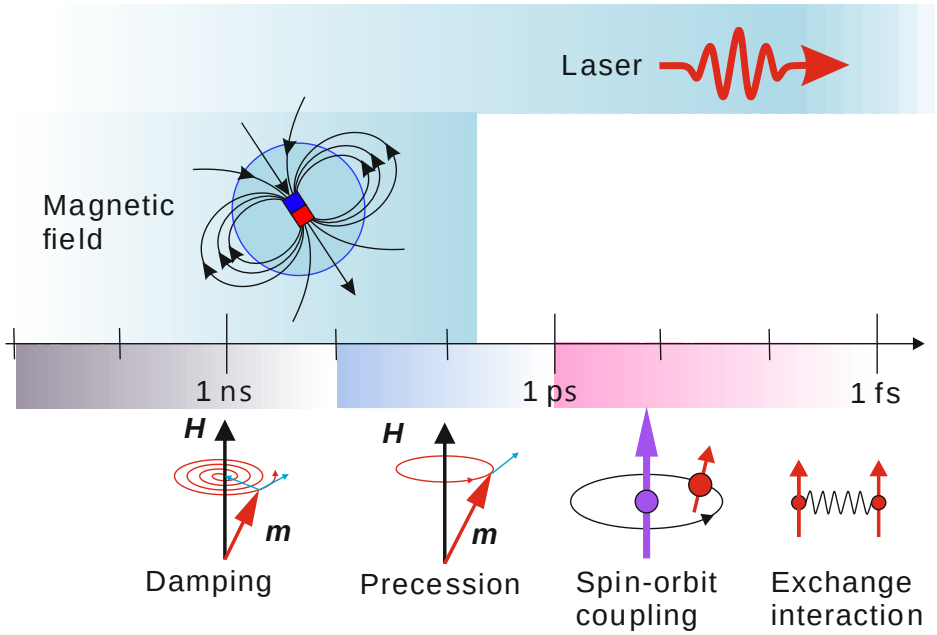

Figure 2.3: Time scales of magnetization dynamics interacted with magnetic field and laser field. Redrawn from [6]

2.2.1 Laser induced ultrafast demagnetization

In 1996, a novel work regarding laser induced demagnetization was done by Beaurepaire *et al*. [11], in which a loss of magnetization on sub-picosecond timescales was observed. In the experiment, a 22 nm ferromagnetic Nickel film was pumped with a 60 fs laser pulse, the hysteresis loops of magneto-optical Kerr effect (MOKE) was measured in longitudinal configuration. A fast drop of the remanent magnetization up to 50% within the first picosecond was demonstrated in the pump-probe MOKE experiment, the result is depicted in Figure 2.4. The time scales of demagnetization in Ni is much faster than earlier reported in Gd [50] and Fe [51], 100 ps and 30 ps respectfully, which were attributed to spin-lattice relaxation. The result of Nickel was explained by a phenomenological three-temperature model (3TM), see Figure 2.4.

In 1997, Hochfeld *et al*. [35] obtained a similar result of demagnetization in polycrystalline bulk Nickel by employing magnetization induced second harmonic generation (MSHG) to measure the nonlinear magneto-optical response. In the same year, spin resolved two-photon photoemission experiments (2PPE) by Scholl *et al*. [53] had confirmed the observation of ultrafast drop of magnetization in ultrathin (0.6 nm and 1.2 nm) Ni films. MSHG experiments of thin Ni and Co films [54, 55] under ultrahigh vacuum (UHV) have also demonstrated an instantaneous loss of magnetization.

The interpretation of MOKE signals was questioned by Koopmans *et al*. [56], it was stated that the difference between MOKE ellipticity and rotation i.e. loss of MO contrast cannot be related to the ultrafast ($0 - 0.5$ ps) drop in magnetization. In addition, the signal reflects mainly optical artifacts, which Koopmans *et al*. proposed to be dominated by state-filling/bleaching effects. In another words, a strong pump pulse generates non-equilibrium electrons and holes in respect to Fermi level and therefore blocks the linear optical transition for the probe pulse, especially for pump and probe pulses with the same photon energy. Similar question whether the magnetic contrast reflects the transient magnetization dynamics was also raised for time-resolved MSHG studies. [57].

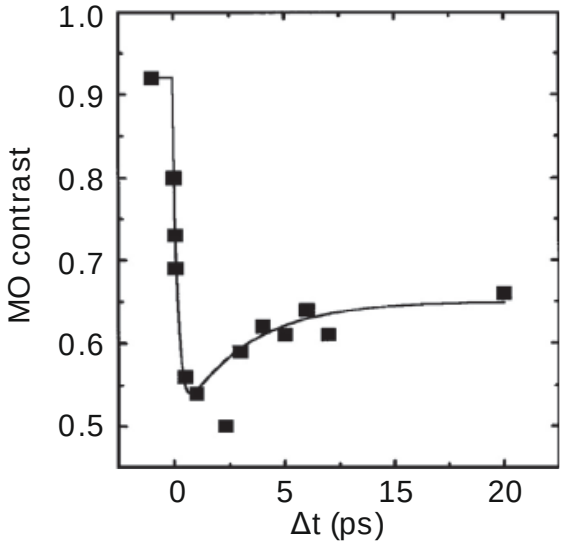

Figure 2.4: Laser induced MOKE signal of a 22 nm polycrystalline Nickel film. The transient magneto-optical (MO) contrast is normalized to the unpumped signal and serves as a measure of the magnetization in the Nickel film. Modified from [11].

However, Guidoni *et al*. [58] and Bigot *et al*. [59] concluded that the MO response indeed reflects the magnetization dynamics on 100 fs time scales in ferromagnetic $CoPt_3$ alloy after electron thermalization. Zhang *et al*. [65] stated that from a theoretical point of view the magnetic signal is reflected in the optical response if the pulse duration is shorter than charge dephasing time. Two-color pump-probe MOKE was employed by Koopmans *et al*. [52] as a probe for magnetization dynamics on <0.5 ps time scales. More recently, the transient spatial magnetization profile can be indeed attributed to the in-depth unequal sensitivity of Kerr ellipticity and rotation, see Wieczorek *et al*. [60].

Laser induced magnetization of 3d transition ferromagnets Fe, Co and Ni were also investigated by other experimental methods such as spin resolved 2PPE [61, 62, 66] and femtosecond X-ray magnetic circular dichroism (XMCD) [63, 64].

Despite the abundant experimental investigations, the microscopic origin of ultrafast demagnetization is still controversial and theoretical descriptions remain contested.

Phenomenological three temperature model (3TM)

The process of magnetization dynamics involves the exchange and dissipation of two basic physical quantities i.e. energy and angular momentum. From the thermodynamic point of view, the electrons, lattice and spins inside the material can be seen as three independent but coupled subsystems. 3TM is applied from the perspective of phenomenology to describe the temperature evolution of three subsystems in time.

In the first few femtoseconds after laser excitation, the energy of the photon is absorbed by the electrons and non-equilibrium electrons are generated. Then within about 100 fs, the electrons are internally thermalized through e-e interactions. Because the heat capacity of the electrons is one or two orders of magnitude less than lattice, the electron temperature rises sharply, while the lattice is still relatively cold. In the time range from 0.1 ps to 10 ps, the lattice is excited via electron-phonon interaction. The temperature of the lattice increases continuously and finally the electron and lattice system reach thermal equilibrium. During this process, the temperature of the spin system evolves with time.

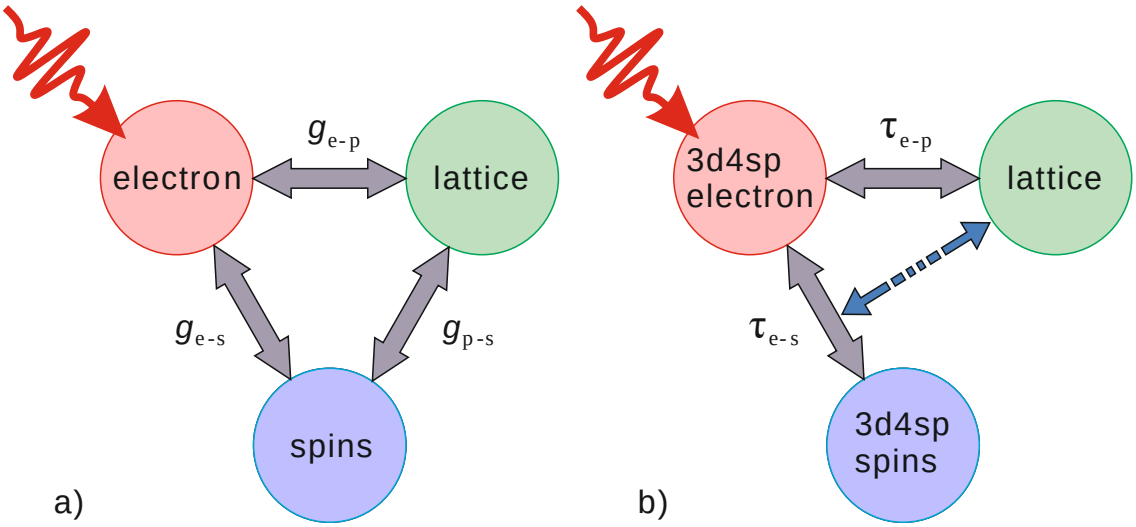

Figure 2.5: Schematic view of three-temperature model, (a) 3TM [11] and (b) M3TM [52] for 3d ferromagnets. Solid arrows represent energy exchange between reservoirs, and the dash arrow indicates transfer of spin angular momentum.

In the first few 100 fs the spin subsystem continuously obtains energy from the electron subsystem. The efficiency of energy transfer depends on the electron-spin coupling strength $g_{e\text{-}s}$. The increase in spin temperature causes thermally induced demagnetization. After that, the energy in the spin system is transferred to the lattice via spin-phonon coupling, and magnetization recovery occurs. Generally, the heat capacity of the spin is very small and the energy exchange of the whole dynamics mainly depends on the electron-phonon coupling $g_{e\text{-}p}$. After the thermalization of the entire system, the temperature of the laser-irradiated area is decreased by heat exchange with the surrounding environment.

The 3TM provides an intuitive picture of the energy redistribution and equilibration in the demagnetization processes. But 3TM did not consider electron-electron thermalization processes and dissipation of spin angular momentum. Koopmans *et al*. [52] presented a microscopic three temperature model (M3TM) that a dissipation channel of angular momentum is included via phonon mediated Elliott-Yafet spin-flip scattering. As suggested in Figure 2.5(b), beside the energy redistribution, the angular momentum can be transferred to lattice [87]. More details about M3TM is reviewed in the next section.

2.2.2 Theories and microscopic mechanism

Photon field and spin-orbit scattering

Zhang et al. [69, 65] and Bigot et al. [70] proposed the light field as the driving force for the demagnetization. The process is a combined effect of intense light field and spin-orbit coupling. A very strong pump pulse modifies the material's potential and changes the symmetry that modified spin-orbit interaction may promote changes in magnetization [71], as far as the light field is present. This process would be less likely to be the dominant effect during demagnetization processes in the present thesis, since it required

such an intense laser field. The absorbed fluence in [70] is 12 mJ/cm^2 and in this present work 0.25 mJ/cm^2, see Chapter 5.

Electron-quasiparticle scattering

The atomistic Landau-Lifshitz-Gilbert and the Landau-Lifzhitz-Bloch approaches [72-75] provide similar results to explain ultrafast spin relaxation and yield a valuable insight, namely that the angular momentum is dumped into the lattice due to an unspecified microscopic mechanism. Laser induced magnetization dynamics in ferromagnets [73] and ferrimagnets [76] can be captured with well-chosen dissipation parameters.

A number of theoretical models based on a particular spin dissipation channel have been proposed to be the microscopic mechanism of ultrafast demagnetization. The possible ultrafast dissipation channels are Elliott-Yafet electron-phonon spin-flip [52], electron-magnon spin-flip [61], and electron-electron spin-flip [77] scatterings.

The Elliot-Yafet theory was originally developed to treat electron-phonon scattering in a semiconductor, and was combined with theory of Gilbert damping to unify magnetization dynamics [78, 79], which was known as phonon-mediated Elliott-Yafet spin-flip scattering. Koopmanns et al. [52] provided arguments in favor of Elliott-Yafet spin-flip scattering as dominant effect for demagnetization processes. This dissipation channel of angular momentum was employed in the microscopic three temperature model. The combined M3TM has successfully classified the spin dynamics between several 3d ferromagnetic transition metals (Ni, Co and alloys such as $CoPt_3$) and rare-earth metal (Gd and alloys TbFe [67]) by the ratio of Curie temperature and atomic magnetic moment, but the calculation of M3TM relies on a number of approximation and phenomenological parameters for each calculated metal.

However, the determination of spin-flip scattering probabilities in M3TM is not accurate according to Carva et al. [68, 80]. The calculated magnetization change rate by thermalized electrons distribution is too small to explain the demagnetization. In the non-equilibrium (NEQ) electron regime, the demagnetization cannot be accounted with alone Elliott-Yafet electron-phonon spin-flip processes, some different mechanisms must play a role in the NEQ regime.

Superdiffusive spin transport

Battiato et al. [17, 81] proposed a superdiffusive spin transport model for ultrafast demagnetization. In this model the local dissipation of spin angular momentum through spin-flip scattering events is not considered, instead the loss of magnetization is described by a spin dependent transport of charge carriers out of the laser excited ferromagnetic layers. As suggested in experiments [82-84] in metallic heterostructures that ultrafast non-equilibrium spin transport is a possible way for the demagnetization processes within few hundred femtoseconds.

Standard diffusive motion shows a linearity of the variance of a particle displacement σ^2 with time, $\sigma^2(t) \propto t^\gamma$ with $\gamma = 1$. Ballistic diffusion has a quadratic relation $\gamma = 2$. In a simple picture the superdiffusive motion $(1 < \gamma < 2)$ experiences first ballistic transport for short times after laser excitation and then become diffusive on several hundred femtoseconds. More details of laser induced spin currents are introduced in the next section.

Spin-orbit mediated spin-flip scattering

It was proposed by the time-dependent density functional theory (TDDFT) [85] and many body theory [86] that demagnetization in ultrafast time scales (~ 100 fs) can be mediated by spin-orbit coupling, as well as some recent experiments [87].

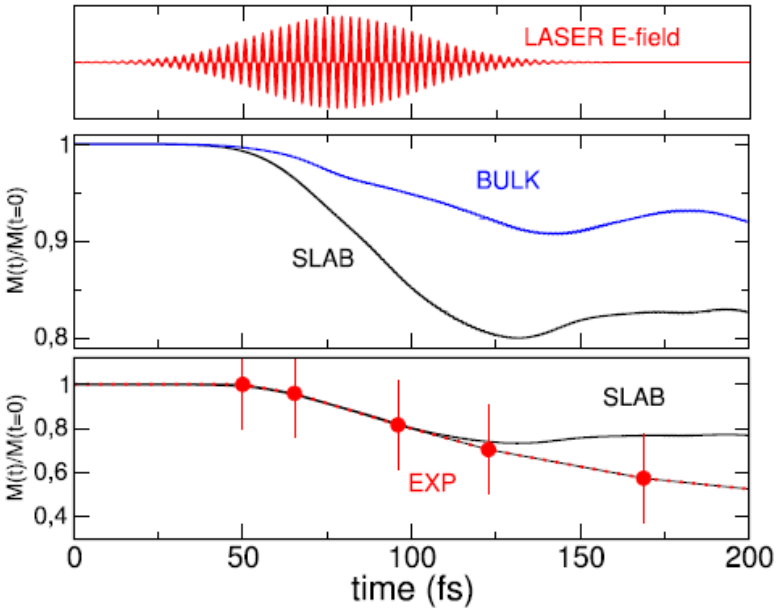

Figure 2.6: TDDFT Simulation of demagnetization dynamics in bulk and thin Ni films. **Top panel**: Applied laser field in calculation with an intensity of 3.8×10^{11} W/cm^2, the laser fluence of 8.05 mJ/cm^2 and full width at half maximum (FWHM) of 40 fs. **Middle panel**: Time evolution of total magnetic moment projected in z direction for bulk Ni (blue line) and thin Ni film (black line). **Lower panel**: the averaged layer resolved magnetic moment in comparison with experimental data (red dots [63]). [96]

Time scales of spin-flip are reflected in the energy strength of spin-orbit coupling via Heisenberg's principle. Upon fs laser irradiation the electrons are excited and the spins are preserved, since the total angular moments are conserved, some localized electrons must flip their spins via spin-orbit coupling, thus the spin angular momentum is transferred to orbital moments in 100 fs time scales. Crucially, the angular momentum is not accumulated in orbital moments since it is quenched in the crystal lattice field [86]. As a result, spin-orbit mediated spin-flip scatterings causes a loss of magnetization.

Ab initio TDDFT

TDDFT is the time-dependent version of material-specific DFT. For a given initial state, the time-dependent external potential is a unique functional of the time-dependent density [88]. A system of non-interacting particles can be chosen so that the density of the non-interacting system is always equal to the density of the interacting system. The wave function of this non-interacting system is described by a Slater determinant of single-particle orbitals. In the noncollinear spin-dependent version, the time-dependent Kohn-Sham (KS) single-particle orbitals are Pauli spinors determined by the equations [85]:

$$\mathrm{i}\frac{\partial \Psi_i(\boldsymbol{r},t)}{\partial t} = \left[\frac{1}{2}\left(-i\nabla + \frac{1}{c}\boldsymbol{A}_{\mathrm{ext}}(t)\right)^2 + v_{\mathrm{s}}(\boldsymbol{r},t) + \frac{1}{2c}\boldsymbol{\sigma}\cdot\boldsymbol{B}_{\mathrm{s}}(\boldsymbol{r},t)\right.$$

$$+\frac{1}{4c^2}\boldsymbol{\sigma}(\nabla v_s(\boldsymbol{r},t)\times -i\nabla)\Big]\Psi_i(\boldsymbol{r},t) \tag{2.9}$$

where $\boldsymbol{A}_{\mathrm{ext}}(t)$ indicates the applied laser field, $\boldsymbol{\sigma}$ the Pauli matrices. The KS effective potential $v_{\mathrm{s}}(\boldsymbol{r},t)=v_{\mathrm{ext}}(\boldsymbol{r},t)+v_{\mathrm{H}}(\boldsymbol{r},t)+v_{\mathrm{XC}}(\boldsymbol{r},t)$ consists of the external potential v_{ext}, the classical electrostatic Hartree potential v_{H} and the exchange-correlation (XC) potential v_{XC}. KS magnetic field $\boldsymbol{B}_{\mathrm{s}}(\boldsymbol{r},t)=\boldsymbol{B}_{\mathrm{ext}}(t)+\boldsymbol{B}_{\mathrm{XC}}(\boldsymbol{r},t)$ corresponds to the magnetic field of laser pulse $\boldsymbol{B}_{\mathrm{ext}}$ plus XC magnetic field $\boldsymbol{B}_{\mathrm{XC}}$. The last term is the spin-orbit coupling (SOC) term.

TDDFT is a parameter free, *ab initio* method. Regarding the vector field $\boldsymbol{A}_{\mathrm{ext}}(t)$, in dipole approximation the spatial dependency of the laser field is viewed as constant, thus, only the time dependent part is applied. SOC is dependent on the gradient of the potential, stronger changing potential trend to have more localized electron, which results in a stronger SOC.

Krieger et al. [96] performed TDDFT simulation with realistic laser pulse parameters, and the main results of demagnetization in bulk and thin Ni films is shown in Figure 2.6. The simulations stated that the demagnetization in bulk is induced by spin orbit coupling in the first ~100 fs after laser excitation. For the ferromagnetic thin Ni films the spin-orbit mediated spin-flip scattering is enhanced due to the broken symmetry of the surface, which increases the rotating spin currents in the system. The demagnetization dynamics of thin Ni films (SLAB curve in Figure 2.6) is then explained by a combination of spin current flow and SOC mediated spin-flip scattering.

TDDFT is however an expensive method. Simulation with the exact laser pulse parameters and bulk system requires month long (or even longer) calculation time considering the current computer capability. In this thesis, a combined study of TDDFT and MSHG experiments on ultrathin Co/Cu(001) films is present in Chapter 5, in which the simulation and experiments are performed under identical sample dimensions and laser pulse parameters.

2.2.3 Optical generation of fs spin current

Spin current in ferromagnetic (FM) metals can be generated by ultrashort laser excitation [17, 82]. It was experimentally demonstrated that the spin current can act as a channel for ultrafast demagnetization [84, 89] and enhance the transient magnetization of a neighboring layer [90], as well as exerting an ultrafast spin-transfer torque in a metallic hetero-structure [13, 14]. The idea of spintronics is that spins can be injected at one location and appear elsewhere without the accompanying charge motion, which dissipates energy through resistance. One note that although the charge is transported, it is screened. Spintronic devices could be made analogous to transistors that do not generate any heat, and can be made smaller than the traditional electronics.

The electronic density of states (DOS) in a ferromagnet is split into majority (spin up) and minority (spin down) bands due to the exchange interaction, as illustrated in Figure 2.7. After the photon energy *hv* is absorbed, an electron can be excited usually from a *d* band to *sp*-like bands above Fermi level. The mobility of *sp*-like electrons is much larger than *d* electrons. With a close look, certain amounts of majority e↑ and minority e↓ are excited to different energy above Fermi level with unequal velocities and lifetimes.

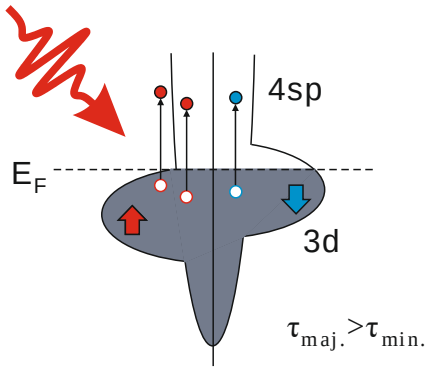

Figure 2.7: Schematic density of state (DOS) of 3d ferromagnetic metals.

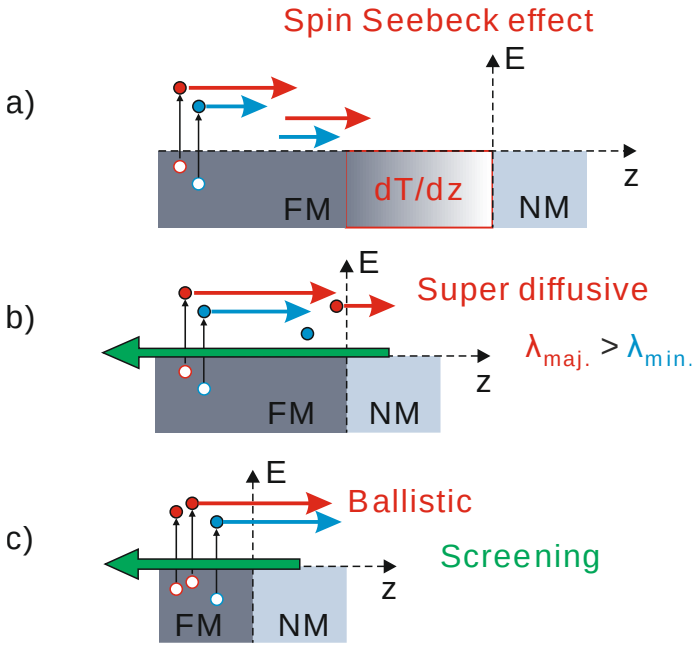

Figure 2.8: Laser induced spin transport in FM/NM heterostructures. (a) $d \gg \lambda_{maj}$, thermal gradient dT/dz drives the spin current across the FM/NM interface through spin dependent Seebeck effect. (b) $\lambda_{min} \leq d \leq \lambda_{maj}$, superdiffusive spin polarized current is generated due to spin dependent MFP. (c) $d < \lambda_{min}$, both excited majority and minority electrons transport out of FM in ballistic regime, a net spin current is caused by unequal number. Red and blue arrows indicate flow of majority and minority, respectively. Green arrow represents a screening current formed by electrons around E_F.

For example, in cobalt, primary excited electrons are calculated to be about 0.7 eV and 1.1 eV higher than Fermi level for majority and minority, respectively [60]. Despite the energy difference, majority electrons usually have larger velocities than minority. Crucially, majority electrons have a longer lifetime τ_{maj} than that of minority. This is due to the fact that empty states around E_F in minority band provide large phase space for scattering, thereby minority electrons have shorter lifetimes. Thus, the optically excited majority electrons have larger inelastic mean free path (MFP) than minority, typically in a factor of 1 – 5. In Ni the spin dependent inelastic MFP is mainly governed by spin dependence of lifetimes, whereby the velocities are more important in Fe [91, 92].

Three regimes of laser induced spin transport can be characterized by the thickness of the ferromagnetic layer and are depicted in Figure 2.8.

In a thicker film where the thickness is much greater than spin dependent inelastic MFP, see Figure 2.8 (a), all the majority and minority electrons have decayed before they reach the interface. However, due to the strong thermal gradient dT/dz caused by scattering events, a spin current in the diffusive regime can be generated by the thermal gradient, which is known as the spin dependent Seebeck effect [93, 94, 95].

For the case of superdiffusive spin transport that FM thickness is smaller but close to MFP, majority electrons can travel through the FM film and across the interface, meanwhile minority electrons are trapped in FM and can be accumulated at the interface. In addition, as shown in Figure 2.8 (b), a screening current in the opposite direction is generated to decline the built up of charge [68]. The carrier flow creates charged regions that generate an electric field. The electric field acts on both spin channels and on all conduction electrons around Fermi energy, excited electrons as well as holes in valence band are also involved. Thus, a back flow is caused necessary to compensate the free charge. By adding the superdiffusive and screening currents, a spin polarized super-diffusive current across FM/NM interface is generated.

A ballistic regime appears when the FM becomes very thin as depicted in Figure 2.8 (c). In this scenario, although both majority and minority electrons can escape from the FM, more majority electrons are pumped into neighboring NM layer. Similar to the superdiffusive regime, charge carriers are also screened. Nevertheless, a net spin polarized current can still be generated. Furthermore, one needs to consider interfaces. The inversion symmetry breaking at the interface between two different materials generates a strong interfacial spin-orbit coupling (ISOC) that may influence the spin and charge transport in hybrid structures.

In general, owning to the nature of exchange splitting in ferromagnetic metals, which results in spin dependent binding energies, velocities, lifetimes and transmission probabilities at the interface, fs spin currents can be generated by laser excitation. This thesis has particularly addressed spin transport in Co/Cu(001) films and the role of interfaces in Chapter 5.

2.3 Electron dynamics at adsorbate/metal interfaces

Optically induced charge transfer at molecule-metal interfaces

Optically induced charge transfer at molecule-metal or -semiconductor interfaces is crucial for many research field such as photocatalysis [97, 98], surface photochemistry [99], solar cells [100] and molecular spintronics [20, 101]. There are abundant studies of charge transfer excitation done by photoelectron spectroscopy [108-110], linear and nonlinear optical methods [111-113].

An isolated molecule in gas phase e.g. shown in the right part of Figure 2.10, which has discrete molecular levels, and the lifetime of those states are infinite. As being brought close to the metal surface, discrete levels are hybridized by coupling with many states of metal. Mixing of the discrete molecular levels with the substrate continuum results in a finite lifetime τ of the molecular level that electrons can escape to the metal with a certain probability. The probability density of molecular states reaches a peak at the molecule-metal interface and gradually disappears in bulk. This leads to a broadened molecular level with width Γ based on Heisenberg's uncertainty:

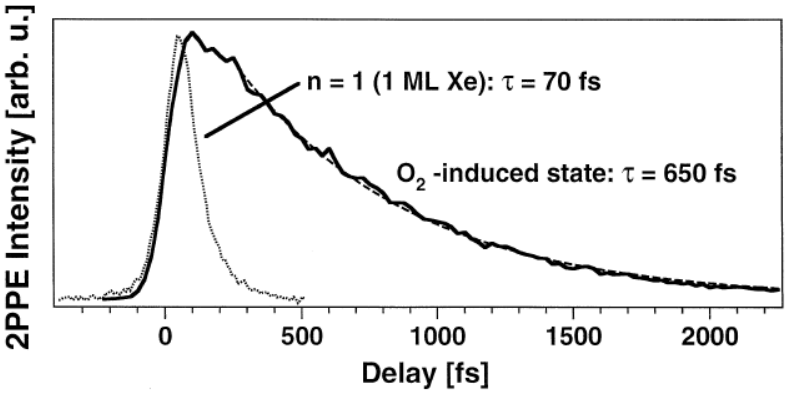

Figure 2.9: 2PPE lifetime measurements of n = 1 image state of 1 ML Xe/Cu(111) and O_2 induced state of 1 ML O_2/1 ML Xe/Cu(111) [103].

$$\Gamma \approx \frac{\hbar}{\tau} \tag{2.10}$$

The energy broadening is in first approximation proportional to the DOS of the metal, depending on the coupling strength, it can range from meV up to few eV [101]. One example to visualize the coupling strength and the lifetime of adsorbate on a metal substrate is Hotzel et al. [102, 103]. They observed a much longer lifetime of interfacial state of physisorbed O_2 on 1 ML Xe/Cu(111) in comparison to physisorbed Xe/Cu(111), see Figure 2.9. They also found that the lifetime can be controlled by varying the coverages of spacing Xe layers between Cu(111) substrate.

Another result of the interaction with metal is that the energy level is shifted in respect to isolated case, this is a combined effect of metal DOS, interfacial dipoles and image forces [104]. Molecules can be physisorbed at metal surface through van der Waals or dispersion forces [105]. The primary difference between physisorption and chemisorption is that significant hybridization of molecular orbitals with metal is involved in chemisorption.

Direct charge transfer excitation

The process of laser induced interfacial charge transfer can be divided into two primary mechanisms: direct and indirect charge transfer. The direct photoexcitation pathways are depicted in Figure 2.10. The electrons are injected to unoccupied molecular states via dipole transition with probability R_{k2} [106]:

$$R_{k2} \propto |\langle 2|\, \boldsymbol{\mu}\, |k\rangle \cdot \boldsymbol{E}|^2 \cdot \delta(E_2 - E_k - h\nu)$$

Where $|k\rangle$ and $\langle 2|$ indicate the initial metal state and unoccupied molecular state, $\boldsymbol{\mu}$ is the transition dipole operator and $\boldsymbol{E}$ the electric field. Optical selection rules can be employed to assign specific molecular orbitals in spectral analysis. If the dipole matrix elements are considered, the symmetry selection rule depends on the polarization of the incident light. Therefore, the direct light-induced charge transfer rate can be controlled by changing the wavelength, intensity and polarization of the incident light.

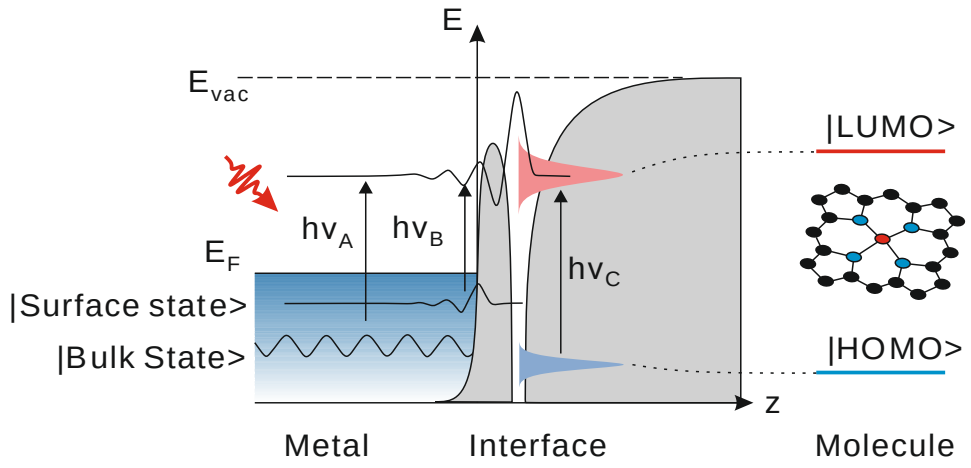

Figure 2.10: Schematic representation of direct optically induced charge transfer at molecule-metal interfaces. Electrons can be excited from bulk continuum or surface state to an unoccupied molecular resonance (LUMO) at different photon energies $h\nu_A$ or $h\nu_B$. Excitation from occupied molecular orbital (HOMO) to LUMO is possible with $h\nu_C$ but does not account for charge transfer from metal. In contrast to discrete levels of isolated molecules, molecular states are energy broadened and shifted at metal surface. Redrawn from [106, 107].

The initial metal wave function and the molecular wave function should co-localized in the same spatial region for the transition dipole moment $M_{k2} = \langle 2| \boldsymbol{\mu} |k\rangle$ to be nonzero. For most molecules, interaction of a localized anionic molecular state with delocalized substrate results in a fast vanishing probability density of molecular states into bulk, so direct charge transfer excitation is not easy to observe. This excitation path is depicted in Figure 2.10 with an excitation energy $h\nu_A$. This spatial co-localization may be the reason why an anionic metal-molecular resonance is rarely observed in 2PPE. Therefore, a direct charge transfer is easily occurred from a delocalized substrate to molecular state with proper energy $h\nu_B$. Electrons in HOMO can also be excited to LUMO with photon energy $h\nu_C$ and transfer back to metal.

One evidence of direct optically induced interfacial charge transfer is provided by 2PPE experiment from Höfer et al. [108]. They observed a quantum beats of coherently excited $n = 3, 4$ image potential states on Cu(001). This quantum interference is suppressed by adsorption of CO molecules [109]. This decoherence is explained by charge transfer into molecular states, because the dephasing is expected to be much faster in molecule. Petek et al. [107] stated that the small dephasing time is measurable for direct induced electron transfer in to antibonding resonance for Cs-Cu(111).

Indirect charge transfer excitation

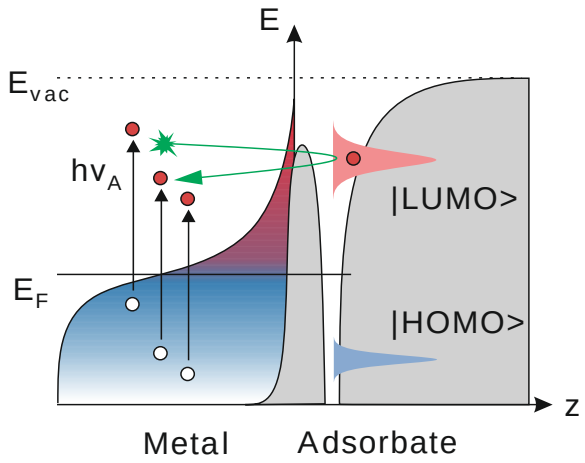

Figure 2.11: Schematic illustration of hot electron transfer to a LUMO state at the surface. Hot electrons are generated in bulk and can be transferred to molecular state indirectly via elastic and inelastic scattering. The green arrow represents inelastic processes coupled to molecular degrees of freedom. Redrawn from [106, 107].

Indirect charge transfer excitation at metal-molecule interface involves mostly the hot electron transfer from metal substrate to molecular states, as schematically depicted in Figure 2.11.

Indirect charge transfer excitation can be understood from the picture of three-step model widely used in photoemission [106]: (i) Laser excitation generates electron-hole pairs in the metal bulk. (ii) The excited electrons and holes migrate to the surface through the lattice, meanwhile secondary electrons can be generated via electron-electron scattering. (iii) Hot electron transfer into unoccupied orbital via tunneling or e-e and e-ph scattering processes. The first two steps are identical to photoemission, but in the last step, the escape of photoelectrons from the surface field is replaced by the interfacial potential barrier. In the linear regime where the excitation density is insufficient to populate states above $E_F + \hbar\nu$ through electron-electron scattering. These electrons close to surface are excited to a Bloch state with appropriate energy and momentum. They may scatter ballistically to unoccupied molecular resonance. Hot electrons in bulk can be scattered to unoccupied states via e-e and e-ph scattering. The inelastic processes are mainly contributed by two effects at interface: intraband e-e interaction and vibrational or rotational excitation of the molecule.

The hot electron mechanism at interfaces has been observed by polarization dependent 2PPE experiment. For example Lee et al. [110] reported that dissociation of phenol molecule on Ag(111) is attributed to hot electron transfer into molecular resonance.

As the interaction of light with molecule-metal is concerned, variables such as wavelength/photon energy, intensity and polarization of the light play an important role to unify the charge transfer excitations. These key factors are explored with surface second harmonic generation (SHG) spectroscopy at 1 ML Fe-porphyrin on Cu(001) in Chapter 6.

3 Nonlinear optics as a surface-sensitive probe

Nonlinear optics has become a fast growing field after the invention of the laser in 1960. At that time in 1961 the first optical second harmonic generation (SHG) experiment by Franken *et al.* [117] was performed through crystalline quartz which yields only 10^{-11} SH-photons per incident fundamental laser pulse. In contrast to SHG from bulk quartz, the absolute SHG yield from surfaces is quite low in the order of 10^{-15} SH-photons per incident photon. This fact points to the need that the incident optical field should have high intensity to efficiently generate nonlinear processes. A big step was then taken after the development of solid state based ultrashort laser systems.

This chapter aims to provide a basic understanding of nonlinear optics of concern in this thesis. In particular, the surface SHG and magnetization induced second harmonic generation (MSHG) are addressed, since they are employed as an optical method to probe the electron and magnetization dynamics at the surface or interface of centrosymmetric materials, where the inversion symmetry is broken.

3.1 Light-matter interaction

Starting from the Maxwell equations, the optical wave equation for the propagation of the electric field through a medium can be derived as in [118]:

$$\nabla \times \nabla \times \boldsymbol{E}(\boldsymbol{r},t) + \frac{1}{c^2}\frac{\partial^2}{\partial t^2}\boldsymbol{E}(\boldsymbol{r},t) = -\frac{4\pi}{c^2}\frac{\partial^2}{\partial t^2}\boldsymbol{P}(\boldsymbol{r},t) \tag{3.1}$$

The optical response of a medium to an incident electromagnetic wave $\boldsymbol{E}(\boldsymbol{r}, t)$ is described by an induced coherent polarization $\boldsymbol{P}(\boldsymbol{r}, t)$ which is the source of linear and nonlinear reflection. One could view it as an oscillating dipole that radiates light.

The induced polarization depends on the strength of the incident electric field and consists of linear $\boldsymbol{P}^L$ and nonlinear term $\boldsymbol{P}^{NL}$:

$$\boldsymbol{P}(\boldsymbol{r},t) = \boldsymbol{P}^L(\boldsymbol{r},t) + \boldsymbol{P}^{NL}(\boldsymbol{r},t) \tag{3.2}$$

The nonlinear term can be ignored for weak electric field ($I < 10^{10}$ W/m^2):

$$\boldsymbol{P}^L(\boldsymbol{r},t) = \int_0^{+\infty} dt_1 \int_{-\infty}^{+\infty} \varepsilon_0 \chi^{(1)}(r - r_1, t - t_1)\boldsymbol{E}(r_1,t_1)d\boldsymbol{r}_1 \tag{3.3}$$

Here ε_0 is the dielectric constant and $\chi^{(1)}$ represents the first order susceptibility of the medium. One note that the linear susceptibility is a second-rank tensor, which means the induced polarization can have a different orientation than the incident electric field. In case of strong incident fields, the nonlinear term should be taken into account. Polarization of higher order can be expanded in a series of the electric field:

$$\boldsymbol{P}^{(n)}(\boldsymbol{r},t) = \int_0^{+\infty} dt_1..dt_n \int_{-\infty}^{+\infty} \varepsilon_0 \chi^{(n)}(\boldsymbol{r}-\boldsymbol{r}_1,..,\boldsymbol{r}-\boldsymbol{r}_n,t-t_1,..,t-t_n) \times E(\boldsymbol{r}_1,t_1)..E(\boldsymbol{r}_n,t_n)d\boldsymbol{r}_1..d\boldsymbol{r}_n \quad (3.4)$$

So the entire resulting polarization is:

$$\boldsymbol{P}(r,t) = \sum_{n=1}^{\infty} \boldsymbol{P}^{(n)}(\boldsymbol{r},t) \quad (3.5)$$

The origin of the nonlinear process can be understood as anharmonic motion of electrons in the medium under strong electromagnetic perturbation. In a weak field, the movement of electrons is similar to a harmonic oscillator. In dipole approximation, the total induced polarization can be expressed in the frequency domain by Fourier transformation:

$$\boldsymbol{P}(\omega) = \boldsymbol{P}^{(1)}(\omega) + \boldsymbol{P}^{(2)}(2\omega) + \boldsymbol{P}^{(3)}(3\omega) + \cdots \quad (3.6)$$

or

$$\boldsymbol{P}(\omega) = \varepsilon_0 \chi^{(1)}(\omega)\boldsymbol{E}(\omega) + \varepsilon_0 \chi^{(2)}(2\omega;\omega_1,\omega_2)\boldsymbol{E}(\omega_1)\boldsymbol{E}(\omega_2) + \cdots \quad (3.7)$$

The induced polarization is then the sum of all possible harmonics. The second order nonlinear processes are described by the susceptibility tensor $\chi^{(2)}$. These processes are second harmonic generation $\chi^{(2)}(2\omega = \omega + \omega)$, sum-frequency generation $\chi^{(2)}(\omega = \omega_1 + \omega_2)$, difference-frequency generation $\chi^{(2)}(\omega = \omega_1 - \omega_2)$ and optical rectification $\chi^{(2)}(0 = \omega - \omega)$. We will focus on second harmonic generation in the next section.

3.2 Surface second harmonic generation

In this section, the optical SHG is introduced as a surface and interface sensitive probe for centrosymmetric media. In particular pump-probe SHG as a technique to study electron dynamics at metal surfaces is reviewed.

Second harmonic generation (SHG) is a degenerate case of sum-frequency generation (SFG) with the incident electric field having the same frequency $\omega = \omega_1 = \omega_2$. In electric dipole approximation where the contributions of the magnetic field of the incident light and electric quadrupole are neglectable, the induced second order polarization can then be expressed as:

$$\boldsymbol{P}_i^{(2)}(2\omega) = \varepsilon_0 \chi_{ijk}^{(2)}(2\omega)\boldsymbol{E}_j(\omega)\boldsymbol{E}_k(\omega). \quad (3.8)$$

This equation shows that the *i*-th component of the second order polarization is induced by the *j*-th and *k*-th components of the incident electric field with susceptibility $\chi_{ijk}^{(2)}$ in Cartesian coordinates.

From the perspective of quantum mechanics, SHG can be described by density matrix formalism [118] as:

$$\chi_{ijk}^{(2)}(2\omega) = -Ne^3 \int \left(\frac{\langle 1,\boldsymbol{k}|r_i|3,\boldsymbol{k}\rangle\langle 3,\boldsymbol{k}|r_j|2,\boldsymbol{k}\rangle\langle 2,\boldsymbol{k}|r_k|1,\boldsymbol{k}\rangle}{[2\hbar\omega - E_{31}(\boldsymbol{k}) - i\hbar\alpha_{31}][\hbar\omega - E_{21}(\boldsymbol{k}) - i\hbar\alpha_{21}]} f_1(\boldsymbol{k}) + \chi^{NR}\right) d\boldsymbol{k} \quad (3.9)$$

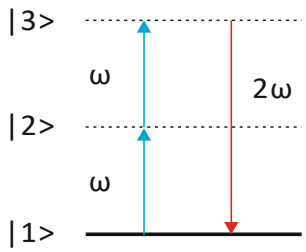

Figure 3.1: Schematic view of SHG process. The optical transition involves ground state $|1\rangle$, intermediate state $|2\rangle$ and final state $|3\rangle$. Dashed line and solid line represent virtual and real state, respectively.

The susceptibility tensor element $\chi_{ijk}^{(2)}$ is proportional to the density of electrons Ne^3 with the Fermi factor $f_1(\boldsymbol{k})$ for state $|1, \boldsymbol{k}\rangle$ integrated for all electron wave vectors $\boldsymbol{k}$. Here $\hbar\alpha$ represents the linewidth of the transitions. For the case the fundamental photon energy does not match the transition energy, $\chi_{ijk}^{(2)}$ is mainly dominated by the non-resonant term χ^{NR}. The SHG process is depicted in Figure 3.1. The ground state $|1\rangle$ interacts with two photons and instantaneously generates a photon with 2ω frequency. The states $|2\rangle$ and $|3\rangle$ can be either virtual or real, the difference is that the SHG can be resonantly enhanced if the photon energies match the involved real transition states.

SHG process is an optical parametric process. Unlike two-photon absorption, there is no net energy and momentum transfer between the quantum state and the interacting optical field, i.e. the quantum state remains unchanged. One note that Figure 3.1 serves only as an intuitive picture of optical transition in SHG processes.

3.2.1 Symmetry considerations

The second order nonlinear effect is given by a third-rank tensor i.e. the susceptibility tensor $\chi_{ijk}^{(2)}$ consists of 27 independent elements and the tensor elements are typically complex. Due to this large number of components in the susceptibility tensor, it is difficult to evaluate the SHG from a medium in a quantitative manner. However, the number of non-zero tensor components can be reduced under symmetry considerations, which simplifies the calculation of SHG signals. A general view of symmetry is developed based on von Neumann's principle [119], which states that the physical properties should be invariant with respect to symmetry operations. First the symmetry properties of centrosymmetric materials are considered as this type of symmetry is the most common in nature and is as well relevant in this work. Due to symmetry, the n-th order susceptibility tensor $\chi^{(n)}$ must be invariant to transformation of coordinate $\boldsymbol{r} \to -\boldsymbol{r}$,

$$\chi^{(n)}(\boldsymbol{r}) = \chi^{(n)}(-\boldsymbol{r}) \tag{3.10}$$

The induced polarization can be written from (3.7) as

$$\boldsymbol{P} = \varepsilon_0\left[\chi^{(1)}\boldsymbol{E} + \chi^{(2)}\boldsymbol{EE} + \chi^{(3)}\boldsymbol{EEE} + \cdots\right] \tag{3.11}$$

According to the symmetry, the $\boldsymbol{E}$ is replaced by $-\boldsymbol{E}$, then $\boldsymbol{P}$ should become $-\boldsymbol{P}$.

$$\chi^{(2n)}(-\boldsymbol{E})^{2n} = -\chi^{(2n)}(\boldsymbol{E})^{2n} \tag{3.12}$$

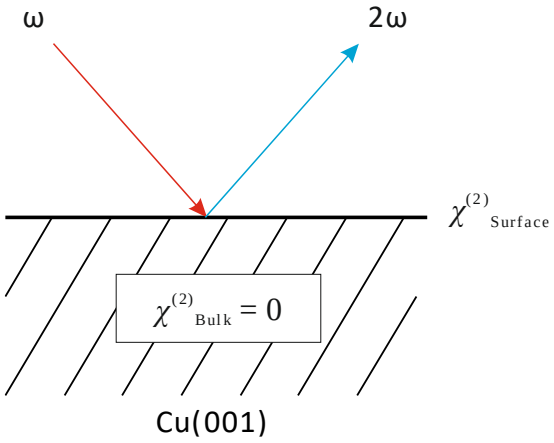

Figure 3.2: Sketch of second harmonic generation from the surface of a centrosymmetric material such as Cu(001). Graph redrawn from [16].

As a result $\chi^{(2n)} = 0$ is obtained, which means that all even order susceptibilities vanish in centrosymmetric materials under electric dipole approximation. For example, glass is centrosymmetric and therefore the lowest order nonlinearity arises from the third- order nonlinear susceptibility.

However, there are regions in centrosymmetric systems where the inversion symmetry is broken. For example, the inversion symmetry is locally broken at the surface or the interface between two different media, which makes the SHG possible again. In the case of metals, the inversion symmetry is broken in the area in which the electron density does not yet match the bulk value. Therefore, for centrosymmetric materials within the electric dipole approximation, the SHG process has intrinsic sensitivity at the surface or interface, see Figure 3.2.

In the special case of SHG processes that the incident photons have the identical frequency, so the number of independent tensor elements is reduced from 27 to 18 due to intrinsic permutation symmetry $\chi^{(2)}_{ijk} = \chi^{(2)}_{ikj}$. The second order polarization $\boldsymbol{P}(2\omega)$ is obtained:

$$\begin{pmatrix} P_x \\ P_y \\ P_z \end{pmatrix} = \begin{pmatrix} \chi_{xxx} & \chi_{xyy} & \chi_{xzz} & \chi_{xyz} & \chi_{xxz} & \chi_{xxy} \\ \chi_{yxx} & \chi_{yyy} & \chi_{yzz} & \chi_{yyz} & \chi_{yxz} & \chi_{yxy} \\ \chi_{zxx} & \chi_{zyy} & \chi_{zzz} & \chi_{zyz} & \chi_{zxz} & \chi_{zxy} \end{pmatrix} \begin{pmatrix} E_x E_x \\ E_y E_y \\ E_z E_z \\ 2E_y E_z \\ 2E_x E_z \\ 2E_x E_y \end{pmatrix} \tag{3.13}$$

The number of non-vanishing independent tensor elements can be further reduced by taking into account some special symmetries of a system, e.g. through the crystallographic orientation of the surface and the experimental geometry. If we consider a (001) surface within the scope of this work, which has C_{4v} (4mm) symmetry in point groups, then only three non-vanishing, independent tensor elements remain [120]:

$$\chi_{zzz}, \qquad \chi_{zxx} = \chi_{zyy}, \qquad \chi_{xzx} = \chi_{yzy} \tag{3.14}$$

So the induced second order polarization $\boldsymbol{P}(2\omega)$ is expressed as:

$$\begin{pmatrix} P_x \\ P_y \\ P_z \end{pmatrix} = \begin{pmatrix} 0 & 0 & 0 & 0 & \chi_{xzx} & 0 \\ 0 & 0 & 0 & \chi_{xzx} & 0 & 0 \\ \chi_{zxx} & \chi_{zxx} & \chi_{zzz} & 0 & 0 & 0 \end{pmatrix} \begin{pmatrix} E_x E_x \\ E_y E_y \\ E_z E_z \\ 2E_y E_z \\ 2E_x E_z \\ 2E_x E_y \end{pmatrix} \tag{3.15}$$

Base on the above symmetry considerations, the nonlinear susceptibility $\chi^{(2)}$ is expected to decrease spatially on both sides of the interface. Then the spatial distribution of $\chi^{(2)}$ can be treated as an infinitesimally thin nonlinear sheet. This is especially true because the characteristic length to be compared is the wavelength of light, which is usually a few hundred nanometers. In metals the electron density at surface exhibits a damped Friedel oscillation [121] with a damping range around $5/k_F$ with fermi vector $k_F^{-1} \approx 1 \cdot 10^{-10}$ m. Therefore, the interacting length of the laser field with the second order susceptibility $\chi^{(2)}$ is then considered to be a few atomic layers [122].

3.2.2 Macroscopic formalism for polarization dependent SHG

A phenomenological view of surface SHG can be sketched as follows. An incident field $\boldsymbol{E}(\omega)$ of the fundamental light drives a second order polarization $\boldsymbol{P}(2\omega)$ in dipole approximation:

$$\boldsymbol{P}(2\omega) = \chi^{(2)}(2\omega; \omega, \omega) : \boldsymbol{E}(\omega) \cdot \boldsymbol{E}(\omega) \tag{3.16}$$

Where the second order susceptibility $\chi^{(2)}(2\omega; \omega, \omega)$ describes the intrinsic ability of the sample to radiate SHG. The reflected second harmonic field $\boldsymbol{E}(2\omega)$ is obtained according to Sipe *et al.* [122]:

$$\boldsymbol{E}(2\omega) \propto \boldsymbol{F}(2\omega) \cdot \chi^{(2)} \cdot \boldsymbol{f}(\omega) \cdot |\boldsymbol{E}(\omega)|^2 \tag{3.17}$$

The Fresnel factors are given by:

$$\boldsymbol{F}(2\omega) = \begin{pmatrix} A_p F_c cos\Phi \\ A_s sin\Phi \\ A_p N^2 F_s cos\Phi \end{pmatrix}; \quad \boldsymbol{f}(2\omega) = \begin{pmatrix} f_c^2 t_p^2 cos^2\phi \\ t_s^2 sin^2\phi \\ f_s^2 t_p^2 cos^2\phi \\ 2 f_s t_p t_s cos\phi sin\phi \\ 2 f_c f_s t_p^2 cos^2\phi \\ 2 f_c t_p t_s cos\phi sin\phi \end{pmatrix} \tag{3.18}$$

with the notations:

$$f_s = \frac{sin\theta}{n(\omega)}, \qquad f_c = \sqrt{1 - f_s^2}, \qquad t_p = \frac{2cos\theta}{n(\omega)cos\theta + f_c},$$
$$t_s = \frac{2cos\theta}{n(\omega)f_c + cos\theta}, \qquad A_{p/s} = \frac{2\pi T_{p/s}}{cos\theta}, \qquad N = n(2\omega) \tag{3.19}$$

The Fresnel factors (3.18) quantify the linear optical properties for both fundamental and second harmonic radiation with all optical information such as refractive index, angle of incidence and polarization of light. In (3.19), quantities related to the fundamental or second harmonic are denoted as lower-case or capital letters, respectively. Here $f_{c,s}$ are the projections of the incident wave onto the spatial coordinates. *N* and *n* are the refractive indices at second harmonic and the fundamental frequencies, which are usually complex.

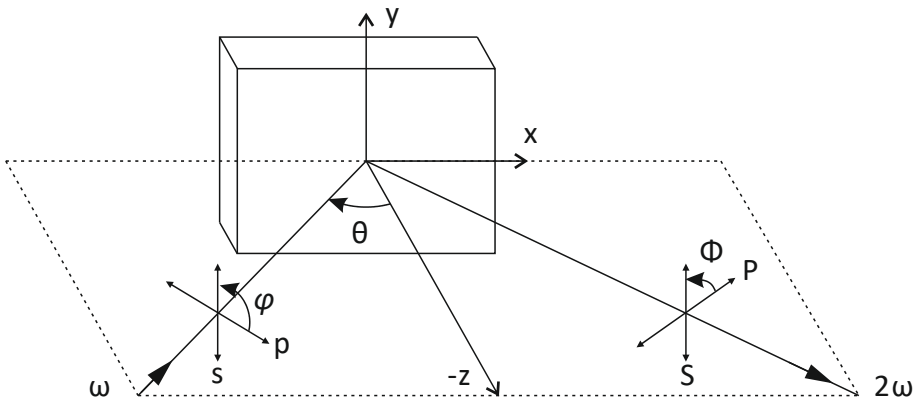

Figure 3.3: Sketch of SHG in reflection from a surface. Graph redrawn from [16].

	s-P	*s-S*	*p-P*	*p-S*	*mix-P*	*mix-S*
(001) or isotropic	zyy	-	zzz, zxx, xzx	-	zzz, zxx, xzx, zyy	yzy
(110)	zyy	-	zzz, zxx, xzx	-	zzz, zxx, xzx, zyy	yzy
(111)	zyy	yyy	zzz, zxx, xzx	yxx	zzz, zxx, xzx, zyy	yzy

Table 3.1: Non-zero elements of $\chi^{(2)}$ for different surface and polarization combinations. Lower-case letters denote polarization of fundamental, capital letters of SHG light. "mix" stands for an incident polarization angle of 45 °[16].

$t_{p,s}$ is the linear transmission coefficients for p- and s-polarized light. $A_{p/s}$ denotes the amplitude of the reflected SHG for p and s polarization. The angles defined in (3.18) and (3.19) are shown in Figure 3.3.

Hence, the generated SH-field $\boldsymbol{E}(2\omega)$ is the product of Fresnel factors and second order susceptibility tensor $\chi^{(2)}$. This sometimes makes the interpretation of SHG very difficult. For isotropic metal surfaces of (001) orientation, there are five non-vanishing tensor elements in $\chi^{(2)}$, but since $x = y$, the number of independent elements is reduced to three as shown in (3.14). One possible way to disentangle their different contributions to SHG is to select certain polarization configuration. Table 3.1 provides the non-zero susceptibility tensor elements for the most common surface symmetries and the polarization combinations for surface SHG.

The generated second harmonic field $\boldsymbol{E}(2\omega)$ from an isotropic Cu(001) surface can be expressed with the corresponding polarization combinations as:

s-P,

$$E_P(2\omega) \propto A_p F_s N^2 \cdot \chi_{zxx} \cdot |E(\omega)|^2 \tag{3.20}$$

p-P,

$$E_P(2\omega) \propto A_p t_p^2 \cdot [2 f_c f_s F_c \cdot \chi_{xzx} + f_c^2 N^2 F_s \cdot \chi_{zxx} + f_s^2 N^2 F_s \cdot \chi_{zzz}] \cdot |E(\omega)|^2 \tag{3.21}$$

mix-S,

$$E_S(2\omega) \propto A_s f_s t_p t_s \cdot \chi_{xzx} \cdot |E(\omega)|^2 \tag{3.22}$$

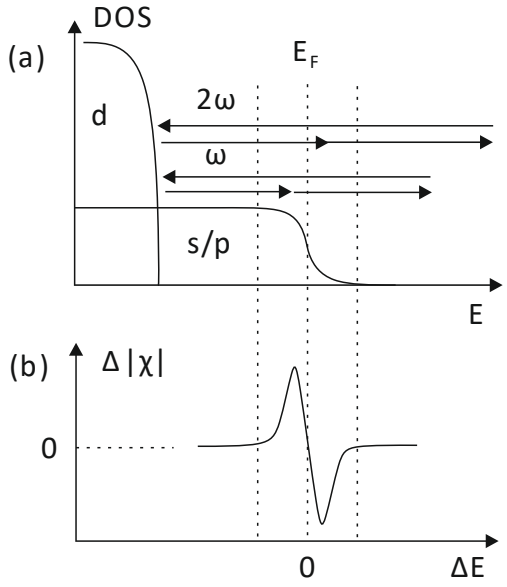

Figure 3.4: (a) Schematic SHG processes with fundamental photon energy near the interband transition threshold (ITT) for noble metals. (b) Transient change of tensor element $|\chi^{(2)}|$ as a function of energy mismatch $\Delta E = \hbar\omega - ITT$. For fundamental photon energy below ITT, an enhancement of $\chi^{(2)}$ is caused by a decrease in the electronic occupancy below Fermi level, while a reduction occurs for $\hbar\omega > ITT$ [26].

Here "s-P" denotes p-polarized SHG generated by s-polarized fundamental incident light. Such polarization combinations are sketched in Figure 3.3. With the equation (3.20) – (3.22), s-P and mix-S SHG depend only on one non-zero tensor element, which enables the separation of different contributions on surface SHG. On the other side, p-P SHG is affected by three independent tensor elements. This turns out the fact that for most common metal, p-P configuration yields the largest SHG from metal surfaces [16].

3.2.3 Pump-probe SHG

Pump-probe SHG has been employed to study the electron dynamics of metal surfaces. The SHG intensity has a quadratic relation to the SH-field $I(2\omega) \propto |E(2\omega)|^2$. Assuming that the SH-field is given by only one single tensor element χ_{ijk}, the transient change can be deduced from the measured SHG intensity by certain polarization combinations:

$$\Delta|\chi_{ijk}| = \sqrt{\frac{I_{2\omega}(t)}{I_{2\omega}(t_0)}} - 1 = \frac{E_{2\omega}(t)}{E_{2\omega}(t_0)} - 1 \tag{3.23}$$

In optical pump-probe SHG experiment, the sample is first perturbed by a strong pump pulse, then followed by another time delayed laser pulse to probe the evolution of the system in time. Here $I_{2\omega}(t_0)$ denotes the unpumped SHG signal. Subsequently, the SHG intensity $I_{2\omega}(t)$ is measured as a function of pump-probe delay t.

In the following the transient character of $\Delta|\chi|$ is discussed. In dipole approximation, the second order susceptibility $\chi^{(2)}$ is sensitive to surface and interface of centro-symmetric media. It can be seen form the general microscopic structure of $\chi^{(2)}$ in (3.9) that in principle the susceptibility can be affected by (i) altering the transition matrix

elements, (ii) changing the probing photon energy and (iii) the Fermi distribution. The transition matrix elements and energy levels are usually not independent. The pump pulse generates hot electrons in metals and redistributes the electron occupation around the Fermi level. Based on the microscopic structure of $\chi^{(2)}$, it becomes obvious that $\chi^{(2)}$ can probe the laser induced electron dynamics.

Depending on the photon energy of fundamental, interband transitions with negative energy mismatch $\hbar\omega < ITT$ will then cause a resonance enhancement of $\chi^{(2)}$, positive energy mismatch corresponds to a reduction of $\chi^{(2)}$. As depicted in Figure 3.4, in case that the Fermi distribution is broadened by hot electrons, an increased density of vacant intermediate states will enhance the SHG for photon energy $\hbar\omega < ITT$, which leads to a positive transient change of $\Delta|\chi|$. For $\hbar\omega > ITT$, the hot electrons populate the states above Fermi level, therefore the transition probability via intermediate state is decreased and caused a negative transient change of $\Delta|\chi|$. The transient behavior of $\chi^{(2)}$ can be expected to be similar to linear reflectivity, but the pump induced relative change is larger and has an opposite sign [26].

3.3 Nonlinear magneto-optics

Investigation of ultrafast magnetization dynamics triggered by femtosecond laser pulses requires methods that are capable to probe the transient changes of the magnetization in the medium with fs time resolution. Almost all studies of ultrafast magnetization dynamics employ similar pump-probe methods, in which the change of the magnetic order is perturbed by an ultrashort laser pulses. Subsequently, the magnetization dynamics can be probed with the aid of a second optical, X-ray or far-infrared/THz pulse as well as the detection of spin-polarized photoelectrons [6]. Different probes provide different views on the very same phenomenon and thus the most complete information can be obtained.

This section briefly introduces the magneto-optical effect and then focuses on magnetization-induced second harmonic generation (MSHG) as well as a formalism for time-resolved measurements in a ferromagnetically ordered sample.

3.3.1 Magneto-optical effect

The magneto-optical effects appear as a change in the polarization state and/or intensity when light is reflected or transmitted from a ferromagnetic material. In reflection this effect is known as magneto-optical Kerr effect (MOKE), and in transmission as the Faraday effect. Voigt effect and Cotton-Mouton effect are also magneto-optical effects.

The origin of magneto-optical effect can be addressed from different perspectives. In a pedagogical point of view, the magneto-optical effects can be explained by the action of the Lorentz force on the electrons. The magnetization breaks the time reversal symmetry of the electron trajectory in the material.

Microscopically, the magneto-optic effect is the coupling of the electric field of light with the magnetic moment of the sample through the spin-orbit interaction. Since the optical response of the medium in the visible spectral range is mainly determined by electrical dipole transitions, and the selection rules for such transitions do not allow spin flipping. Hence the linear and nonlinear magneto-optical effects are mainly mediated by the spin-orbit coupling [181].

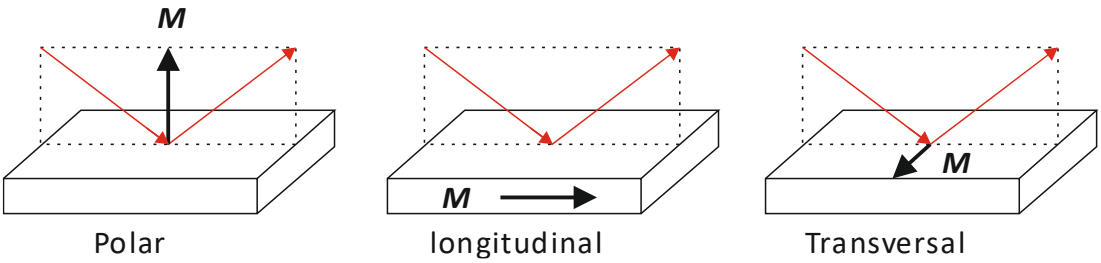

Figure 3.5: Experimental configurations for linear and nonlinear magneto-optics. Dashed line represents the plane of incidence. The magnetization is normal to the surface for polar configuration, parallel to the optical plane for longitudinal and perpendicular to the plane for the transversal configuration, respectively. [125]

In the macroscopic theory, the magneto-optical effects can be described by dielectric constant tensor. The dielectric tensor describes the optical response of the medium. The tensor can be written as:

$$\varepsilon(\omega) = \begin{pmatrix} \varepsilon_{xx} & \varepsilon_{xy} & -\varepsilon_{xz} \\ -\varepsilon_{xy} & \varepsilon_{xx} & \varepsilon_{yz} \\ \varepsilon_{xz} & -\varepsilon_{yx} & \varepsilon_{xx} \end{pmatrix} \tag{3.24}$$

The optical response of the medium in the presence of magnetization becomes optically anisotropic. The magneto-optical effect is caused the asymmetry of these off-diagonal complex tensor components in the dielectric tensor $\varepsilon(\omega)$. We take MOKE as an example to explain the magneto-optical effect. Schematic experimental geometry of MOKE is depicted in Figure 3.5. In polar and longitudinal configurations, the reflected light manifests itself with a rotation and ellipticity of the linear polarized incident beam. In transversal geometry, the intensity of the reflected light is modified.

This phenomenon can be quantified within the macroscopic picture. An incident linear polarized laser beam can be decomposed into left and right circular polarized light. Due to the asymmetry of the off-diagonal elements in the dielectric constant tensor, magneto-optical effects occur. The effect can be explained with the real and imaginary part of the complex susceptibility. The interaction with the real part results in different propagation velocities of left-handed and right-handed polarized light in the sample. This results in a phase shift between the left and right circular polarization components, which causes the polarization plane of light to rotate. In the same way, the difference in the imaginary part of the complex dielectric constant makes the samples have different absorption strengths for left-handed polarized light and right-handed polarized light, which leads to changes in the ellipticity of reflected light. When the linearly polarized light is reflected from the magnetic surface, the linearly polarized light is converted into elliptically polarized light.

3.3.2 Magnetization induced second harmonic generation

SHG is allowed at surfaces or interfaces of a centrosymmetric medium and can be applied as a surface/interface sensitive probe. For crystals or ferromagnetic thin films with a spontaneous or magnetic field induced magnetization ***M***, see Figure 3.6, the induced nonlinear second order optical polarization of a medium can be written as:

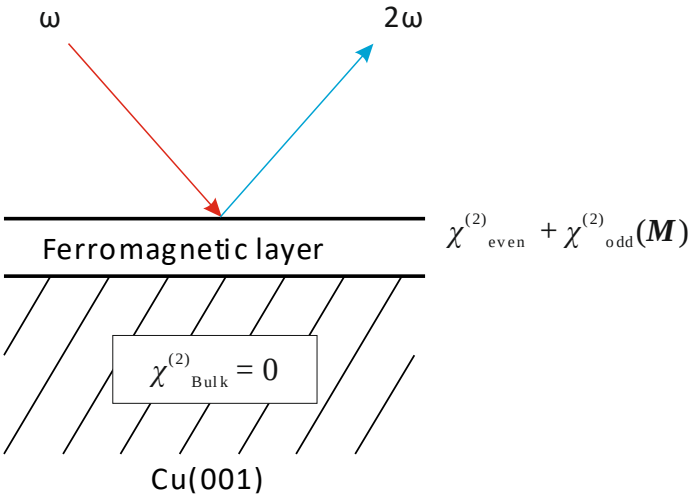

Figure 3.6: Sketch of SHG from ferromagnetic surfaces. Beside the nonmagnetic tensor, new non-vanishing tensor elements are induced by the presence of magnetization in the film. Graph redrawn from [16].

$$P_i^{(2)}(2\omega) = \chi_{ijk}^{(2)} E_j(\omega) E_k(\omega) + \chi_{ijkl}^{(3)} E_j(\omega) E_k(\omega) M_l \tag{3.25}$$

In this equation the first term does not depend on the magnetization and hence describes the purely crystallographic contribution. The second term only exists in the presence of a magnetization $\boldsymbol{M}$ and describes the magnetization-induced SHG. The magnetization-induced susceptibility tensor can be defined as:

$$\chi_{ijk}^{(2)}(M) = \chi_{ijkl}^{(3)} M_l \tag{3.26}$$

Being affected by the magnetization, the tensor elements can be classified as *even* or *odd* with respect to $\boldsymbol{M}$:

$$\chi_{ijk}^{(2)} = \left[\chi_{even}^{(2)}\right]_{ijk} + \left[\chi_{odd}^{(2)}(\boldsymbol{M})\right]_{ijk} \tag{3.27}$$

with the odd dependence

$$\chi_{odd}^{(2)}(\boldsymbol{M}) = -\chi_{odd}^{(2)}(-\boldsymbol{M}) \tag{3.28}$$

Since $\boldsymbol{M}$ is an axial vector, the inversion symmetry of the bulk material is not broken, which conserves the surface/interface sensitivity for magnetic materials. However, the presence of magnetization breaks the time reversal symmetry in the material. In other words, the presence of magnetization can lower the symmetry properties and induce new non-zero tensor elements. For the case of a (001) surface, these new non-zero tensor elements in respect to the orientation of magnetization are given as [15]:

$$\boldsymbol{M} \parallel \boldsymbol{x}\text{: } \chi_{odd}^{(2)}(\boldsymbol{M}) = \begin{pmatrix} 0 & 0 & 0 & 0 & 0 & \chi_{xxy} \\ \chi_{yxx} & \chi_{yyy} & \chi_{yzz} & 0 & 0 & 0 \\ 0 & 0 & 0 & \chi_{zzy} & 0 & 0 \end{pmatrix} \tag{3.29}$$

$$\boldsymbol{M} \parallel \boldsymbol{y}\text{: } \chi_{odd}^{(2)}(\boldsymbol{M}) = \begin{pmatrix} \chi_{xxx} & \chi_{xxy} & \chi_{xzz} & 0 & 0 & 0 \\ 0 & 0 & 0 & 0 & 0 & \chi_{yyz} \\ 0 & 0 & 0 & 0 & \chi_{zzx} & 0 \end{pmatrix} \tag{3.30}$$

	s-P	*s-S*	*p-P*	*p-S*	*mix-P*	*mix-S*
Even	zyy	-	zzz, zxx, xzx	-	zzz, zxx, xzx, zyy	yzy
Odd $\boldsymbol{M} \parallel \boldsymbol{x}$	-	yyy	-	yxx, yzz	xxy, zzy	yxx, yyy, yzz
Odd $\boldsymbol{M} \parallel \boldsymbol{y}$	xyy	-	xxx, xzz zzx	-	xxx, xyy, xzz, zzx	yxy
Odd $\boldsymbol{M} \parallel \boldsymbol{z}$	-	-	-	yxz	xzy, zxy	yxz

Table 3.2: Non-zero tensor elements for a C_{6v} surface symmetry for different polarization combinations and magnetization orientations.

$$\boldsymbol{M} \parallel \boldsymbol{z}\text{: } \chi_{odd}^{(2)}(\boldsymbol{M}) = \begin{pmatrix} 0 & 0 & 0 & \chi_{xzy} & 0 & 0 \\ 0 & 0 & 0 & 0 & \chi_{yxz} & 0 \\ 0 & 0 & 0 & 0 & 0 & \chi_{zxy} \end{pmatrix} \tag{3.31}$$

The magnetization induced non-vanishing tensor elements are summarized in Table 3.2 for various polarization geometries. Experimentally the SHG intensity is measured for opposite orientation of magnetization and can be expressed as:

$$I^{2\omega}(\pm\boldsymbol{M}) \propto |E_{even}^{2\omega} \pm E_{odd}^{2\omega}(\boldsymbol{M})|^2 \tag{3.33}$$

The even and odd second harmonic field are generated through the crystallographic and magnetization-induced susceptibility tensor. Thus, one can obtain the total SHG intensity:

$$I^{2\omega}(\pm\boldsymbol{M}) \propto |E_{even}^{2\omega}|^2 + |E_{odd}^{2\omega}(\boldsymbol{M})|^2 \pm 2|E_{even}^{2\omega}|\left|E_{odd}^{2\omega}(\boldsymbol{M})\right| \cdot cos\varphi \tag{3.33}$$

where φ represents the relative phase difference between the even and odd SH field, see Figure 3.7. It becomes obvious that the phase could influence the magnetization-induced signal, for instance for $\varphi = 90°$, no MSHG signal can be derived. For the investigated system in this thesis i.e. epitaxial Co/Cu(001), Conrad et al. [123] measured that the phase difference is less than 20 ° and it remains fairly constant in various coverages of epitaxial Co layers on Cu(001).

Magnetic contrast or magnetic asymmetry can be defined from the measured SHG intensity for opposite magnetization directions as [55, 57]:

$$\rho = \frac{I^{2\omega}(\boldsymbol{M}) - I^{2\omega}(-\boldsymbol{M})}{I^{2\omega}(\boldsymbol{M}) + I^{2\omega}(-\boldsymbol{M})} \tag{3.34}$$

A more direct expression between magnetic contrast and the magnetization of the probed region can be obtained:

$$\rho \approx 2\frac{\left|\chi_{odd}^{(2)}\right|}{\left|\chi_{even}^{(2)}\right|} M \cdot cos\varphi \tag{3.35}$$

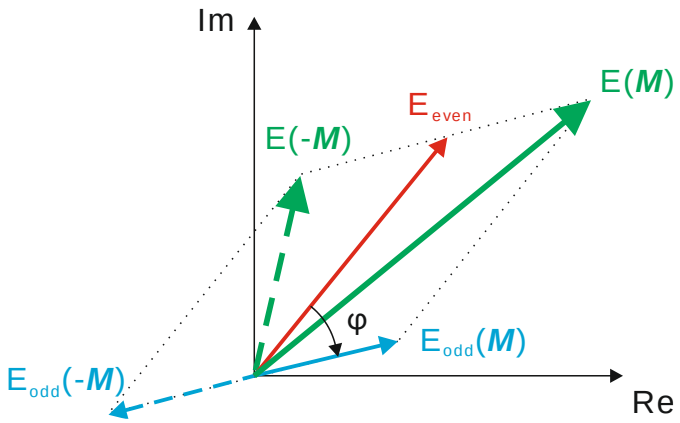

Figure 3.7 : Schematic illustration of MSHG for opposite orientation of magnetization in complex plane. E_{even} and E_{odd} has a phase difference of φ. Reversal of magnetization causes a 180 °phase shift of the generated odd field E_{odd}. Graph redrawn from [123].

Considering that $|E_{odd}^{2\omega}|^2 \ll |E_{even}^{2\omega}|^2$ and the phase is rather constant for Co/Cu(001) with few ML coverages, one can conclude that the magnetic contrast serve as a good measure for the surface magnetization.

3.3.3 Formalism for time-resolved mSHG

We denote $I_{\uparrow\downarrow}^{2\omega}(t)$ as the measured SHG intensity for opposite magnetization directions as a function of pump-probe delay, $I_{\uparrow\downarrow}^{2\omega}(t_0)$ refers to the unpumped SHG signal following literature [35, 125]:

$$I_{\uparrow}^{2\omega}(t) + I_{\downarrow}^{2\omega}(t) = 2|E_{even}^{2\omega}(t)|^2 + 2|E_{odd}^{2\omega}(t)|^2 \tag{3.36}$$

$$I_{\uparrow}^{2\omega}(t) - I_{\downarrow}^{2\omega}(t) = 4|E_{even}^{2\omega}(t)|\left|E_{odd}^{2\omega}(t)\right| \cdot \cos\varphi(t) \tag{3.37}$$

We define R(t) through equation (3.36) and (3.37) as

$$R^{\pm}(t) = \frac{I_{\uparrow}^{2\omega}(t) \pm I_{\downarrow}^{2\omega}(t)}{I_{\uparrow}^{2\omega}(t_0) \pm I_{\downarrow}^{2\omega}(t_0)} \tag{3.38}$$

Considering $|E_{odd}^{2\omega}|^2 \ll |E_{even}^{2\omega}|^2$, the normalized ratio of the transient even SH-field can be approximated and derived as:

$$\Delta_{even} = \sqrt{R^{+}(t)} - 1 \approx \frac{E_{even}(t)}{E_{even}(t_0)} - 1 \tag{3.39}$$

Here Δ_{even} mostly reflects the dynamics of the electronic system. The magnetization dynamics can be derived in the following way:

$$\Delta_{odd} = \frac{R^{-}(t)}{\sqrt{R^{+}(t)}} - 1 \approx \frac{E_{odd}(t)\cos\phi(t)}{E_{odd}(t_0)\cos\phi(t_0)} - 1 \tag{3.40}$$

$$\approx \frac{M(t)}{M(t_0)} \cdot \frac{\cos\varphi(t)}{\cos\varphi(t_0)} - 1 \tag{3.41}$$

In the above expression Δ_{odd} consists of the normalized transient magnetization and a phase factor. It should be clarified whether Δ_{odd} reflects the magnetization dynamics of the probed region. In the present work, as derived from the static phase sensitive measurement that $\varphi < 20°$ for Co/Cu(001) [123], $\cos\varphi(t_0) \approx 1$ can be assumed. According to pump-probe MSHG performed on Ni [124], the transient change of phase is small and can be neglected as $\cos\varphi(t) / \cos\varphi(t_0) \approx 1$. So based on the above considerations, it is concluded that in this thesis, Δ_{odd} probes the magnetization dynamics for the investigated system.

4 Experimental details

In this chapter, the experimental setup used in the present work will be introduced. Two investigated material systems i.e. Co/Cu(001) and FeOEP/Cu(001) are *in situ* prepared in the ultra-high vacuum (UHV) chamber. A femtosecond laser source based on a cavity dumped home-built Ti:Sa Oscillator has been employed to perform time-resolved MSHG studies on Co/Cu(001) films. The second sample system i.e. FeOEP/Cu(001) interface is studied by surface SHG spectroscopy, where the light source is provided via noncollinear optical parametric amplifier (NOPA) pumped by 100 kHz regenerative amplifier (RegA). Details related to UHV, sample preparation, Ti:Sa laser system, NOPA, diagnostics and detection system will be given.

4.1 UHV and sample preparation

In order to ensure the investigations of a clean surface, a ultra-high vacuum (UHV) condition with the pressure $p < 10^{-10}$ mbar should be achieved. UHV is a necessary condition for the preparation of high quality ultrathin metal films without surface contamination, e.g. *in situ* Cobalt on Cu (001).

In the present work, a pump stage (Pfeiffer) consists of a turbomolecular pump and a diaphragm pump serves as a pre-vacuum pump for the UHV chamber, after that the chamber is pumped by a turbomolecular pump (Leybold). In order to obtain a lower pressure, careful bake-out of the chamber is required to exclude the water. Then the chamber is carried out by the cycles of titanium sublimation pump (TSP) pumping and degassing. At the end a pressure of 10^{-11} mbar in the chamber can be reached with the help of an ion getter pump. A quadrupole mass spectrometer (QMS) is available for analyzing the residual gas.

In principle the UHV chamber can be divided in two levels due to its function i.e. the sample preparation of thin films and the optical measurements, as depicted in Figure 4.1. In the preparation level, two evaporators are installed i.e. electron beam evaporator for Cobalt and thermal evaporator for iron octaethylporphyrin chloride (FeOEP) molecules. The long range structural order of the deposited thin Co films can be characterized by low electron energy diffraction (LEED). Quartz crystal microbalance (QCM) monitors the deposition rate of the molecules.

In order to have a better focus of the light at the sample and a larger pump fluence an in-depth entrance flange is installed for the optical measurements. With this construction the laser beam can be focused down to ~60μm diameter at the sample surface, which results in a laser fluence of ~1 mJ/cm^2 for the nonlinear optical measurements. In this thesis, fused silica UHV windows with a thickness of 4 mm is used, which can provide high transmissions > 90% over a broad spectral range of 250 nm – 2 μm wavelength for the entrance and exit of laser beam. In addition, an electromagnetic coil is installed and characterized in air with a Hall probe (see Figure 4.1). The coil produces sufficient magnetic field to switch the orientation of magnetization of thin Co/Cu(001) along the easy axis. Outside of the UHV chamber, a set of microscope and camera is installed for the purpose of alignment of spatial pump-probe overlap.

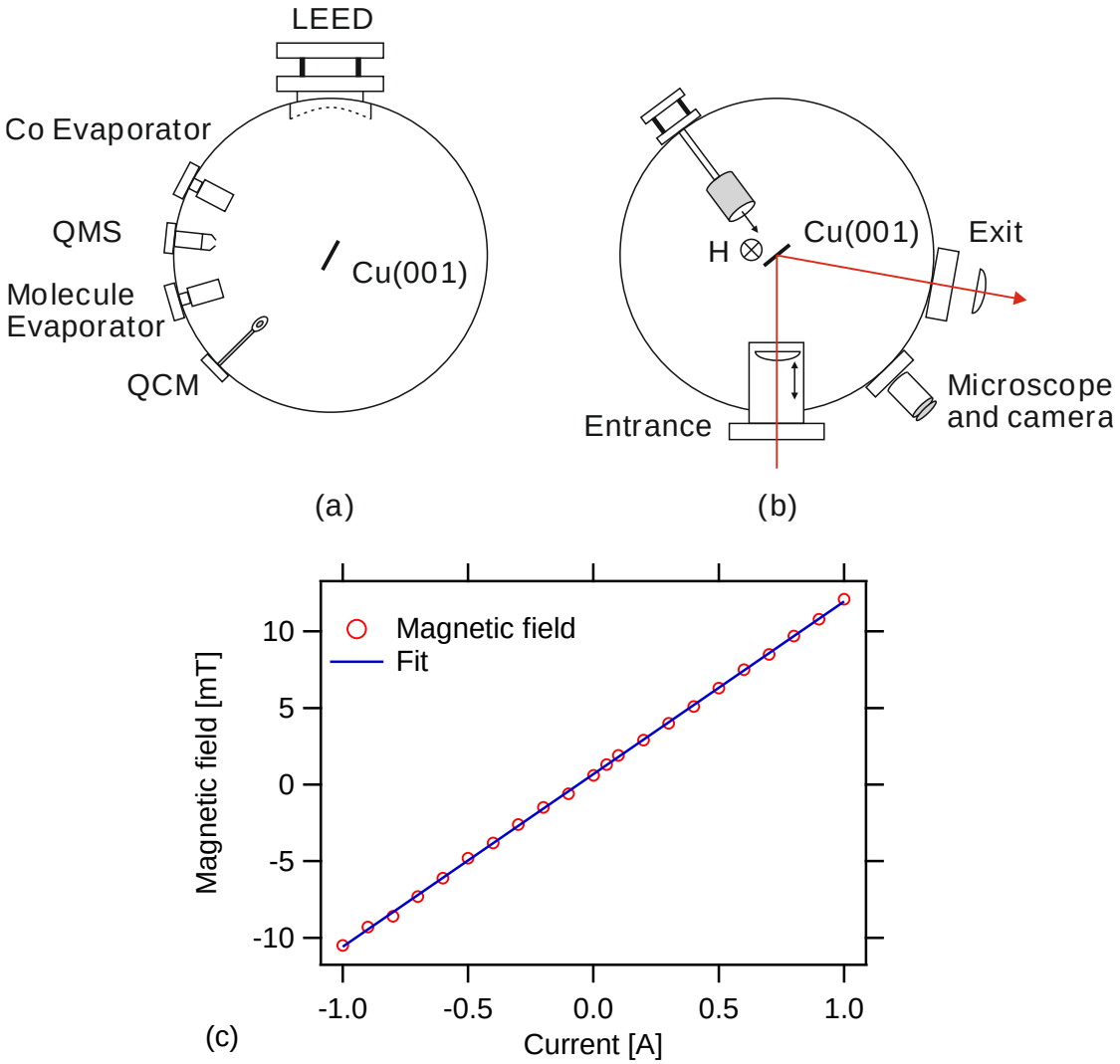

Figure 4.1: Schematic view of the UHV chamber in (a) level of sample preparation and characterization, (b) level of optical measurements with microscope and camera for alignment. The electromagnetic coil generates magnetic field in the transverse direction with respect to optical plane. (c) The magnetic field as a function of electric current is calibrated by a Hall probe.

A single crystal Cu(001) is available as substrate for sample preparation. The crystal is mounted on a sample holder fastened with tungsten wires. With a manipulator the sample can be moved in x, y, z direction and rotated around the z axis. Since a clean Cu(001) surface is very important for the *in situ* preparation of the metal films, it is necessary to obtain a clean Cu(001) surface by serval cycles of Ar ion sputtering and annealing processes before each deposition. In the sputtering process the copper surface is bombarded with Ar ions of 1.5 keV energy under a gas pressure of 5×10^{-6} mbar. The sputtering time is usually 10 minutes but would be longer if there are multiple or thicker layers adsorbate on the copper surface. During the subsequent annealing, the copper substrate is heated to 300 ℃ by a current of 7.5 A and then held at this temperature for 10 minutes. Such an annealing process last 17 minutes, after that a smooth copper surface is obtained. Sample preparation can be started when the copper substrate is cooled to 80 ℃, which is monitored through the thermo-voltage of an W/Re thermocouple.

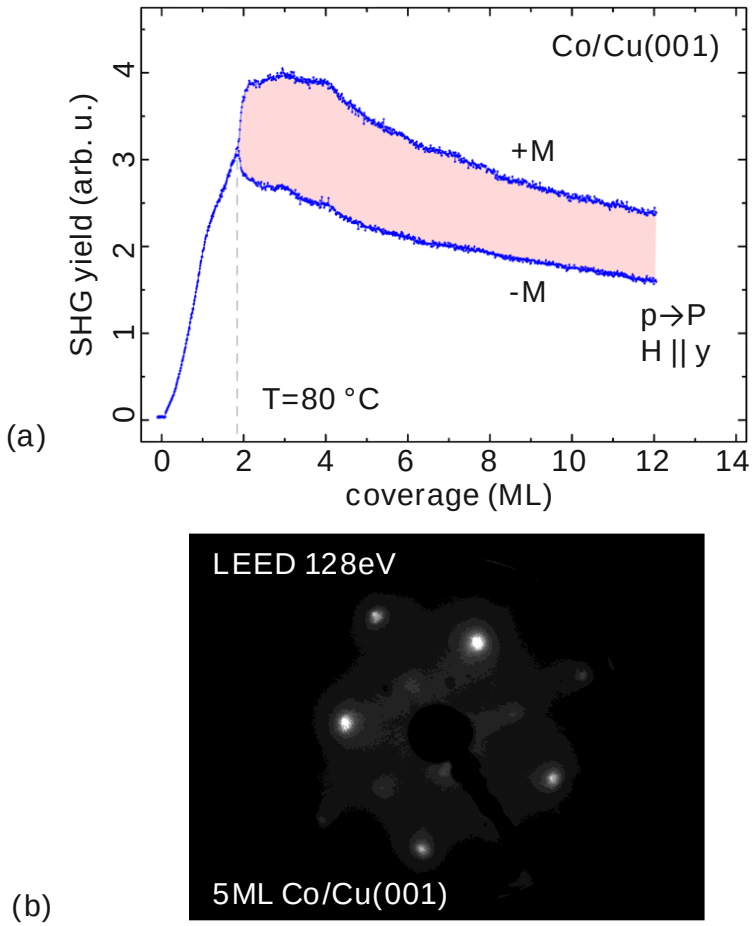

Figure 4.2: (a) Coverage dependent MSHG intensity of epitaxial Co/Cu(001) films from [126], the measurement was performed by transverse geometry in p-P combination at 80 ℃ substrate temperature. (b) LEED pattern from 5 ML Co/Cu(001) film at electron kinetic energy of 128 eV at room temperature.

The growth of ultrathin cobalt films on Cu(001) is well known in the literature [127]. First, a clean Cu(001) should be prepared and cooled below 80 ℃. Solid cobalt rods with a purity of 99.99% are then evaporated in electron beam evaporators ($\sim 10^{-10}$ mbar), in which the electrons are directly accelerated onto the cobalt rod. The Cobalt films can be epitaxially grown on Cu(001) with a constant flow (of 0.2 monolayers per minute) of cobalt atoms [128]. In this way, cobalt can be stabilized in a face-centered structure (fcc) on Cu(001). Due to technical reasons the thickness of cobalt films could not be calibrated with quartz crystal microbalance (QCM). Instead, the film thickness is determined with generated ion current inside the evaporator, which is proportional to the deposition rate [129]. A precise calibration of Co film thickness can be done due to the fact that epitaxial Co/Cu(001) films exhibit a ferromagnetic order as far as the cobalt coverage is above 1.8 monolayers (ML) at T = 80 ℃ [126], which can be probed by MSHG. Figure 4.2 shows that a magnetic contrast appears for Co coverages larger than 1.8 ML. The surface structure of Co/Cu(001) is characterized by LEED, see Figure 4.2 for an example of 5 ML Co/Cu(001), Co atoms stack on Cu(001) substrate and shows a four-fold symmetry that differs clearly from the nature close-packed hexagonal solid phase.

In this work, the same recipe as in Wende et al. [22] is used for the vapor deposition of the porphyrin molecules. The crucible evaporator is basically a thermal evaporator. The molecule evaporator is slowly preheated to 475K, at the same time the system is cooled with cooling water, which serves to thermally stabilize the QCM, because otherwise the frequency would change due to a change in temperature, which could alter the thickness. Once the clean Cu(001) is prepared, the FeOEP molecules are then sublimated at 485K from power and deposited on the copper substrate. The coverage of the porphyrin molecules is determined by the QCM, since a monolayer of FeOEP/Cu(001) corresponds to a frequency change of 10 Hz at QCM. This frequency change was obtained by AG Wende, we note that we applied the same evaporator and recipe when preparing porphyrin molecules.

4.2 Ti:Sa oscillator based ultrashort light source

Optical pump-probe spectroscopy relies on the generation of ultrashort laser pulse. In this thesis the light source is based on a home-built Titanium:Sapphire oscillator. The Ti:Sa oscillator can be operated in: (i) Normal mode-locked oscillator mode, which provides an ultrashort laser pulse with high repetition rate of 78 MHz, high average power and relative low energy per pulse around 6 nJ. In order to drive nonlinear optical processes in the optical parametric amplifiers, this normal oscillator mode has been used as a seeding pulse for a 100 kHz regenerative amplifier, and is introduced in section 4.2.2. (ii) Cavity dumped oscillator mode, which offers higher energy per pulse with variable repetition rate, 40 nJ and 2.53 MHz for the present work, hence is suitable for time-resolved MSHG experiment due to compromise between high pulse energy and high repetition rate. A detailed pump-probe MSHG setup will be given on section 4.4. A pulse duration as short as 35 fs can be generated for both modes. We first introduce the cavity-dumped Ti:Sa oscillator due to strategic development of ultrashort light source in the lab, since it was a well-established light source which performed serval experimental works in ultrafast spin dynamics [60, 62, 125, 126, 133] as well as within the present thesis [18, 19].

4.2.1 Cavity dumped Ti:Sa oscillator

The length of the cavity allows standing waves with certain frequencies as longitudinal modes inside the cavity. These longitudinal modes usually oscillate with random phase in the cavity. Generation of ultrashort laser pulse is based on a technique called mode-locking, which forces all the modes to oscillate in the same phase i.e. different frequencies will be added constructively at one point in the time domain. This superposition of all modes results in a pulse train of intense and ultrashort light burst. In general, a broader spectral bandwidth allows more modes to generate shorter laser pulse. The titanium doped Al_2O_3 crystal (Ti:Sa) crystal is an active laser medium that shows a broad spectral bandwidth of absorption and emission, therefore it has the ability to generate ultrashort laser pulses. Practically, in this thesis the passive mode-locking [182] is achieved through nonlinear optical Kerr effect, which induces Kerr lens (self-focusing) effect and self-phase modulation (SFM) in the Ti:Sa crystal.

The third-order nonlinear effect modifies the refractive index of the Ti:Sa crystal, which is proportional to the intensity. Laser beam with a spatial Gaussian profile excites the gain medium and causes a transient lens (spatial gain modulation), which leads to self-focusing of the input beam. Upon an increase of the incident beam, the beam size of

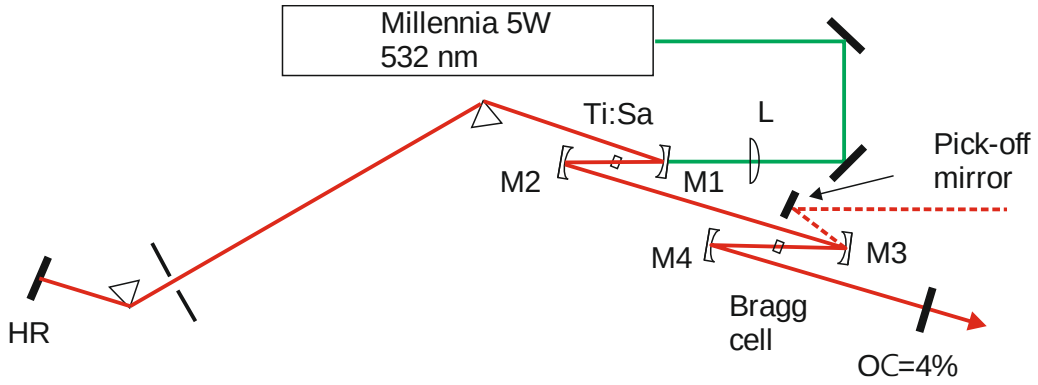

Figure 4.3: Simplified sketch of the Ti:Sa oscillator with the cavity dumper. The Ti:Sa crystal is pumped by a 5W continuous-wave Millennia laser. Four curved mirrors M1, M2, M3 and M4 have the radius R = 10 cm. A fused silica acousto-optic modulator serves as Bragg cell. The optical cavity ends with a high reflective mirror HR and out-couples with an OC mirror of 4% transmission. The dashed line denotes that the cavity-dumped beam travels vertically in respect to the optical table.

the transmitted beam will be focused and decreased accordingly. Hence, the weak intensity modes and the competing cw-mode are suppressed and only stronger intensity modes survive after many round-trips through the Ti:Sa crystal inside the optical cavity.

The nonlinear optical Kerr effect can also modify the intensity distribution of the ultrashort pulse in the time domain. The modulation of the rising and falling edges of the intensity in the time domain is similar to spatial self-focusing, which will cause a change in the phase of the electric field, thereby generating new frequency components in the laser pulse that is equal to a broadening of the spectral width. Even shorter laser pulses can be generated by self-phase modulation.

However, the generation of ultrashort laser pulses is based on the combined and balanced effect of the self-phase modulation and the group velocity dispersion (GVD). Each round-trip of the laser beam passes through the Ti:Sa crystal producing a positive GVD of the optical components, which will eventually lead to a temporal broadening of the laser pulse. In order to obtain ultrashort pulses, elements with negative GVD should be inserted into the cavity, such as a prism pair. But this is only achievable up to second order GVD, higher order GVD can be compensated with chirped mirrors.

A schematic structure of the cavity-dumped oscillator is depicted in Figure 4.3. The Ti:Sa crystal is pumped by a 5W diode laser (Millennia) and placed in Brewster angle to minimize the reflection. The Ti:Sa crystal is enclosed with two curved dichroic mirrors M1 and M2, transparent for 532 nm and high reflective for radiation centered at 800 nm. The 800 nm beam is then focused on the crystal to enhance the Kerr effect. Two reflected beams form a Z shaped configuration with asymmetric optical path. In the longer optical arm, a prism pair is installed for GVD compensation. Between the two prisms, there is a slit for tuning the wavelength. A second optical cavity with the Bragg cell is inserted in the shorter optical arm. The out-coupling in the oscillator is around 4%. Practically, mode-locking can be initiated by slightly tapping the intra-cavity prism or the high reflective mirror at the dispersive side of the oscillator back and forth.

The cavity dumper is based on the acousto-optic effect. First, an electric signal is applied to a piezoelectric transducer attached to the fused silica crystal, therefore generates acoustic waves inside the crystal. Then the reflective index of the fused silica

is modulated by the acoustic waves and forms a transient optical grating. By switching on and off the electric signal, the first order diffraction of the laser beam on the Bragg cell can be deflected from the initial direction and dumped out of the cavity for experimental usage. The control unit (APE Berlin) for the Bragg cell is synchronized at the repetition rate of the oscillator and triggered by a signal of a fast photodiode. More technical details of the oscillator can be found in [126]. Finally, the cavity-dumped Ti:Sa oscillator produces laser pulses with 35 fs pulse duration, 40 nJ pulse energy and 800 nm central wavelength at a repetition rate of 2.53 MHz for the MSHG experiments.

4.2.2 Seeding pulse: a reconstructed oscillator

In order to seed a 100 kHz amplifier, the oscillator is required to be constructed in a more compact form to fit the limited space on the optical table. One simple and efficient solution is to keep all the parameters of the cavity the same but fold the long optical arm, the sketch of the folded oscillator can be seen on Figure 4.4 (b).

The optical resonator plays a crucial role in the design of the laser. The optical resonator must be constructed in a way that the radiation can still be captured after several passes inside the resonator, thus, the amplification of the radiation is accomplished. In such cases, the parameters of the laser configuration can be modified only within certain ranges i.e. the stability zones. For the purpose of alignment, the prism pair is first retracted from the beam. Then the oscillator can be operated in linear configuration, the layout of the structure is given in Figure 4.4 (a). In this new construction, the Ti:Sa crystal is pumped by a (Coherent Verdi) solid state laser operating at 4.3 W. The linear oscillator consists of 4 curved cavity mirrors and 2 flat mirrors close the linear cavity, one acts as high reflector and one as an output coupler. OC is replaced with a mirror of 6% transmission. Here both arms should have the same optical length as in Figure 4.3 to ensure identical stability conditions.

The stability zones of 6-mirror laser cavity can be calculated through ABCD matrix formalism [131]. In contrast to 4-mirror laser cavity, with the addition of two curved mirrors, the stability zone becomes a two dimensional plot, shown in Figure 4.4. Now the stability depends on the distance between the Ti:Sa focusing mirror M1 and M2 as well as the distance between the cavity dumped mirrors M3 and M4. Two regions of stability can be distinguished in Figure 4.4 (c) by colored areas, stability zone I and II are separated by a gap where the laser resonator is unstable, which is a result of unequal optical arm length. With inclusion of Kerr-lens in the calculation, a shift of second stability zone is found. It is concluded form such simple analysis that the high intensity mode-locking should preferentially be operated at the inner border of second stability zone [132].

In practice, we first align the oscillator in linear configuration to find the stability zone, then we insert the prism pair for mode-locking. The output power of the oscillator is measured as a function of the distance between the two curved mirror M1-M2, see Figure 4.4 (d). For a relative distance of 0.5 – 2.0 mm between M1 and M2, cw-mode is running stable with higher output power of 250 mW, while mode-locking can not be achieved in this region. Near the border of the second peak, mode-locking was found to be possible, no hard aperture was needed at this position. At this areas, the competing cw-mode produces an output power of 50 mW while mode-locking generates around 150 mW. This output is then used to seed a 100 kHz amplifier.

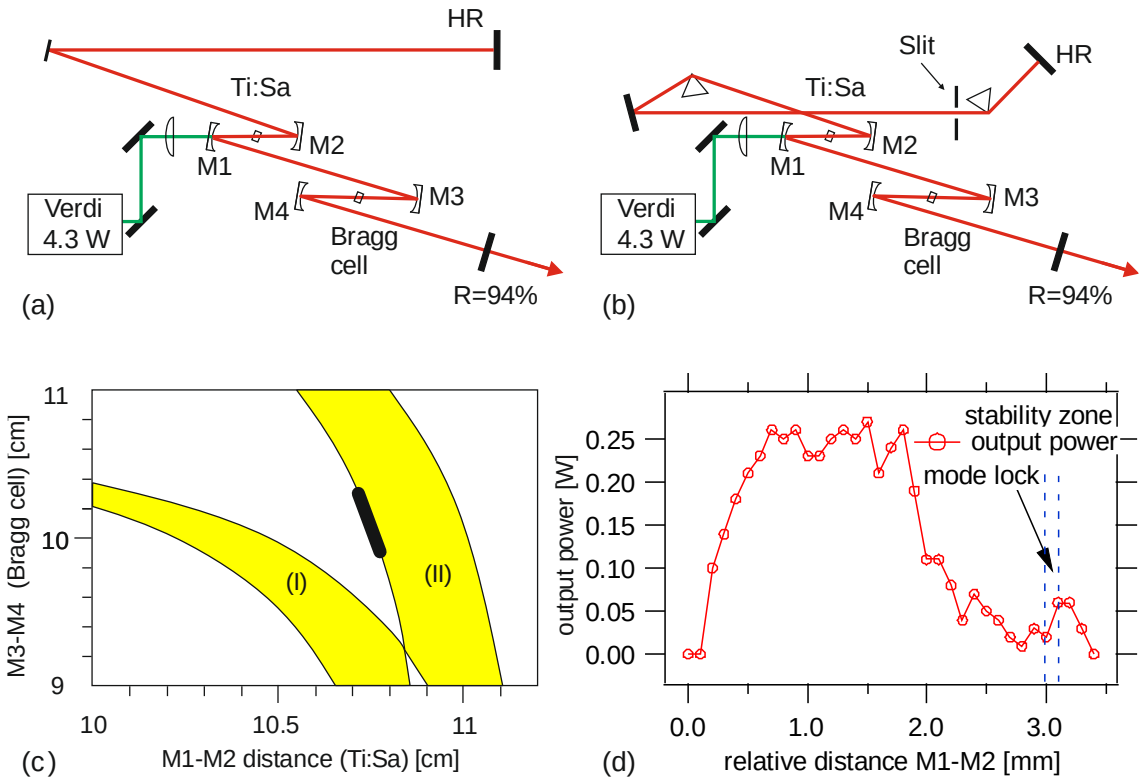

Figure **4.4**: Sketch of a reconstructed Ti:Sa oscillator in (a) linear configuration and (b) prism pair configuration. (c) Calculated stability zone for a Ti:Sa oscillator for 6 mirrors cavity [130], the optimal position of mode-locking is mark at the inner border of zone II. (d) Measured out-coupling power as a function of M1-M2 distance for the layout in (b).

4.2.3 100 kHz amplifier

Ultrashort laser pulse generated by the laser amplifier can meet the requirement of high intensity (10^{12} W/cm^2) per pulse to pump an optical parametric amplifier (OPA). The generation of ultrashort and intense laser pulse is based on the method of chirped-pulse amplification (CPA) [134]. The ultrashort laser pulse from an oscillator is chirped and stretched to a longer pulse duration by means of a strong dispersion element e.g. a grating pair or a long fiber before passing through the amplifier medium. Thus the peak intensity of the pulse is reduced to a level that can avoid thermal heating in the gain medium. After the laser pulse is amplified by the gain medium, a dispersive compressor such as a grating pair is used to eliminate the chirp and compress the pulse in time domain, so that the pulse duration is similar to the duration of input.

An overview of the 100 kHz amplified laser system is schematically illustrated in Figure 4.5. A laser pulse of 1.9 nJ with 78 MHz repetition rate out-coupled from the Ti:Sa oscillator is expanded in by one grating (reflected twice) in Stretcher/Compressor (Coherent). Then the remaining pulse of 1.2 nJ from stretcher is guided into regenerative amplifier (RegA), which generates an amplified power of 17.4 µJ per pulse with 100 kHz repetition rate. In the last stage of the laser system, the pulse is then compressed by the grating in the compressor. The corresponding spectrum of the laser beam at different stages of the amplifier are shown in Figure 4.6. Thus, an output of 12 µJ per pulse (a factor of 10^5 to the seeding pulse) and pulse duration of 70 fs at 800 nm central wavelength is achieved.

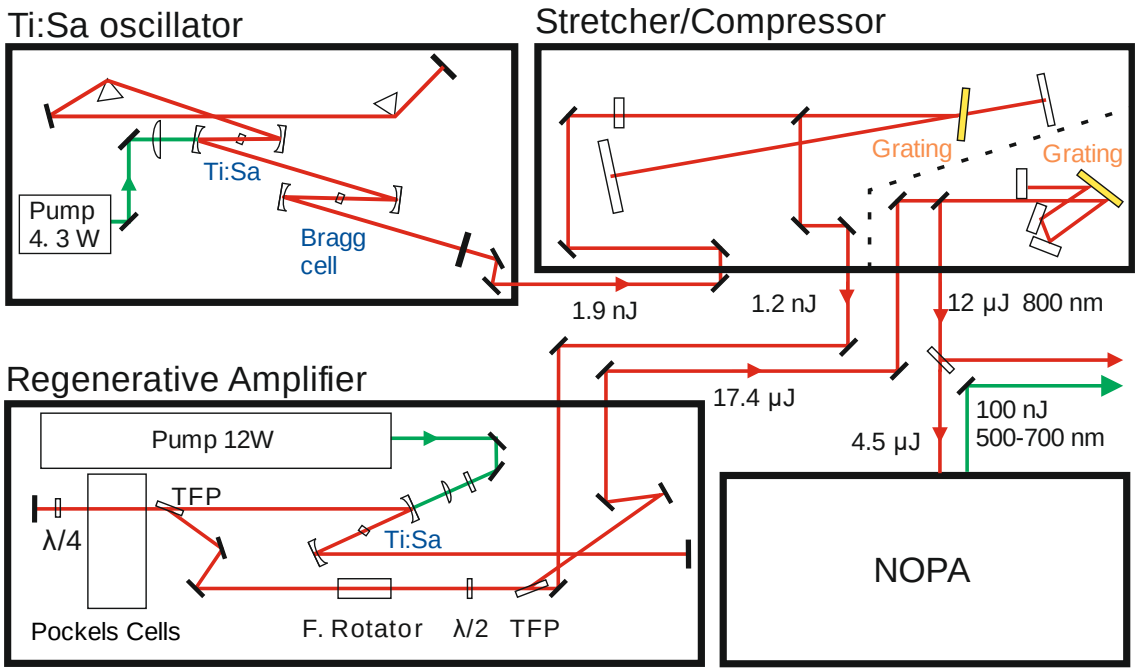

Figure 4.5: Layout of the 100 kHz amplifier. The femtosecond laser system consists of three building blocks: (i) Ti:Sa oscillator as seed, (ii) Stretcher & compressor (Coherent) and (iii) Pulsed-laser (Q-series) pumped Regenerative amplifier (RegA).

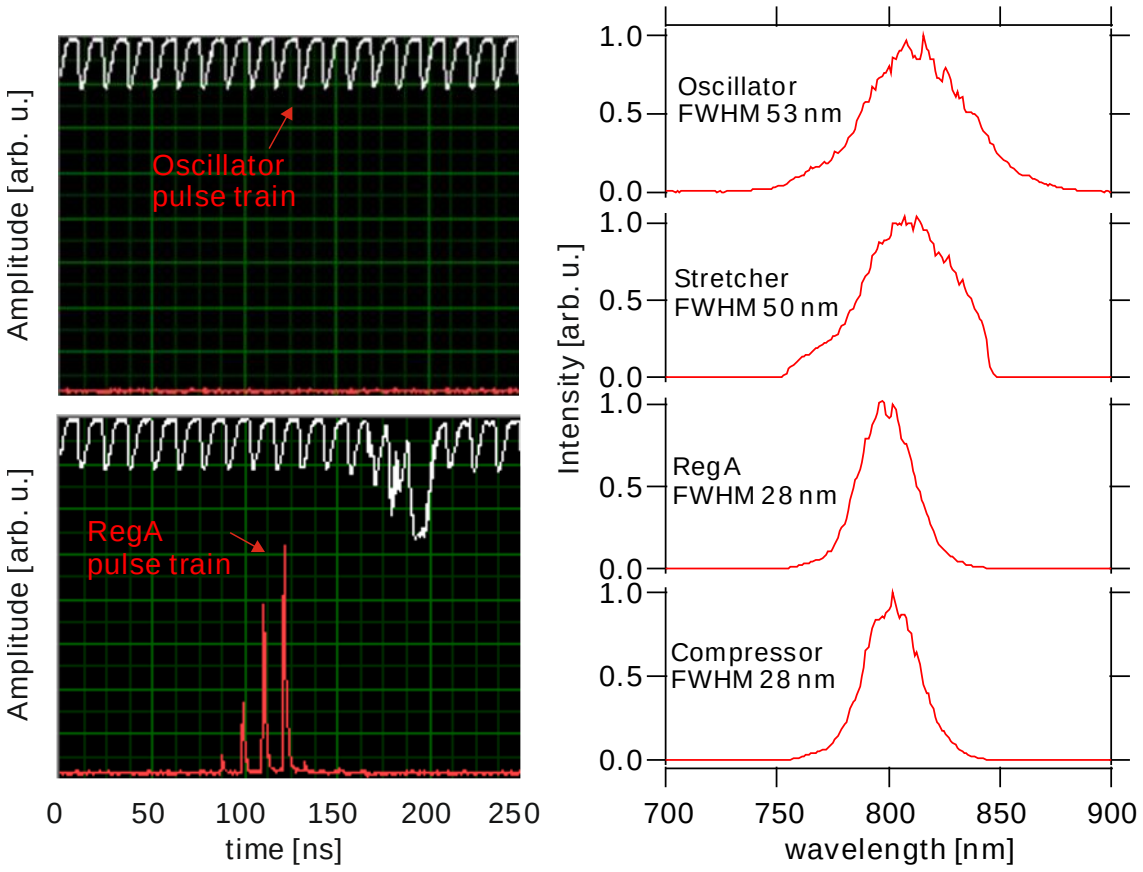

Figure 4.6: Left: the out-coupled pulse train from Ti:Sa oscillator and RegA. Right: the measured spectrum of the out-coupled laser pulses at four different stages in the amplified laser system.

With a closer look at the RegA in Figure 4.5, the initial seed pulse is injected into the resonator through polarization gates i.e. a Faraday rotator (polarization rotator based on the Faraday effect), a half wave plate and a thin film polarizer (TFP). This unit is used to separate the input and output pulses. Inside the cavity of the regenerative amplifier (RegA), the Ti:Sa crystal is pumped by a pulsed (Q-switch Nd:YAG) laser with the power of 12 W. The seed pulses travel about 8 round trips in the resonator. See the pulse train in Figure 4.6, for each round trip, the laser pulse is being amplified. Here, the seed pulse extracts some energy from population inversion for each round trip. The laser amplifier involves optical excitation and the amplifier stores energy by absorbing pump photons, the signal is amplified by stimulated emission. Finally, through a quarter wave plate and Pockels cell, which acts like an electrically switching wave plate, the saturated energy pulses are coupled out from the resonator. In regard to the usage of amplified pulses, a beam splitter is inserted at the output of the compressor, where 4.5 μJ pulse energy serves as a pump for a noncollinear optical parametric amplifier (NOPA), which generates sub 20 fs laser pulse with pulse energy around 100 nJ in $500 - 700$ nm wavelength range, as discussed below.

4.3 Noncollinear optical parametric amplifier

The advancement of ultrafast laser technology and discovery of new nonlinear optical crystals promoted the introduction of the noncollinear optical parametric amplifier (NOPA) as a practical source of femtosecond pulses that can be tuned in the visible and infrared spectral ranges [183, 135], which serves as an ideal light source for pump-probe spectroscopy.

In this work, we focus on the generation of sub-20 fs pulse in the visible range (500-700 nm). The employed NOPA was initially adapted from [136]. Based on that the output pulse energy and pulse duration are optimized. Details will be given in this chapter.

4.3.1 Basic principles

The physical principles of optical parametric amplification (OPA) differ from laser amplification. Laser involves electronic transitions and the optical cavity stores energy by absorbing pump photons, during which the output signal is amplified by stimulated emission. Limited by the gain medium, laser amplifier only works at certain wavelengths. On the other side, the crystal in an OPA does not absorb photons so that no energy is stored in the crystal. The signal is amplified by three wave mixing, or more accurately, difference frequency generation (DFG). The working wavelength is limited by the crystal transmission. In the optical parametric process, there is no net transfer of energy, momentum or angular momentum between the optical field and the material system.

The principle of OPA or DFG is quite simple. A low frequency, low intensity beam (the signal beam at frequency ω_s) is amplified by a higher frequency, higher intensity beam (the pump beam at frequency ω_p) in a suitable nonlinear crystal; meanwhile, a third beam (the idler beam at frequency ω_i, with $\omega_i < \omega_s < \omega_p$) is generated. In the process, the energy conservation, as shown in Figure 4.7,

$$\hbar\omega_p = \hbar\omega_s + \hbar\omega_i \tag{4.1}$$

is satisfied. In order to make the amplification process more efficient, it is necessary to fulfill the momentum conservation or phase matching condition:

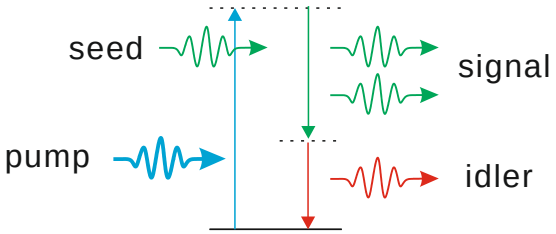

Figure 4.7: Energy conservation of optical parametric amplification (OPA) process. The pump wave is converted into a signal and an idler wave through three wave mixing with in a nonlinear crystal.

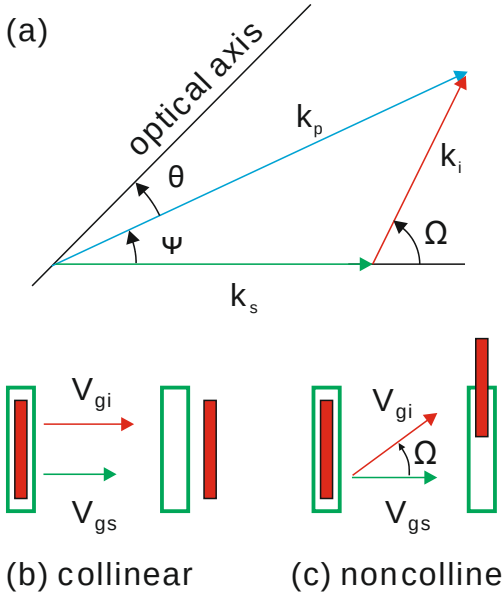

Figure 4.8: (a) Schematic of momentum conservation in noncollinear geometry with respect to optical axis of nonlinear crystal. (b) Illustrated propagation of signal and idler pulse for collinear geometry and for (c) noncollinear geometry. Redrawn from [135].

$$\hbar \boldsymbol{k}_p = \hbar \boldsymbol{k}_s + \hbar \boldsymbol{k}_i \tag{4.2}$$

where $\mathbf{k}_p$, $\mathbf{k}_s$ and $\mathbf{k}_i$ are the wave vectors of pump, signal and idler beam, respectively. The frequency of the signal beam to be amplified can vary from $\omega_p/2$ to ω_p, and the ilder beam varies from $\omega_p/2$ to 0. In summary, the energy of a high-intensity pump beam is transferred to a low-intensity signal beam, thereby generating a third idler beam. This amplification process requires an intensity in the order of GW/cm^2, which can be easily achieved via femtosecond laser pulses with pulse energy of the order of a few microjoules.

In OPAs operated in the collinear interaction geometry, the propagation direction in the nonlinear crystal is selected to meet the phase-matching condition $\Delta k = 0$ for a given signal frequency. In this collinear geometry, the group velocities of the signal and idler wave are fixed, and the process only works for a certain frequency due to narrow phase matching bandwidth. One way to increase the phase-matching bandwidth is to operate the OPA in a noncollinear geometry. As illustrated in Figure 4.8, pump and signal wave vectors form an angle Ψ, and the idler wave is emitted at an angle Ω with respect to the signal. Therefore, the phase matching condition has to fulfill a vector equation, which can be decomposed in directions parallel and perpendicular to the signal wave vector,

$$\Delta k_{\parallel} = k_p cos\Psi - k_s - k_i cos\Psi = 0 \tag{4.3}$$

$$\Delta k_{\perp} = k_p sin\Psi - k_i sin\Psi = 0 \tag{4.4}$$

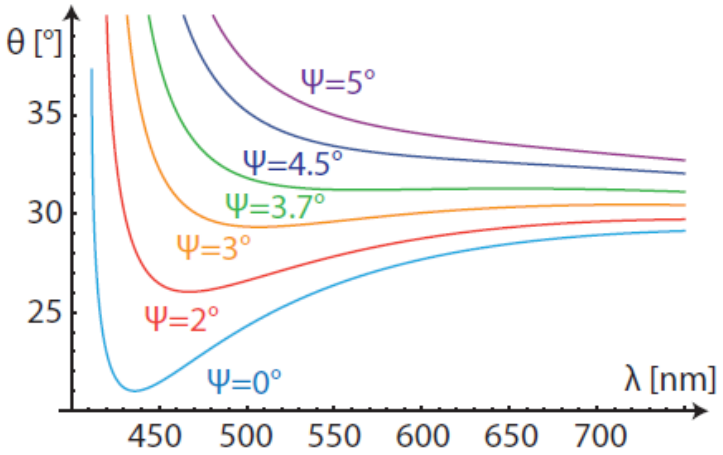

Figure 4.9: Phase matching curve for type I BBO crystal pumped at 400 nm, the curves are plotted at different noncollinear angle Ψ between the pump and signal vectors. θ denotes the phase matching angle between the optical axis of nonlinear crystal and the pump vector. Ψ = 0 °corresponds to OPA in collinear geometry, while at Ψ = 3.7 °, phase match condition is fulfilled over a large spectral bandwidth started form 500 nm. Graph taken from [136].

If the signal frequency increases by $\Delta\omega$ and the idler are decreases by $\Delta\omega$, then the phase mismatch projected in the two direction can be approximated in first order as

$$\Delta k_{\parallel} \approx -\frac{\partial k_s}{\partial \omega_s}\Delta\omega + \frac{\partial k_i}{\partial \omega_i} cos\Psi \cdot \Delta\omega - k_i sin\Psi \cdot \frac{\partial k_s}{\partial \omega_s}\Delta\omega \tag{4.5}$$

$$\Delta k_{\perp} \approx \frac{\partial k_i}{\partial \omega_i} sin\Psi \cdot \Delta\omega + k_i cos\Psi \cdot \frac{\partial \Omega}{\partial \omega_i}\Delta\omega \tag{4.6}$$

In order to achieve broadband phase matching, both phase mismatch $\Delta k_{\parallel}$ and $\Delta k_{\perp}$ must be equal to zero. Adding the equation (4.5) and (4.6) multiplied by $sin\Psi$ and $cos\Psi$, respectively, we get the phase matching condition,

$$\frac{\partial k_i}{\partial \omega_i} - cos\Omega \frac{\partial k_s}{\partial \omega_s} = 0 \tag{4.7}$$

or simplified as

$$v_{gs} = v_{gi} \cdot cos\Omega \tag{4.8}$$

It is intuitive that a broadband phase matching can be achieved by a noncollinear angle **Ω**, so that the projected group velocity of idler wave equals signal wave. This group velocity mismatch is illustrated in Figure 4.8 (b) and (c). For collinear OPA, the signal and idler pulses are quickly separated after propagation in the nonlinear crystal with different group velocities. In contrast, noncollinear geometry allows the two pulse to be effectively overlapped during the interaction. One should note here that this is only satisfied if $v_{gi} > v_{gs}$, which is always the case for widely used type I phase matching in negative uniaxial crystal, where both signal and idler are affected by the ordinary refractive index. As an example, NOPA is facilitated by type I β-barium-borate (BBO) crystal to generate signal beam in the visible spectrum, where the BBO crystal is pumped at 400 nm. In Figure 4.9, the corresponding phase matching curves are shown. In case of collinear configuration, the single wave depends strongly on the wavelength and is restricted by the narrow phase match bandwidth at a given fixed crystal orientation. Until Ψ = 3.7°, a broadband phase matching is simultaneously achieved from 500 – 750 nm at

crystal orientation $\theta = 31.3°$. Using such broad phase matching bandwidth, it was demonstrated that pulses as short as 13 fs can be generated [137]. Moreover, generation of broadband tunable sub 20 fs laser pulses seeded by white-light continuum in NOPA were reported [138-140].

4.3.2 Optimization and characterization

The NOPA aims to provide suitable laser pulses with sufficient pulse energy, short pulse duration as well as wavelength tunability to perform pump-probe SHG spectroscopy at surface. Therefore, we have optimized the NOPA performance based on the following points: (i) Increasing of SHG efficiency through the BBO crystal, where the pump signal lifts up the overall NOPA output power. (i) Chirped SHG by fused silica made stretcher to interact with as many as possible spectral components of chirped white-light pulse in time domain, from that an output of broad spectral width can be generated. (iii) Use of reflective optical elements to minimize higher order GVD. These aspects will be covered in this section.

In general, the optimized NOPA setup is schematically depicted in Figure 4.10. The fundamental 800 nm input beam of 4.5 μJ pulse energy is divided by a beam splitter, where 15% of the pulse energy is used for generation of white-light (WL) continuum via a sapphire crystal. The remaining 85% energy is used to generate the 400 nm pump beam through a 200 μm thick BBO crystal. The WL beam and 400 nm pump beam are focused at the same spot on the NOPA-BBO crystal, while the temporal overlap is controlled by a delay stage. The spatial overlap means here that the signal and pump should not only focus at the same spot, but also with similar beam profile to ensure optimal NOPA efficiency. This purpose is served by an aperture to optimize the beam profile of WL pulse to achieve maximal spatial overlap. After the NOPA-BBO crystal, signal in the spectral range 500 – 740 nm as well as idler beam in the infrared wavelength can be generated, the latter one is not depicted in the layout.

In order to obtain the highest possible intensity of the pump beam, the fundamental beam can be strongly focused on the BBO crystal in the space (with a L = 200 mm focusing lens) and time domain (with a pulse duration 50 fs). However, such a high intensity exceeds the destruction threshold of the BBO crystal. Due to this fact, the BBO crystal is not placed directly at the Gaussian beam waist focused by the lens, but rather a few mm away. Regarding the transient peak intensity of fundamental beam, two steps can be followed to optimize this issue. First, we use a fundamental beam of rather narrow bandwidth i.e. longer pulse for SHG, and convert the frequency components as much as possible to increase the BBO-SHG efficiency. Second, optimal compression of fundamental should aim at producing a maximal SHG bandwidth. Such an example is shown in Figure 4.12 (a-b), where the SHG bandwidth generated from a 100 μm BBO crystal is increased from 5 nm to 8.5 nm by reducing the 35 nm fundamental bandwidth down to 28 nm. For the case of (a), the spectrum is optimized for a maximal SHG intensity, while in (b) the fundamental beam is slightly chirped at the point of SHG. This spectral narrowing effect can be explained that if all the frequency components of the fundamental electric field are localized in the crystal at the same time, sum frequency generation between distant parts of the spectrum occurs and leads to loss of spectrum [141]. In summary, we use a rather long (80 fs) and slightly chirped fundamental 800 nm beam, which is slightly defocused on the BBO crystal to avoid third order GVD and to achieve SHG with broad spectrum and high efficiency up to $\eta = 42\%$. To have a higher 400 nm pump beam intensity, a 200 μm thick BBO crystal (with protective coating, Bluebean optical tech) is applied for 400 nm SHG in NOPA.

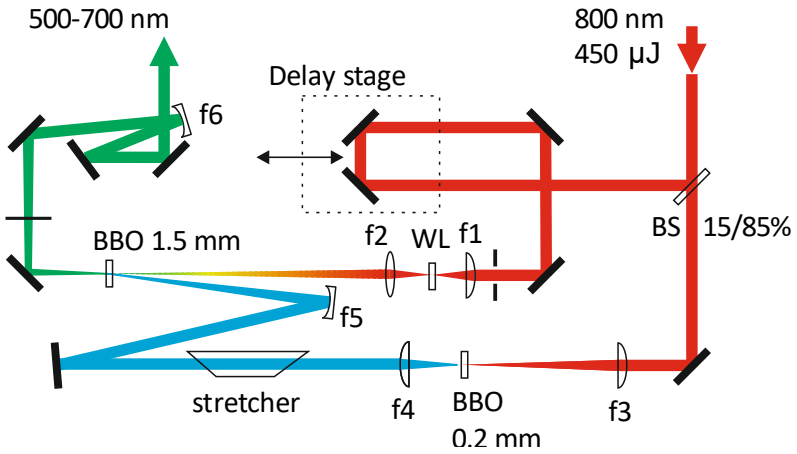

Figure 4.10: Schematic structure of NOPA. At the entrance stands a beam splitter (BS) for 800 nm beam with 15% to 85% ratio. On the white-light (WL) path, the light is focused on sapphire crystal by fused silica lens f1 = 50 mm and imaged by f2 = 40 mm on NOPA-BBO. An aperture is inserted before lens f1 to control the spatial profile of WL beam. On the frequency doubling path, fused silica lenses f3 = 250 mm and f4 = 100 mm are coupled to a 0.2 mm thick SHG-BBO crystal. The 400 nm pump beam is chirped by a pair of 6 mm fused silica glass plate oriented at Brewster angle (Stretcher), and focused by a curved f5 = 200 mm mirror on the 1.5 mm thick NOPA-BBO crystal, at which the seeding white-light pulse and 400 nm pump pulse are spatially and temporally overlapped. Finally, the amplified signal beam is coupled out through a curved mirror f6 = 500 mm. We note that the noncollinear angle between pump and signal lies in the vertical plane with respect to optical table, although it is depicted horizontally in the layout.

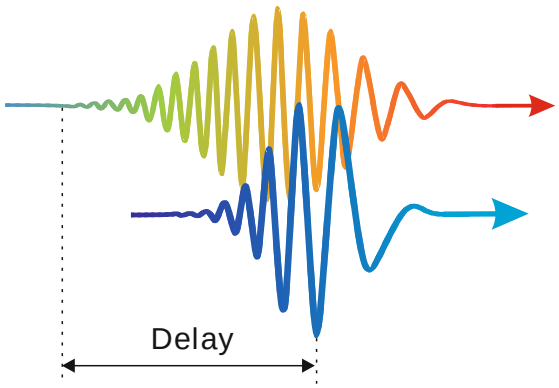

Figure 4.11: Schematic of chirped WL pulse and SHG pump pulse overlapped in time domain. Different frequency components can be amplified by varying the time delay between the signal (WL) and pump (SHG) pulse.

The second aspect is to generate broad spectral NOPA output. The WL continuum, which is generated by self-phase modulation in sapphire crystal, is shown in Figure 4.12 (c). Such a broad continuum indicates a strong linear chirp in a sapphire crystal between 500 nm and 700 nm [140], thus, the WL pulse duration is usually longer than the 400 nm pump. We then employ a stretcher (the construction was provided by Prof. E. Riedle, LMU, Munich) with two 6 mm thick fused silica plate oriented at Brewster angle to chirp the 400 nm pump beam. The interaction of WL with the pump beam is illustrated in Figure 4.11, a broader WL bandwidth can be simultaneously amplified by chirped SHG pulse in the time domain. The spectrum of the NOPA output is shown in Figure 4.12 (d).

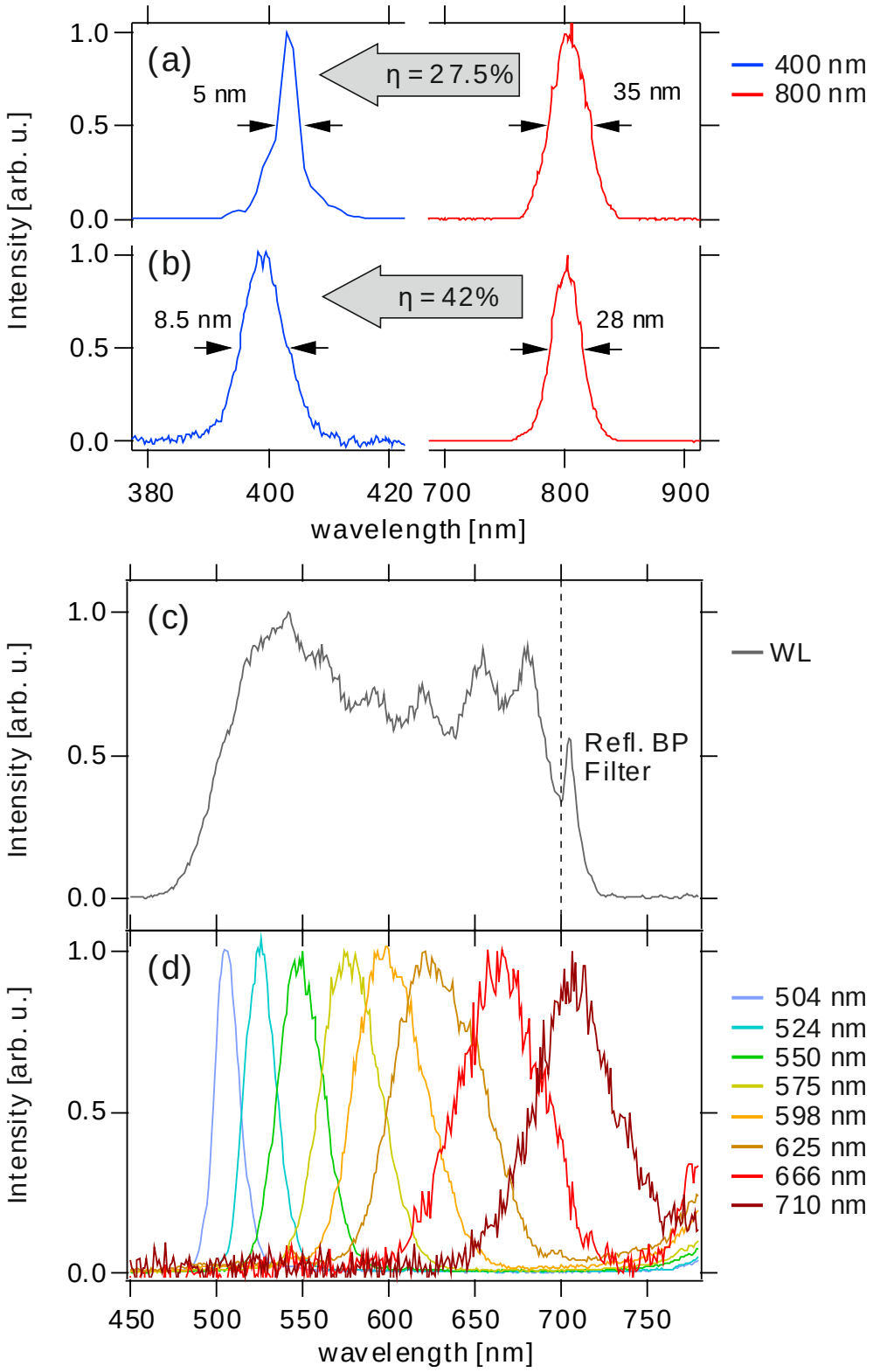

Figure 4.12: Panels (a and b), SHG spectrum from a 100 µm BBO crystal pumped by fundamental 800 nm beam with (a) 35 nm FWHM and 64 fs pulse duration, (b) 28 nm FWHM and 80 fs pulse duration, which corresponds to a SHG efficiency of 27.5% and 42%, respectively. (c) White light (WL) continuum generated from a sapphire crystal, the spectrum of fundamental 800 nm beam was cut by a reflective band pass (BP) filter. Panel (d) shows the measured NOPA output spectrum in 500 – 710 nm wavelength range.

Wavelength [nm]	*FWHM [nm]*	*Pulse energy [nJ]*	*Pulse duration [fs]*
504	16	100	-
524	21	110	34
550	30	95	30
575	39	80	25
598	49	82	20
625	60	75	20
666	57	80	24
710	50	70	21

Table 4.1: FWHM, pulse energy and duration of NOPA output at different wavelength.

To ensure a minimal third order group velocity dispersion (TOD), we have used fused silica lens in NOPA setup and curved mirror for focusing and out-coupling. Nevertheless, dispersion caused by the NOPA-BBO crystal itself cannot be avoided. So far as shown in Table 4.1, the optimized NOPA offers a broad spectral output in 500 – 710 nm range. The output has a measured pulse energy after prism pair compressor around 70 – 100 nJ. We note that, changing the delay between the pump and WL pulse can vary the NOPA output wavelength. In order to obtain a broad spectral width and high pulse energy, it requires a careful alignment of the spatial and temporal overlap as well as chirp control.

4.3.3 Pulse compression

In this part, we take the NOPA output pulse centered at 605 nm wavelength as an example to demonstrate the individual effort of pulse compression accomplished by (i) chirped mirror (CM) pair and (ii) prism pair compressor.

The pulse compression setup and related diagnostics are schematically depicted in Figure 4.13. First, the output beam encounters wedge plates of BK7 and quartz. This unit compensates the vertical lateral dispersion of the beam. Then the beam could be either compressed by the CM pair or prism pair through the flip mirror. After the beam is pre-compressed, we then diagnose the pulse duration and beam profile by the technique of frequency resolved optical gating (FROG) and a CCD camera, respectively. In order to minimize the dispersion during FROG measurements, we use a 10 μm thin type I BBO crystal (Bluebeam optical tech), where the BBO crystal is cemented with 1 mm thick fused silica plate to prevent destruction. For sake of achieving an ultrashort pulse duration at the sample surface inside the UHV chamber, we insert a 4 mm UVFS plate of same thickness as UHV entrance window before the FROG measurement. A small fraction of the compressed beam is monitored by a CCD camera to maintain a good shape of the beam profile.

Before the characterization of pulse duration by FROG, the optimization of the beam profile has a relatively high priority, this can greatly reduce the numbers of iteration in the alignment for achieving the shortest pulse duration. Usually, the NOPA output beam has a tilted ellipse like shape due to lateral dispersion, displayed in Figure 4.14 (a). The vertical lateral dispersion is optimized by tuning the angle of BK7 & quartz wedge, which works like a prism pair. In addition, the horizontal lateral dispersion is controlled by carefully varying the angle of second prism in Figure 4.13. These two combined actions bring together all the color components to be centered at one spot, see Figure 4.14 (b-c).

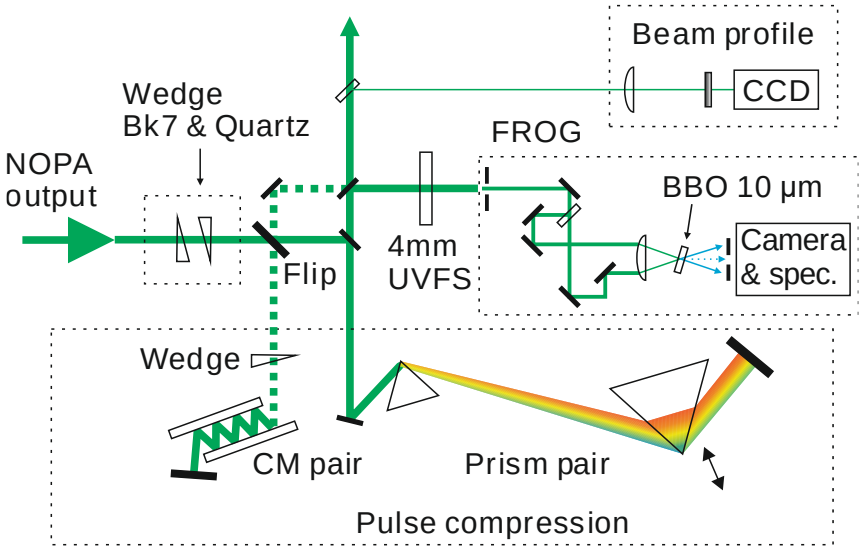

Figure 4.13: Schematic of NOPA pulse compression and associated diagnostic blocks. A combination of BK7 and quartz wedges are placed in the beam path, and the wedge angle lies on the plane perpendicular to the optical table. A set of flip mirrors (Flip) can either guide the beam to chirp mirror (CM) pair or prism pair, which are depicted inside the pulse compression unit. A 4 mm thick fused silica (UVFS) plate serves as pre-compression of the UHV entrance window. The pulse duration is characterized by a frequency resolved optical gating (FROG) unit, which involves a 10 µm thin BBO crystal and a set of camera and spectrometer. A small fraction of the compressed beam is sent into a CCD camera for optimizing the beam profile, before that the intensity of the beam is further reduced by a gray filter. The dashed line in the figure represents the beam path modified by the flip mirror.

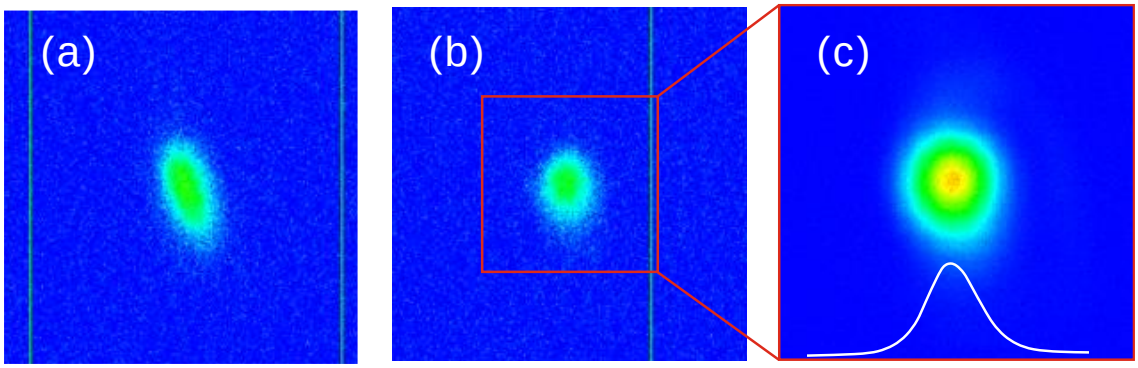

Figure 4.14: Measurements of NOPA beam profile. (a) Without any dispersion control, the beam profile of NOPA output exhibits a tilted elliptic shape. (b) A round shape is achieved through alignment of wedge BK7 & quartz and prism pair, which optimize the vertical and horizontal lateral dispersion, respectively. (c) Zoom in image with higher contrast, the FWHM diameter of the beam is about 240 µm.

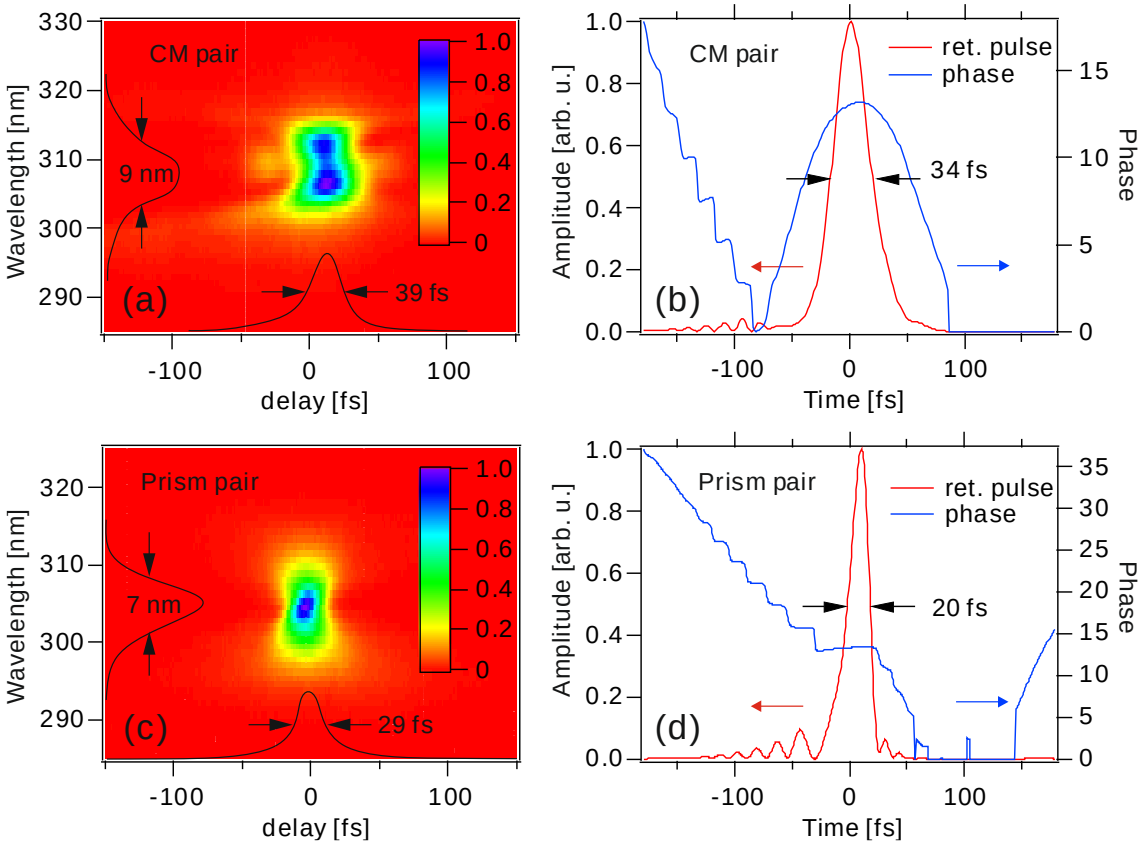

Figure 4.15: FROG measurements and pulse retrieval. (a) Measured FROG trace through 24 reflections between CM, and the NOPA beam is pre-compressed with one 2 mm BK7, 1 mm and 4 mm UVFS plate, one additional quartz wedge is used for precise control of linear chirp. (b) Retrieved pulse form and phase in time domain for FROG using CM pair. (c) Measured FROG trace for NOPA pulse compressed by prism pair, a 4 mm UVFS plate is considered for pre-compensation as well. (d) Pulse retrieval for FROG in case of prism pair. (See Figure 8.3 in Appendix C for more data)

Chirped mirror provides negative GVD for each time the beam is being reflected. The implemented CM (Optikwerkstatt, UDE) was designed for a dispersion control over spectral ranges 400 – 700 nm, i.e. high reflective in this ranges. The input beam depicted in Figure 4.13 for CM has a small rising angle, so that the beam after multiple reflections can couple vertically out for pulse diagnostics. An example of FROG measurement is shown in Figure 4.15 (a), the FROG trace shows a 9 nm spectral width and 39 fs auto-correlation (AC) length. We analyze the FROG trace by pulse retrieval algorithm (Femtosoft Technologies) [142], the retrieved pulse of 34 fs duration and phase in time domain is displayed in Figure 4.15 (b). As can be noticed, the trace is slightly linear tilted, this is probably due to a lack of compensation of horizontal lateral dispersion, since we implemented only one set of wedges for CMs compressor. The FROG retrieval indicates that the pulse experiences a positive linear chirp, which captured by the parabolic dependence of the retrieved phase. Although a third order GVD is still present, it can be strongly suppressed by the CMs, such a third order modulation is reflected as a tail in the retrieved pulse.

Similar to the CMs, the forward beam into prism compressor is vertically tilted, so the backward beam is coupled out in the vertical direction. In this setup, the two prisms are

placed more than 1 m apart to produce sufficient negative linear chirp. The measured FROG trace and retrieved pulse are shown in Figure 4.15 (c-d), respectively. From the result, a spectral width of 7 nm and an AC length of 29 fs is obtained. The FROG trace exhibits no tilted form, that the lateral dispersion is fully compensated. However, the AC length is rather narrow at the center of the spectrum and broad on both side, this feature implies some remaining uncompensated third order dispersion. We can see that the retrieved pulse has a FWHM of 20 fs and a modulated tail. And the retrieved phase suggest that the linear chirp is vanished in contrast to CMs.

In summary, the effect of third order dispersion becomes relevant if the pulse duration is as short as 20 fs. The CMs can reduce third order GVD produced by the dispersive optical elements. A full control of the pulse duration requires a balance of reflections on CM and the amount of inserted wedges to suppress the linear chirp. On the other side, the prism pair compressor can compensate the linear chirp but generate additional third order GVD through the prism itself. In fact, the prism compressor is easier and consumes less time to align for different wavelengths. For the purpose of SHG spectroscopic study and we considered that the third order GVD will not alter the pump-probe result. We have thus employed the prism compressor in the experiments. We note that a full compression of pulses down to 10 fs would be possible through combined effort and CMs and prism pair, but a numerical pre-calculation as well as a precise dispersion control are required and were not attempted here.

4.4 Pump-Probe SHG/mSHG scheme

This section describes two pump-probe schemes based on two light sources. One uses the 800 nm laser pulse generated by cavity dumped Ti:Sa oscillator, the other employs the NOPA output in ranges 500 – 700 nm. The two schemes have some building blocks and diagnostics in overlap, details will be given.

The layout of pump-probe mSHG using cavity dumped Ti:Sa oscillator is illustrated in Figure 4.16. An external prism compressor is installed at the exit of the oscillator to compensate additional GVD acquired from the dispersive optical elements, such as beam splitter, lens, wave plate and UHV window. The beam is separated into 1:4 for probe and pump beam. In the pump path, a reference channel detecting the SHG signal from a BBO crystal is installed for monitoring the fluctuations of the laser intensity and pulse duration. The pump beam is delayed with respect to the probe beam. A chopper with 500 Hz is inserted in the pump path, so that the probe signal can be measured with presence and absence of pump. In front the entrance window stands a fused silica lens f = 100 mm, then the pump and probe beam are noncollinearly focused with an incident angle about 39 °on the sample. The pump beam has a pulse energy of 32 nJ and can be focused by a 100 mm lens down to 30 μm, which results in a laser fluence of 4.5 mJ/cm^2 in focus. The focus quality and the pump-probe overlap at the sample surface can be optimized by a set of microscope and CCD camera.

After reflection from the sample, the fundamental and SHG beam are first separated by a dichroic mirror and then guided to the detection scheme, which consists of two parts. One is detecting the linear reflectivity and another one detecting the SHG yield. The linear reflectivity is measured by a photodiode and a lock-in amplifier, meanwhile the SH reflectivity is detected with a photomultiplier and a photon counter, which is operated in single photon counting mode. To ensure that only pure SH photons are harvested and fundamental light is filtered, an additional BG39 filter and a monochromator are installed.

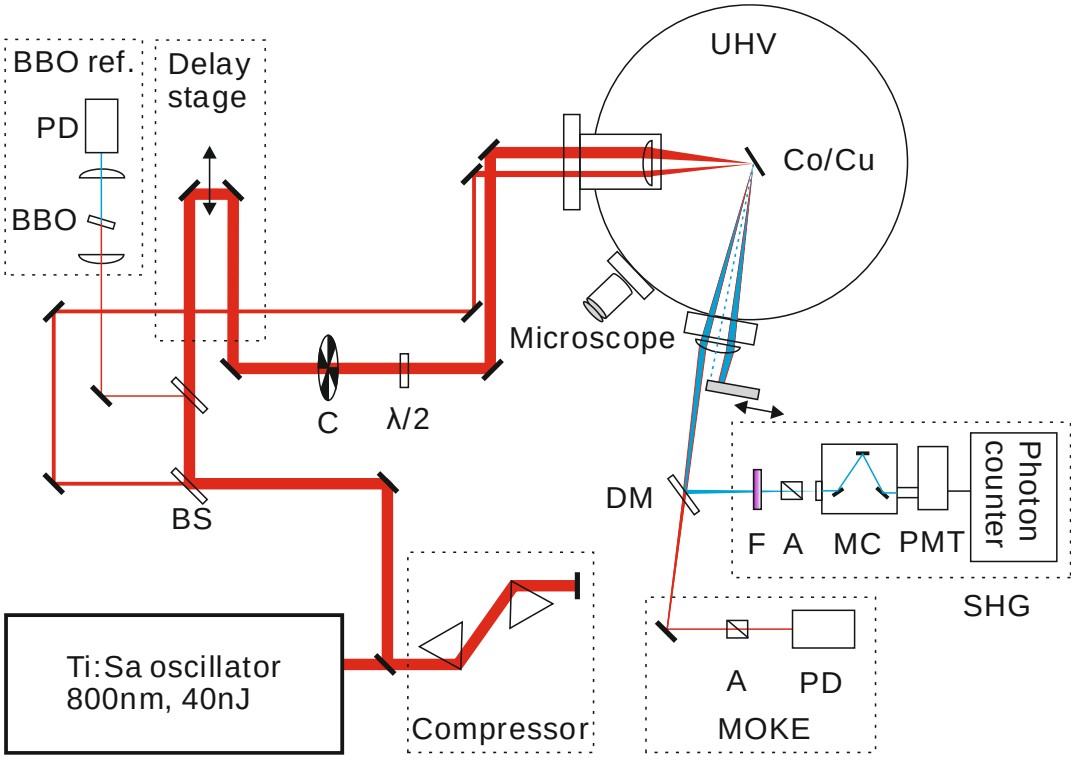

Figure 4.16: Experimental setup of time-resolved MSHG. The output of cavity dumped Ti:Sa oscillator is pre-compressed by a prism pair, divided by a beam splitter (BS) into a ratio of 1:4 for probe and pump beam, respectively. A light chopper (C) and half wave plate λ/2 are inserted in the pump path. The stability of the laser pulse is monitored by reference canal, where the SHG signal from a BBO crystal is detected by a photodiode (PD). A block outside the exit window can close the reflected pump and cross correlation beam (dashed blue line), while a dichroic mirror separates the fundamental and SHG beam. Reflectivity of fundamental beam is captured by a photo diode. The SHG detection block involves a BG39 filter (F), a polarization analyzer (A), a monochromator (MC), a photomultiplier (PMT) and a photon counter.

We note that the dichroic mirror reflects around 1% of the 800 nm wavelength beam. This will be blocked by the BG39 filter, which has only around 0.005% transmission for 800 nm beam. In addition, for polarization dependent SHG measurements, a λ/2 half wave plate is inserted in the pump path to rotate the polarization of the beam, while the polarization state of the reflected SHG is selected by a Glan-Taylor polarizer.

Regarding the time-resolved measurements, both lock-in amplifier and photon counter are synchronized with the light chopper. The temporal overlap and pulse duration at sample surface is determined by the cross-correlation between the pump and probe beam, which spatially lies between the reflected pump and probe beam. In particular, when measuring the pump induced change of the linear and second order reflectivity signal, the pump beam and the XC are blocked in front of the exit UHV window. The whole setup is covered by a light protective tent to avoid noise from the environmental light. With this setup, the reflected SHG from 5 ML Co/Cu(001) surface yields typically around 10^5 photon counts per second.

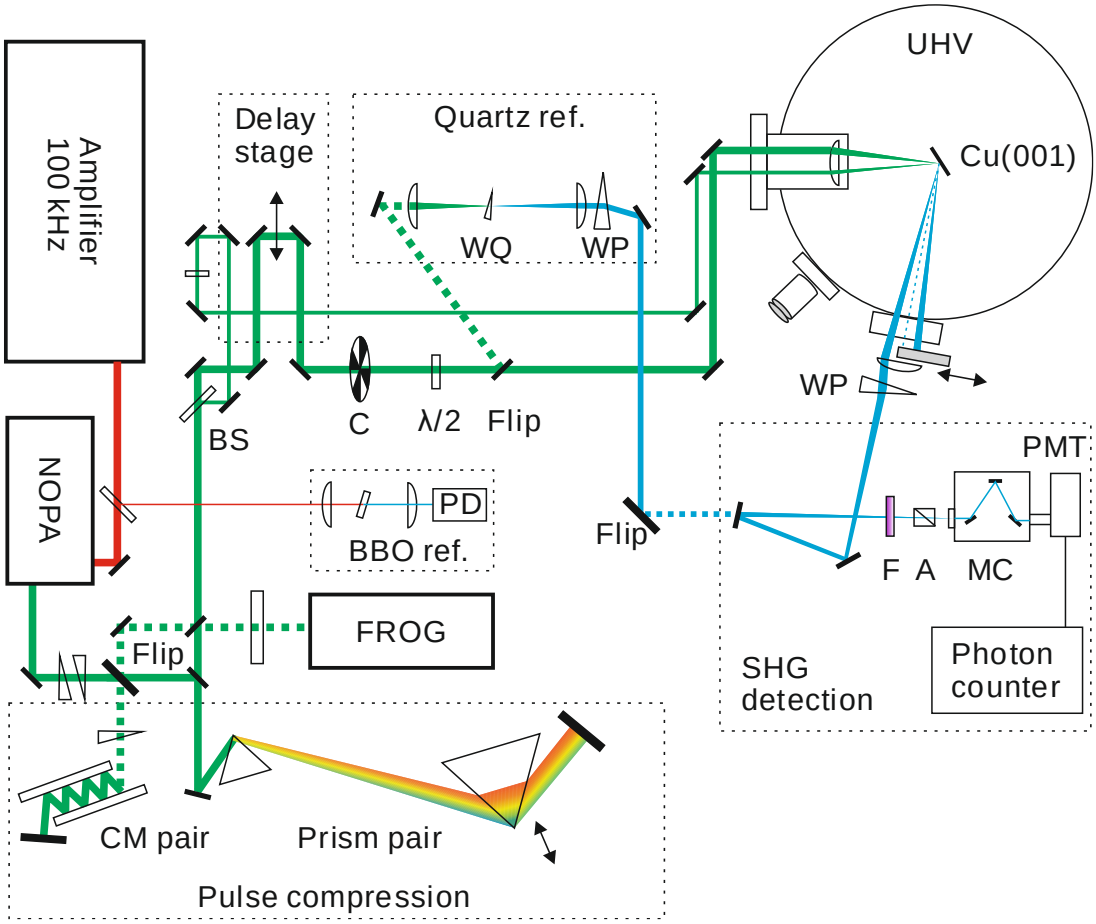

Figure 4.17: Pump-probe scheme using the NOPA light source. NOPA is first pumped by 100 kHz amplifier, while a small fraction of 800 nm beam is used for BBO reference channel. Then the NOPA output beam is pre-compressed by prism pair and optimized by FROG. After beam splitter (BS), pump and probe are focused and overlapped on the sample surface. The reflected SHG beam is captured by the SHG detection unit. Red solid line denotes 800 nm laser beam, greed solid line indicates 500 – 700 nm beam and 250 – 400 nm is represented by blue solid line. Dashed lines in the figure illustrated beam path switched by flip mirror (Flip).

The pump-probe scheme employing the NOPA light source is depicted in Figure 4.18. It adapts serval components from Figure 4.17 and new building blocks will be introduced. Depending on the working wavelength, the scheme can be divided into three wavelength ranges i.e. infrared 800 nm, visible 500 – 700 nm and ultraviolet (UV) 250 – 400 nm, the applied guiding mirrors are HR 800 nm coated mirror, protected silver mirrors (Thorlabs) and UV enhanced aluminum mirror (Thorlabs, Newport), respectively. After the NOPA stage, the laser pulse is guided to compression block and optimized by FROG, details of this part is previously in section 4.3.3 introduced. Then the NOPA beam is divided in to 1:4 ratios by a beam splitter (Layertec), which has a broadband (460 – 1000 nm) and low group delay dispersion (GDD) coating on front side of 1 mm thick fused silica substrate, with anti-reflection coating on the rear side. On one hand, a 1 mm UVFS compensating plate is inserted in the probe path, on the other hand, the pump beam passes through delay stage, light chopper and an achromatic λ/2 wave plate (400 – 800 nm, Thorlabs). Finally, both the pump and probe beam are guided to the UHV chamber and focused with a UVFS lens (f = 100 mm, AR coated, Thorlabs) on the sample with a spot diameter of 34 μm.

The SHG detection system is adapted from Figure 4.17 but modified to fit the purpose of spectroscopic measurement. We employ a wedged prism (WP, wedge angle 20 °) to separate the fundamental and SHG. By changing the angle of the reflective mirror, a selection of different UV wavelength can be achieved. In addition, an UV filter is placed in front of the monochromator (MC). Together with the effort of WQ, filter and MC, a detection of exclusive SH photon is guaranteed. Regarding polarization dependent SHG, we insert an UV Glan-Laser polarizer (Thorlabs) on the SHG path. Based on this setup, a typical SHG count rate from copper surface in the order of 10^4 photons per second can be detected.

Since the NOPA provides different output power at different wavelength, and the SHG yield depends on the intensity of the fundamental beam, it is important to have a reference channel for the fundamental beam. We employed a reference channel based on the quartz crystal. On the pump path, the beam can be switched to reference channel, which consists of a focusing fused silica lens (f = 100 mm), a y-cut wedged quartz (WQ) crystal [143], an imaging lens (f = 250 mm) and a WP with wedge angle 20 °. Since in quartz crystal, the SHG process depends exclusively on one susceptibility element in a certain geometry [144, 145], quartz is commonly applied as a reference for surface SHG spectroscopy [146]. The detailed characteristics of quartz SHG can be found in Appendix A. At the end, the fundamental and SHG is spatially separated by a WP. In order to protect the PMT, only 2.5% of fundamental power is used to generate second harmonic in WQ, which yields comparable SH photon counts to surface SHG.

5 Ultrafast charge and spin dynamics on Co/Cu(001) films

Ultrashort laser pulses can drive magnetic ordered materials into a highly nonequilibrium state, and by the timescales of femtosecond to picosecond the system exhibits interesting effect such as ultrafast demagnetization [11], all-optical switching [6] and coherent control of magnons [180]. In particular, ultrashort laser pulses induce femtosecond spin current [17, 82, 84] in ferromagnetic-paramagnetic (FM/PM) metallic heterostructures, which are promised as building blocks for future spintronic devices.

This chapter is devoted to the investigation of laser induced ultrafast charge and spin dynamics on Co/Cu(001) films by means of MSHG technique. In the first part, by varying the thickness of the Co films, spin current generation in nano-scale ferromagnetic films is analyzed by MSHG, where the magnetization dynamics are interpreted as two interfacial contributions i.e. vacuum/Co and Co/Cu(001) interfaces. We demonstrate the strength of MSGH to probe surfaces and buried interfaces and the inhomogeneous magnetization dynamics in fs timescales. In the second part, we focus on the same sample system of Co/Cu(001) but a reduction in the z direction down to few layer to explore the role of interface in spin dynamics, which is accomplished by the combined effort of fs-MSHG and ab initio TDDFT, hence, this unravels a competition of spin transfer cross the interface and local spin dynamics i.e. spin orbit coupling (SOC) mediated spin flip.

The investigated epitaxial Co/Cu(001) films are *in situ* prepared in UHV and the followed MSHG measurements are performed in transversal geometry with an incident angle of 39 ° at room temperature. The femtosecond light source is provided by a cavity dumped Ti:Sa oscillator centered at 800 nm wavelength with a pulse duration of 35 fs and pulse energy of 40 nJ in repetition rate of 2.35 MHz. Detailed experimental setup is referred to Chapter 4.4.

5.1 Inhomogeneous magnetization dynamics on Co/Cu(001) films

Ultrafast spin current generation trigged by laser excitation has revealed the possibilities to manipulate the magnetic order in metallic heterostructure. Experimental methods capable of probing magnetization dynamics in metallic multilayers should be interface sensitive. In this section, we have particularly addressed the issue of inhomogeneous magnetization dynamics on Co/Cu(001) films by time-resolved MSHG experiments, the experimental schematic is depicted in Figure 5.1. The static properties of Co/Cu(001) are first being characterized. A simple two interfaces model is applied to describe the Co thickness dependent MSHG signal, which can be disentangled as contributions from vacuum/Co and Co/Cu interface. We further analyze the transient magnetization profile in different Co film thickness after laser excitation. The transient profile reflects the MFP of spin majority and minority that escapes from ferromagnetic Co to conducting Cu substrate.

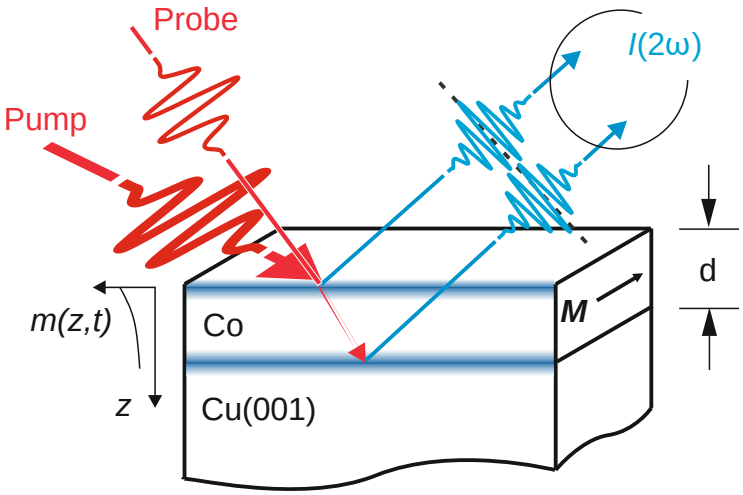

Figure 5.1: Schematic illustration of pump-probe MSHG experiments on Co/Cu(001) films of different thickness 0.4 – 10 nm. Ultrafast demagnetization is induced by a s-polarized pump beam that causes a spatially inhomogeneous change in the magnetization inside the film. Subsequently the magnetization dynamics is probed by another laser pulse, by which the interface sensitive p-P polarized SHG is measured as a function of pump-probe delay for opposite magnetization orientation. The incident angle of pump beam is about 40 °, noncollinear angle between pump and probe beam is less than 3 °. Redrawn from [18].

5.1.1 Static properties of Co/Cu(001)

By means of MSHG studies on ferromagnetic (001) surfaces in the present section, static properties are referred to magnetic hysteresis loop, polarization dependent and thickness dependent MSHG measurements on Co/Cu(001) films.

Hysteresis loop

Epitaxial growth of Co films on Cu(001) is a well-established process, in which the Co atoms initially form islands and become closed layers at coverage of 1.8 ML [147]. A sudden jump of Curie temperature occurs at this critical coverage and the film exhibits ferromagnetism at room temperature, where the magnetization oriented in plane. Magneto-optics relies on a measureable magnetic contrast from the sample. The magnetic contrast can be illustrated in the magnetization hysteresis loop, which yields valuable information about magnetic anisotropy, magnetization orientation of the ferromagnetic film. In case of nonlinear magneto-optics i.e. MSHG, the reflected SHG intensity from the ferromagnetic film as a function of external magnetic field is recorded. As an example, the magnetization hysteresis curve of 1 nm Co/Cu(001) film is shown in Figure 5.2. The hysteresis curve is recorded in transversal geometry, where the magnetization is perpendicular to the optical plane and in the sample surface. One recognizes a sharp turnaround of magnetization under 2 mT external magnetic field, this confirmed that the easy axis of magnetization lies in the plane.

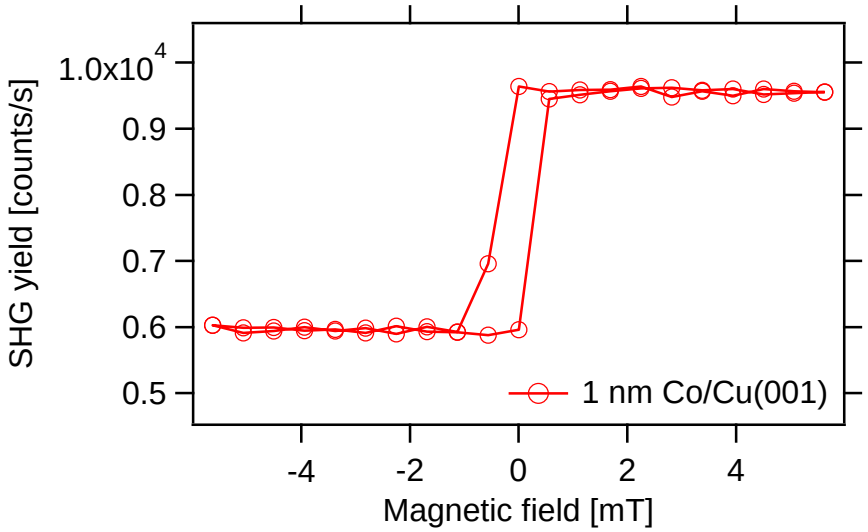

Figure 5.2: MSHG hysteresis curve of 1 nm Co/Cu(001) film at room temperature. The measurement was taken in transversal geometry and p-P polarization configuration i.e. p-polarized fundamental beam with p-polarized SHG. A switching of magnetization of the film under external magnetic field of less than 2 mT and the shape indicate that the easy axis of magnetization lies on the plane parallel to the surface.

Polarization dependent MSHG

Valuable information such as symmetry, magnetic contrast, particular susceptibility $\chi^{(2)}$ tensor elements etc. can be deduced from polarization dependent MSHG. The polarization dependent behavior of MSHG of 1 nm Co/Cu(001) film is depicted as an example in Figure 5.2. Three noticeable features can be seen on the polarization dependent pattern.

First, the p-P configuration yields the strongest SHG due to the fact that new non-zero susceptibility tensor elements appear in this polarization combination (see Table 3.2). And particularly the tensor element with *z* components is involved, which has the largest contribution caused by the discontinued spatial extend of solid discontinued and field discontinuity in z direction. As shown in the figure, enhancement of SHG intensity occurs on Co/Cu(001) in comparison to bare Cu(001) surface (further SHG analysis of Cu(001) surface can be found in chapter 6), the SHG enhancement is caused by the increased probability of SHG transition via states around Fermi level, because more states are available for transition metal in contrast to noble metal [16]. In addition, this configuration offers considerable amount of magnetic contrast.

Secondly, s-P polarized SHG is one order of magnitude weaker than p-P SHG, yet stronger than s-P polarized SHG on Cu(001). As previously introduced in Chapter 3, s-P SHG depends exclusively on crystallographic contribution χ_{zyy} and magnetization-induced susceptibility tensor element $\chi_{xyy}(\boldsymbol{M})$, so the total SHG yield is expected to be small. More importantly, the magnetic contrast is small, which implies that the phase between even and odd at 5 ML coverage is close to 90 °[123].

At last, a very similar SHG pattern in comparison to bare Cu(001) is observed for mixed-S polarization combination. Mix-S SHG is determined by χ_{yzy} and $\chi_{yxy}(\boldsymbol{M})$ and rather less affected by the modification of electronic structure at metal surfaces, the SHG pattern mainly reflects the 4-fold symmetry of (001) metal surface. Certain amount of the

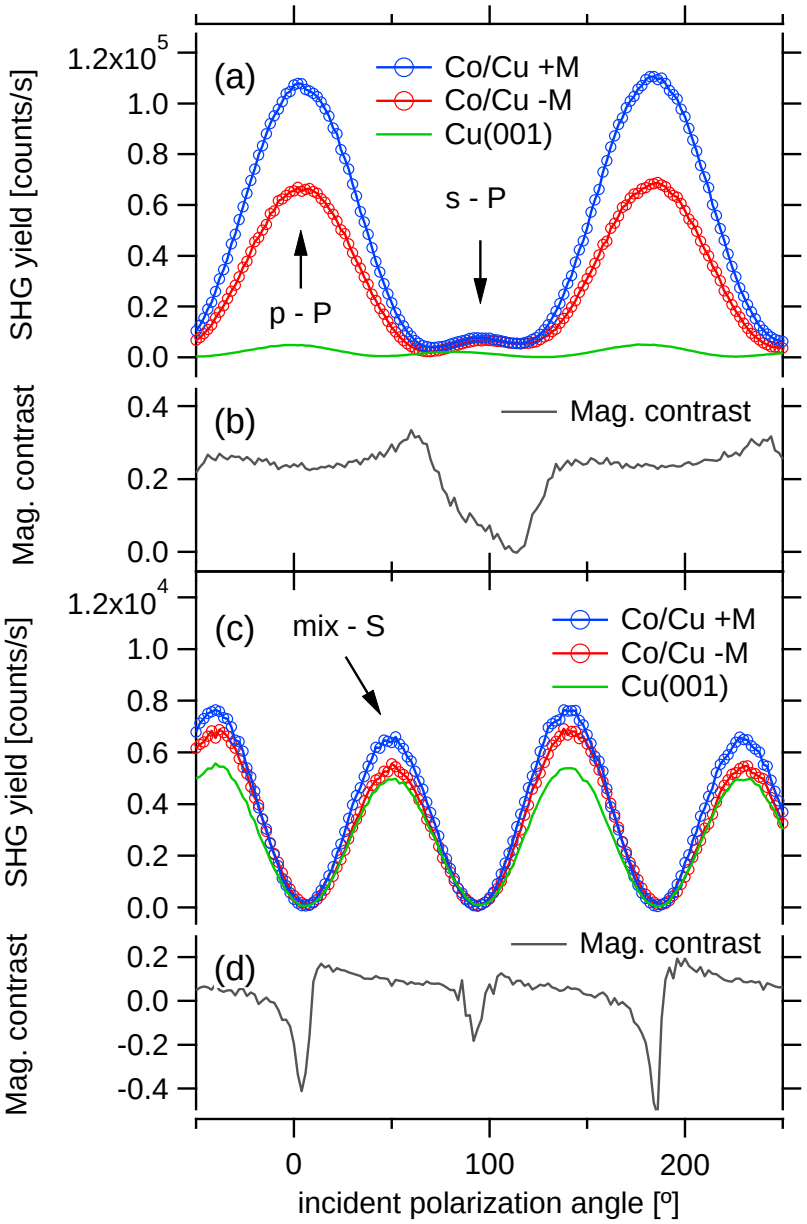

Figure 5.3: Polarization dependent SHG measurements on 5 ML Co/Cu(001) film for an output of (a) P-polarized SHG and (b) S-polarized SHG. The SHG intensity is plotted as a function of incident polarization angle with opposite orientation of magnetization. Blue and red solid lines represent the measurements of Co/Cu(001). Measurement on bare Cu(001) surface is denoted by green solid lines. Polarization angle of 45 ° for fundamental beam is denoted by "mix". In (b) and (d), the corresponding magnetic contrast for (a) and (c) is displayed. respectively.

magnetic contrast is present at this configuration, but the SHG yield is not significantly enhanced, this indicates that the absolute value of magnetization dependent element $\chi_{yxy}(\boldsymbol{M})$ is considered to be small.

Based on the fact that the p-P polarization combination provides the largest magnetic contrast with reasonable MSHG yield, we have chosen this configuration for further thickness dependent and time-resolved MSHG studies.

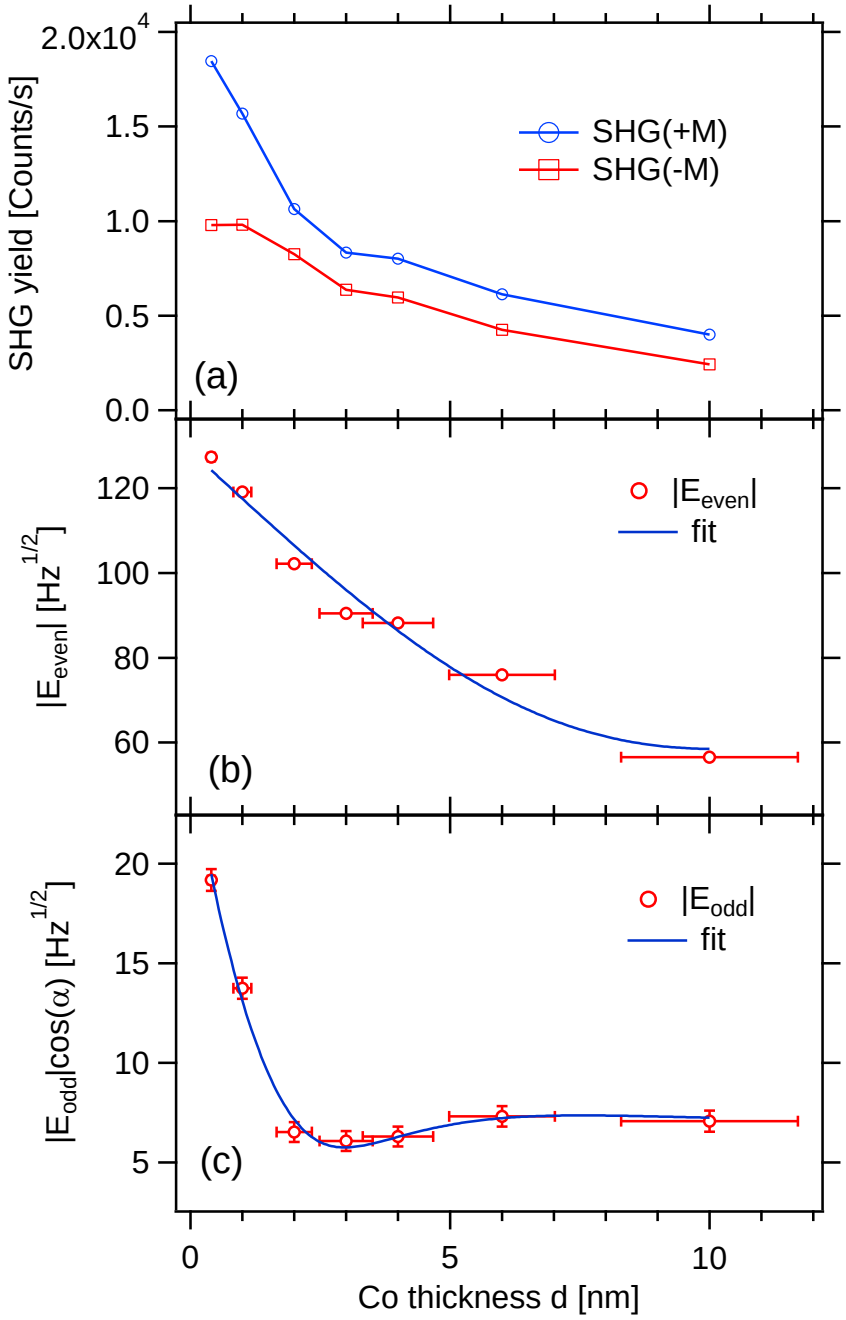

Figure 5.4: Thickness dependence of (a) MSHG intensity, (b) absolute value of $|E_{even}^{2\omega}|$ field and (c) $\left|E_{odd}^{2\omega}\right|$ field. Solid lines in (b) and (c) are fitted by equation (5.10) and (5.11).

Thickness dependence of p-P polarized MSHG

The thickness dependence of p-P polarized MSHG intensity in range of 0.4 nm $\leq d \leq$ 10 nm is shown in Figure 5.4 (a). According to equation (3.33), the SHG intensity is made up by the square of non-magnetic and magnetic term, as well as an associated cross term, which is dependent on the magnetization. We can derive the magnetization-independent SH field as:

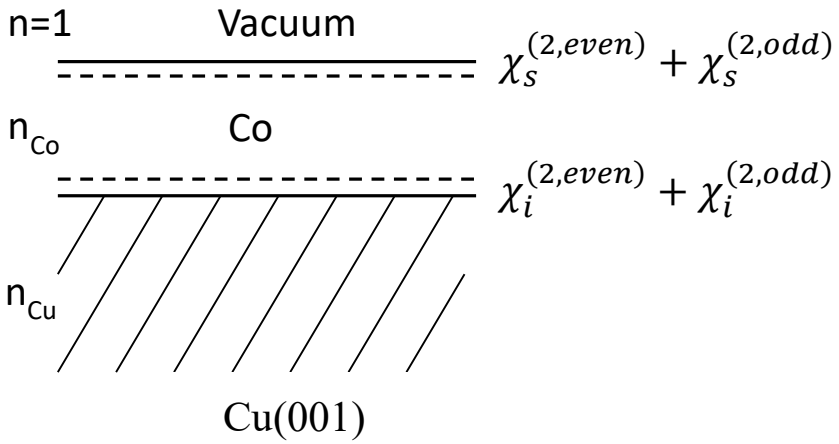

Figure 5.5: Schematic illustration of MSHG from Co/Cu(001) with surface and interface susceptibility tensor components $\chi_s^{(2)}$ and $\chi_i^{(2)}$.

$$|E_{even}^{2\omega}| \approx \sqrt{\frac{I^{\uparrow} + I^{\downarrow}}{2}} \tag{5.1}$$

and the magnetization-dependent SH field

$$\left|E_{odd}^{2\omega}\right|\cos(\alpha) \approx \frac{I^{\uparrow} - I^{\downarrow}}{4|E_{even}^{2\omega}|} \tag{5.2}$$

Here, α represents the phase between $|E_{even}^{2\omega}|$ and $\left|E_{odd}^{2\omega}\right|$. The phase α is close to zero and stay constant for small d [123]. In the following analysis, $\alpha = 0$ is assumed. The derived $|E_{even}^{2\omega}|$ and $\left|E_{odd}^{2\omega}\right|$ is plotted in Figure 5.4 (b-c) as a function of thickness. In general, the MSHG intensity and $|E_{even}^{2\omega}|$ decreases for thicker films. $\left|E_{odd}^{2\omega}\right|$ shows a decreasing behavior until about d = 3 nm, recovers back and finally stays rather constant as the thickness keep increasing. Such behavior looks like a strongly damped oscillator and hints that the phase between the two interfaces may play a role, where the SHG intrinsically probes.

Considering that the total detected SHG signal is made up by the reflected SHGs form vacuum/Co and Co/Cu interfaces, then the total SHG signal can be described by the susceptibility tensor at surface $\chi_{s,even}^{(2)} + \chi_{s,odd}^{(2)}(M)$ and at interface $\chi_{i,even}^{(2)} + \chi_{i,odd}^{(2)}(M)$, both consist of magnetization-independent (even) and magnetization-induced (odd) term. The nonlinear susceptibilities of a Co/Cu(001) film is depicted in Figure 5.5. Therefore, the resulting SH fields from the surface can be expressed by two contributions:

$$E_{s,even}^{2\omega} = a_s \cdot E^{\omega}E^{\omega} \cdot \chi_{s,even}^{(2)} \tag{5.3}$$

$$E_{s,odd}^{2\omega} = a_s \cdot E^{\omega}E^{\omega} \cdot \chi_{s,odd}^{(2)}(M) \tag{5.4}$$

As well as the SH fields from the interface:

$$E_{i,\,even}^{2\omega}(d) = a_i \cdot E^{\omega}E^{\omega} \cdot {U_{\omega}}^2 \cdot \chi_{i,\,even}^{(2)} \cdot U_{2\omega} \tag{5.5}$$

$$E_{i,\,odd}^{2\omega}(d) = a_i \cdot E^{\omega}E^{\omega} \cdot {U_{\omega}}^2 \cdot \chi_{i,\,odd}^{(2)}(M) \cdot U_{2\omega} \tag{5.6}$$

Where a_s and a_i represent the Fresnel factor, E^{ω} denotes the electric field of the incident fundamental beam. Additionally, a new term $U_{\omega}(d)$ and $U_{2\omega}$ appears for SH field generated from the Co/Cu interface with the expression:

$$U_{\omega}(d) = e^{i\omega \boldsymbol{n}(\omega)d} = e^{i\frac{2\pi}{\lambda}\boldsymbol{n}(\omega)d} \tag{5.7}$$

which describes the damping and phase shift of fundamental and SH electric field in Co over thickness *d*, respectively. Here, $\boldsymbol{n}(\omega) = n + iK$ is the complex refractive of bulk Co, numbers are taken form [155]. Thus, the total reflected SH field can be decomposed as magnetization-independent part:

$$|E^{2\omega}_{even}| = \left|E^{2\omega}_{s,even} + E^{2\omega}_{i,even}(d)\right| \tag{5.8}$$

And magnetization-dependent part

$$\left|E^{2\omega}_{odd}\right| = \left|E^{2\omega}_{s,odd} + E^{2\omega}_{i,odd}(d)\right| \tag{5.9}$$

To be more specific, equations (5.8) and (5.9) for an incident angle of θ can be reformed as:

$$|E^{2\omega}_{even}| = \left|A^{S}_{even} + A^{I}_{even} \cdot e^{-\beta\cdot\frac{d}{\cos\theta}} \cdot e^{i\left(\varphi + 2\pi\frac{n_{\omega}+n_{2\omega}}{\lambda_{2\omega}}\frac{d}{\cos\theta}\right)}\right| \tag{5.10}$$

$$\left|E^{2\omega}_{odd}\right| = \left|A^{S}_{odd} + A^{I}_{odd} \cdot e^{-\beta\cdot\frac{d}{\cos\theta}} \cdot e^{i\left(\varphi + 2\pi\frac{n_{\omega}+n_{2\omega}}{\lambda_{2\omega}}\frac{d}{\cos\theta}\right)}\right| \tag{5.11}$$

with

$$A^{S}_{even} = a_s E^{\omega} E^{\omega} \chi^{(2)}_{s,even}, \qquad A^{I}_{even} = a_i E^{\omega} E^{\omega} \chi^{(2)}_{i,even} \tag{5.12}$$

$$A^{S}_{odd} = a_s E^{\omega} E^{\omega} \chi^{(2)}_{s,odd}(M), \qquad A^{I}_{odd} = a_i E^{\omega} E^{\omega} \chi^{(2)}_{i,odd}(M) \tag{5.13}$$

where the parameter β describes the effective damping in Co, and φ denotes the phase shift between surface and interface SH field. The experimental data $|E^{2\omega}_{even}|$ and $\left|E^{2\omega}_{odd}\right|$ are fitted with equation (5.10) and (5.11) and are shown in Figure 5.4.

Here we assume that the surface contribution is not altered and does not depend on the thickness *d*, the arguments are provided below. In general, the surface roughness is increased for large thickness d of epitaxial Co/Cu(001) films i.e. 3D growth. One expect to see an increased surface SH signal due to increasing roughness. However, as displayed in the data, $|E^{2\omega}_{even}|$ shows decreasing behavior for large thickness, this implies that surface roughness could play a role but only a minor effect. Moreover, for case of $\left|E^{2\omega}_{odd}\right|$, It was previously established that the surface roughness contributes at most 20% of the total SHG signal in Co/Cu(001) and does not affect the magnetization-induced part [148]. Hence, we neglect the effect of surface roughness in our experiments.

Another concern is the lattice mismatch and the corresponding strain relaxation for large Co film thickness. It was suggested by reflection high-energy electron diffraction (RHEED) [149], that a weak relaxation of strain starts at 15 ML (approx. 3 nm) and the film is still strongly strained up to thickness of 40 ML (approx. 7 nm), which is within most of our investigated thickness range. In addition, p-P polarized SHG is dominated by the susceptibility tensor, by which components normal to surface plane are involved, while the strain is mainly relaxed in the in-plane direction, thereby affects the s-P polarized SHG signal. Based on the above considerations, the surface contribution is justified to be constant within our investigated thickness range.

Parameters of $|E_{even}^{2\omega}|$

A_{even}^{S}	68.51 ± 5.86
A_{odd}^{I}	60.83 ± 5.16
β	-0.13 ± 0.04
φ	$10.81° \pm 16.60°$

Parameters of $|E_{odd}^{2\omega}|$

A_{odd}^{S}	7.06 ± 0.42
A_{odd}^{I}	32.15 ± 1.17
β	-0.38 ± 0.05
φ	$185.93° \pm 7.81°$

Table 5.1: Fit parameters base on equations (5.10 – 5.13) applied for the thickness dependent static SHG measurements in figure 5.4.

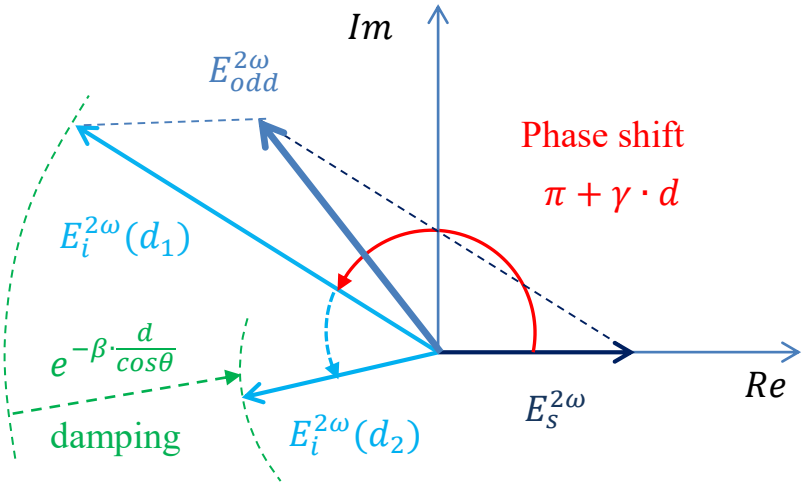

Figure 5.6: Schematic of destructive interference for $E_{odd}^{2\omega}$. Surface and interface term are initially differed by a 180 °phase difference. With increasing thickness *d*, the interface term is damped and further phase-shifted.

In our case the optical constant is not measured *in situ* due to technical reasons, we leave β as a free fit parameter, since the optical constants of bulk material can be different for thin film. The overall fitting results are shown in Table 5.1.

Hence, the total SH field is quantified by a constant surface contribution and a damped interface contribution with associated phase shift. As mentioned, the model involves the least amount of parameters to describe the result. The fitting results show a phase difference of $\varphi = 11 \pm 16°$ for $|E_{even}^{2\omega}|$ and $\varphi = 186 \pm 8°$ for $\left|E_{odd}^{2\omega}\right|$, where the latter one shows a destructive interference of the surface and interface contribution. Such effect can be understood that the vacuum/Co and Co/Cu interfaces are mirrored by a plane, where the presence of magnetization induces a 180 phase difference between their tensor elements, which is consistent with earlier findings [150].

Together with Figure 5.6, the thickness dependence of $|E_{odd}^{2\omega}|$ is illustrated. The total field is initially dominant by the interface contribution with phase difference of π to surface SH field. As the Co thickness is increased to 3 nm, the interface contribution is reduced and phase-shifted, which leads to a minimum of observed $|E_{odd}^{2\omega}|$. For $d \geq 3$nm, $|E_{odd}^{2\omega}|$ recovers back and eventually dominated by the surface contribution. For the case of $|E_{even}^{2\omega}|$, the phase difference is small that no destructive interference occurs and the total signal continuous decreases for the whole investigated thickness range.

5.1.2 Thickness dependent time-resolved MSHG

With detailed static MSHG properties of ferromagnetic Co/Cu(001) films from previous section, we then investigate the dynamics properties of the system by pump-probe technique. The system is excited by an intense pump pulse, followed by a weaker, delayed probe pulse to monitor the temporal evolution of the system. In particular, the reflected probe pulse at the second harmonic photon frequency is detected. For MSHG, the dynamical behavior of electronic and magnetic system is simultaneously measured. The main goal is to analyze the spin current by performing a systematic thickness dependent studies. We have disentangled the magnetization dynamics from the vacuum/Co and Co/Cu interfaces and thereby characterized the spin dependent mean free path (MFP).

According to equation (3.39) (3.40), the measured pump-probe MSHG data can be derived into magnetization-independent $\Delta_{even}(t,d)$ and magnetization dynamics $\Delta_{odd}(t,d)$, the result is displayed in Figure 5.7. As a technical note, the data is analyzed for $\left|E_{odd}^{2\omega}\right|^2 \ll |E_{even}^{2\omega}|^2$, which is indeed the case through thickness dependent static MSHG measurements. In order to prevent any surface contamination due to residual gas adsorption, etc., the pump-probe MSHG data are collected for fresh prepared Co/Cu(001) film within 12 hours after sample preparation.

At first glance in Figure 5.7, we observe clearly two different trends of dynamics for Δ_{even} and Δ_{odd} for an increasing thickness of Co film. A negative pump-induced change in Δ_{even} for all film thicknesses is observed, while the magnetic part Δ_{odd} shows a complex behavior including a sign change. Generally, Δ_{odd} reflects the time-dependent MSHG magnetic contrast of the sample. Or more specifically, it probes the pump-induced relative change of $|E_{odd}^{2\omega}|$, normalized to the value before pump pulse excitation. Starting from 0.4 nm (approximately 2.2 ML) Co/Cu(001) film, Δ_{odd} shows a negative pump induced change in the first tens fs and the signal relaxes back at longer delay, which is expected as laser-induced demagnetization dynamics. However, for 2 nm $\leq d \leq$ 4 nm thickness, a positive pump-induced change is observed. Interestingly, Δ_{odd} shows for $d \geq 6$ nm initially negative but later positive signal i.e. a sign change in the transient response. Additionally, the time scale when the maximal changes occur in odd and even are different. The transient minimum in Δ_{even} occurs at same time delay, only the absolute amount of laser induced change is varying. In Δ_{odd}, the maximal pump-induced change is around 50 fs for $d = 0.4$ nm. The delay time of maximal change shifts to around 100 fs for 2 nm $\leq d \leq$ 4 nm, and it occurs for $d \geq 6$ nm around zero delay.

Due to these two clear different trends, we conclude that Δ_{odd} dynamics cannot be dominated by artifacts. Moreover, we applied a polarization combination to avoid artifacts. The sample is pumped with s-polarized beam and probed by p-polarized SHG, so that the artifacts induced by pump-probe correlation and effect such as state-filling [56] are excluded.

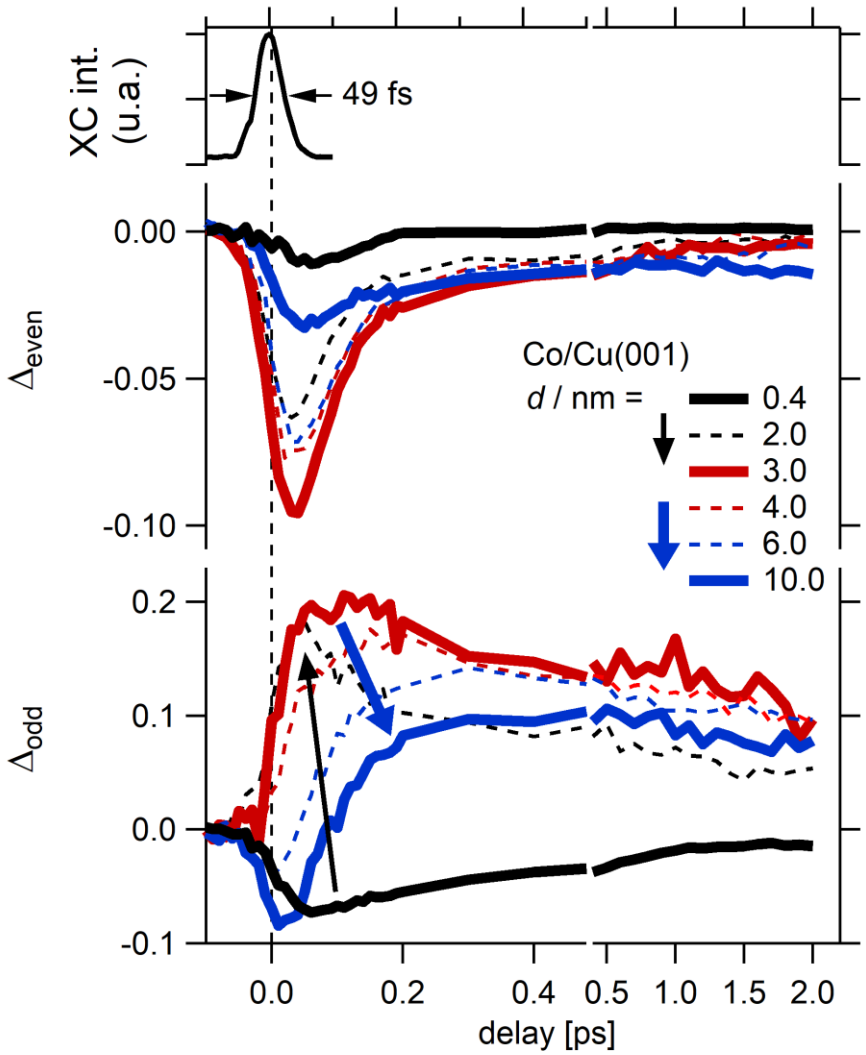

Figure 5.7: Thickness dependent time-resolved MSHG data versus the pump-probe delay. On top, the pump-probe cross-correlation (XC) is measured at the sample surface and shows a FWHM about 49 fs. The pump-induced change of magnetization-independent part $\Delta_{even}(t,d)$ and magnetic part $\Delta_{odd}(t,d)$ are displayed in middle and at bottom, respectively. Arrows at bottom figure serve as eyes guide to track the signal changes with increasing thickness.

Since MSHG probes the vacuum/Co surface and Co/Cu(001) interfaces, it is naturally to consider the thickness dependent behavior of Δ_{odd} as an interplay between these two interfaces, i.e. a spatially inhomogeneous magnetization dynamics in the Co/Cu(001) film, which can be caused by the competition between laser-induced local and nonlocal spin current [60].

5.1.3 Two interfaces model: what does $\Delta_{odd}(d)$ probe?

Based on the static thickness dependent results, the MSHG signal is dominated by the Co/Cu(001) interface at low d and the vacuum/Co interface at higher d. Therefore, we approximate $\Delta_{odd}(10\,\mathrm{nm})$ and $\Delta_{odd}(0.4\,\mathrm{nm})$ as Δ^{S}_{odd} and Δ^{I}_{odd}, respectively. In the simplest approach, the linear combination of these two items should be able to capture the evolution of experimental data with thickness changes.:

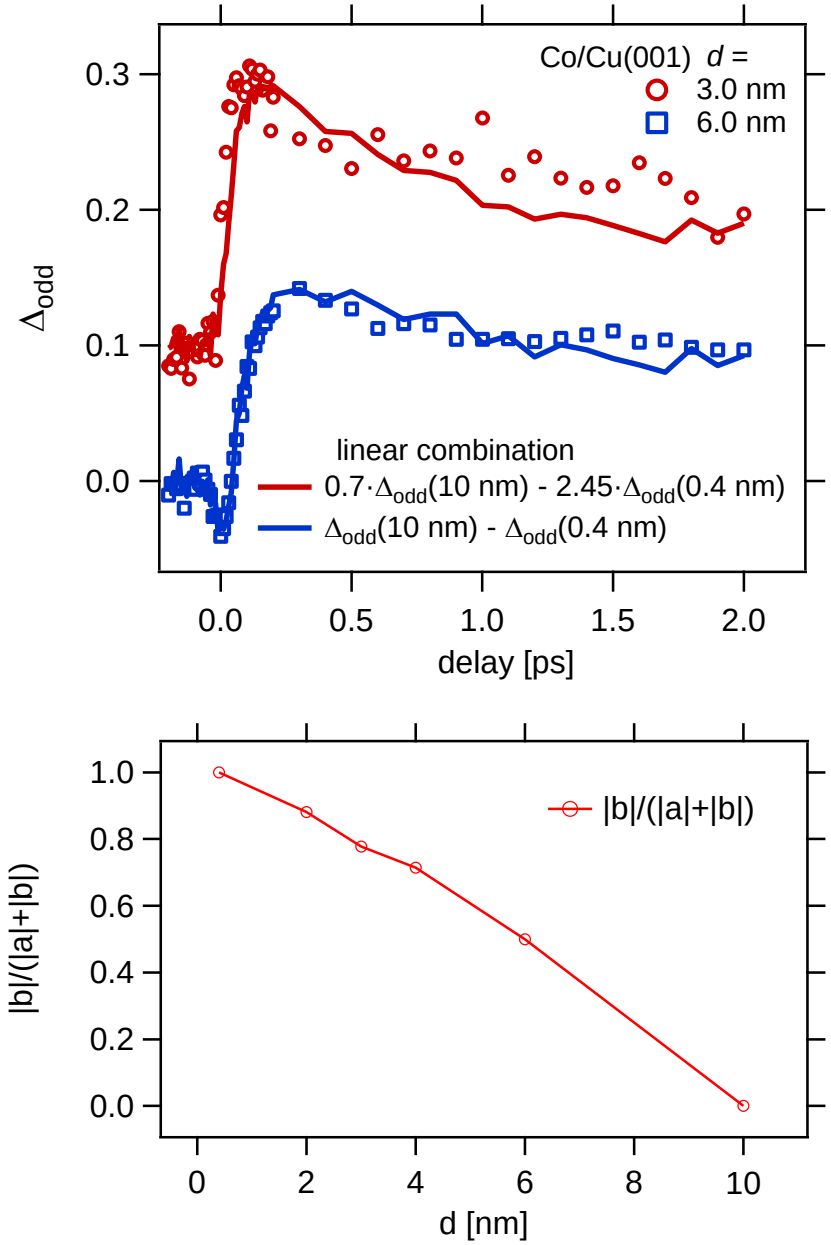

Figure 5.8: **Top**: Modeling of $\Delta_{odd}(d)$ by a linear combination of $\Delta_{odd}(0.4\,nm)$ and $\Delta_{odd}(10\,nm)$, 3 nm data and corresponding modeling is offset for visibility of data. **Bottom**: normalized factor of interface contribution $|b|$ in the model of linear combination.

$$\Delta_{odd}(d) = a \cdot \Delta_{odd}(10\,nm) + b \cdot \Delta_{odd}(0.4\,nm) \tag{5.14}$$

where a and b indicate the corresponding contributions from interface and surface. For example, the linear combination of 3 nm and 6 nm data are shown in Figure 5.8. The transient change of $\Delta_{odd}(3\,nm)$ and $\Delta_{odd}(6\,nm)$ up to 0.5 ps can be well described by the linear combination, while deviations start to appear for delay time > 500 fs. At this timescale the electronic system is thermalized and the temperature begin to equalize with lattice. For the 3 nm and 6 nm thickness the value of b is negative, which is caused by a 180 °phase shift between the surface and the interface. The ratio of factor i.e. $|b|/(|a|+|b|)$

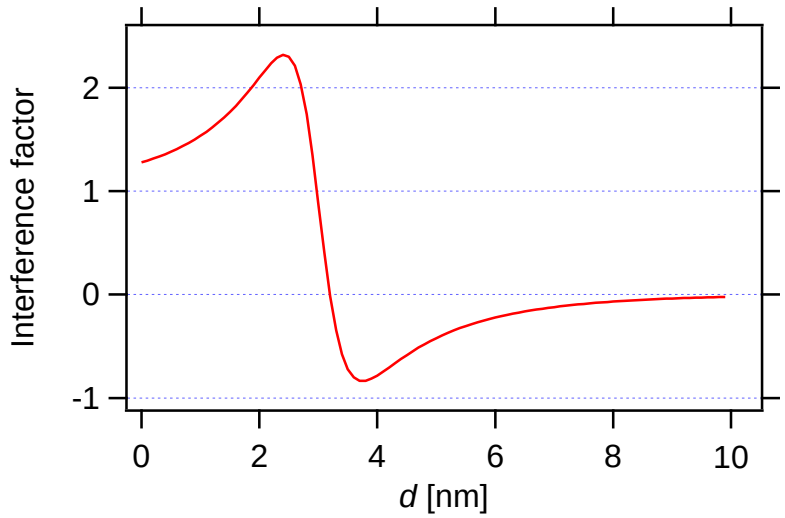

Figure 5.9: Calculated interference factor between the odd contribution from vacuum/Co and Co/Cu interfaces.

is shown in Figure 5.8, which indicates that the relative contribution of the interface is decreasing with *d*. The dynamic data set is consistent with the static studies that the interface contribution is partially cancelled by the surface, so the thickness dependent evolution of $\Delta_{odd}(d)$ could be viewed as a competition between surface and interface.

The thickness dependent evolution of Δ_{odd} is linked to the transient magnetization at the Co surface $m_s(t)$ and the Co/Cu(001) interface $m_i(t)$. We define the relative change of magnetization dynamics or demagnetization as

$$\Delta m_s(t) = \frac{E^{2\omega}_{s,\,odd}(t)}{E^{2\omega}_{s,\,odd}(t<0)} - 1 = m_s(t) - 1 \tag{5.15}$$

$$\Delta m_i(t) = \frac{E^{2\omega}_{i,\,odd}(t)}{E^{2\omega}_{i,\,odd}(t<0)} - 1 = m_i(t) - 1 \tag{5.16}$$

In order to extract the magnetization profile from $\Delta_{odd}(d)$, we can express $\Delta_{odd}(d)$ with equation (3.40), (5.4) and (5.6) in the first order approximation as:

$$\Delta_{odd}(d) \approx \Delta m_s(t) + int(d) \cdot [\Delta m_i(t) - \Delta m_s(t)] \tag{5.17}$$

with *int*(*d*) defined as real part of $E^{2\omega}_{i,odd}(d)$ projected on total $E^{2\omega}_{odd}$:

$$int(d) = Re\left(\frac{E^{2\omega}_{i,odd}(d)}{E^{2\omega}_{s,odd} + E^{2\omega}_{i,odd}(d)}\right) \tag{5.18}$$

Here, we term *int*(*d*) as interference factor. Together with the calculated *int*(*d*) shown in Figure 5.9 and the expression (5.17), we explain the *d* dependent changes of $\Delta_{odd}(d)$ that $\Delta_{odd}(d)$ monitors the amount of demagnetization of surface for Co large thickness, while the difference between the surface and interface i.e. magnetization profile $\Delta m_i(t) - \Delta m_s(t)$ enters into the observed signal by *int*(*d*), which becomes significant for 1 nm $<$ d $<$ 6 nm. For a Co film d $<$ 1nm, the surface contribution is almost cancelled by the interface. In another words, for ultrathin Co/Cu(001) film of only a few monolayers, the boundary between the surface and the interface is difficult to define. In this case, $\Delta_{odd}(d)$ probes the magnetization dynamics of the whole thin film, which is dominated by the character of Co/Cu(001) interface.

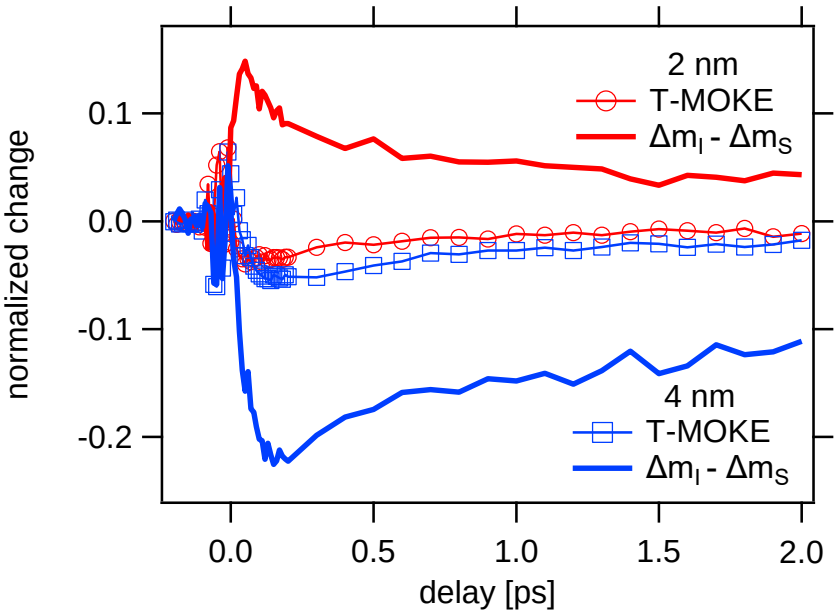

Figure 5.10: Transient magnetization gradient $\Delta m_i(t) - \Delta m_s(t)$ for 2 nm and 4 nm Co thickness, represented by solid lines. Circle and squad points are measured T-MOKE contrast.

5.1.4 Spatial inhomogeneous magnetization dynamics

In this section, we show that the magnetization profile can be analyzed by following approach. In time-resolved MSHG measurements, the linear reflectivity for opposite magnetization direction was simultaneously acquired. We denote $\delta_k(t)$ as transient T-MOKE contrast, which probes the averaged magnetization of the films [154]:

$$\delta_k = \int_0^d \zeta(z) \cdot m(z) \cdot dz \tag{5.19}$$

In the expression (5.19), δ_k integrates the magnetic contrast of individual layers over whole thickness range with associated in-depth T-MOKE sensitivity $\zeta(z)$. Since $\zeta(z)$ is rather flat and uniform for 2 nm $<$ d $<$ 6 nm [151], the average demagnetization of the film, in the most simplest scenario that the film approximated as two interfacial layers, can be expressed as:

$$\Delta\delta_k(t) \approx \Delta m_{aver}(t) = \frac{\Delta m_i(t) + \Delta m_s(t)}{2} \tag{5.20}$$

After a subtraction of (5.17) and (5.18), the magnetization gradient can be derived:

$$\Delta m_i(t) - \Delta m_s(t) \approx \frac{\Delta_{odd}(d) - \Delta m_{aver}(t)}{int(d) - \frac{1}{2}} \tag{5.21}$$

With the T-MOKE data, the transient magnetization gradient for 2 nm and 4 nm is shown in Figure 5.10. We obtain a positive transient profile $\Delta m_i - \Delta m_s > 0$ for 2 nm and negative $\Delta m_i - \Delta m_s < 0$ for 4 nm. As defined in (5.15) and (5.16), $\Delta m_i(t)$ and $\Delta m_s(t)$ are negative value to represent the laser induced changes. The results obtained by (5.21) are equal as $|\Delta m_s| > |\Delta m_i|$ for d $\leq$ 3 nm, and $|\Delta m_s| < |\Delta m_i|$ for d $\geq$ 4 nm.

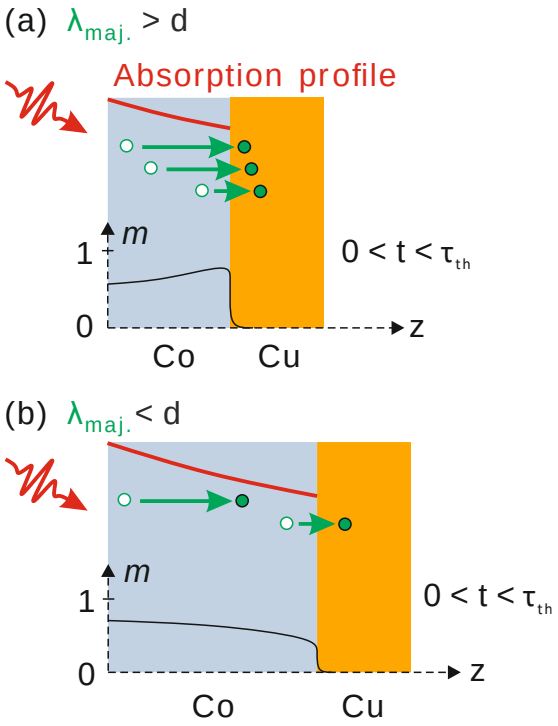

Figure 5.11: Schematic illustration of inhomogeneous magnetization profile for (a) $\lambda_{maj.} > d$, inelastic MFP of majority electrons larger than Co film thickness, and (b) $\lambda_{maj.} < d$. Sign of the magnetization gradient is influenced by laser induced spin current, indicated by green arrows.

Here, the spatial gradient of magnetization shows a sign flip at $d \approx 3$ nm. Intuitively, one expects the surface to lose more spin polarization due to inhomogeneous laser absorption profile. Such as illustrated in Figure 5.11, since the surface absorbs more laser fluence than the interface, effect of laser induced demagnetization should be stronger at the surface. But this picture is too simple for the whole story, and it only holds when we consider local spin current i.e. spin-flip scatterings as the main mechanism of laser induced demagnetization. According to the sign change in Figure 5.10, something that is nonlocal, proceeds at a timescale of 100 femtoseconds, must play a role and influences the magnetization profile. Since ultrafast laser excitation can generate fs spin current cross ferromagnetic films with a conducting substrate, which primarily drives the ultrafast demagnetization before the electron system is thermalized [17, 82, 84, 89], we conclude that the sign change of magnetization gradient $\Delta m_i - \Delta m_s$ for 3 nm $\leq d \leq$ 4 nm must be connected to inelastic spin dependent MFPs, which is typically a few nanometers for 3*d* transition metal ferromagnets [91, 152, 153].

This scenario of inhomogeneous absorption profile is indeed the case that we observed a magnetization gradient $|\Delta m_s| > |\Delta m_i|$ for for $d \leq 3$ nm, as can be seen in Figure 5.11. Spin majority at the surface can travel through the Co film without changing the spin states, then escapes into Cu substrate with high transmission probabilities [91, 92]. Because of excitation profile, more majority electrons are excited at the surface and form a spin current through the films. The surface is stronger demagnetized than the interface at a timescale before electron thermalization. Although the minority electrons can also propagate in the ferromagnetic, the minorities have shorter lifetimes [152, 153] and low

transmission probabilities [91, 92] due to large phase space for scattering. Flow of minorities does not have significant impact to the result for $d \leq 3$ nm.

For Co film thickness exceeds 3 nm, at which a sign flip of magnetization gradient occurs, this effect is related to spin current generation and inelastic spin-dependent electron MFP. The spin current formed by majority electrons begins at the surface cannot flow into the substrate before any inelastic scattering, whilst majority electrons near the interface still have high probabilities to cross the Co/Cu interface, which then becomes stronger demagnetized than the surface region, as illustrated in Figure 5.11 (b). The effect of magnetization gradient $|\Delta m_s| < |\Delta m_i|$ can be enhanced by the fact that minority spins with low inelastic MFPs and low transmission probabilities are trapped inside the Co films and accumulated at the interface. The transient magnetization gradient is thus strongly influenced by the thickness of the ferromagnetic films and the inelastic spin-dependent MFPs. Our results that magnetization gradient $\Delta m_i(t) - \Delta m_s(t)$ changes sign between d = 3 nm and d = 4 nm agrees with the fact that minority electron MFP is about 1 – 2 nm [91], while majority electron MFP within the energy window of 1.5 eV above the Fermi level can be 1.5 – 3 times larger [91, 152, 153]. Despite the approximation according to equation (5.20) is not well suitable for $d \geq 6$ nm because T-MOKE does not provide a homogeneous probe of the average magnetization Δm_{aver}, the effect of magnetization gradient is still present on the measured data. $\Delta_{odd}(d \geq 6\,nm)$ shows a sign change pump-induced change around 100 fs, which is caused by stronger demagnetization at the interface due to spin transport, as previous analyzed by bulk-sensitive time-resolved linear magneto-optical measurements [60].

Besides such a laser induced spin current, it is well known that ultrafast laser excitation is followed by generation of strain wave perpendicular to the metallic thin film [155] i.e. coherent longitudinal acoustic phonon, which is also an important dissipation channel for energy and momentum. Propagation of strain wave is well established and can be approximated in the continuum model based on sound velocity. For bulk cobalt, the sound velocity is around 4500 m/s (equals to 4.5 nm/ps), we consider a 4 nm Co film, so that the strain wave would have an impact on the dynamics of interface at a timescale of 900 fs. This timescale cannot explain the experimental data of $\Delta_{odd}(d)$ and the sign change of transient magnetization gradient that occurs at around 100 fs. Therefore, we conclude that the strain wave generation does not influence the magnetization dynamics of Co/Cu interface in the present work, which is mainly caused by flow of spin current across the interface before electron thermalization time.

In summary, these results indicate that MSHG is sensitive to spatially inhomogeneous spin dynamics on a few nanometers length scale, which is much shorter than the optical penetration depth of 3d transition metals (usually 10-20 nm e.g. 13 nm for an excitation wavelength of 800 nm in cobalt), such inhomogeneous excitation profile could lead to superdiffusive transfer of hot electrons. Our thickness dependent studies provide an experimental analysis of elastic spin dependent MFPs. At 3 nm $\leq d \leq$ 4 nm, the sign change of transient magnetization gradient reveals the effective MFP of majority electrons of about 3 nm.

5.1.5 Conclusions

We have employed thickness dependent time-resolved MSHG measurements on epitaxial Co/Cu(001) films to investigate the laser induced magnetization dynamics. Through polarization dependent SHG measurements, p-P polarization geometry is revealed to be optimal for pump-probe scheme with reasonable magnetic contrast and high SHG yield. The thickness dependent SHG yield is found to be made up by the interference between vacuum/Co and Co/Cu interfaces, where the interface generates magnetization-induced contribution with a phase shift around 180 °.

The main observations are that laser induced change in magnetization-induced SH field Δ_{odd} shows a complex thickness dependent behavior, which is explained by a simple model of linear combination. Based on these observation, we identify transient spatial magnetization gradient in the direction normal to the surface during the ultrafast demagnetization. A sign change of magnetization gradient is linked to spin current propagation from ferromagnetic Co to Cu substrate at a timescale before thermalization of the electron system. We find that the thickness dependent evolution of magnetization profile reflects the effective escape depth of fs spin current from Co to Cu. As can be concluded, the spin-dependent inelastic mean free path of majority electrons in Co films is around 3 nm.

5.2 Ultrathin Co/Cu(001) films: elementary processes at interfaces

In the previous part, we have analyzed the spin current generation in Co/Cu(001) films where the film thickness is comparable with the majority electron MFP. The spin current is shown to play an important role in metallic heterostructures. One issue need to be addressed further is microscopic processes at the interface directly.

At the interfaces of a metallic heterostructure, light-induced charge transfer [156, 157] is one of the basic processes and is highly dynamic. Charge carriers across the interface can also be spin polarized, which is known as spin injection [158, 159]. In particular, the symmetry breaking at FM-NM interface modifies the interfacial spin-orbit coupling, transfer processes could be strongly influenced. From the perspective of potential application, one would like to have the spin polarized electrons being transferred without spin-flip scattering. Therefore, it is important to identify the relevant processes and their respective timescales and length scales.

In this section, we combine interface-sensitive time-resolved magnetization-induced second harmonic generation (MSHG) and *ab initio* time-dependent density functional theory (TDDFT) to investigate the elementary processes at a model system of Co/Cu(001) interfaces [19]. Here, it should be acknowledged that the TDDFT results discussed in this section were carried by the group of Dr. S. Sharma.

We aim to provide a microscopic picture that goes beyond classical or semi classical treatment of laser induced dynamics through the combined effort of experiment and theory. We show that laser induced spin dynamics at Co/Cu(001) interface is governed by spin dependent charge transfer between Co and Cu before 35 fs. The spin transfer is in competition with local dissipation of spin angular momentum, which is mediated by spin-orbit coupling on 100 fs timescales.

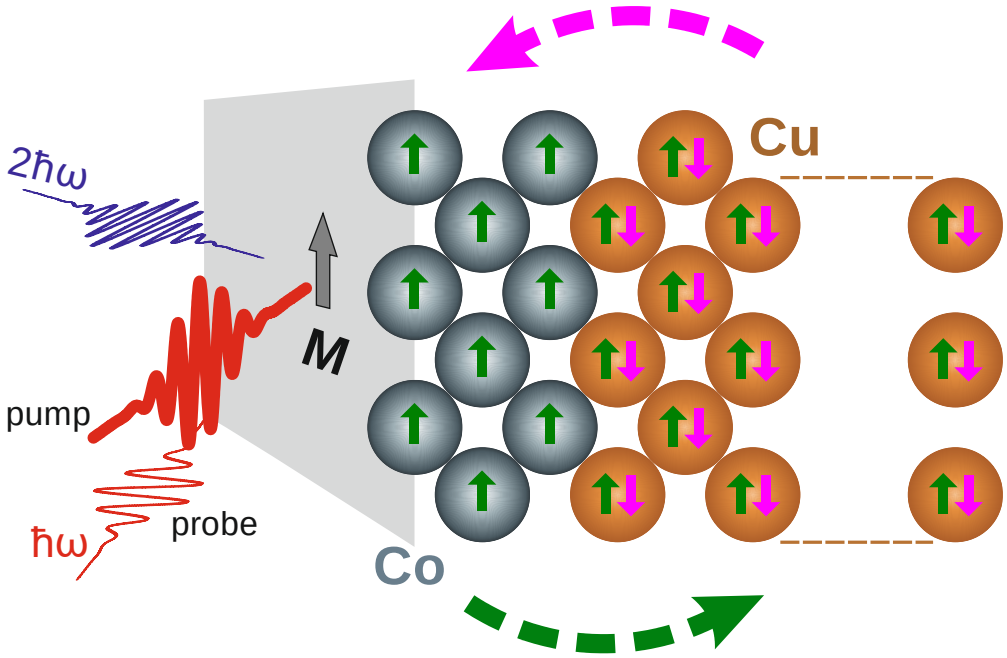

Figure 5.12: Schematic of pump-probe MSHG experiments on epitaxial model interface of Co/Cu(001). Pump and probe pulse are s- and p-polarized, respectively. Dash arrows indicate majority (green) and minority (pink) spin transfer. [19]

5.2.1 MSHG experiment vs TDDFT

In order to identify and quantify the microscopic processes, the experiment and the theory should be performed on the identical sample system and identical laser pulse parameters.

As illustrated in Figure 5.12, the MSHG experiment is performed in transversal geometry. The sample is pumped by a s-polarized 800 nm pulse with 35 fs pulse duration and 4 mJ/cm^2 laser fluence at 40 ° incident angle, followed by a probe pulse, the p-P polarized SHG is measured by various pump-probe delay for opposite magnetization direction of the sample.

We perform pump-probe MSHG experiments on epitaxial 3 ML and 5 ML Co/Cu(001) mainly due to three reasons. (i) At these thickness, the Co film has a Curie temperature well above room temperature and are stable [147]. (ii) Such thickness of 3 ML (0.53 nm) and 5 ML (0.88 nm) is close to the probing depth of SHG, which is in the order of 0.5 nm for metallic interface defined by electron density. As previous discussed in Section 5.1.1 and 5.1.3, interference between interfaces can play a role for thicker film, while for low coverage film thickness, the boundary between surface and interface becomes blurred. Based on the fact that the Co/Cu(001) interface contribution dominants the SHG and the film thickness is comparable with the probing depth, we conclude that MSHG probes the magnetism of the whole thin Co films. (iii) Although TDDFT is an exact theory to handle systems in non-equilibrium states, the method is limited by the computing power of current status, it will be very time-consuming to perform calculations on a fairly thick Co/Cu (001) film. Here, 3 ML and 5 ML Co/Cu(001) both can be exact approached by MSHG and TDDFT. Difference in the layer coverage, as a fine tweak of the interface properties, can influence the charge and spin dynamics after laser excitation, which may allow us to justify the strength of TDDFT.

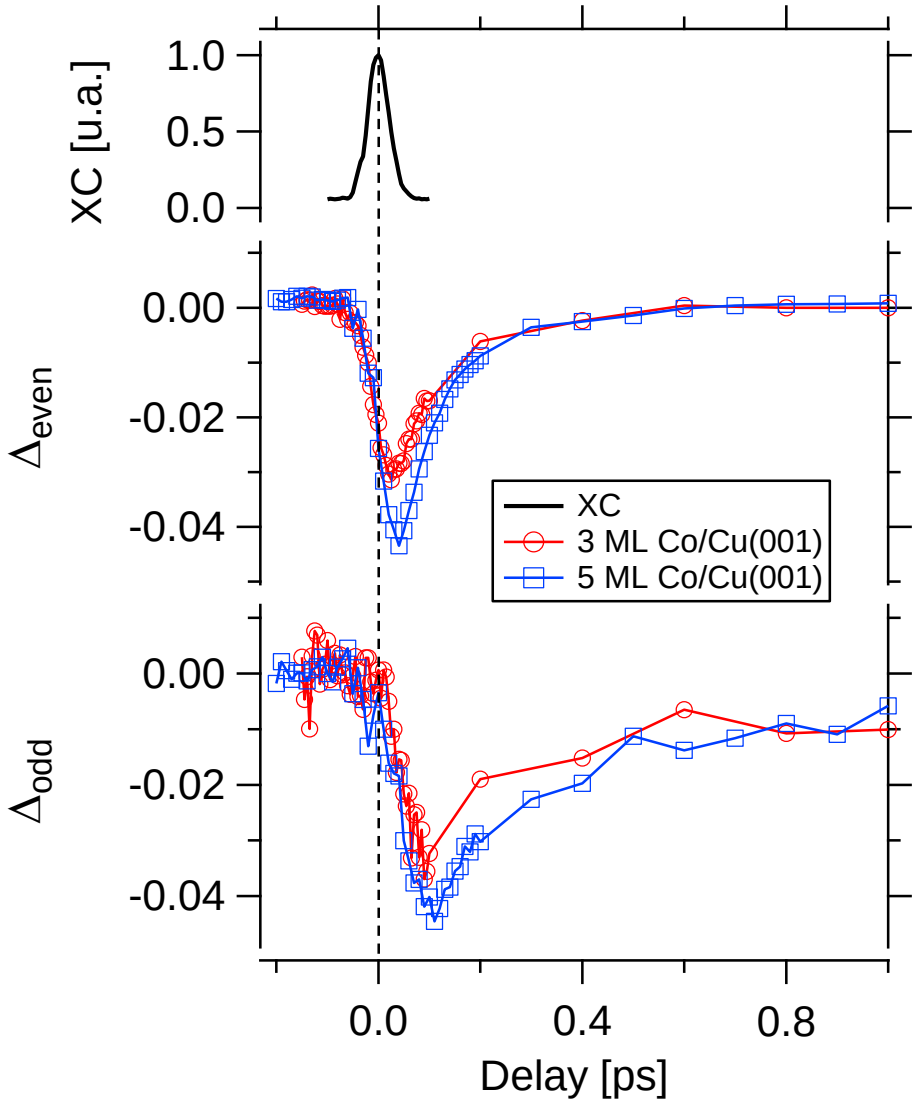

Figure 5.13: Pump induced variation in even and odd SH field for epitaxial 3 ML and 5 ML Co/Cu(001) films. The zero delay t = 0 fs is defined by when the maximal pump-probe cross correlation (XC) occurs. XC is plotted on top panel with a FWHM of 49 fs.

In Figure 5.13 the experimental results of 3 ML and 5 ML Co/Cu(001) films are shown. As being discussed, the interference effect between the surface and the interface can be neglected. The pump induced change Δ_{even} reflects the charge dynamics, while Δ_{odd} represents the laser-induced magnetization dynamics of the Co films. Here we see that Δ_{even} reaches the maximum change at a timescale < 50 fs faster than Δ_{odd}, where the maximum change occurs at around 100 fs. This clear difference of timescale implies that the charge system responses faster than the spin system after laser excitation. Both signals recover back to the value before pump excitation at a timescale in the order of few picoseconds. We note that the repetition rate of the laser pulse is 2.53 MHz, which corresponds to around 400 ns, so that accumulation of pump effect is excluded. Here we remind that the results of time-resolved data are not altered by the pump-probe cross correlation (XC), which is excluded by experimental geometry, see Section 4.4. For instance, any reminiscent XC signal would dominate the trace in Δ_{even} and Δ_{odd} within the pump-probe overlap, which appears as a positive delta-function like signal.

Based on the experimental results, we are mainly interested in the processes within timescale t < 100 fs, by when different timescales between Δ_{even} and Δ_{odd} occur, which should be governed by different microscopic processes i.e. spin transfer and SOC mediated spin flips. At longer delay time, coherent [155] and incoherent [52] lattice excitation plays an important role, which are not included in our theoretical analysis. Data in 0 – 200 fs can be found in Figure 5.14 and 5.15, detailed discussion will be given later together with the theoretical calculation.

The spin-dependent microscopic processes in respect to laser induced dynamics on Co/Cu(001) are theoretically analyzed by parameter free, fully ab initio TDDFT. In the previous section 2.2.2, a brief introduction has been given. Some additional technical details of TDDFT applied in this project are given below.

To be consistent with experiment, the TDDFT calculations are performed on 3 and 5 ML Co on top of 7 ML Cu(001) slabs. The pump pulse in TDDFT incidents normal to the surface, the parameters are FWHM 35 fs pulse duration, 800 nm wavelength and a laser fluence of 0.25 mJ/cm^2. The applied pump fluence TDDFT is equal to absorbed laser fluence in the Co/Cu(001) film. This number is obtained through IMD calculation on thin Co/Cu(001) film [160, 154] that 94% of the incident pump fluence is reflected from the sample surface. In the theoretical calculation, the incident pump pulse is fully absorbed in the Co/Cu(001) slab and not reflected from the surface. This is due to the fact that it is too computationally demanding to calculate the coupled dynamics of the electronic system and Maxwell's equation. In order to overcome this technical limitation, the same absorbed laser fluence in the calculation is applied as in the experiment.

TDDFT is considered to be a powerful tool that can yield valuable information for systems in non-equilibrium. For strongly correlated systems e.g. Mott insulator, additional treatments in functional such as LDA+U would be required. Since in our case the metallic Co/Cu(001) interface does not feature strong electron correlation, no additional treatments are presented in this work. Earlier studies regarding TDDFT in bulk transition metal ferromagnets (Ni and Co) have been demonstrated [161].

Since lattice excitation can only affect the dynamics at a timescale later than 100 fs, phonon interactions are not included in the TDDFT calculations for the present work. Following this point, we have neglected the effect of longitudinal and transverse strain waves in the calculation. Given the sound velocity of 4500 m/s in Co, for 3 ML and 5 ML film, the corresponding time scale for a longitudinal strain wave to propagate would be around 120 fs and 200 fs, respectively. These timescales occur later than the electronic excitation Δ_{even}, which reaches a maximum change at 35 fs. At this delay time already half of the magnetization have been evaluated. With that being said, longitudinal strain wave can only affect the dynamics on a longer time scale of 100 fs, where the pump-induced change recovers back to the initial state. In addition, we do not observe any periodic effect such as oscillating and echo behavior [155] in the experiment, which was considered to be induced by the strain wave. On the other side, the transverse strain wave is more relevant as it can be the ultimate slink for spin and orbital angular momentum [87], these coherent lattice dynamics of transverse acoustic strain occur on a much longer timescale in comparison to our experimental data. Therefore, we conclude that longitudinal and transverse strain waves cannot be responsible for the observed Δ_{even} and Δ_{odd} dynamics. Base on above points of view, excitations of strain wave are not considered in the theoretical calculation.

5.2.2 Spin transfer

In order to justify the charge transfer with TDDFT, the number of spin-integrated charge carriers in Co film n_{Co} is being calculated, with the definition:

$$n_{Co} = n_{Co}^{\uparrow} + n_{Co}^{\downarrow} \tag{5.22}$$

Here, n_{Co} represents the sum of majority and minority electrons. Then we define the relative change of charge carrier as:

$$\Delta n_{Co}(t) = \frac{n_{Co}(t) - n_{Co}(t<0)}{n_{Co}(t<0)} \tag{5.23}$$

The TDDFT calculation is shown in Figure 5.14. We observe a pump-induced decrease of n_{Co}. Since the total count of charge carrier in the Co/Cu(001) system is conserved, a decrease of the quantity $n_{Co}(t)$ in time domain can be interpreted as optically excited spin-integrated charge transfer from Co film to the Cu substrate.

Comparison between Δ_{even} and Δn_{Co} is illustrated in Figure 5.14, it appears that these two quantities exhibit different transient evolution (slope) in the initial drop. The experimental data changes already before zero delay, while the theoretical calculation of $n_{Co}(t)$ only starts to evaluate at positive delay time. The difference between pump-induced even SH field Δ_{even} and relative change of charge carriers Δn_{Co} is mainly caused by two points. First of all, we need to clarify the fact that a probe pulse of finite duration is applied to monitor the dynamics in pump-probe experiment, where the time-resolution is determined by the width of pump-probe cross correlation, while in real time calculation of TDDFT, no correlation probe is required to extract the information of physical quantities. Secondly, during the pump-probe overlap, the leading edge of pump pulse induces a collective motion of electrons, which precedes a coherent charge response or polarization, this coherent polarization is being probed in the experiment and reflected in Δ_{even}, in particular during pump-probe overlap and at negative delay times. In contrast, TDDFT does not treat the coherent polarization (diagonal elements in density matrix) due to limitations in computer power. TDDFT calculates exclusively the pump-induced incoherent spin-dependent dynamics. In another words, TDDFT extracts the pump-induced population dynamics (diagonal elements in density matrix). Collective excitation or coherent polarization is followed by phase breaking events, which eventually leads to photon absorption, hence, so the population is changed. We note that the experimental observed Δ_{even} is not only sensitive to coherent polarization, but also probes the population, as can be seen from the relaxation of Δ_{even} on several hundred femtosecond, where the pump pulse is already absent.

With above arguments, we can compare the experimental and the theoretical charge response. Given the required dephasing time ≈ 10 fs for charge population to build up in metal, the maximum population change extracted by TDDFT at 25 fs agrees well with estimated value of 35 fs /2 + 10 fs = 27 fs. As being compared, Δ_{even} and Δn_{Co} reach their maximal changes at the same timescales within uncertainties. Therefore, we conclude that the buildup of Δ_{even} is dominated spin-integrated charge transfer dynamics across the interface. In addition, the fine difference in the magnitude for 3 ML and 5 ML Δ_{even} is captured by TDDFT. The number of charge carrier $n_{Co}(t)$ drops to a minimum at about 25 fs then exhibits a recovery after 30 fs. This recovery of $n_{Co}(t)$ is in fact caused by spin back transfer from Cu to Co, which will be discussed later in detail.

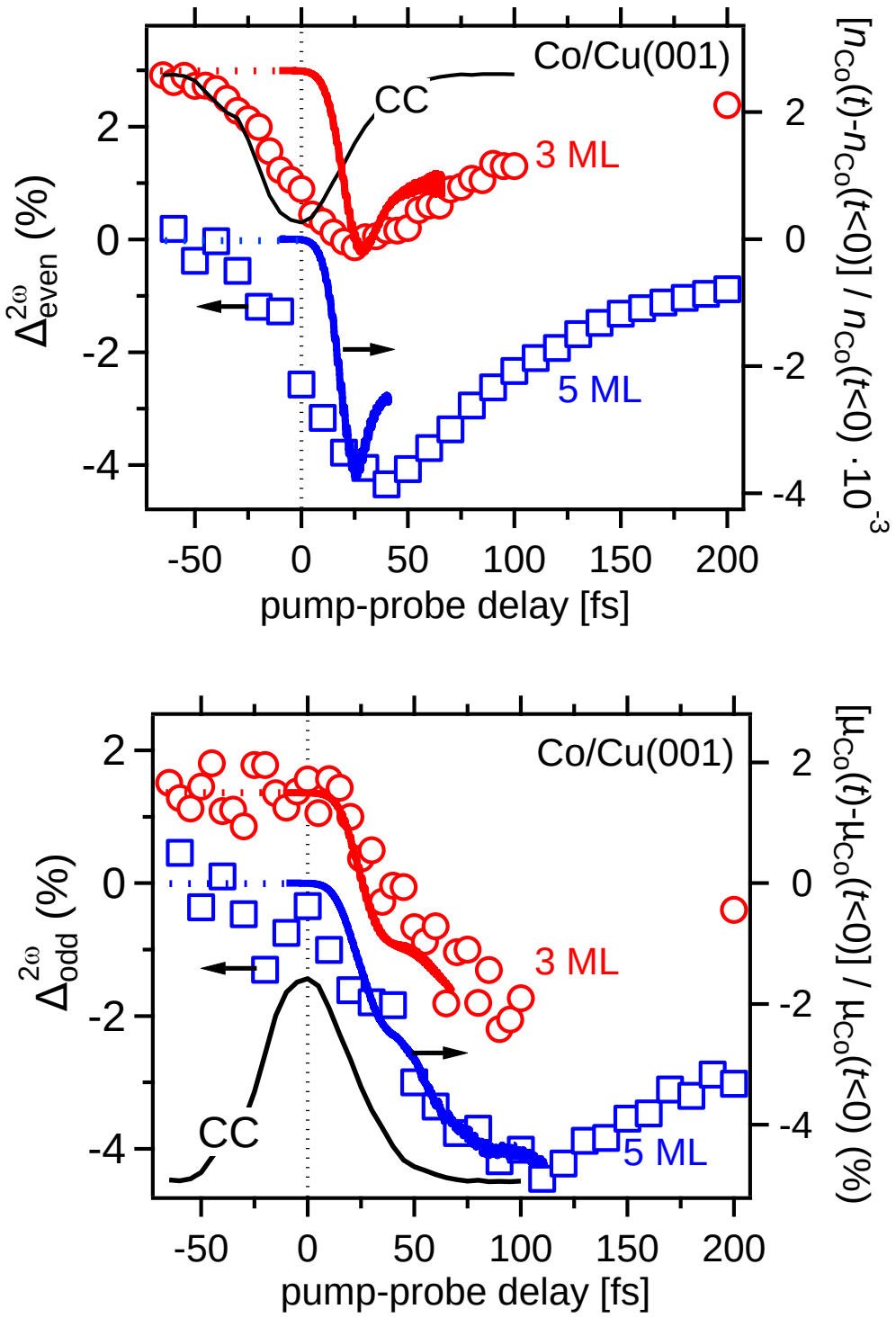

Figure 5.14: **Top**: pump-induced relative changes in even SH field Δ_{even} versus the relative change of spin-integrated charge carriers Δn_{Co}. **Bottom**: Comparison of relative changes in odd SH field Δ_{odd} with theoretically calculated spin magnetic moment $\Delta\mu_{Co}$. Experimental data of 3 ML and 5 ML Co/Cu(001) films are represented by red circles and blue squares, while solid line indicate the TDDFT calculations. 3 ML data set are offset for data visibility. The black solid line indicates the pump-probe XC, which serves as a reference for delay time. [19]

As a last point concerning Δ_{even}, magnetization induced quadratic effect in Δ_{even} is discussed below. The expression of Δ_{even} includes quadratic term of even and odd SH field:

$$\Delta_{even} = \sqrt{\frac{I_{\uparrow}^{2\omega}(t) + I_{\downarrow}^{2\omega}(t)}{I_{\uparrow}^{2\omega}(t<0) + I_{\downarrow}^{2\omega}(t<0)}} - 1 = \sqrt{\frac{|E_{even}^{2\omega}(t)|^2 + |E_{odd}^{2\omega}(t)|^2}{|E_{even}^{2\omega}(t<0)|^2 + |E_{odd}^{2\omega}(t<0)|^2}} - 1 \tag{5.24}$$

For the case of thin Co/Cu(001) films, the even SH field $|E_{even}^{2\omega}|$ is much larger than the odd field $|E_{odd}^{2\omega}|$, in thickness ranges of few monolayers in this present work, the ratio of $|E_{even}^{2\omega}|/|E_{odd}^{2\omega}|$ is approximately 10 [123]. Therefore the quadratic term of odd field can be neglected in the expression of Δ_{even}. We observed non-zero signal Δ_{even} before time zero, where Δ_{odd} is still zero, which implies an exclusion of magnetic response in Δ_{even}. We note that quadratic effect of $\boldsymbol{M}$ is more pronounced in Dielectric materials, which yields weaker charge response due to lack of free carriers. In principle, the separation of linear and quadratic effect of M allows one to disentangle the changes in the absolute value of M or just a projection on a preferential quantization axis [184].

On the other side, Δ_{odd} in Figure 5.14 exhibits a different behavior. Δ_{odd} only starts to build up the change on positive delay time. The magnetization dynamics of 3 ML and 5 ML Co film reaches a minimum delay time of 100 fs with about 4% and 5% demagnetization, respectively. Since Δ_{odd} probes the magnetization dynamics of the whole ultrathin Co film, the corresponding physical quantity to be calculated by TDDFT should be the Co spin magnetic moment μ_{Co}:

$$\mu_{Co} \propto n_{Co}^{\uparrow} - n_{Co}^{\downarrow} \tag{5.25}$$

which is proportional to the number difference of majority and minority carriers. We then define the relative change of spin magnetic moment $\Delta\mu_{Co}$ as:

$$\Delta\mu_{Co}(t) = \frac{\mu_{Co}(t) - \mu_{Co}(t<0)}{\mu_{Co}(t<0)} \tag{5.26}$$

The theoretical calculations of $\Delta\mu_{Co}(t)$ for 3 ML and 5 ML Co are depicted in Figure 5.14. The simulation quantitatively reproduces the dynamics of 3 ML and 5 ML Co in the timescale and the amount of absolute pump induced change. Here, the experimental result of Δ_{odd} does not broaden due to pump-probe correlation, which is because that the observation of spin-dependent dynamics requires a population change of charge carrier. In other words, magnetization dependent polarization can be detected at negative delay, while Δ_{odd} shows no signal at such time delays. Based on the agreement between the experiment and theory, we can derive further information from the theory, such as timescales of microscopic processes that is crucial for charge and spin dynamics. We note that theoretical results shown in Figure 5.14 are calculated only up to 100 fs after laser excitation. Since lattice interaction is not considered, the time-dependent evolution of $\Delta n_{Co}(t)$ and $\Delta\mu_{Co}(t)$ would stay constant if the calculations proceed further.

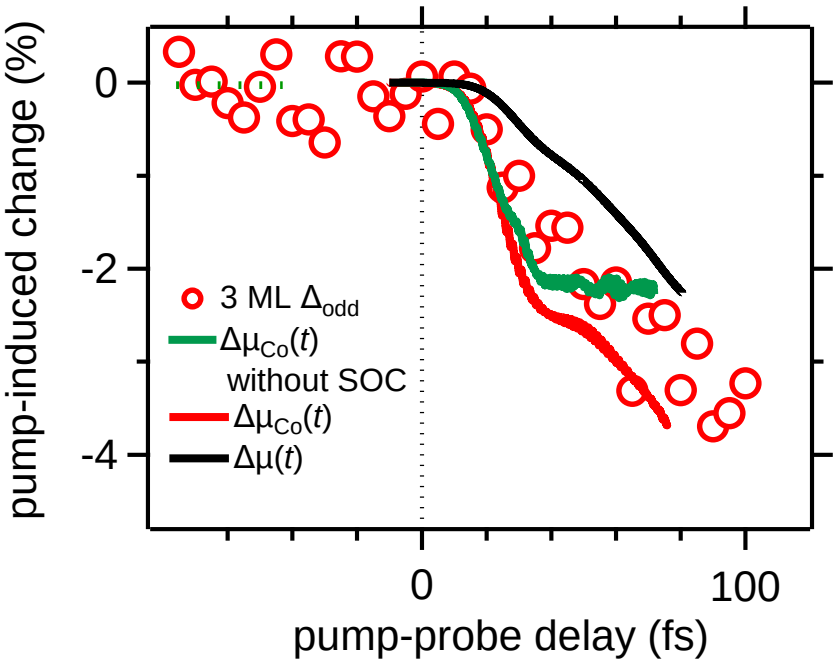

Figure 5.15: Comparison of measured pump-induced change of magnetization for 3 ML Co/Cu(001) (circles) with theoretically calculated relative changes of total spin moment in Co/Cu(001) $\Delta\mu$ (black solid line), spin moment in Co layers $\Delta\mu_{Co}$ with and without SOC (red and greed solid lines, respectively). [19]

5.2.3 Role of Spin-orbit coupling - spin flip

So far we have identified the spin transfer across the interface, which occurs at a timescale of 30 fs. Meanwhile, the magnetization dynamics of the film already drops to half of the maximal change. Considering that (i) local spin current i.e. spin-flip scattering drives the further demagnetization processes and (ii) lattice as a sink for angular momentum but the relevant timescale lies > 100 fs, the missing part should be spin-orbit coupling (SOC) that couples the magnetic moment with the lattice.

In order to reveal the microscopic processes that proceed the magnetization dynamics at timescales later than spin transfer, three theoretically calculated quantities are taken into account in comparison with experimental data. As depicted in Figure 5.15, these quantities are the Co contribution $\Delta\mu_{Co}$ with and without SOC, and the relative change of spin moment in the full heterostructure $\Delta\mu$, where $\mu = \mu_{Co} + \mu_{Cu}$. Due to spin-dependent transfer, local moments are redistributed between the Co layers and the Cu substrate. Without SOC, the magnetic moment in Co layers drops to half of the maximal change and stops after 35 fs, which occurs on the same timescale as spin transfer. For the calculation that the SOC is included, the loss of magnetic moment continues up to 100 fs. These results indicate that spin transfer and SOC contribute to laser induced demagnetization in a similar weight, but dominate on separate timescales for the Co/Cu(001) interface. Base on the quantitative agreement between theory and experiment, we identify a SOC-mediated contribution to ultrafast demagnetization, which was proposed earlier [85, 86, 161].

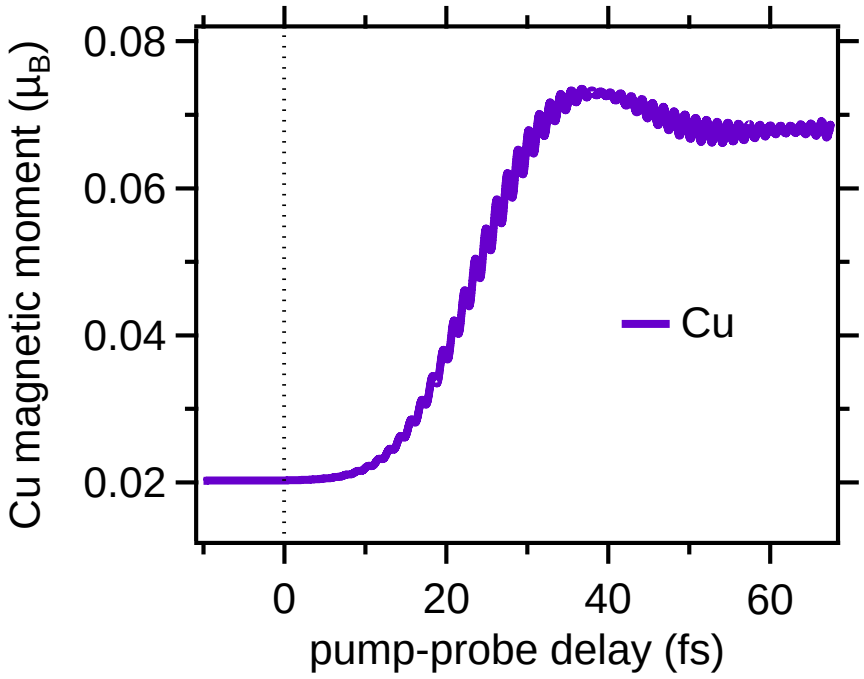

Figure 5.16: Calculated magnetic moment in Cu substrate due to spin transfer across the interface. [19]

Additionally, $\mu_{Co}(t)$ shows a larger pump-induced change than $\mu(t)$ within the calculated time interval. The difference between the total magnetic moment and Co magnetic moment results in dynamics of injected spin moment in Cu substrate, shown in Figure 5.16. The transient enhancement of magnetic moment $\mu_{Cu}(t)$ reaches the maximum at t = 35 fs and features a decrease on longer delay time, this reduction is caused by SOC mediated spin-flip.

Spin-orbit interaction couples the magnetic moment with lattice. The lattice therefore serves as an ultimate sink for local magnetic moment change. In a naive picture, the spin angular momentum is transferred to the orbital angular momentum, and finally dumped in to lattice. From the perspective of TDDFT, the expectation value of spin angular momentum S can be calculated in the ground state as well as in excited states i.e. as a function of time, while calculation of expectation value of orbital angular momentum is still a challenge in numerical manner. This issue is associated with the classical angular momentum of the crystal that the crystal would rotate in free space with certain rate. At what timescales the momentum is transferred to lattice remains as a question to be clarify. [86] suggested that the orbital angular momentum is quenched in crystal field at the timescale of 1 fs, but no clear physical picture is proposed.

Quenching of orbital angular momentum is refer to the fact the ground state orbital angular momentum of electrons in a cubic crystal lattice is strongly reduced compared to atomic value [185]. Orbital angular momentum is a good quantum number for the atomic problem because the Coulomb potential between the electron and nucleus is rotationally invariant, but the potential an electron feels in a crystal is not. Now the orbiting electron will experience a Coulomb repulsion near the corners of the bonding square where the negative neighbor ions are located and the orbiting electron will form a standing wave by superposition of two oppositely waves with ±Lz, with charge maxima away from the neighbor corners. One may say the in-plane orbit of the electron is broken up through the formation of molecular orbitals. Therefore, the corresponding orbital momentum along

the normal of the bonding plane, will be quenched. In transition metal ferromagnetic like Fe, Co and Ni, the orbital angular moment is close to zero and smaller than expected from Hund's rules [185].

Based on the TDDFT calculations we define the spin injection efficiency from Co to Cu at the interface with the expression:

$$\eta(t) = \frac{|\mu_{Cu}(t) - \mu_{Cu}(t<0)|}{|\mu_{Co}(t) - \mu_{Co}(t<0)|} \tag{5.27}$$

Before the SOC-mediated spin flip scatterings dominate the spin dynamics, we obtain a spin injection efficiency at t = 35 fs of $\eta = 40\%$ and $\eta = 25\%$ for 3 ML and 5 ML Co/Cu(001), respectively.

5.2.4 Spin back transfer

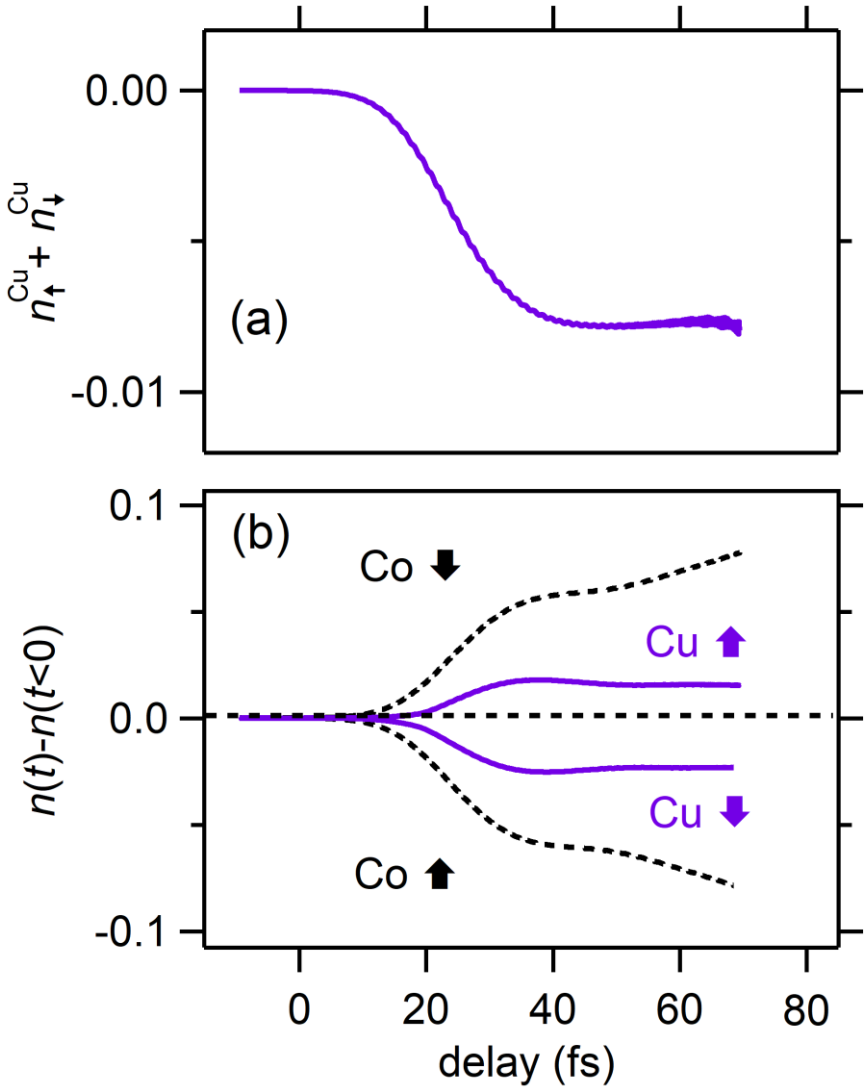

Figure 5.17: (a) Time-dependent evolution of spin-integrated charge carriers in Cu. (b) Count of excited majority and minority carriers that localized at Co and Cu for 3 ML Co/Cu(001). [19]

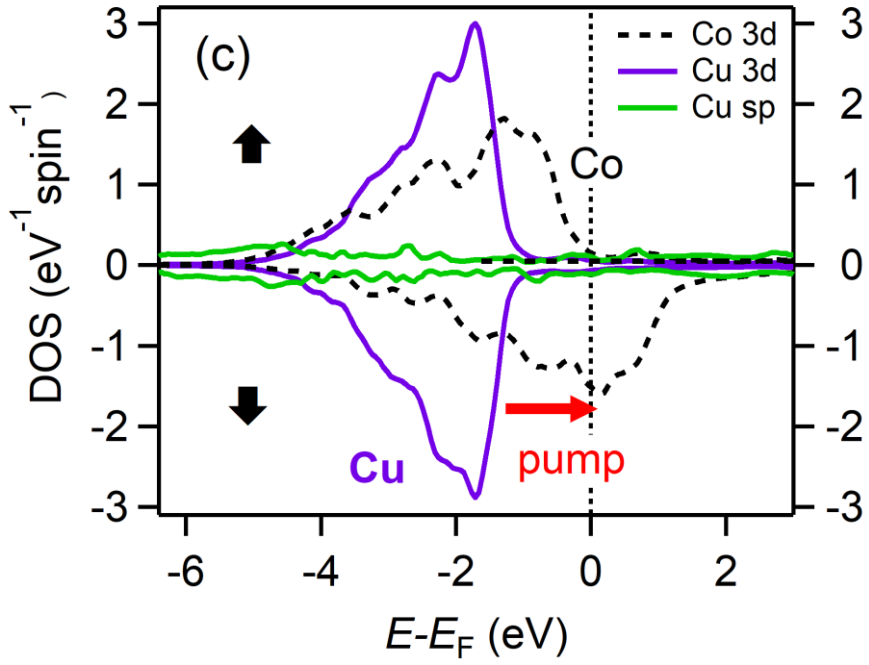

Figure 5.18: Calculated density of states (DOS) of the interfacial Co and Cu layers. Solid purple and green line represent Cu *3d* and *sp* states, respectively. Dashed line denotes Co *3d* states. Red arrow indicates optical transition from Cu *3d* to Co *3d* states. [19]

Spins injected in to the Cu substrate can cause a transient magnetization enhancement in Cu. However, when we extract the spin-integrated charge carriers in Cu, as shown in Figure 5.17, a decrease of the charge carriers count is observed in the Cu substrate. The pump induced change saturates after 35 fs. The result hints at a spin back transfer from Cu to Co.

We then theoretically monitor the time evolution of majority and minority electrons in both Co and Cu. In Figure 5.17, the calculated time-dependent change of the number of majority and minority electrons in Co and Cu layers are displayed. The increase of majority in Cu and decrease of majority in Co is the consequence of spin transfer from Co layers to Cu substrate. However, the amount of increase in Cu is much less than the decrease in Co, this difference is due to SOC mediated spin-flips, which suppresses the majority spin injection efficiency from Co to Cu. One notices that the different changing rate of majority and minority electron in Co evolves over delay time, which reflects the competition between spin transfer across interface and local spin flip due to SOC. The turning point in times located at around 35 fs, which corresponds to the pump pulse duration applied in TDDFT. The result then suggests that spin transfer occurs as long as the pump pulse is present at the interface.

In addition, we find that the carrier flow of majority and minority in Cu is unequal. As shown in Figure 5.17, more minority electrons escape Cu than majority electrons flow in. This leads to a minority spin back transfer from the Cu substrate to Co layers, which eventually enhance the ultrafast demagnetization in the Co film. The spin back transfer is explained by a resonant optical excitation from occupied Cu 3d states to unoccupied Co 3d minority states. In Figure 5.18, the calculated electronic density of states is depicted, which supports this scenario that the employed 1.55 eV pump photon energy matches the energy difference between the states. We note that the spin back transfer is

an interface induced effect, this is caused by the hybrid state between Cu and Co interfacial layers, which generates new Cu 3d states differ from its bulk value and appear closer to Fermi energy [162].

We note that the spin back transfer with the actual interface electronic DOS derived from TDDFT goes beyond models such as superdiffusive spin transport in bulk materials [17, 81], which mainly caused by spatial transport gradients in films based on spin-dependent lifetimes and velocities in ferromagnet. Spin back transfer can in fact contribute to the demagnetization dynamics.

5.2.5 Conclusions

The laser induced ultrafast charge and spin dynamics have been investigated based on Co/Cu(001) interfaces, which is considered to be a model system. Interface sensitive time-resolved MSHG and *ab initio* TDDFT have been performed on 3 ML and 5 ML coverages of Co films on Cu(001) substrate. The main experimental observation is that the charge and spin dynamics are governed at two different timescales, as well as subtle differences appear for 3 ML and 5 ML data. Theoretical calculations quantitatively reproduce the magnetization dynamics observed in experiment.

Through the combined effort between experiment and theory, the present work reveals three different microscopic processes that contribute optically induced ultrafast demagnetization at Co/Cu(001) interfaces. At first, the optical excitation triggers spin transfer and back transfer across the interface at $t < 35$ fs, here we conclude that the minority spin back transfer from Cu to Co is induced by resonant optical transition in the interface layers. At later delay time 35 fs $< t <$ 100 fs the spin dynamics is dominated by SOC-mediated spin-flip scatterings, which limit the spin injection efficiency in this time window. Phonon excitation can mediate further demagnetization, but also serve as a sink for angular momentum that we experimentally observe a relaxation for timescales latter than 100 fs. The energy is dissipated through heat transport from ferromagnet to the conducting substrate.

6 Ultrafast electron dynamics at molecule-metal interfaces

Photoinduced electron transfer across a molecule-metal interface has been an interesting topic in many disciplines: electron transport in nanoscales metal-molecule-metal junctions [163, 164], charge injection at molecule-metal interfaces in organic light light emitting diodes [165, 166], interfacial electron transfer mediated reactions in chemistry [167, 168], and electron injection in dye-sensitized solar cells [100, 169]. The recent interest in molecular-based electronics has surged in demand for quantitative answers to this topic.

Porphyrin molecules with a metallic center are of special interest in photochemistry [114] and molecular spintronics [22, 115]. They have the potential to be the future building block of molecule-based devices [22], since the spin state of porphyrin molecules can be quite easily modified with different ligands [170] as well as magnetic substrates [171]. The prospect of switching the spin in the metalloporphyrin ring is a particularly interesting one, as this could be used, for example, for spin-dependent electric transport through biomolecular devices. Photoinduced charge transfer is essentially an important process that can modify the exchange coupling, and thereby manipulate the magnetic properties of the system.

The first question on charge transfer at molecule-metal interface is where molecular orbitals are located energetically with respect to the metal Fermi level. Previously, the occupied molecular orbitals (MOs) are usually characterized by one-photon photoemission spectroscopy, while unoccupied MOs can be mapped by 2PPE [172]. In the present work, we have particularly addressed the issue of energy alignment of the molecular state on metallic substrate and photoinduced charge transfer across the interface with nonlinear optical spectroscopy. A model system of in-situ-prepared monolayer (ML) Fe(III) octaethylporphyrin (FeOEP) chloride molecule on Cu(001) substrate is investigated. We experimentally approach the FeOEP/Cu(001) with interface-sensitive time-resolved SHG spectroscopy. As illustrated in Figure 6.1, we employ a femtosecond light source with tunable photon energy generated from NOPA to perform static and time-resolved SHG experiments on FeOEP-/Cu(001) interfaces.

This chapter is structured as follows: We first characterize the static SHG properties with and without iron porphyrin molecules on a Cu(001) substrate. Through that, we identify an interface assisted resonant SHG enhancement. We then perform pump-probe measurements at resonant and off-resonant excitation photon energies.

6.1 Static properties of FeOEP/Cu(001) interfaces

As a pre-studies for pump-probe experiments, the static SHG properties of clean Cu(001) as well as FeOEP/Cu(001) need to be addressed. In the following, we first review the previous studies of FeOEP/Cu(001), then we present the results of polarization dependence and wavelength dependence of SHG measurements on the above-mentioned

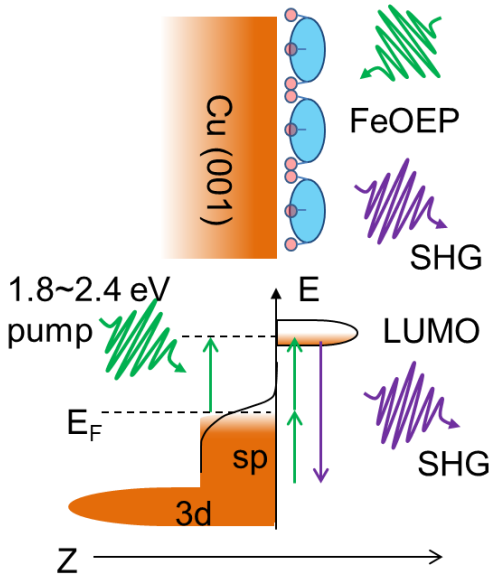

Figure 6.1: **Top**: Schematic of pump-probe SHG spectroscopy on 1 ML FeOEP/Cu(001). The sample is pumped with tunable photon energy in the visible wavelength range (1.8 – 2.4 eV), and probed with another delayed pulse, while the intensity of the reflected SHG is measured. **Bottom**: Excitation scheme of FeOEP/Cu(001) interface. By varying the pump photon energy, charge carriers can be excited to interfacial LUMO state. Here, the charge transfer dynamics is probed by another delayed laser pulse, by which the reflected SHG intensity is recorded.

two systems. Since SHG is an interface sensitive method to probe adsorbed molecules on surfaces [118, 173], we expect to find the spectroscopic signature of FeOEP molecule adsorbed on Cu(001). In order to obtain defined molecule coverages as in [22, 116], We used a molecular evaporator with the same design and the same recipe provided by AG Wende to prepare the samples.

6.1.1 Previous studies of iron porphyrin molecules on Cu(001)

The ongoing search for new materials which can be used in magnetic switching devices has brought phthalocyanine and porphyrin molecules with transition-metal centers into focus because they arrange themselves flat on surfaces and are relatively easy to handle experimentally under ultrahigh vacuum (UHV) conditions.

The chemical structure of iron (III) octaethylporphyrin (FeOEP) chloride molecule is depicted in Figure 6.2 (a). Porphyrins are a group of ring structured organic compounds. In the center, the Fe atom is connected to four N atoms, which are bound to the parent structure of porphyrin. Chlorine ligand is connected to the metallic center and normal to the plane of the molecule. At the edge of the porphyrin molecule, eight ethyl group CH_3 are attached. In Figure 6.2 (b), a measurement of scanning tunneling microscopy (STM) of 0.4 ML FeOEP/Cu(001) at room temperature is provided. As can be seen from the image, porphyrin molecules adsorb flat on the copper substrate, this implies an absence of chemical bounding between the molecule and the substrate. The STM picture shows that molecules with and without Cl ligands have a ratio of about 1:3, this indicates that Cl ligands are not completely removed at the surface, since the molecule can face up or down to the surface.

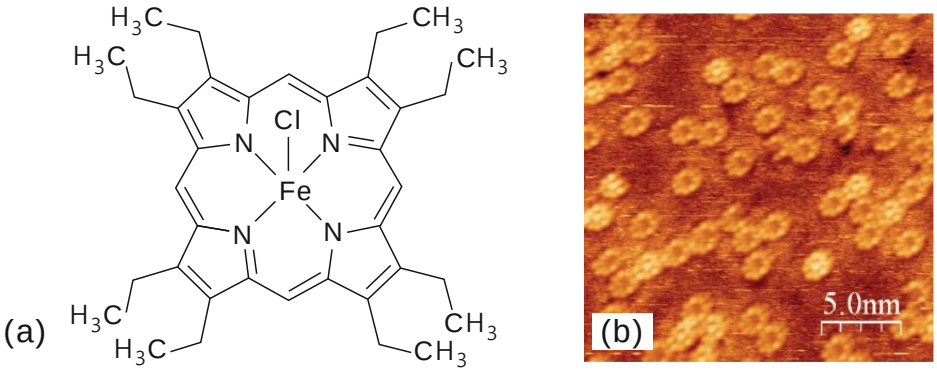

Figure 6.2: (a) Sketch of Fe octaethylporphyrin (OEP) chloride molecule. (b) STM images of 0.4 ML FeOEP(Cl) on Cu(001) at room temperature. [116]

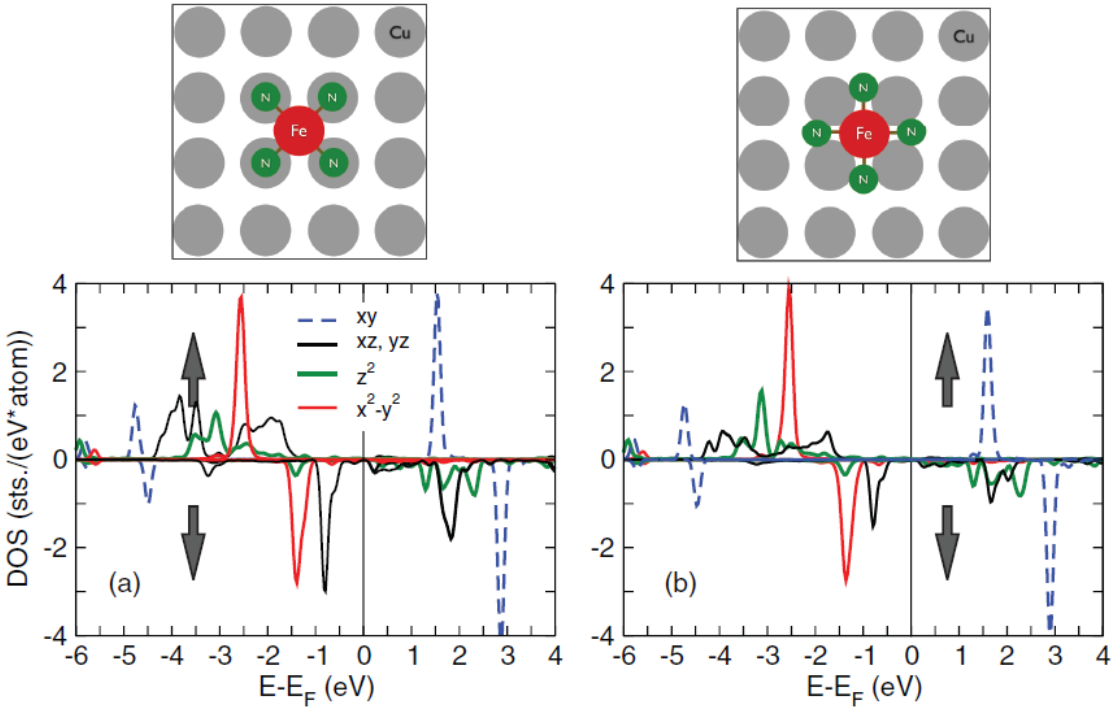

Figure 6.3: Calculated DOS of Fe d orbitals in FeOEP/Cu(001) with inclusion of van der Waals interaction for (a) hollow site configuration (b) molecule rotated by 45 °. [116]

The structural and magnetic properties of porphyrin molecules in bulk and on surfaces have been studied by density functional theory (DFT) methods and x-ray absorption spectroscopy [116]. In the case of a Cu(001) surface, the FeOEP molecule prefers to arrange itself in the hollow-site configuration, as illustrated in Figure 6.3, whereby the four N atoms are located on top of the under neighboring Cu atoms of the substrate. The calculated distance between the molecule and the substrate with and with van der Waals interaction amounts to 2.66 Å and 3.10 Å [116], respectively. A rotation of the porphyrin molecule by 45 ° will cause an increase of energy by 0.31 eV (or .0068 eV without van der Waals interaction).

The density of states of Fe d orbitals of FeOEP molecule by hollow-site and 45 °rotated absorption configuration on the Cu(001) substrate are depicted in Figure 6.3. For the ground state calculations, $d_{x^2-y^2}$ orbitals are mostly filled, while d_{xy} orbitals are mostly

empty. Other $d_{xz,yz}$ and d_{z^2} orbitals exhibit lowest unoccupied molecular orbital (LUMO) of about 2 eV above the metal Fermi level. In contrast to FeOEP molecules in the gas-phase, no clear gap between highest occupied molecular orbital (HOMO) and LUMO state can be observed due to broadening of the density of states [116]. Theoretical investigations have revealed that FeOEP molecules are chemisorbed at ferromagnetic surfaces whereby the magnetic coupling is mediated by the N atoms. [22, 174]. In the case of Cu(001), the hybridization effects and charge-transfer effects indicate that interaction between Fe atom and surface is indirect, mediated via the N atoms.

6.1.2 SHG spectroscopy

Static spectroscopic measurements of SHG in reflection from clean Cu(001) and FeOEP/Cu(001) sample aim to identify the spectral feature induced by molecules adsorbed on the surface. We first characterize the polarization dependent pattern on a clean Cu(001) surface. Details of the sample preparation of clean Cu(001) surfaces and the FeOEP adsorption on Cu(001) can be found in Chapter 4.1.

Polarization dependent SHG

Based on the macroscopic formalism of SHG introduced in Section 3.2.2, in principle, one can separate the individual non-zero tensor components through polarization dependent measurements. As mentioned in Chapter 4.4 that the setup based on NOPA light sources is used to carry out SHG experiments.

Depending on the polarization geometry described in equations (3.20) – (3.22), we can simplify the expression of generated SH field from a (001) surface in form of linear optical coefficients γ_{ijk} and nonlinear susceptibility tensor elements $\chi^{(2)}_{ijk}$ as:

$$E^{2\omega}_{p-P} = \left|\gamma_{zzz}\chi^{(2)}_{zzz} + \gamma_{zxx}\chi^{(2)}_{zxx} + \gamma_{xzx}\chi^{(2)}_{xzx}\right| \tag{6.1}$$

$$E^{2\omega}_{s-P} = \left|\gamma_{zxx}\chi^{(2)}_{zxx}\right| \tag{6.2}$$

$$E^{2\omega}_{45-S} = \left|\gamma_{xzx}\chi^{(2)}_{xzx}\right| \tag{6.3}$$

In Figure 6.4, the measured polarization dependent SHG patterns from Cu(001) are depicted as an example. For p-polarized configuration, the p-P SHG yield is almost a factor of 3 larger than s-P SHG, because (i) more non-zero susceptibility tensor elements are involved in the p-P geometry and (ii) the intrinsic absolute value of $|\chi^{(2)}_{zzz}|$ is much larger than the only relevant component $|\chi^{(2)}_{zxx}|$ in s-P polarization combination [16]. We notice here that the minimal SHG yield at the polarization angle between p- (0 °) and s-polarization (90 °) is offset around 300 counts per second, this implies that the phase between the SH field $E^{2\omega}_{p-P}$ and $E^{2\omega}_{s-P}$ is not close to zero [186].

The polarization dependent pattern for an output of S-polarized SHG, as depicted in Figure 6.4, shows a four-fold symmetry, since only one tensor element $\chi^{(2)}_{xzx}$ plays a role. Together with previous results on Co/Cu(001) and [16], it can be stated that S-polarized SHG pattern mainly reflects the surface symmetry and is less affected by the electronic state. We note that the detected S-polarized SHG intensity is one order of magnitude smaller than in the P-polarized case within our investigated fundamental wavelength range 500 – 700 nm (1.8 – 2.4 eV).

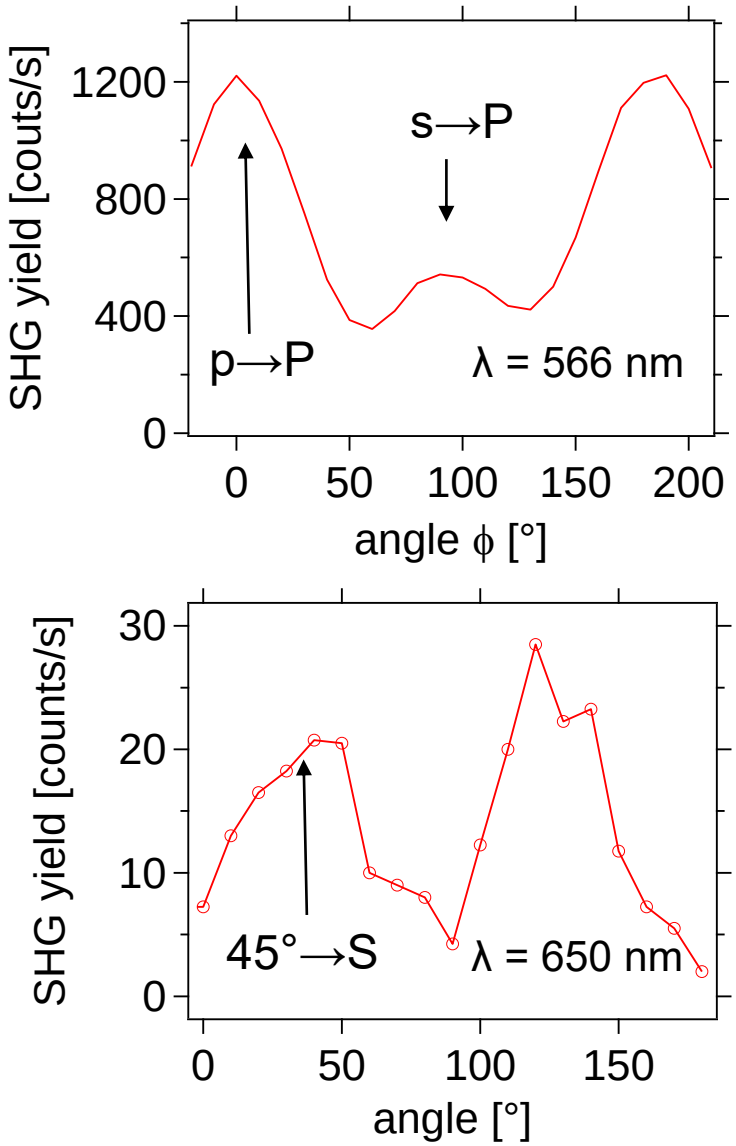

Figure 6.4: Polarization dependent SHG on clean Cu(001). **Top**: an output of P-polarized SHG with fundamental wavelength of 566 nm. **Bottom**: S-polarized SHG with 650 nm fundamental input. Both measurements are depicted as a function of incident polarization angle.

Wavelength dependence

In order to determine the energy level of LUMO state of FeOEP/Cu(001), we measure the spectral dependence of the SHG intensity reflected from the sample surface for both p-P and s-P polarization combinations. Since the measured SHG intensity is dependent on the intensity of the fundamental beam, we applied here a wedged quartz crystal as a SHG reference channel, which can be used to measure the intensity of the fundamental beam. The spectral p-P and s-P SHG data are normalized to the quartz SHG (see also Appendix A) by the following expression:

$$I_{p-P}^{2\omega} \cdot \frac{\left|R_{Quartz}\right|}{I_{Quartz}^{2\omega}} \propto \left|\gamma_{p-P}\chi_{p-P}^{(2)}\right|^2 \tag{6.4}$$

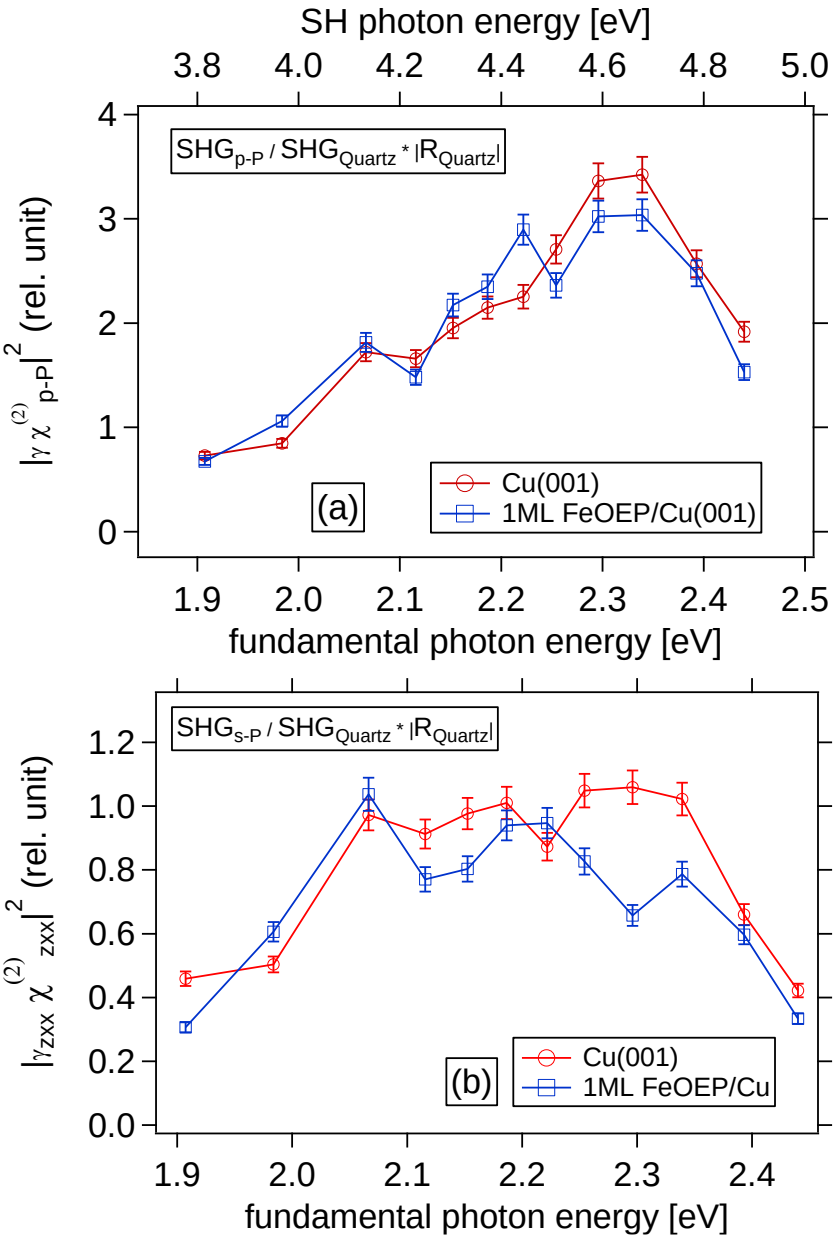

Figure 6.5: Normalized spectral dependence of SHG by (a) p-P and (b) s-P polarization combinations as a function of fundamental photon energy. The spectral data set of clean Cu(001) surface and 1 ML FeOEP/Cu(001) interface are represent by red circle and blue square, correspondingly.

$$I_{s-P}^{2\omega} \cdot \frac{|R_{Quartz}|}{I_{Quartz}^{2\omega}} \propto \left|\gamma_{zxx}\chi_{zxx}^{(2)}\right|^2 \tag{6.5}$$

As depicted in Figure 6.5 (a), the p-P polarized SHG spectrum of Cu(001) surface increases continuously and reaches a maximum value at fundamental photon energy 2.35 eV, and decreases for larger photon energy. The presence of 1 ML FeOEP molecule causes an enhancement of SHG for energy window 1.9 – 2.25 eV and suppression for 2.25 – 2.45 eV. In particular, 20% increase of SHG yield occurs at around 2.23 eV. For the case of s-P configuration, the SHG yield is generally smaller and approximately one third of the p-P polarized SHG for the investigated energy window. FeOEP molecules in

general suppress the SHG yield, but a small amount of enhancement in s-P SHG is found at around 1.95 – 2.06 eV. Regarding the absolute scale of the SHG spectral data, only 2.5% of the fundamental power is applied for the quartz reference channel, so the quartz SHG efficiency is 10^4 times higher than Cu(001) surface. With the calculated values of quartz reference factor $R_{Quartz} = I^{2\omega}_{Quartz}/(I^{\omega}_{Laser})^2$ in the order of 10^{-22}, then the surface spectral SHG lies in the order of 10^{-26}. For the sake of simplicity, we display the relative units in the Figure 6.5.

The normalized value of s-P polarized SHG is proportional to $|\gamma_{zxx}\chi^{(2)}_{zxx}|^2$, while p-P is determined by three tensor components $\chi^{(2)}_{zzz}$, $\chi^{(2)}_{zxx}$, and $\chi^{(2)}_{xzx}$. Based on the fact that the observed 45 °-S polarized SHG yield is one order of magnitude smaller than p-P SHG, we neglect the contribution of $\chi^{(2)}_{xzx}$. Then, the expression of p-P polarized SHG intensity $I^{2\omega}_{p-P}$ can be approximated as:

$$I^{2\omega}_{p-P} \approx \left|\gamma_{zzz}\chi^{(2)}_{zzz} + \gamma_{zxx}\chi^{(2)}_{zxx}\right|^2 \tag{6.6}$$

$$I^{2\omega}_{p-P} \approx \left|\gamma_{zzz}\chi^{(2)}_{zzz}\right|^2 + \left|\gamma_{zxx}\chi^{(2)}_{zxx}\right|^2 + 2\left|\gamma_{zzz}\gamma_{zxx}\cdot\chi^{(2)}_{zxx}\chi^{(2)}_{zzz}\right| \tag{6.7}$$

In order to disentangle the contributions involved in p-P polarized SHG, we calculate the spectral response of the linear coefficients. In the calculation, we do not account for the effect of the adsorbed molecules, since a few MLs of molecules present on the metal surface are only expected to cause a change of linear reflectivity in the order of 0.01% – 1% [175]. According to equations (3.18) – (3.21), the linear coefficients can be expressed as:

$$\gamma_{zzz} = A_p \cdot t_p^2 \cdot F_s \cdot f_s^2 \cdot n^2(\omega) \tag{6.8}$$

$$\gamma_{zxx} = A_p \cdot t_p^2 \cdot F_s^2 \cdot f_c^2 \cdot n^2(2\omega) \tag{6.9}$$

whereby $n(\omega)$ is the refractive index of bulk copper [176]. The linear coefficients of the fundamental and the reflected second harmonic beams are indicated by lower-case and capital letters, respectively.

The calculated absolute values of the linear coefficients are shown in figure 6.7. In absolute numbers, $|\gamma_{zzz}|$ is one order of magnitude smaller than $|\gamma_{zxx}|$. This justifies the dominant contribution of $\chi^{(2)}_{zzz}$ over $\chi^{(2)}_{zxx}$ for p-P SHG [16]. On the other side, $|\gamma_{zzz}|$ and $|\gamma_{zxx}|$ have similar shape, they both reach the local maximum at a fundamental photon energy of 2.3 eV. Together with the spectral dependence of p-P SHG, we can conclude that the SHG enhancement at 2.3 eV is mainly caused by linear coefficients i.e. one ω resonance in the SHG process. This enhancement can be explained with the DOS of copper. Since the 3*d* band peak of copper lies about 2.3 eV below Fermi level [177, 178], a fundamental beam at this photon energy can resonantly excite 3*d* state to the Fermi level (intermediate state), which largely increases the overall probability of SHG processes at copper surface. At last, we turn the attention to the cross term $|\gamma_{zzz}\gamma_{zxx}|$ that could affect the out-going p-P SHG yield. As depicted in Figure 6.7, the magnitude is one order lower than $|\gamma_{zzz}|$, and the trace shows a similar shape with local maximum at 2.3 eV. Based on the low absolute value provided by $|\gamma_{zzz}\gamma_{zxx}|$, we have neglected the contribution from the cross term $\left|\gamma_{zzz}\gamma_{zxx}\cdot\chi^{(2)}_{zxx}\chi^{(2)}_{zzz}\right|$ in equation (6.7). Therefore, we can approximate the spectral response of $\Gamma_{zzz}\chi^{(2)}_{zzz}$ by taking the difference of $I^{2\omega}_{p-P}$ and $I^{2\omega}_{s-P}$:

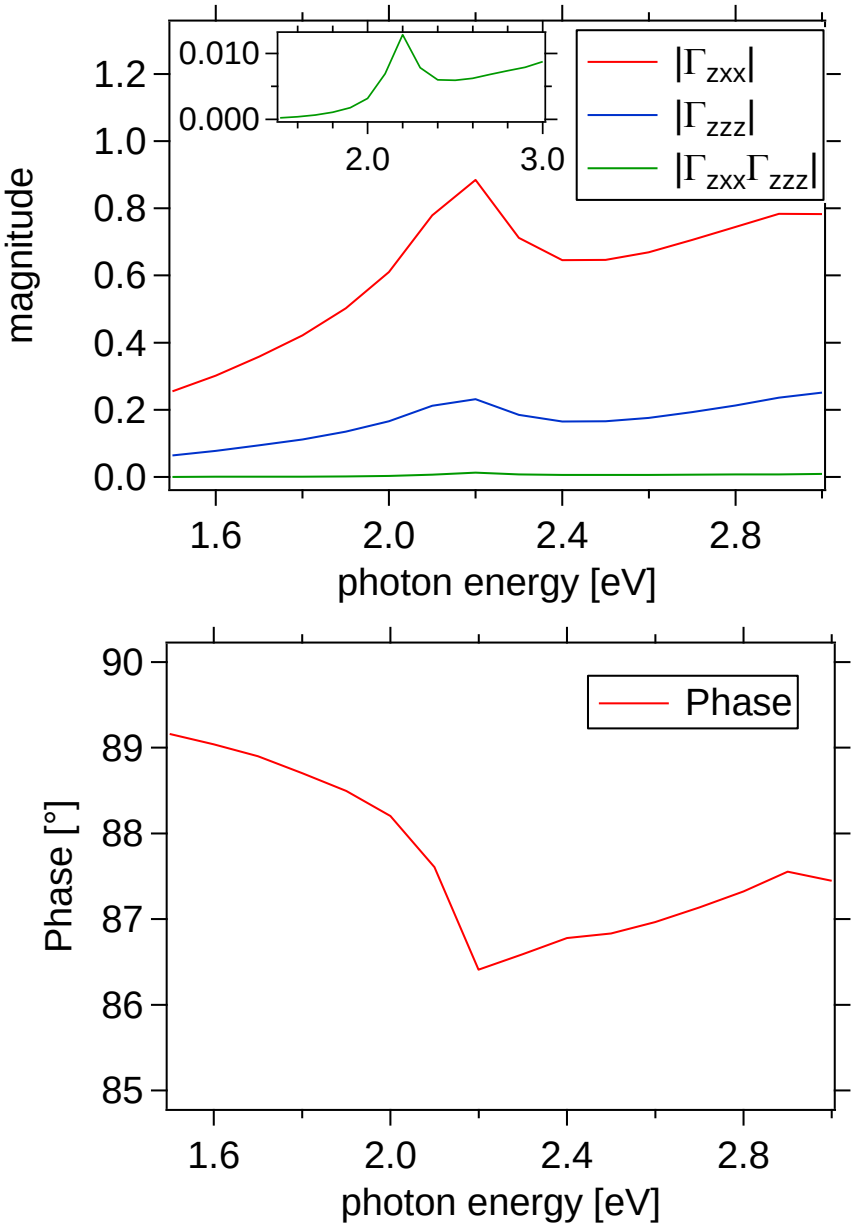

Figure 6.7: (a) Calculated absolute values of linear coefficients γ_{zzz} (blue), γ_{zxx} (blue) and the cross term $\gamma_{zzz} \cdot \gamma_{zzz}$ (green). A zoom-in of the absolute scale of the cross term is depicted in the inset for better visibility. (b) Calculated phase difference between γ_{zzz} and γ_{zxx}.

$$\left|\Gamma_{zzz}\chi^{(2)}_{zzz}\right|^2 \approx I^{2\omega}_{p-P} - I^{2\omega}_{s-P} \tag{6.10}$$

In addition, we have determined the phase difference between γ_{zzz} and γ_{zxx} in complex plane, the result is depicted in Figure 6.7 (b). As can be seen, the phase difference stays rather constant within the energy range 1.6 – 3.0 eV with an average angle of 87 °. The result is consistent with the experimental observation of polarization dependent p-P SHG, see Figure 6.4. The polarization pattern exhibits non-vanishing SHG yield at off p- and s-polarization angle, which should not be misunderstood as back ground counts.

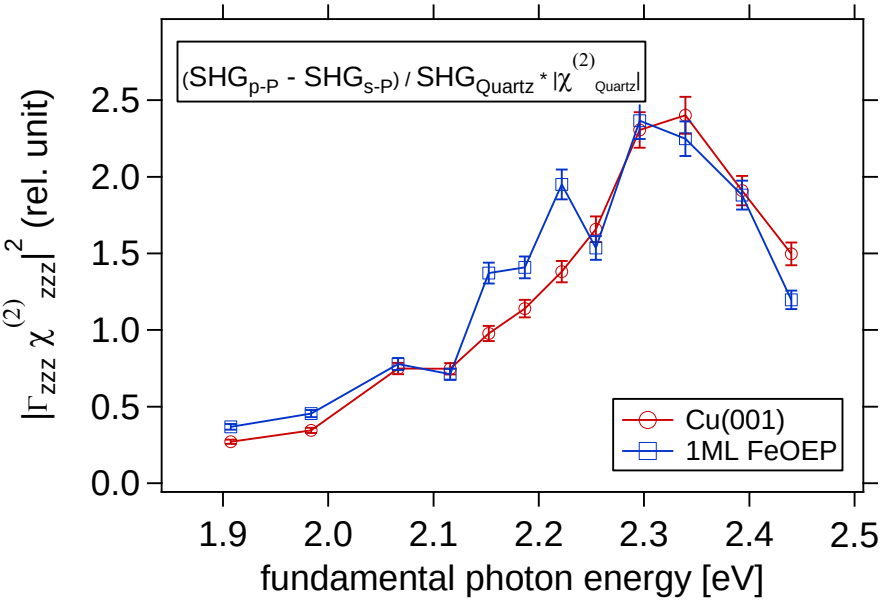

Figure 6.8: Retrieved spectral dependence of $|\gamma_{zzz}\chi^{(2)}_{zzz}|^2$ for Cu(001) surface (red circle) and 1 ML FeOEP/Cu(001) interface (blue square) as function of fundamental photon energy.

According to the equation (6.10), the spectral dependence of $|\gamma_{zzz}\chi^{(2)}_{zzz}|^2$ is displayed in Figure 6.8. We then identify a FeOEP/Cu(001) interface induced SHG enhancement by the fundamental photon energy of around 2.2 eV. First, for a bare Cu(001) surface, $|\gamma_{zzz}\chi^{(2)}_{zzz}|^2$ increases continuously with a maximum at 2.33 eV, then shows a decreasing trend. This spectral dependence is explained by one ω resonance due to the DOS of copper. After 1 ML FeOEP is adsorbed on the Cu(001) surface, as can be seen in the Figure 6.8, $|\gamma_{zzz}\chi^{(2)}_{zzz}|^2$ exhibits a similar spectral dependence to clean Cu(001) surface except a noticeable 30% enhancement at 2.2 eV with a width less than 100 meV.

Since 2.2 eV is below the Copper d-band peak with a photon energy of 2.3 eV, we then attribute the enhancement of $|\gamma_{zzz}\chi^{(2)}_{zzz}|^2$ to a LUMO state of 2.2 eV above Fermi level. This process can be explained with the help of the SHG excitation scheme in Figure 6.1. The light excites electrons in metal to intermediate state at fermi level, as far as the incident photon energy matches the difference between LUMO and Fermi level, electrons can be further resonantly excited to interfacial LUMO state, which increases the probability of SHG processes. The enhancement cannot be explained by linear coefficient γ_{zzz}. One monolayer coverages of molecule barely change the linear reflectivity of metal surfaces, only in the order of 0.01 – 1% [175], which is too low compare to our observation of 30% change. Moreover, considering that FeOEP molecules are physi-sorbed on copper surfaces, the electronic structure of the copper surface is not expected to be altered, which can cause a change in reflectivity. The maximal peak of the SHG spectrum of 1 ML FeOEP/Cu(001), which occurs at 2.33 eV due to Cu 3*d* electrons, would be shifted if the Cu DOS is being modified. Consequently, we clearly observe a molecule-metal interface induced enhancement at 2.2 eV. Based on the above analysis and arguments, we conclude that the enhancement of $|\gamma_{zzz}\chi^{(2)}_{zzz}|^2$ at 2.2 eV is exclusively governed by $\chi^{(2)}_{zzz}$ due to FeOEP/Cu(001) interface assisted resonant excitation.

6.2 Wavelength dependent electron dynamics at interfaces

So far, the static spectral SHG landscape of 1 ML FeOEP/Cu(001) interface has been addressed by polarization and photon energy dependent measurements. To further identify the SHG resonance and charge transfer dynamics at the molecule-metal interface, we perform pump-probe SHG experiments at on and off-resonant photon energy. The idea is to excite electrons from the metal to unoccupied molecular states, and then resonantly probe the charge response of the molecule-metal interface via time-resolved SHG.

Wavelength [nm]	*Photon energy [eV]*	*XC FWHM [fs]*	*Pump fluence [mJ/cm^2]*	*Absorbed fluence [mJ/cm^2]*
518	2.39	50	4.2	1.38
530	2.33	48	4.8	1.53
562	2.21	30	3.2	0.86
566	2.18	28	3.0	0.75
600	2.06	30	3.0	0.42
800	1.55	90	11.4	0.46

Table 6.1: Parameters of optical pulses applied in the time-resolved SHG spectroscopy. Here, 518 – 600 nm beams are generated through NOPA, while 800 nm beam is obtained from the 100 kHz amplifier. Absorbed fluence is calculated through refractive index of copper. Remember that in pump-probe experiments, the probe beam has only 25% power of the pump beam.

In this section, we investigate the electron dynamics at the surfaces of Cu(001) substrate and charge transfer dynamics at 1 ML FeOEP/Cu(001) interface. Based on the SHG spectrum in figure 6.8, we have chosen photon energies below, above and exactly at 2.2 eV for pump-probe SHG. The parameters of the laser pulse used in the experiments are listed in table 6.1. The time-resolved SHG data are normalized to the unpumped signal with the equantion:

$$\Delta|\chi_{zzz}| = \sqrt{\frac{I_{p-P}^{2\omega}(t)}{I_{p-P}^{2\omega}(t_0)}} - 1 \tag{6.11}$$

where $\Delta|\chi_{zzz}|$ represents the pump-induced change of the p-P SH field, which is considered to be dominated by the change of tensor element $|\chi_{zzz}|$. In order to avoid optical artifact, we use s-polarized pump and p-polarized probe beams. Details of the pump-probe setup have been introduced in Chapter 4.4. All time-resolved SHG data are collected at room temperature.

6.2.1 Electron relaxation dynamics at Cu(001) surfaces

The transient SHG reflectivity signal from the Cu(001) surface shows a strong wave-length dependence near the interband transition threshold (ITT) [26], the energy is around 2 eV for the case of copper [33]. The pump-probe SHG data is depicted in Figure 6.9. A convolution of Gaussian and step function is applied to fit the data points, see also Appendix B.

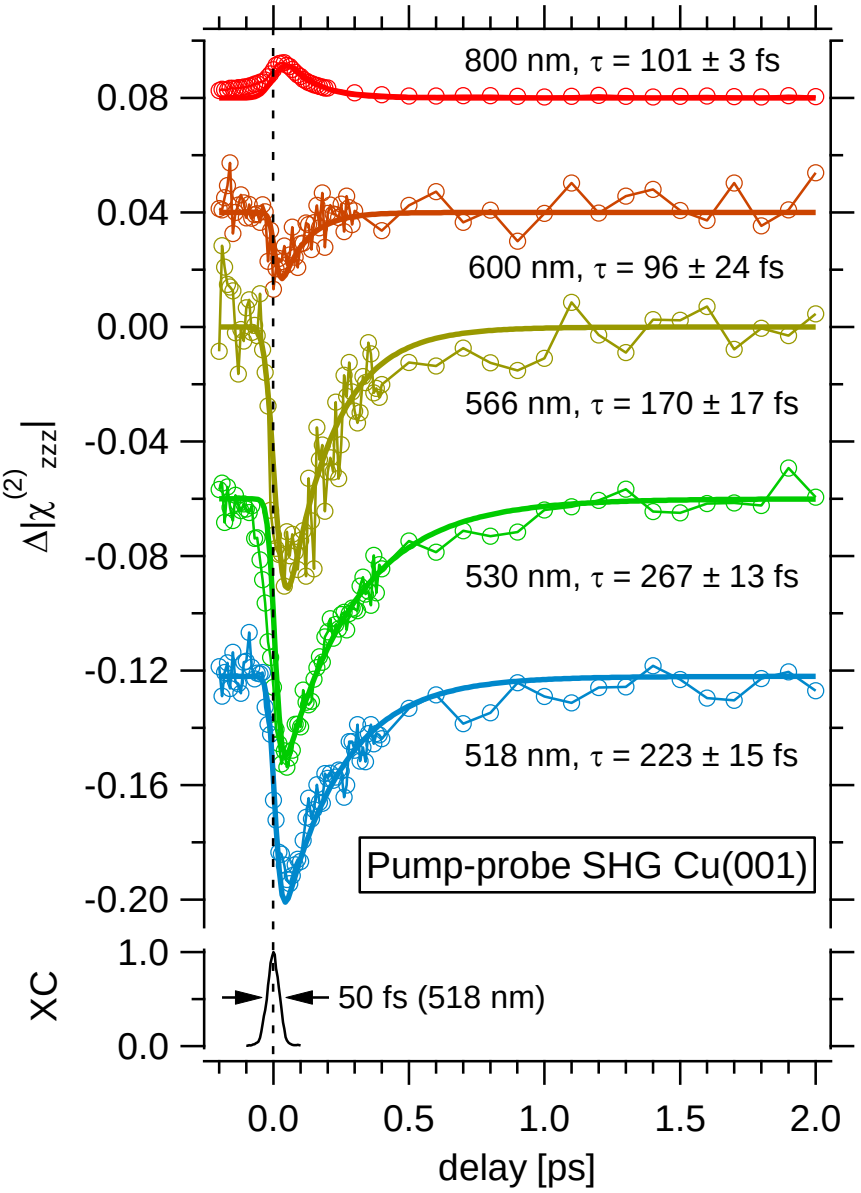

Figure 6.9: Pump induced relative change of p-P SH field on clean Cu(001) surface at photon energy of 1.55 – 2.39 eV (800 – 518 nm). Zero delay is defined by the maximal SHG intensity of (p-polarized) pump-probe cross correlation (XC). Experimental data is indicated by circles, and solid lines represent exponential fit (see Appendix B).

The pump-induced change of the reflected SHG intensity exhibits a sign flip at photon energy of 2.06 eV. That means at a probing photon energy of the fundamental beam less than 2.06 eV, the optical pumping induces an increase of the transient reflected SHG intensity, which is exactly the experimental observation of 1.55 eV pump-probe SHG shown in Figure 6.9 (a). On the other side for photon energy higher than 2.06 eV, pump excitation of copper is followed by a decrease of the reflected SHG intensity. This effect of positive and negative pump induced change is related to interband transition in noble metals [26]. In contrast to transient SHG reflectivity from metal, the wavelength dependent transient linear reflectivity shows opposite sign change near ITT, which has been experimentally demonstrated in gold [26] and in copper [33]. Based on the sign change of reflected SHG signal near ITT, we conclude that transient SHG reflectivity is exclusively governed by $|\chi_{zzz}|$, which probes the charge response at metal surfaces.

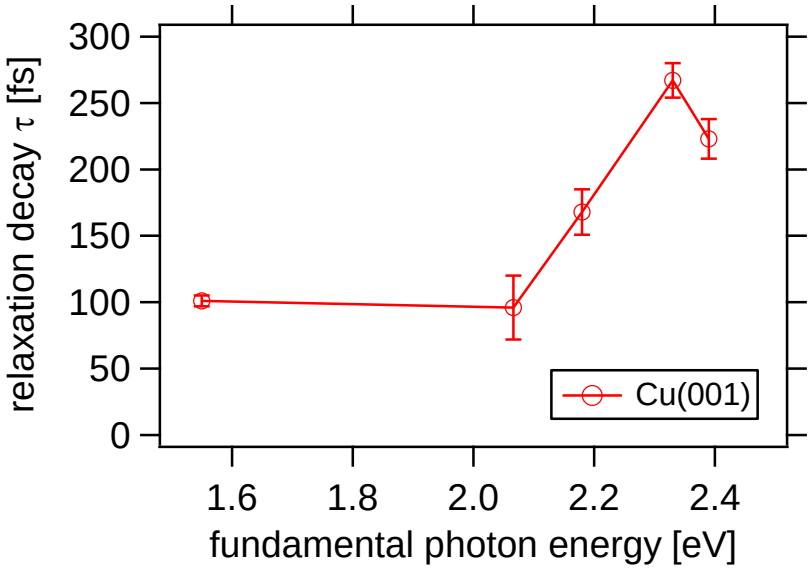

Figure 6.10: Photon energy dependent time-resolved SHG relaxation time constant for a clean Cu(001) substrate.

The maximal amount of pump-induced change increases as the pump photon energy is getting close to 2.3 eV. Although we applied different pump fluence, such pump effect is most likely related to the absorbed fluence, which corresponds to an increased absorption due to 3*d* – 4*sp* transition. See Table 6.1 for the calculated absorbed fluence.

The relaxation dynamics of the pump-induced SH response also depends on the fundamental photon energy. We characterize the relaxation parts of the transient signal by exponential decay function e.g. in the time range 0.1 – 2.0 ps of the pump-probe data. The decay time constants as function of photon energy are shown in Figure 6.10. For photon energies below 2.06 eV, the SHG relaxation dynamics shows a very fast decay time of $\tau \approx 100\ fs$. The decay constant increases to 265 fs when the photon energy reaches 2.33 eV, which corresponds to energy difference of 3*d* band to Fermi level in copper. Finally, τ decreases further for photon energies exceeding the Cu 3*d* band peak.

Since we employ degenerate pump and probe wavelength to perform pump-probe SHG, one question that needs to be clarified is that the energy dependence of the relaxation time constant is caused by the pump or the probe beam. We propose that the slower relaxation time for photon energies above ITT is mainly caused by interband photoexcitation that promotes 3*d* electrons to *sp* bands. This effect can be explained with the excitation scheme in Figure 6.11. As far as the pump photon energy is large enough to excite *d* band electrons above the Fermi level, vacancy in 3*d* band and occupancy at Fermi level reduce the probability of SHG processes, so that the transient SHG signal exhibits a negative pump induced change (see also Figure 3.4). Because SHG is cascade process, the SHG transition probability is then influenced by the initial, the intermediate and the final state. Hence, the interpretation of the pump-probe SHG data is not trivial. Based on the results, the slower transient SHG relaxation time can be explained by two possible effects: (i) A longer lifetime of excited electrons with small energy above Fermi level, whereby the electron-electron scattering rate is low according to Landau-Fermi-liquid theory (FLT) [37, 38]. (ii) Long-lived 3*d*-band hole in copper [187, 188], which can affect the relaxation dynamics of hot electrons. In both cases, the SHG transition is continuously suppressed by the vacancy of initial state and occupation of intermediate state, which corresponds to the long-lived 3*d* hole and hot electrons around Fermi level, respectively.

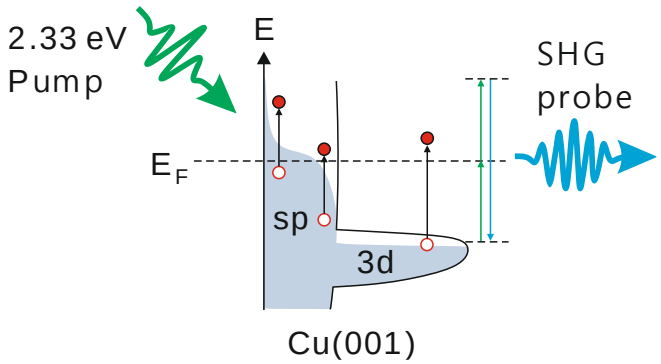

Figure 6.11: Schematic of interband photoexcitation at Cu(001) surface. Pump photons excite hot electrons (red solid dot) and hole (empty circle) in Copper. The gray area represents the electron distribution.

Another feature should be discussed is the fast decay time of 100 fs for $E \leq 2.06\ eV$, since it is faster than the reported value of the thermalization time in noble metal [26, 33] e.g. $\tau_{th} = 258\ fs$ in epitaxial copper, $\tau_{th} = 350\ fs$ in polycrystalline silver [34] and $\tau_{th} = 500\ fs$ in polycrystalline gold thin films [29]. One notes that the dacay time cannot be simply interpreted as the internal electron thermalization time. Although the electron thermalization time in copper is faster due to screening of electron-electron Coulomb interaction by *d* band electrons, the value is still larger than the SHG relaxation time. The fast decay time implies another channel for energy loss of nonequilibrium electrons, namely that energy carried by electrons can dissipate from surface into bulk [179, 187]. Ballistic and diffusive transport may strongly affect the observed energy relaxation dynamics near the surface. We propose that the SHG decay time τ indicates how fast the absorbed energy from the laser pulse is redistributed at the copper surface, which is not exclusively dominated by one process but a competition of electron transport, electron-electron and electron-phonon scattering.

We emphasize that the interpretation is based only on quantitative analysis of the data, a full picture of the SHG relaxation time constant (e.g. 2D map of relaxation constant) would require further systematic studies, such as pump fluence dependent measurements, two-color pump-probe SHG experiment and sophisticated theoretical modeling.

To be summarized, we have investigated the electron relaxation dynamics at Cu(001) surfaces via one-color pump-probe SHG spectroscopy. The sign of pump-induced change is determined by the fundamental probing wavelength. For $h\nu > 2.06\ eV$ pump, the faster SHG decay is due to electron transport effect from the Cu(001) surface to bulk, which serves as an additional energy dissipation channel. Slower SHG relaxation time was observed than that of $h\nu < 2.06\ eV$, which is caused by interband photoexcitation from 3*d* to *sp* band in copper. Possible explanation can be long life time of hot electrons near Fermi level or long-lived 3*d*-band hole in copper.

6.2.2 Charge transfer excitation at FeOEP/Cu(001) interfaces

According to the SHG spectrum of FeOEP/Cu(001), we have measured the transient SHG reflectivity of FeOEP/Cu(001) interfaces at on- and off-resonant fundamental photon energies. A comparison with a clean Cu(001) surface is depicted in Figure 6.12, for the photon energy 2.06 eV (600 nm), 2.18 eV (566 nm) and 2.33 eV (530 nm).

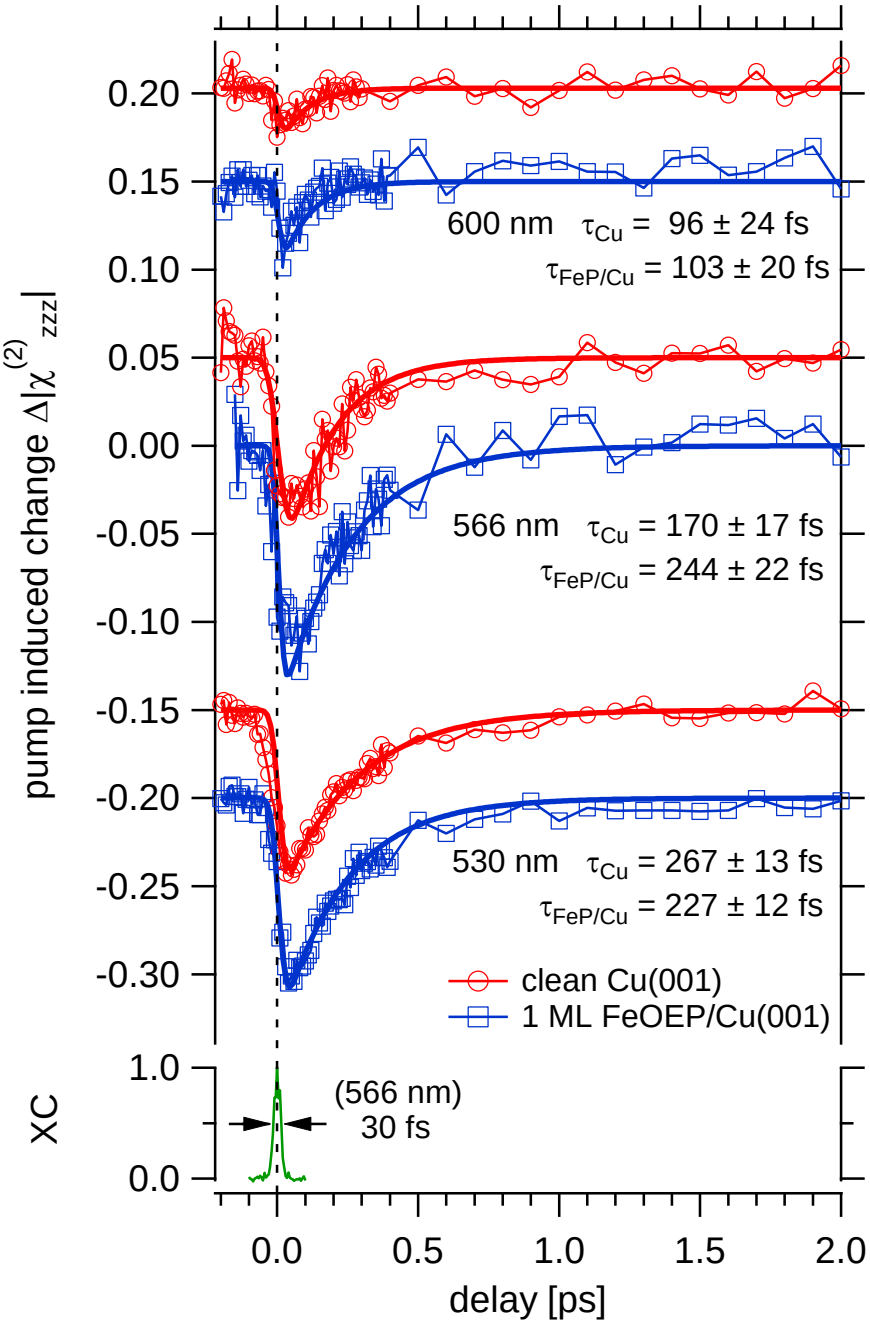

Figure 6.12: Pump induced relative change of p-P SH field by photon energy 2.06 eV (600 nm), 2.18 eV (566 nm) and 2.33 eV (530 nm). Data of clean Cu(001) are denoted by red circle, while blue squares indicate 1 ML FeOEP/Cu(001). Time zero is determined by pump-probe XC SHG trace (green curve). The experimental data is fitted through the convolution of Gaussian sharp pulse with an exponential decay of time constant τ (see Appendix B).

At first glance, the presence of FeOEP molecules on Cu(001) still leads to a negative pump induced change of the reflected SH field. Two features in the transient SH field can be noticed: (i) pump effect i.e. amount of pump induced change and (ii) SHG relaxation time τ with and without FeOEP molecule, which can be related to charge transfer processes at the molecule/metal interface.

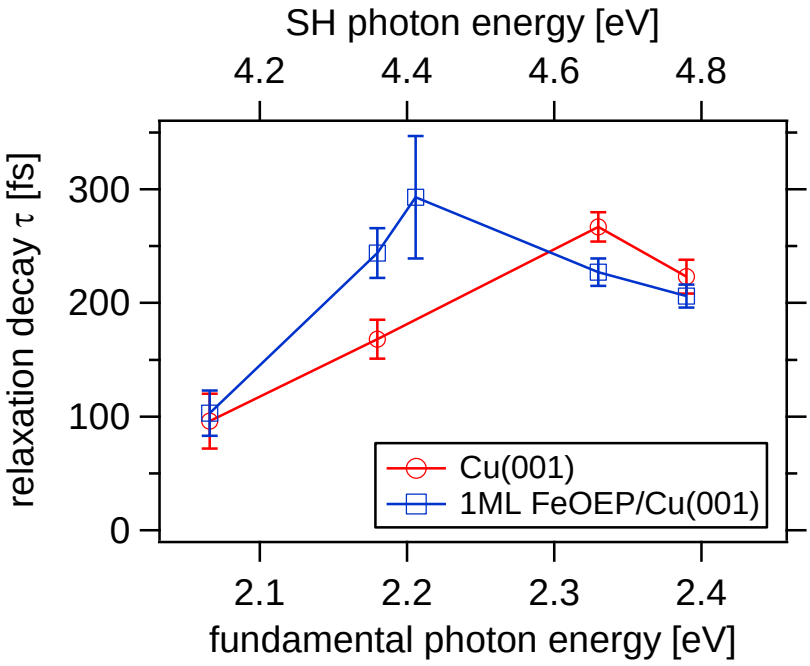

Figure 6.13: SHG relaxation time constant of Cu(001) surface (red circle) and 1 ML FeOEP/Cu(001) interface (blue square) as a function of photon energy.

In general, a stronger pump induced maximal change is observed for the case of 1 ML FeOEP/Cu(001). This effect is pronounced at pump photon energy 2.18 eV with 30% increased pump effect, while at other excitation energies the change is small. Since changes to the linear refractive index of copper can be neglected at 1 ML coverage of FeOEP molecule, we can exclude that the pump effect is due to increased absorption in the Cu(001) substrate. This pump induced change of SH field can be related to charge transfer excitation from metal to unoccupied molecular resonance. As illustrated in Figure 6.14, SHG is a cascade process, transient occupation of virtual intermediate and (virtual) final state can lower the transition probabilities. According to the static SHG spectrum, it is clear that the absolute SHG yield is enhanced at around 2.2 eV. In pump-probe SHG, the pump field promotes electrons from fermi level to molecular states. Subsequently, the delayed probe pulse arrivals, the occupied final state causes a decrease of the reflected SH field.

After the reflected SH field reaches maximal change, the signal starts to relax back to the equilibrium value. This brings us to the second feature of transient signal i.e. photon energy dependent decay time τ, as depicted in Figure 6.12. Here, the transient behavior is characterized by Gaussian sharp convoluted exponential decay. In comparison with clean Cu(001) surface, decay time $\tau_{FeP/Cu}$ increases from 170 ± 17 fs to 244 ± 22 fs at 2.18 eV and becomes slowest 293 ± 54 fs at 2.21 eV. For pump photon energy 2.33 eV, the SHG decay time is even faster than Cu(001). We propose that slower and faster decay times after FeOEP molecule adsorption are related to direct and indirect charge transfer from metal to molecule, respectively.

As shown in Figure 6.14, the 2.2 eV pump excites a certain amount of nonequilibrium electrons on copper, whereby a fraction of electrons is resonantly transfered from copper to the interfacial molecular state. For the case of 1 ML FeOEP/Cu(001), such transition would be *sp* electrons from Cu to 3*d* states of FeOEP molecule. Since the molecular state has a finite line width due to physisorption, the lifetime of the molecular state is expected

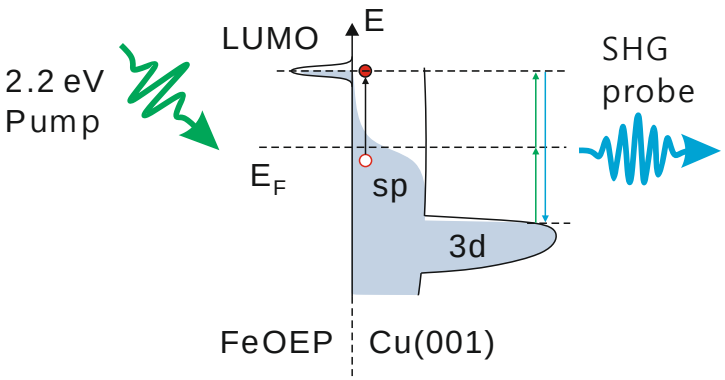

Figure 6.14: Schematic of charge transfer excitation at 1 ML FeOEP/Cu(001) interface. LUMP state of FeOEP molecule (and Cu DOS) is depicted on the left (right) side of the energy axis.

to be much longer than electron thermalization time of Cu(001). Relaxation of two sets of electrons with faster and slower lifetime results in a slower decay time compared to bare Cu(001) surface. Here, the SHG decay time reflects the timescale of electron redistribution at the probing surface region. One note that the resonant charge transfer at 2.2 eV is consistent with static data and similar to previous findings of back spin transfer at Co/Cu(001) interfaces [19].

Intuitively, one expects photoinduced direct charge transfer to occur for pump photon energies exceeding the transition threshold of 2.2 eV, since porphyrin molecules are adsorbed on copper surface, which has a continuous band below the Fermi level. In this picture, a slower SHG relaxation time is expected. However, for photon energy at 2.33 eV, resonant charge transfer excitation seems to be not pronounced, instead, faster decay time is observed. Faster decay time with iron porphyrin molecules on copper could be due to the probing wavelength. We mention that at off resonance at 2.06 eV and 2.4 eV, the relaxation time with and without molecules remains fairly the same, which indicates that neither the pump and the probe photon energy matches the resonant transition.

At 2.33 eV (530 nm), the SHG is not probing the molecular resonance, instead, the SHG process is sensitive to transient electron distribution around the Fermi level and the occupancy of Cu 3*d* band. This effect of faster decay time implies an additional channel that accelerate the electron relaxation processes, which can be explained by indirect charge transfer i.e. hot electron mediated charge transfer. The 2.33 eV pump pulse generates hot electrons and most importantly, the pump pulse populates certain amounts of d band electrons to above Fermi level. The energy carried by excited electrons can then be thermalized through electron transport, e-e and e-ph scattering [179]. The adsorption of 1ML FeOEP on the Cu(001) surface serves as an additional channel for hot electrons. They can dissipate the energy via charge transfer to the molecule, so that hot electrons relax faster than Cu(001). In this scenario, the decay time constant can be described by the rate equation:

$$\frac{1}{\tau_{FeP/Cu}} = \frac{1}{\tau_{Cu}} + \frac{1}{\tau_{FeP}} \tag{6.12}$$

where τ_{FeP} represents the lifetime of an electron in the molecular state. Based on the decay time at 2.33 eV, we obtain a lifetime of $\tau_{FeP} \approx 1515$ fs, which corresponds to a line width of $\Gamma_{FeP} \approx 43.4\, meV$ according to $\Gamma_{FeP} \approx \hbar/\tau_{FeP}$ (Planck's constant $\hbar = 6.58 \cdot 10^{-16}\, eVs$). The simply estimated line width is in the same order of energy

resolution of static SHG spectrum, this means that a clear and precise determination of the line width of molecular state would require further experimental and theoretical investigations.

We point out that to fully address the complete picture of charge transfer processes at molecule/metal interfaces, further investigations are required, e.g. fundamental two-color pump-probe spectroscopy, pump polarization & fluence dependent studies and even theoretical approach.

In summary, we identify the charge transfer processes at FeOEP/Cu(001) interface by pump-probe SHG spectroscopy. Resonant excitation occurs at 2.2 eV pump photon energy, the observed slower relaxation time is explained by equilibration of two sets of electrons. For photon energy at 2.33 eV, the faster decay time is attributed to the probing wavelength, which reflects the energy relaxation of hot electrons due to additional charge transfer channel induced by the FeOEP molecule.

6.3 Conclusions

In this chapter, we have employed time-resolved SHG spectroscopy to analyze the electron dynamics on Cu(001)s surface and 1 ML FeOEP/Cu(001) interfaces.

Through polarization and wavelength dependent SHG studies, we disentangle the individual SHG contribution and conclude that interband transitions of 3*d* – *sp* play a major role for the spectral dependence of p-P SHG from Cu(001) surfaces. Transient SHG reflectivity shows a strong wavelength dependence. Positive and negative pump-induced change is attributed to the fundamental probe photon energy that exceeds ITT. For pump photon energy $h\nu \leq 2.06\ eV$, transport effect from the Cu(001) surface to bulk can be concluded from the fast SHG decay time. While for $2.06\ eV < h\nu < 2.39\ eV$, interband excitation plays a major role. The resulting slow SHG decay time is explained by long-lived hot electrons close to Fermi level and also the long-lived 3*d* band hole.

In case of iron porphyrin molecules adsorbed on Cu(001), we identify a molecule-metal interface induced SHG enhancement at 2.2 eV, which is explained by resonant charge transfer excitation from metal to molecule. Distinctive SHG relaxation dynamics were observed by on- and off-resonant pump photon energies. The effects of stronger pump-induced magnitude and longer SHG relaxation time at 2.2 eV pump are assigned to resonant charge transfer excitation, which is consistent with static SHG results. We also demonstrate that hot electron mediated charge transfer process can be analyzed via resonantly probing the relaxation of 3*d* electrons at Cu(001) surface by time-resolved SHG spectroscopy.

7 Summary and outlook

This thesis was dedicated to the studies of laser induced charge and spin dynamics at solid heterogeneous interfaces. Two interfacial model systems have been addressed in this thesis: epitaxial Co/Cu(001) films and iron octaethylporphyrin (FeOEP) molecules on Cu(001). The main issues addressed in the thesis are: (i) Length scale of spin-dependent inelastic mean free path (MFP) in Co/Cu(001) films, (ii) Competitive microscopic processes at Co/Cu(001) interfaces and (iii) Charge transfer dynamics at FeOEP/Cu(001) interfaces. The experimental tools are femtosecond nonlinear optical techniques i.e. time-resolved second harmonic generation (SHG) and magnetization-induced SHG (MSHG), which provide information about the electron and magnetization dynamics at the surfaces and buried interfaces of centrosymmetric materials.

Charge and spin dynamics in Co/Cu(001) films

Femtosecond laser pulses can trigger spin currents in a ferromagnetic metallic film. One issue to be addressed is the length scale of the laser excited charge carriers in ferro-magnetic/non-ferromagnetic (FM/NM) heterostructures. The present thesis demonstrated that the laser induced spin current in Co/Cu(001) films can be analyzed through systematic thickness dependent studies of time-resolved MSHG, which serves as a sensitive probe for spatially inhomogeneous magnetization dynamics. In details, the reflected MSHG signals from the sample are carefully characterized for various thickness of Co films on Cu(001). The thickness dependence of MSHG can be quantitatively described by a simple two interface model i.e. vacuum/Co and Co/Cu(001) interfaces, which makes up the overall MSHG signal. For the magnetization-dependent SH fields, a 180 ° phase shift was found to be induced between the vacuum/Co and the Co/Cu(001) interfaces. Therefore, the magnetization-dependent SH fields from two interfaces can be disentangled. Consequently, it was observed that pump induced magnetization dynamics in Co/Cu(001) depends on the Co thickness. Based on the two interfaces model, the observed dynamics can be described as a linear combination of the vacuum/Co and Co/Cu(001) interfaces. By analyzing the transient magnetization profile between the vacuum/Co and the Co/Cu(001) interfaces, it was found that the spatial magnetization gradient flips the sign for Co thickness increasing from 2 nm to 4 nm. Such a spatial inhomogeneity of transient magnetization was attributed to the length scales of spin currents propagating through the Co films to the Cu(001) substrate. Upon the laser excitation, spin currents are generated in the Co film. For small Co thickness, all the excited majority spins in Co can travel to the Cu substrate without any inelastic scattering. For large Co thickness, only the majority spins near the buried Co/Cu(001) interfaces can escape to the Cu substrate. Based on the analysis, we have concluded that the inelastic mean free path of the excited majority spins in Co films is around 3 nm. [18]

Another goal of this project was to investigate the role of the interface in the processes of laser induced ultrafast demagnetization in metallic FM/NM heterostructures. For this purpose, time-resolved MSHG was performed at ultrathin Co/Cu(001) films (3 ML and 5 ML Co), which serves as a model interface system. Laser induced demagnetization

dynamics on the Co/Cu(001) films was observed. In particular, it was found that the magnetization-independent SH field (charge system) responds faster than the magnetization-induced SH field (spin system). In order to identify the competing elementary processes at Co/Cu(001) interfaces and the characteristic timescales, the experimental results were interpreted with the help of *ab initio* time-dependent density functional theory (TDDFT) calculations. The MSHG experiment and TDDFT were conducted on the identical sample thickness and laser parameter (wavelength, pulse duration and adsorbed laser fluence). Since the lattice excitations play a role on the timescales later than 100 fs and were not included in the TDDFT, we mainly focus on the dynamics in the first 100 fs after laser excitation. The theoretical calculations quantitatively agree with the measured pump-induced dynamics for both 3 ML and 5 ML Co/Cu(001) films. By combining the experiment and the theory, we have identified three interface assisted features. In the early 35 fs after laser excitation, the ultrafast quenching of magnetic order of the Co film is governed by the charge system i.e. spin independent transfer from Co film to Cu(001) substrate. Meanwhile, minority-spin can be excited from Cu substrate to Co films within the first 35 fs. The effect of spin back transfer was attributed to resonant optical transition in the minority spin channel from Cu 3d to Co 3d state at Co/Cu(001) interface, where the pump photon energy match the interfacial density of state (DOS). Subsequently, further loss of the magnetization is caused by spin-orbit coupling (SOC) mediated local spin-flip process in 35 – 100 fs after laser excitation. In this process, the spin angular momentum is transferred through SOC to lattice, which serves as an ultimate sink of angular momentum. These findings provide not only fundamental insights into laser induced demagnetization dynamics, but also new opportunities to control the ultrafast spin dynamics at the FM/NM metal interfaces by tuning the pump photon energy. [19]

Electron dynamics at FeOEP/Cu(001) interfaces

In addition to the FM/NM interfaces, the present thesis also studies the molecule/metal interfaces. In particular, the thesis focuses on the issue of charge transfer dynamics at the FeOEP/Cu(001) interfaces, which serves as a prototype system. In order to investigate the FeOEP molecule induced features, static and time-resolved SHG studies were performed at Cu(001) and at 1 ML FeOEP/Cu(001).

Regarding Cu(001) surface, it was found that at fundamental photon energy of 2.3 eV, the SHG yield is enhanced via an interband transition from 3*d*- to *sp*-band. Furthermore, we have also demonstrated that the relaxation dynamics of electrons and holes at the surface can be investigated with time-resolved SHG spectroscopy. For pump photon energy below the interband transition threshold (ITT), hot carrier transport from copper surface to bulk was concluded to be an additional channel for energy to dissipate at the Cu(001) surface. For photon energy exceeding the ITT, the hot electron relaxation dynamics observed by SHG was explained by the long life time of low energy electrons and the 3*d* holes [187] due to interband photo-excitation.

In contrast to SHG signals from Cu(001), a distinct resonant enhancement of surface SHG at 2.2 eV photon energy was observed for 1 ML FeOEP/Cu(001). This enhancement was assigned to an interfacial unoccupied molecular orbital (LUMO) that lies above Fermi level 2.2 eV. When the fundamental photon energy matches the difference between LUMO and Fermi level, the SHG transition can be resonantly excited. In order to verify the molecule/metal interface induced feature, pump-probe SHG experiments were performed at on- and off-resonant photon energies. Depending on the photon energy, the

pump-induced dynamics can be modified. By analyzing the SHG relaxation dynamics at resonant excitation, distinctly longer decay time was observed at the FeOEP/Cu(001) interface than that of Cu(001) surface. This effect was explained by charge transfer from Cu(001) to FeOEP molecules, because the electron lifetime in the molecular state is expected to be longer than that of Cu(001). Based on the results, we have concluded that the adsorbed FeOEP molecules on Cu(001) open up a new channel for the excited hot electrons to transfer and dissipate at the interface. This work demonstrated the capability of surface SHG to probe the charge transfer dynamics at molecule/metal interfaces, and also serve as a reference for future studies of molecule/metal interfaces.

Outlook

Based on the insight provided by femtosecond nonlinear optical techniques, several interesting points could be investigated further. For the Co/Cu(001) system, one interesting point would be experimental manipulation of spin back transfer. According to our result, spin back transfer should be possible to be controlled by the pump photon energy. Meanwhile, spin back transfer is also an interface induced effect, that makes interface-sensitive fs nonlinear magneto-optics i.e. MSHG the ideal method to investigate this effect. Specifically, to enhance the interfacial effect, the experiment can be conducted on $[\mathrm{Cu/Co/Cu(001)}]_n$ multilayer structures. Beside the nonlinear optical probe, with the large facilities based soft x-ray sources or even HHG based lab sources, a direct identification of spin back transfer should be possible through the element-specific fs XMCD technique.

Regarding charge transfer dynamics at FeOEP/Cu(001) interface, two color pump-probe SHG spectroscopy could provide a full picture of resonant excitation at the molecule/metal interfaces. Complete information about hot electron relaxation dynamics at Cu(001) surface could also be obtained as well. In addition, spin transfer dynamics of FeOEP molecules on Co/Cu(001) films [22] i.e. molecule/ferromagnetic interface would also be an interesting topic.

In view of the further development of ultrafast spintronics, optical control of magnetic order will continue to attract the attention of many research activities. The breakthrough of various new technologies will prompt the arrival of an “ultrafast” low power digital world.

Appendix

A: Quartz SHG reference

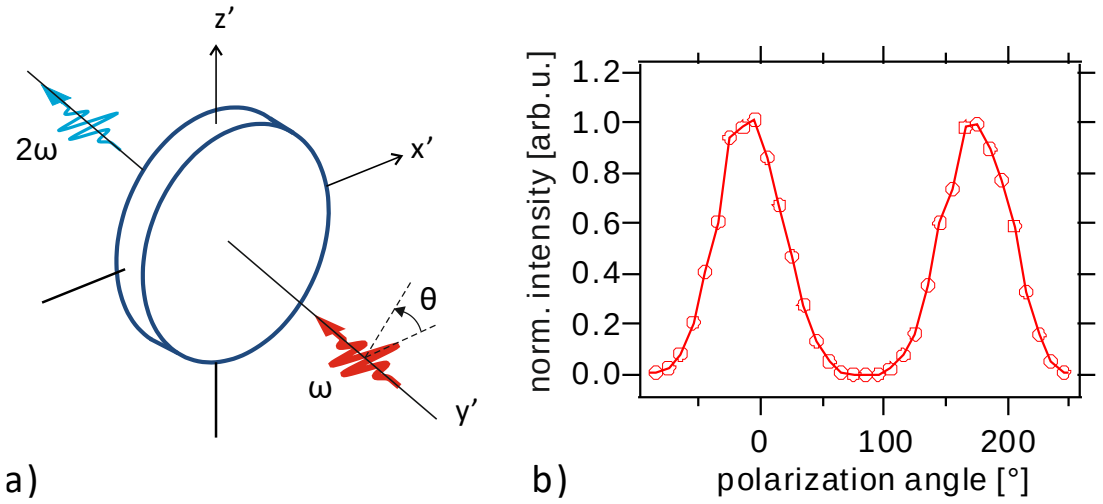

Figure 8.1: (a) Schematic of quartz SHG. x′, y′ and z' indicate the crystal Coordinate system with z' being the optical axis. (b) Polarization dependent quartz SHG.

In the present thesis, a quartz reference channel is employed to determine the nonlinear surface susceptibility. The reference channel was adapted from [143]. The optical path can be found in Figure 4.17, Chapter 4.4. A y-cut wedge quartz plate (1.2 mm thick with a wedge angle of 0.8 °, from Korth Kristalle GmbH) was built in the reference channel.

In principle, SHG from a quartz crystal is a three wave mixing process. This process is often classified as *Type 0* SHG, that means two extraordinary wave generate a third extraordinary wave. The SH field generated from a quartz plate can be expressed as [144]:

$$\boldsymbol{P}_{2\omega} = \begin{pmatrix} d_{11} & -d_{11} & 0 & d_{14} & 0 & 0 \\ 0 & 0 & 0 & 0 & -d_{14} & -2d_{11} \\ 0 & 0 & 0 & 0 & 0 & 0 \end{pmatrix} \begin{pmatrix} E_x^2 \\ E_y^2 \\ E_z^2 \\ E_y E_z \\ E_x E_z \\ E_x E_y \end{pmatrix} \tag{8.1}$$

$$\boldsymbol{P}_{2\omega} = \begin{pmatrix} d_{11}\left(E_{x'}^2 - E_{y'}^2\right) \\ -2d_{11}E_{x'}E_{y'} \\ 0 \end{pmatrix} \tag{8.2}$$

Where by the induced SH field $\boldsymbol{P}_{2\omega}$ depends only on the susceptibility element d_{11} and the fundamental field. Therefore, the radiated SHG intensity in the x′ axis is:

$$I_{2\omega}^{x} = R_{Quartz} \cdot (I_{\omega}^{x})^2 \tag{8.3}$$

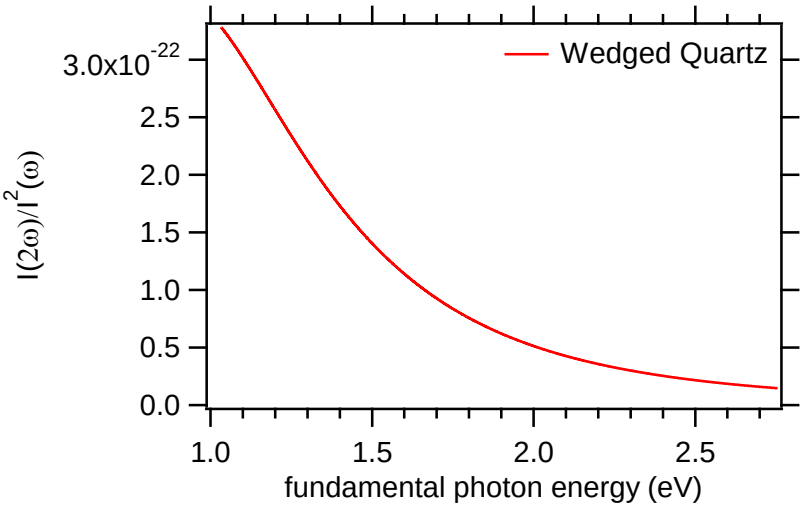

Figure 8.2: Wedged Quartz SHG reference. Calculated ratio of SHG intensity to square of fundamental based on the refractive index of alpha quartz from [190].

As depicted in Figure 8.1 (a), the fundamental beam and the second harmonic beam both have a polarization parallel to the crystal axis x′. The x′ axis was calibrated by varying the polarization angle of the fundamental beam, see Figure 8.1 (b). In (8.3), the reference factor R_{Quartz} defined as [145, 146]:

$$R_{Quartz} = \frac{(8\pi)^3}{c(n_\omega^2 - n_{2\omega}^2)^2} \cdot d_{11}^2 \cdot t'^4_\omega \cdot T''_{2\omega} \tag{8.4}$$

$$t'_\omega = \frac{2}{n_\omega + 1} \tag{8.5}$$

$$T''_{2\omega} = 2n_{2\omega} \frac{(n_\omega + 1)(n_{2\omega} + n_\omega)}{(n_{2\omega} + 1)^3} \tag{8.6}$$

Where t'_ω denotes the Fresnel factor and $T''_{2\omega}$ indicates the transmission factor for the SH-field. According to Miller's rule [144], the nonlinear susceptibility of a piezoelectric crystal can be coupled to the linear susceptibilities:

$$\chi_{ijk}^{(2)}(\omega) = \chi_{ii}^{(1)}(2\omega) \cdot \chi_{jj}^{(1)}(\omega) \cdot \chi_{kk}^{(1)}(\omega) \cdot \delta_{ijk} \tag{8.7}$$

Then the tensor element d_{11} can be determined with the equation:

$$d_{11}^{(cgs)} = \frac{3 \cdot 10^4}{4\pi} \epsilon_0 \delta_{11}^{(SI)} (n_{2\omega}^2 - 1)(n_\omega^2 - 1)^2 \tag{8.8}$$

With the factor $\delta_{11}^{(SI)} = 2.2 \times 10^{-2}\ m^2/c$ [189], ϵ_0 represents the vacuum permittivity and n indicates the refractive index of alpha quartz. The conversion factor from SI to *cgs*-unit is:

$$[1\ V^{-1}m] = \left[3 \times \frac{10^4}{4\pi} (erg\ cm^{-3})^{-\frac{1}{2}}\right] \tag{8.9}$$

Together with equation (8.4 – 8.9), the SH spectral dependence of quartz crystal i.e. reference factor $R_{Quartz} = I(2\omega)/I^2(\omega)$ can be calculated. As depicted in Figure 8.2, R_{Quartz} shows a fairly smooth and continuous dependence in the visible wavelength range (1.7 – 2.5 eV).

B: Fitting procedure

In the following, the fitting procedure used in Chapter 6.2 is introduced. The transient SHG response to an extreme short laser pulse (like a delta function in the time domain) is assumed to be a step function, which consists of (i) a constant value before the sample is interacting with the light and (ii) an exponential decay with the relaxation time constant τ_0:

$$f(x) = \begin{cases} 0, & x < 0 \\ A_0 \cdot \exp\left(-\frac{x}{\tau_0}\right), & x \geq 0 \end{cases} \tag{8.1}$$

Where the parameter A_0 indicates the pump induced change at $x = 0$. In reality, this instantons response is induced and probed by laser pulses with finite pulse duration. The correlation between the pump and the probe pulses is characterized by a Gaussian function:

$$g(x) = \frac{2}{B_0}\sqrt{\frac{ln2}{\pi}} \cdot \exp\left[-\left(\frac{2\sqrt{ln2}}{B_0} \cdot x\right)^2\right] \tag{8.2}$$

Here, B_0 represents the FWHM of the pump-probe correlation. Hence, the response of the system can be described by a convolution between *f* and *g*:

$$F(t) = (f * g)(t) \tag{8.3}$$

In Chapter 6, we have used the function $F(t)$ to fit the experimental pump-probe SHG data, see Figure 6.9 and 6.12. Only A_0 and τ_0 were set as free parameters, B_0 was experimentally determined through surface XC measurement.

C: Additional data of FROG retrieval

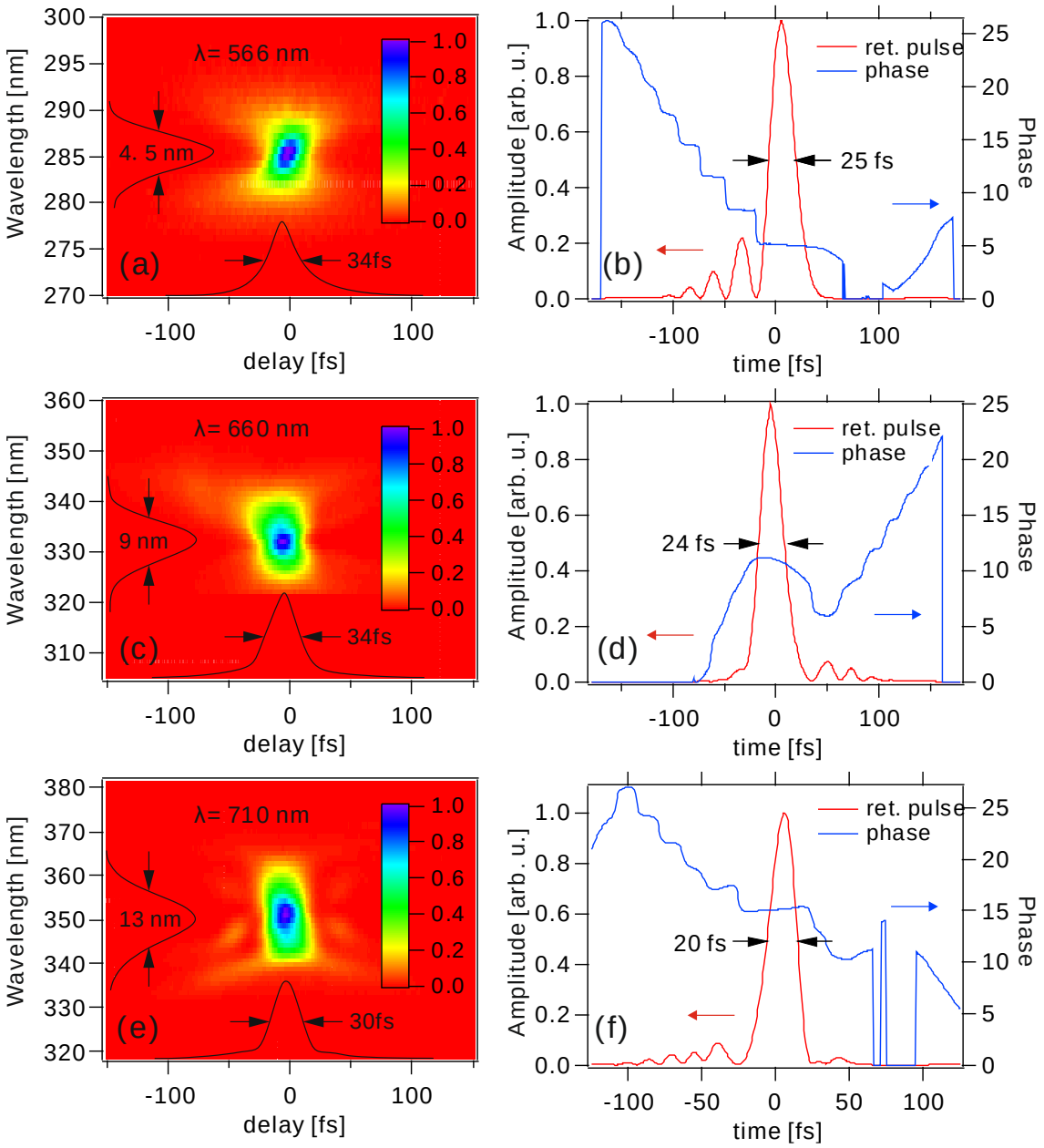

Figure 8.3: FROG measurements (a, c, d) and the corresponding retrieval pulses (b, d, f) at 566 nm, 660 nm and 710 nm. The NOPA pulse was compresses via UVFS prism pair.

Literature

[1] M. Dayarathna, Y. Wen, and R. Fan. Data Center Energy Consumption Modeling: A Survey. *IEEE Communications Surveys & Tutorials* **18**, 732 (2016).

[2] Wikipedia, https://en.wikipedia.org/wiki/Valdemar_Poulsen

[3] B. Hillebrands and K. Ounadjela. Spin dynamics in confined magnetic structures I. Springer, Berlin (2002).

[4] P. Grünberg, R. Schreiber, Y. Pang, M. B. Brodsky, and H. Sowers. Layered Magnetic Structures: Evidence for Antiferromagnetic Coupling of Fe Layers across Cr Interlayers. *Phys. Rev. Lett*. **57**, 2442 (1986).

[5] J. S. Moodera, Lisa R. Kinder, Terrilyn M. Wong, and R. Meservey. Large Magnetoresistance at Room Temperature in Ferromagnetic Thin Film Tunnel Junctions. *Phys. Rev. Lett*. **74**, 3273 (1995).

[6] A. Kirilyuk, A. V. Kimel, and T. Rasing. Ultrafast optical manipulation of magnetic order. *Rev. Mod. Phys.* **82**, 273 (2010).

[7] I. Tudosa, C. Stamm, A. Kashuba, F. King, H. Siegmann, J. Stöhr, G. Ju, B. Lu, and D. Weller. The ultimate speed of magnetic switching in granular recording media. *Nature* **428**, 831 (2004).

[8] S. Iwasaki. Discoveries that guided the beginning of perpendicular magnetic recording. *J. Magn. Magn. Matter*. **226**, 277 (2001).

[9] C. Chappert, A. Fert, and F. N. Dau. The emergence of spin electronics in data storage. *Nat. Mater.* **6**, 813 (2007).

[10] K. Carva. Give it a whirl. *Nature Phys.* **10**, 552 (2014).

[11] E. Beaurepaire, J.-C. Merle, A. Daunois, and J.-Y. Bigot. Ultrafast Spin Dynamics in Ferromagnetic Nickel. *Phys. Rev.* Lett. **76**, 4250 (1996).

[12] G. Malinowski, F. Dalla Longa, J. H. H. Rietjens, P. V. Paluskar, R. Huijink, H. J. M. Swagten, and B. Koopmans. Control of speed and efficiency of ultrafast demagnetization by direct transfer of spin angular momentum. *Nat. Phys.* **4**, 855 (2008).

[13] A. Schellekens, K. Kuiper, R. de Wit, and B. Koopmans. Ultrafast spin-transfer torque driven by femtosecond pulsed-laser excitation. *Nature Commun.* **5**, 4333 (2014).

[14] G. Choi, B. Min, K. Lee, and D. G. Cahill. Spin current generated by thermally driven ultrafast demagnetization. *Nature Commun.* **5**, 4334 (2014).

[15] R.-P. Pan, H. D. Wei, and Y. R. Shen, Optical second-harmonic generation from magnetized surfaces. *Phys. Rev. B* **39**, 1229 (1989).

[16] K. Bennenmann. Nonlinear optics in metals. Clarendon press Oxford (1998).

[17] M. Battiato, K. Carva, and P. M. Oppeneer. Superdiffusive Spin Transport as a Mechanism of Ultrafast Demagnetization. *Phys. Rev. Lett.* **105**, 027203 (2010).

[18] J. Chen, J. Wieczorek, A. Eschenlohr, S. Xiao, A. Tarasevitch, and U. Bovensiepen. Ultrafast inhomogeneous magnetization dynamics analyzed by interface-sensitive nonlinear magneto-optics. *Appl. Phys. Lett.* **110**, 092407 (2017).

[19] J. Chen, U. Bovensiepen, A. Eschenlohr, T. Müller, P. Elliott, E. K. U. Gross, J. K. Dewhurst, and S. Sharma. Competing spin transfer and dissipation at Co/Cu(001) interfaces on femtosecond timescales. *Phys. Rev. Lett*. **122**, 067202 (2019).

[20] J. Moodera, B. Koopmans, and P. Oppeneer. On the path toward organic spintronics. *MRS Bulletin*, **39**, 578 (2014).

[21] K. Raman, A. Kamerbeek, A. Mukherjee, et al. Interface-engineered templates for molecular spin memory devices. *Nature* **493**, 509 (2013).

[22] H. Wende, M. Bernien, J. Luo, et al. Substrate-induced magnetic ordering and switching of iron porphyrin molecules. *Nature Mater.* **6**, 516 (2007).

[23] U. Bovensiepen and P. Kirchmann. Elementary relaxation processes investigated by femtosecond photoelectron spectroscopy of two-dimensional materials. *Laser & Photonics Reviews*, **6**, 589 (2012).

[24] M. Fox. Optical Properties of Solids. *Oxford University Press* (2010).

[25] B. Rethfeld, K. Sokolowski-Tinten, D. von der Linde, and S.I. Anisimov. Time-scales in the response of materials to femtosecond laser excitation. *Appl. Phys. A* **79**, 767 (2004).

[26] J. Hohlfeld, S. Wellershoff, J. Güdde, U. Conrad, V. Jähnke, and E. Matthias. Electron and lattice dynamics following optical excitation of metals. *Chem. Phys.* **251**, 237 (2000).

[27] N. W. Ashcroft and K. Sturm. Interband Absorption and the Optical Properties of Polyvalent Metals. *Phys. Rev. B* **3**, 1898 (1971).

[28] D. Fisher, M. Fraenkel, Z. Henis, E. Moshe, and S. Eliezer. Interband and intra-band (Drude) contributions to femtosecond laser absorption in aluminum. *Phys. Rev. E* **65**, 016409 (2001).

[29] C.-K. Sun, F. Vallée, L. H. Acioli, E. P. Ippen, and J. G. Fujimoto. Femtosecond-tunable measurement of electron thermalization in gold. *Phys. Rev. B* **50**, 15337 (1994).

[30] D. F. Price, R. M. More, R. S. Walling, G. Guethlein, R. L. Shepherd, R. E. Stewart, and W. E. White. Absorption of Ultrashort Laser Pulses by Solid Targets Heated Rapidly to Temperatures 1–1000 eV. *Phys. Rev. Lett.* **75**, 252 (1995).

[31] A. Borisov, D. Sánchez-Portal, R. Díez Muiño, and P. M. Echenique, Building up the screening below the femtosecond scale. *Chem. Phys. Lett*. **387**, 95 (2004).

[32] H. Petek and S. Ogawa. Femtosecond time-resolved two-photon photoemission studies of electron dynamics in metals. *Prog. Surf. Sci.* **56**, 239 (1997).

[33] X. Shen, Y. Timalsina, T. Lu, and M. Yamaguchi. Experimental study of electron-phonon coupling and electron internal thermalization in epitaxially grown ultrathin copper films. *Phys. Rev. B* **91**, 045129 (2015).

[34] N. Del Fatti, C. Voisin, M. Achermann, S. Tzortzakis, D. Christofilos, and F. Vallée. Nonequilibrium electron dynamics in noble metals. *Phys. Rev. B* **61**, 16956 (2000).

[35] J. Hohlfeld, E. Matthias, R. Knorren, and K. H. Bennemann. Nonequilibrium Magnetization Dynamics of Nickel. *Phys. Rev. Lett*. **78**, 4861 (1997).

[36] L. Rettig. PhD thesis: Ultrafast Dynamics of Correlated Electrons. (2012)

[37] J. Quinn. Range of excited electrons in metals. *Phys. Rev.* **126**, 1453 (1962).

[38] P. Nozieres and D. Pines. The theory of quantum liquids. *Benjamin* New York, (1966).

[39] C. Suárez, W. E. Bron, and T. Juhasz. Dynamics and Transport of Electronic Carriers in Thin Gold Films. *Phys. Rev. Lett.* **75**, 4536 (1995).

[40] T. Juhasz, H. E. Elsayed-Ali, G. O. Smith, C. Suárez, and W. E. Bron. Direct measurements of the transport of nonequilibrium electrons in gold films with different crystal structures. *Phys. Rev. B* **48**, 15488 (1993).

[41] J. Hohlfeld, J. Müller, S. Wellershoff, and E. Matthias. Time-resolved thermoreflectivity of thin gold films and its dependence on film thickness. *Appl. Phys. B* **64**, 387 (1997).

[42] N.W. Ashcroft and N.D. Mermin. Solid State Physics, 1st ed. *Saunders College Publishing, Philadelphia*, (1976).

[43] M. Aeschlimann, M. Bauer, S. Pawlik, W. Weber, R. Burgermeister, D. Oberli, and H.C. Siegman. Ultrafast spin-dependent electron dynamics in fcc Co. *Phys. Rev. Lett.* **79**, 5158 (1997).

[44] O. B. Wrighta and V. E. Gusev. Ultrafast acoustic phonon generation in gold. *Physica B* **219**, 770 (1996).

[45] F. Budde, T. F. Heinz, M. M. T. Loy, J. A. Misewich, F. de Rougemont, and H. Zacharias. Femtosecond time-resolved measurement of desorption. *Phys. Rev. Lett*. **66**, 3024 (1991).

[46] S. D. Brorson, A. Kazeroonian, J. S. Moodera, D. W. Face, T. K. Cheng, E. P. Ippen, M. S. Dresselhaus, and G. Dresselhaus. Femtosecond room temperature measurement of the electron-phonon coupling constant γ in metallic superconductors. *Phys. Rev. Lett*. **64**, 2172 (1990).

[47] S. I. Anisimov, B. L. Kapeliovich, and T. L. Perelman, Electron emission from metal surfaces exposed to ultrashort laser pulses. *Sov. Phys. JETP* **39**, 375 (1974).

[48] E. Carpene, E. Mancini, C. Dallera, M. Brenna, E. Puppin, and S. De Silvestri. Dynamics of electron-magnon interaction and ultrafast demagnetization in thin iron films. *Phys. Rev. B* **78**, 174422 (2008).

[49] M. Haag, C. Illg, and M. Fähnle. Role of electron-magnon scatterings in ultrafast demagnetization. *Phys. Rev. B* **90**, 014417 (2014).

[50] A. Vaterlaus, T. Beutler, and F. Meier. Spin-lattice relaxation time of ferromagnetic gadolinium determined with time-resolved spin-polarized photoemission. *Phys. Rev. Lett.* **67**, 3314 (1991).

[51] A. Vaterlaus, T. Beutler, D. Guarisco, M. Lutz, and F. Meier. Spin-lattice relaxation in ferromagnets studied by time-resolved spin-polarized photoemission. *Phys. Rev. B* **46**, 5280 (1992).

[52] B. Koopmans, G. Malinowski, F. Dalla Longa, D. Steiauf, M. Fähnle, T. Roth, M. Cinchetti, and M. Aeschlimann. Explaining the paradoxical diversity of ultrafast laser-induced demagnetization. *Nat. Mater.* **9**, 259 (2010).

[53] A. Scholl, L. Baumgarten, R. Jacquemin, and W. Eberhardt. Ultrafast Spin Dynamics of Ferromagnetic Thin Films Observed by fs Spin-Resolved Two-Photon Photoemission. *Phys. Rev. Lett.* **79**, 5146 (1997).

[54] U. Conrad, J. Güdde, V. Jähnke, E. Matthias. Ultrafast electron and magnetization dynamics of thin Ni and Co films on Cu(001) observed by time-resolved SHG. *Appl. Phys. B* **68**, 511–517 (1999).

[55] J. Güdde, U. Conrad, V. Jähnke, J. Hohlfeld, and E. Matthias. Magnetization dynamics of Ni and Co films on Cu(001) and of bulk nickel surfaces. *Phys. Rev. B* **59**, R6608 (1999).

[56] B. Koopmans, M. van Kampen, J. T. Kohlhepp, and W. J. M. de Jonge. Ultrafast Magneto-Optics in Nickel: Magnetism or Optics? *Phys. Rev. Lett.* **85**, 844 (2000).

[57] H. Regensburger, R. Vollmer, and J. Kirschner. Time-resolved magnetization-induced second-harmonic generation from the Ni(110) surface. *Phys. Rev. B* **61**, 14716 (2000).

[58] L. Guidoni, E. Beaurepaire, and J.-Y. Bigot. Magneto-optics in the Ultrafast Regime: Thermalization of Spin Populations in Ferromagnetic Films. *Phys. Rev. Lett.* **89**, 017401 (2002).

[59] J.-Y. Bigot, L. Guidoni, E. Beaurepaire, and P. N. Saeta. Femtosecond Spectrotemporal Magneto-optics. *Phys. Rev. Lett.* **93**, 077401 (2004).

[60] J. Wieczorek, A. Eschenlohr, B. Weidtmann, M. Rösner, N. Bergeard, A. Tarasevitch, T. O. Wehling, and U. Bovensiepen. Separation of ultrafast spin currents and spin-flip scattering in Co/Cu(001) driven by femtosecond laser excitation employing the complex magneto-optical Kerr effect. *Phys. Rev. B* **92**, 174410 (2015).

[61] A. B. Schmidt, M. Pickel, M. Donath, P. Buczek, A. Ernst, V.P. Zhukov, P.M.Echenique, L.M. Sandratskii, E.V. Chulkov, and M. Weinelt. Ultrafast magnon generation in an Fe film on Cu(100). *Phys. Rev. Lett.* **105**, 197401 (2010).

[62] A. B. Schmidt, M. Pickel, T. Allmers, M. Budke, J. Braun, M. Weinelt, and M. Donath. Surface electronic structure of fcc Co films: a combined spin-resolved one- and two-photon-photoemission study. *J. Phys. D: Appl. Phys.* **41**, 164003 (2008).

[63] C. Stamm, T. Kachel, N. Pontius, R. Mitzner., T. Quast, K. Holldack, S. Khan, C. Lupulescu, E. F. Aziz, M. Wietstruk, H.A. Dürr, and W. Eberhardt. Femtosecond modication of electron localization and transfer of angular momentum in nickel. *Nature Mater.* **6**, 740 (2007).

[64] C. Stamm, N. Pontius, T. Kachel, M. Wietstruk, and H.A. Dürr. Femtosecond x-ray absorption spectroscopy of spin and orbital angular momentum in photoexcited Ni films during ultrafast demagnetization. *Phys. Rev. B* **81**, 104425 (2010).

[65] G. P. Zhang, W. Hübner, G. Lefkidis, Y. Bai, and T. F. George. Paradigm of the time-resolved magneto-optical Kerr effect for femtosecond magnetism. *Nature Phys*. **5**, 499 (2009).

[66] S. Eich, M. Plötzing, M. Rollinger, S. Emmerich, R. Adam, Cong. Chen, C. Kapteyn, M. Murnane, L. Plucinski, D. Steil, B. Stadtmüller, M. Cinchetti, M. Aeschlimann, C. M. Schneider, and S. Mathias. Band structure evolution during the ultrafast ferromagnetic-paramagnetic phase transition in cobalt. *Sci. Adv*. **3** 160209 (2017).

[67] J. Kim, K. Lee, J. Jeong, and S. Shin. Ultrafast spin demagnetization by non-thermal electrons of TbFe alloy film. *Appl. Phys. Lett*. **94**, 192506 (2009).

[68] K. Carva, M. Battiato, D. Legut, and P.M. Oppeneer. Ab initio theory of electron-phonon mediated ultrafast spin relaxation of laser-excited hot electrons in transition-metal ferromagnets. *Phys. Rev. B* **87**, 184425 (2013).

[69] G. P. Zhang and W. Hübner. Laser-induced ultrafast demagnetization in ferro-magnetic metals. *Phys. Rev. Lett.* **85**, 3025 (2000).

[70] J. Bigot, M. Vomir, and E. Beaurepaire. Coherent ultrafast magnetism induced by femtosecond laser pulses. *Nature Phys.* **5**, 515 (2009).

[71] U. Bovensiepen. Magnetism in step with light. *Nature Phys.* **5**, 461 (2009).

[72] K. Vahaplar, A. M. Kalashnikova, A. V. Kimel, D. Hinzke, U. Nowak, R. Chantrell, A. Tsukamoto, A. Itoh, A. Kirilyuk, and Th. Rasing. Ultrafast Path for Optical Magnetization Reversal via a Strongly Nonequilibrium State. *Phys. Rev. Lett.* **103**, 117201 (2009).

[73] U. Atxitia, O. Chubykalo-Fesenko, J. Walowski, A. Mann, and M. Münzenberg. Evidence for thermal mechanisms in laser-induced femtosecond spin dynamics. *Phys. Rev. B* **81**, 174401 (2010).

[74] U. Atxitia, O. Chubykalo-Fesenko, N. Kazantseva, D. Hinzke, U. Nowak, and R. W. Chantrell, Micromagnetic modeling of laser-induced magnetization dynamics using the Landau-Lifshitz-Bloch equation. *Appl. Phys. Lett*. **91**, 232507 (2007).

[75] N. Kazantseva, D. Hinzke, U. Nowak, R. W. Chantrell, U. Atxitia, and O. Chubykalo-Fesenko. Towards multiscale modeling of magnetic materials: Simulations of FePt. *Phys. Rev. B* **77**, 184428 (2008).

[76] I. Radu, K. Vahaplar, C. Stamm, T. Kachel, N. Pontius, H. A. Durr, T. A. Ostler, J. Barker, R. F. L. Evans, R. W. Chantrell, A. Tsukamoto, A. Itoh, A. Kirilyuk, T. Rasing, and A. V. Kimel, Transient ferromagnetic-like state mediating ultrafast reversal of antiferromagnetically coupled spins. *Nature* **472**, 205 (2011).

[77] M. Krauss, T. Roth, S. Alebrand, D. Steil, M. Cinchetti, M. Aeschlimann, and H. C. Schneider. Ultrafast demagnetization of ferromagnetic transition metals: The role of the Coulomb interaction. *Phys. Rev. B* **80**, 180407 (2009).

[78] B. Koopmans, J. J.M. Ruigrok, F. D. Longa, and W. J.M. de Jonge. Unifying ultrafast magnetization dynamics. *Phys. Rev. Lett*. **95**, 267207 (2005).

[79] R. J. Elliott. Theory of the Effect of Spin-Orbit Coupling on Magnetic Resonance in Some Semiconductors. *Phys. Rev.* **96**, 266 (1954).

[80] K. Carva, M. Battiato, and P. M. Oppeneer. *Ab Initio* Investigation of the Elliott-Yafet Electron-Phonon Mechanism in Laser-Induced Ultrafast Demagnetization. *Phys. Rev. Lett.* **107**, 207201 (2011).

[81] M. Battiato, K. Carva, and P. M. Oppeneer. Theory of laser-induced ultrafast superdiffusive spin transport in layered heterostructures. *Phys. Rev. B* **86**, 024404 (2012).

[82] A. Melnikov, I. Razdolski, T. O. Wehling, E. T. Papaioannou, V. Roddatis, P. Fumagalli, O. Aktsipetrov, A. I. Lichtenstein, and U. Bovensiepen. Ultrafast Transport of Laser-Excited Spin-Polarized Carriers in Au/Fe/MgO(001). *Phys. Rev. Lett.* **107**, 076601 (2011).

[83] E. Turgut, C. La-o vorakiat, J. M. Shaw, P. Grychtol, H. T. Nembach, D. Rudolf, R. Adam,M. Aeschlimann, C. M. Schneider, T. J. Silva, M. M. Murnane, H. C. Kapteyn, and S. Mathias. Controlling the Competition between Optically Induced Ultrafast Spin-Flip Scattering and Spin Transport in Magnetic Multilayers. *Phys. Rev. Lett.* **110**, 197201 (2013).

[84] A. Eschenlohr, M. Battiato, P. Maldonado, N. Pontius, T. Kachel, K. Holldack, R. Mitzner, A. Fhlisch, P.M. Oppeneer, and C. Stamm. Ultrafast spin transport as key to femtosecond demagnetization. *Nature Mater.* **12**, 332 (2013).

[85] K. Krieger, J. K. Dewhurst, P. Elliott, S. Sharma, and E. K.U. Gross. Laser-Induced Demagnetization at Ultrashort Time Scales: Predictions of TDDFT. *J. Chem. Theory Comput.* **11**, 4870 (2015).

[86] W. Töws and G. M. Pastor. Many-Body Theory of Ultrafast Demagnetization and Angular Momentum Transfer in Ferromagnetic Transition Metals. *Phys. Rev. Lett*. **115**, 217204 (2015).

[87] C. Dornes, Y. Acremann, M. Savoini, M. Kubli, M. J. Neugebauer, E. Abreu, L. Huber, G. Lantz, C. A. F. Vaz, H. Lemke, E. M. Bothschafter, M. Porer, V. Esposito, L. Rettig, M. Buzzi, A. Alberca, Y. W. Windsor, P. Beaud, U. Staub, Diling Zhu, Sanghoon Song, J. M. Glownia and S. L. Johnson. The ultrafast Einstein–de Haas effect. *Nature* **565**, 209 (2019).

[88] Erich Runge and E. K. U. Gross. Density-Functional Theory for Time-Dependent Systems. *Phys. Rev. Lett*. **52**, 997 (1984).

[89] G. Malinowski, F. Dalla Longa, J. H. H. Rietjens, P. V. Paluskar, R. Huijink, H. J. M. Swagten, and B. Koopmans. Control of speed and efficiency of ultrafast demagnetization by direct transfer of spin angular momentum. *Nature Phys*. **4**, 855 (2008).

[90] D. Rudolf, C. La-O-Vorakiat, M. Battiato, R. Adam, J. M. Shaw, E. Turgut, P. Maldonado, S. Mathias, P. Grychtol, H. T. Nembach et al. Ultrafast magnetization enhancement in metallic multilayers driven by superdiffusive spin current. *Nature Commun*. **3**, 1037 (2012).

[91] V. P. Zhukov, E. V. Chulkov, and P. M. Echenique. Lifetimes and inelastic mean free path of low-energy excited electrons in Fe, Ni, Pt, and Au: Ab initio GW+T calculations. *Phys. Rev. B* **73**, 125105 (2006).

[92] V. P. Zhukov, E. V. Chulkov, and P. M. Echenique. Lifetimes of Excited Electrons in Fe and Ni: First-Principles GW and the T-Matrix Theory. *Phys. Rev. Lett*. **93**, 096401 (2004).

[93] K. Uchida, S. Takahaschi, K. Harii, J. Ieda, W. Koshibae, K. Ando, S. Maekawa, and E. Saitoh. Observation of the spin Seebeck effect. *Nature* **455**, 778 (2008).

[94] A. Alekhin, I. Razdolski, N. Ilin, J. Meyburg, D. Diesing, V. Roddatis, I. Rungger, M. Stamenova, S. Sanvito, U. Bovensiepen, and A. Melnikov. Femtosecond Spin Current Pulses Generated by the Nonthermal Spin-Dependent Seebeck Effect and Interacting with Ferromagnets in Spin Valves. *Phys. Rev. Lett*. **119**, 017202 (2017).

[95] G. Choi, C. Moon, B. Min, K. Lee, and D. G. Cahill. Thermal spintransfer torque driven by the spin-dependent Seebeck effect in metallic spinvalves. *Nat. Phys*. **11**, 576 (2015).

[96] K. Krieger, P. Elliott, T. Müller, N. Singh, J. K. Dewhurt, E. K. U. Gross, and S Sharma. Ultrafast demagnetization in bulk versus thin films: an *ab initio* study. *J. Phys. Condens. Matter* **29**, 224001 (2017).

[97] P. V. Kamat. Photochemistry on nonreactive and reactive (semiconductor) surfaces. *Chem. Rev.* **93**, 267 (1993).

[98] A. Linsebigler, G. Lu, and J. Yates. Photocatalysis on Ti02 Surfaces: Principles, Mechanisms, and Selected Results. *Chem. Rev.* **95**, 735 (1995).

[99] H. Guo. P. Saalfrank and T. Seidemann. Theory of photoinduced surface reactions of admolecules. Prog. Surf. Sci. **62**, 239 (1999).

[100] M. Gratzel. Dye-sensitized solid-state heterojunction solar cells. *MRS Bull*. **30**, 23. (2005).

[101] M. Galbiati, S. Tatay, C. Barraud, A. Dediu, F. Petroff, R. Mattana, and P. Seneor. Spinterface: Crafting spintronics at the molecular scale. *MRS Bull*. **39**, 602 (2014).

[102] A. Hotzel, G. Moos, K. Ishioka, M. Wolf, and G. Ertl. Femtosecond electron dynamics at adsorbate–metal interfaces and the dielectric continuum model. *Appl. Phys. B* **68**, 615 (1999).

[103] A. Hotzel, K. Ishioka, E. Knoesel, M. Wolf, and G. Ertl. Can we control lifetimes of electronic states at surfaces by adsorbate resonances? *Chem. Phys. Lett.* **285**, 271 (1998).

[104] M. Perrin, C. Verzijl, C. Martin, A. Shaikh, R. Eelkema, J. van Esch, J. van Ruitenbeek, J. Thijssen, H. van der Zant, and D. Dulić. Large tunable image-charge effects in single-molecule junctions. *Nat. Nanotechnol*. **8**, 282 (2013).

[105] A. Zangwill. Physics at Surfaces. *Cambridge University Press* (1988).

[106] C. Lindstrom and X. Zhu. Photoinduced electron transfer at molecule-metal interfaces. *Chem. Rev.* **106**, 4281 (2006).

[107] H. Petek. Photoexcitation of adsorbates on metal surfaces: One-step or three-step. J. Chem. Phys. **137**, 091704 (2012).

[108] U. Höfer, I. Shumay, Ch. Reuß, U. Thomann, W. Wallauer, and Th. Fauster. Time-resolved coherent photoelectron spectroscopy of quantized electronic states on metal surfaces. *Science* **277**, 1480 (1997).

[109] Ch. Reuß, I. Shumay, U. Thomann, M. Kutschera, M. Weinelt, Th. Fauster, and U. Höfer. Control of the dephasing of image-potential states by CO adsorption on Cu(100). *Phys. Rev. Lett.* **82**, 153 (1999).

[110] J. Lee, S. Ryu, J. Chang, S. Kim, and S. Kim. Direct observation of an intermediate state for a surface photochemical reaction initiated by hot electron Transfer. *J. Phys. Chem. B* **109**, 14481 (2005).

[111] G. Walker, P. Barbara, S. Doom, Y. Dong, and J. Hupp. Ultrafast measurements on direct photo-induced electron transfer in a mixed-valence complex. *J. Phys. Chem*. **95**, 5712 (1991).

[112] K. Kott, D. Higgins, R. McMahon, and R. Corn. Observation of photoinduced electron transfer at a liquid-liquid interface by optical second harmonic generation. *J. Am. Chem. Soc.* **115**, 5342-5343 (1993).

[113] X. Su, P. Cremer, Y. Shen, and G. Somorjai. High-pressure CO oxidation on Pt(111) monitored with infrared-visible sum frequency generation (SFG). *J. Am. Chem. Soc.* **119**, 3994 (1997).

[114] W. Auwarter, D. Ecija, F. Klappenberger, and J. V. Barth. Porphyrins at interfaces. *Nature Chem* **7**, 105 (2015).

[115] J. Zeng and K. Chen. Spin filtering, magnetic and electronic switching behaviors in manganese porphyrin-based spintronic devices. *J. Mater. Chem. C* **1**, 4014 (2013).

[116] H. C. Herper, M. Bernien, S. Bhandary, C. F. Hermanns, A. Krüger, J. Miguel, C. Weis, C. Schmitz-Antoniak, B. Krumme, D. Bovenschen, C. Tieg, B. Sanyal, E. Weschke, C. Czekelius, W. Kuch, H. Wende, and O. Eriksson. Iron porphyrin molecules on Cu(001): Influence of adlayers and ligands on the magnetic properties. *Phys. Rev. B* **87**, 174425 (2013).

[117] P. A. Franken, A. E. Hill, C. W. Peters, and G. Weinreich. Generation of Optical Harmonics. *Phys. Rev. Lett*. **7**, 118 (1961).

[118] Y. R. Shen. The Principles of Nonlinear Optics. *Wiley-Interscience*, John Wiley and Sons, 1st edition (1984).

[119] R. R. Birss. Symmetry and magnetism. *North-Holland Publishing Company*, 2nd edition, (1966).

[120] R. W. Boyd. Nonlinear optics. *Academic Press*, Boston, 1. Auflage (1992).

[121] M. Henzler and W. Göpel. Oberflächenphysik des Festkörpers. B. G. Teubner, Stuttgart, 1. Auflage (1991).

[122] J. E. Sipe, D. J. Moss, and H. M. van Driel. Phenomenological theory of optical second- and third-harmonic generation from cubic centrosymmetric crystals. *Phys. Rev. B* **35**, 1129 (1987).

[123] U. Conrad, J. Güdde, V. Jähnke, and E. Matthias. Phase effects in magnetic second-harmonic generation on ultrathin Co and Ni films on Cu(001). *Phys. Rev. B* **63**, 144417 (2001).

[124] A. Melnikov, J. Güdde, and E. Matthias. Demagnetization following optical excitation in nickel and permalloy films. *Appl. Phys. B* **74**, 735 (2002).

[125] I. Radu. PhD thesis: Ultrafast electron, lattice and spin dynamics on rare-earth metal surfaces. (2006)

[126] U. Conrad. PhD thesis: Statische und dynamische Untersuchungen ultradünner Metallfilme mit optischer Frequenzverdopplung und nichtlineare Mikroskopie. (1999).

[127] H. Li and B. P. Tonner. Structure and growth mode of metastable fcc cobalt ultrathin films on Cu(001) as determined by angle-resolved x-ray photoemission scattering. *Surface Science* **237**, 141 (1990).

[128] J. J. de Miguel, A. Cebollada, J. M. Gallego, R. Miranda, C. M. Schneider, P. Schuster, and J. Kirschner. Influence of the growth conditions on the magnetic properties of fcc cobalt films: from monolayers to superlattices. *J. Magn. Magn. Mater*. **93**, 1 (1991).

[129] O. NanoTechnology, Instruction Manual UHV Evaporator EFM 2/3/3s/4.

[130] W. P. de Boeij. PhD thesis: Ultrafast solvation dynamics explored by nonlinear optical spectroscopy. University of Groningen, (1997).

[131] A. E. Siegman, Lasers (University Science, Mill Valey, Calif.), Chap. 14 and 19 (1986).

[132] M. Piché and F. Salin. Self-mode locking of solid-state lasers without apertures. *Opt. Lett*. **18**, 1041 (1993).

[133] M. Sultan, U. Atxitia, A. Melnikov, O. Chubykalo-Fesenko, and U. Bovensiepen. Electron- and phonon-mediated ultrafast magnetization dynamics of Gd(0001). *Phys. Rev. B* **85**, 184407 (2012).

[134] D. Strickland and G. Mourou. Compression of amplified chirped optical pulses. *Opt. Commun.* **56**, 219 (1985).

[135] G. Cerullo and S. De Silvestri. Ultrafast optical parametric amplifiers. *Rev. Sci. Instrum.* **74**, 1 (2003).

[136] D. Wegkamp. Diplomarbeit: Schnelle Elektronendynamiken an Grenzflächen untersucht mit einer NOPA-basierenden Femtosekunden-Lichtquelle. FU Berlin, (2009).

[137] T. J. Driscoll, G. M. Gale, and F. Hache. Ti:sapphire second-harmonic-pumped visible range femtosecond optical parametric oscillator. *Opt. Commun.* **110**, 638 (1994).

[138] T. Wilhelm, J. Piel, and E. Riedle. Sub-20-fs pulses tunable across the visible from a blue-pumped single-pass noncollinear parametric converter. *Opt. Lett.* **22**, 1494 (1997).

[139] J. Piel, E. Riedle, L. Gundlach, R. Ernstorfer, and R. Eichberger. Sub-20 fs visible pulses with 750 nJ energy from a 100-kHz NOPA. *Opt. Lett.* **31**, 1289 (2006).

[140] G. Cerullo, M. Nisoli, and S. De Silvestri. Generation of 11 fs pulses tunable across the visible by optical parametric amplification. *Appl. Phys. Lett.* **71**, 3616 (1997).

[141] P. Baum, S. Lochbrunner, and E. Riedle. Generation of tunable 7-fs ultraviolet pulses: achromatic phase matching and chirp management. *Appl. Phys. B* **79**, 1027 (2004).

[142] R. Trebino, K. DeLong, D. Fittinghoff, J. Sweetser, M. Krumbügel, and B. Richman. Measuring ultrashort laser pulses in the time-frequency domain using frequency-resolved optical gating. *Review of Scientific Instruments* **68**, 3277 (1997).

[143] E. Wüst. Bachelor thesis: Aufbau eines Referenzkanals (2016).

[144] R. C. Miller. Mechanism of second harmonic generation of optical maser beams in quartz. *Phys. Rev.* **131**, 95 (1963).

[145] R. C. Miller. Optical second harmonic generation in piezoelectric crystals. *Appl. Phys. Lett.* **5**, 17 (1964).

[146] U. Höfer. Nonlinear optical investigations of the dynamics of hydrogen interaction with silicon surfaces. *Appl. Phys. A* **63**, 533 (1996).

[147] U. Bovensiepen, P. Poulopoulos, W. Platow, M. Farle, and K. Baberschkel. Sudden jump of the Curie temperature at the coalescence of Co islands on Cu(001). *J. Magn. Magn. Mater.* **192**, L386 (1999).

[148] V. Jähnke, U. Conrad, J. Güdde, and E. Matthias. SHG investigations of the magnetization of thin Ni and Co films on Cu(001). *Appl. Phys. B* **68**, 485 (1999).

[149] W. Weber, A. Bischof, R. Allenspach, C. H. Back, J. Fassbender, U. May, B. Schirmer, R. M. Jungblut, G. Güntherodt, and B. Hillebrands. Structural relaxation and magnetic anisotropy in Co/Cu(001) films. *Phys. Rev. B* **54**, 4075 (1996).

[150] H. A. Wierenga, M. W. J. Prins, D. L. Abraham, and Th. Rasing. Magnetization-induced optical second-harmonic generation: A probe for interface magnetism. *Phys. Rev. B* **50**, 1282 (1994).

[151] A. Eschenlohr, J. Wieczorek, J. Chen, B. Weidtmann, M. R€osner, N. Bergeard, A. Tarasevitch, T. O. Wehling, and U. Bovensiepen. Analyzing ultrafast laser-induced demagnetization in Co/Cu(001) via the depth sensitivity of the time-resolved transversal magneto-optical Kerr effect. *Proc. SPIE* **9746**, 97461E (2016).

[152] A. Goris, K. M. Döbrich, I. Panzer, A. B. Schmidt, M. Donath, and M. Weinelt. Role of Spin-Flip Exchange Scattering for Hot-Electron Lifetimes in Cobalt. *Phys. Rev. Lett.* **107**, 026601 (2011).

[153] S. Kaltenborn and H. Schneider. Spin-orbit coupling effects on spin-dependent inelastic electronic lifetimes in ferromagnets. *Phys. Rev. B* **90**, 201104 (2014).

[154] J. Wieczorek. PhD thesis: Separation von laserinduzierten ultraschnellen Transporteffekten und Spin-Flip-Streuung in Co/Cu(001). (2015).

[155] T. Henighan, M. Trigo, S. Bonetti, P. Granitzka, D. Higley, Z. Chen, M. P. Jiang, R. Kukreja, A. Gray, A. H. Reid, E. Jal, M. C. Hoffmann, M. Kozina, S. Song, M. Chollet, D. Zhu, P. F. Xu, J. Jeong, K. Carva, P. Maldonado, P. M. Oppeneer, M. G. Samant, S. S. P. Parkin, D. A. Reis, and H. A. Dürr. Generation mechanism of terahertz coherent acoustic phonons in Fe. *Phys. Rev. B* **93**, 220301(R) (2016).

[156] L. Rothberg. Photo-Induced Charge Transfer. *World Scientific*, Singapore, (2000).

[157] J. Stähler, U. Bovensiepen, M. Meyer, and M. Wolf. A surface science approach to ultrafast electron transfer and solvation dynamics at interfaces. *Chem. Soc. Rev.* **37**, 2180 (2008).

[158] M. Cinchetti, K. Heimer, J. Wüstenberg, O. Andreyev, M. Bauer, S. Lach, C. Ziegler, Y. Gao, and M. Aeschlimann. Determination of spin injection and transport in a ferromagnet/organic semiconductor heterojunction by two-photon photon- emission. *Nature Mater.* **8**, 115 (2009).

[159] W. Chang, D. N. Congreve, E. Hontz, M. E. Bahlke, D. P. McMahon, S. Reineke, T. C. Wu, V. Bulović, T.V. Voorhis, and M. A. Baldo. Spin-dependent charge transfer state design rules in organic photovoltaics. *Nature Commun.* **6**, 6415 (2015).

[160] D. L. Windt, IMD - Software for modeling the optical properties of multilayer films. *Computers in Physics*, **12**, 360 (1998).

[161] V. Shokeen, M. Sanchez Piaia, J.-Y. Bigot, T. Müller, P. Elliott, J. K. Dewhurst, S. Sharma, and E. K. U. Gross. Spin Flips versus Spin Transport in Nonthermal Electrons Excited by Ultrashort Optical Pulses in Transition Metals. *Phys. Rev. Lett.* **119**, 107203 (2017).

[162] A. Nilsson, J. Stöhr, T. Wiell, M. Aldén, P. Bennich, N. Wassdahl, M. G. Samant, S. S. P. Parkin, N. Mårtensson, J. Nordgren, B. Johansson, and H. L. Skriver. Determination of the electronic density of states near buried interfaces: Application to Co/Cu multilayers. *Phys. Rev. B* **54**, 2917 (1996).

[163] A. Nitzan. Electron transmission through molecules and molecular interfaces. *Annu. ReV. Phys. Chem.* **52**, 681, (2001).

[164] A. Nitzan and M. Ratner. Electron Transport in Molecular Wire Junctions. Science **300**, 1384, (2003).

[165] H. Ishii, K. Sugiyama, E. Ito, and K. Seki. Energy Level Alignment and Interfacial Electronic Structures at Organic/Metal and Organic/Organic Interfaces. *Adv. Mater.* **11**, 605, (1999).

[166] D. Cahen and A. Kahn. Electron energetics at surfaces and interfaces: concepts and experiments. *Adv. Mater*. **15**, 271 (2003).

[167] X.-Y. Zhu. Surface photochemistry. *Annu. ReV. Phys. Chem*. **45**, 113 (1994).

[168] F. Zimmermann and W. Ho. State resolved studies of photochemical dynamics at surfaces. *Surf. Sci. Rep.* **22**, 127 (1995).

[169] J. Asbury, E. Hao, Y. Wang, H. Ghosh, and T. Lian. Ultrafast electron transfer dynamics from molecular adsorbates to semiconductor nanocrystalline thin films. *J. Phys. Chem. B.* **105**, 4545 (2001).

[170] M.-S. Liao and S. Scheiner. Electronic structure and bonding in unligated and ligated FeII porphyrins. *J. Chem. Phys.* **116**, 3635 (2002).

[171] S. Bhandary, B. Brena, P. M. Panchmatia, I. Brumboiu, M. Bernien, C. Weis, B. Krumme, C. Etz, W. Kuch, H. Wende, O. Eriksson, and B. Sanyal. Manipulation of spin state of iron porphyrin by chemisorption on magnetic substrates. *Phys. Rev. B* **88**, 024401 (2013).

[172] X.-Y. Zhu. Charge transport at metal-molecule interfaces: a spectroscopic view. *J. Phys. Chem. B* **108**, 8778 (2004).

[173] R. Corn and D. Higgins. Optical second harmonic generation as a probe of surface chemistry. *Chemical Reviews* **94**, 107 (1994).

[174] S. Lach, A. Altenhof, K. Tarafder, F. Schmitt, M. E. Ali, M. Vogel, J. Sauther, P. M. Oppeneer, and C. Ziegler. Metal–organic hybrid interface states of a ferromagnet/organic semiconductor hybrid junction as basis for engineering spin injection in organic spintronics. *Adv. Funct. Mater.* **22**, 989 (2012).

[175] J. Dvorak and H. Dai. Optical reflectivity changes induced by adsorption on metal surfaces: The origin and applications to monitoring adsorption kinetics. *J. Chem. Phys.* **112**, 923 (2000).

[176] S. Babar and J. H. Weaver. Optical constants of Cu, Ag, and Au revisited. *Appl. Opt.* **54**, 477 (2015).

[177] O. Jepsen, D. Glötzel, and A. R. Mackintosh. Potentials, band structures, and Fermi surfaces in the noble metals. *Phys. Rev. B* **23**, 2684 (1981).

[178] R. Courths and S. Hüfner. Photoemission experiments on copper. *Physics Reports* **112**, 53 (1984).

[179] M. Lisowski, P. Loukakos, U. Bovensiepen, J. Stähler, C. Gahl, and M. Wolf. Ultra-fast dynamics of electron thermalization, cooling and transport effects in Ru(001). *Appl. Phys. A* **78**, 165 (2004).

[180] T. Kampfrath, A. Sell, G. Klatt, A. Pashkin, S. Mährlein, T. Dekorsy, M. Wolf, M. Fiebig, A. Leitenstorfer, and R. Huber. Coherent terahertz control of antiferromagnetic spin waves. *Nature Photonics* **5**, 31 (2011).

[181] P. Argyres. Theory of the Faraday and Kerr Effects in Ferromagnetics. *Phys. Rev.* **97**, 334 (1955)

[182] D. Spence, P. Kean, and W. Sibbett. 60-fsec pulse generation from a self-mode-locked Ti:sapphire laser. *Opt. Lett.* **16**, 42 (1991).

[183] M. Reed, M. Steiner-Shepard, and D. Negus. Widely tunable femtosecond optical parametric amplifier at 250 kHz with a Ti:sapphire regenerative amplifier. *Opt. Lett*. **19**, 1855 (1994).

[184] A. Kalashnikova, A. Kimel, R. Pisarev, V. Gridnev, P. Usachev, A. Kirilyuk, and Th. Rasing. Impulsive excitation of coherent magnons and phonons by subpicosecond laser pulses in the weak ferromagnet $FeBO_3$. *Phys. Rev. B* **78**, 104301 (2008).

[185] S. Blundell. Magnetism in condensed matter. *Oxford University Press* (2001).

[186] J. Chen. Master thesis: Nonlinear optics at metal-molecule interfaces. (2016).

[187] E. Knoesel, A. Hotzel, and M. Wolf. Ultrafast dynamics of hot electrons and holes in copper: Excitation, energy relaxation, and transport effects. *Phys. Rev. B* **57**, 12812 (1998).

[188] H. Petek, H. Nagano, and S. Ogawa. Hole Decoherence of d Bands in Copper. *Phys. Rev. Lett.* **83**, 832 (1999).

[189] S. Kurtz, J. Jerphagnon and M. Choy. Nonlinear dielectric susceptibilities. *Springer-Verlag* (1979).

[190] I. Malitson. Interspecimen comparison of the refractive index of fused silica, *J. Opt. Soc. Am.* **55**, 1205 (1965).

Publications list

- A. Eschenlohr, J. Wieczorek, J. Chen, B. Weidtmann, M. Rösner, N. Bergeard, A. Tarasevitch, T. O. Wehling, U. Bovensiepen. Analyzing ultrafast laser-induced demagnetization in Co/Cu(001) via the depth sensitivity of the time-resolved transversal magneto-optical Kerr effect. *Proc. SPIE* **9746**, Ultrafast Phenomena and Nanophotonics XX, 97461E (2016).
- S. Xiao, J. Chen, A. Eschenlohr, and U. Bovensiepen. Charge transfer excitation at the Fe-OEP/Cu(001) interface probed by optical second harmonic generation. (unpublished 2017)
- J. Chen, J. Wieczorek, A. Eschenlohr, S. Xiao, A. Tarasevitch, and U. Bovensiepen. Ultrafast inhomogeneous magnetization dynamics analyzed by interface-sensitive nonlinear magneto-optics. *Appl. Phys. Lett.* **110**, 092407 (2017).
- J. Chen, U. Bovensiepen, A. Eschenlohr, T. Müller, P. Elliott, E. K. U. Gross, J. K. Dewhurst, and S. Sharma. Competing spin transfer and dissipation at Co/Cu(001) interfaces on femtosecond timescales. *Phys. Rev. Lett*. **122**, 067202 (2019).

Acknowledgements/Danksagung

This research was supported by the German Research Foundation via SPP QUTIF 1840 and SFB1242. This work would have not been possible without the help and support of many people to whom I would like to express my gratitude.

First of all, I would like to express my sincere gratitude to my thesis advisor Prof. Dr. Uwe Bovensiepen for giving me the opportunity to perform my PhD studies in his research group. I appreciate his knowledge in ultrafast science, motivating discussions, even down to fundamental physics, and insightful comments of my thesis. I am also thankful for your patience and encouragement.

I also want to thank Prof. Dr. Jens Güdde (Philipps-Universität Marburg) for becoming the second referee of this thesis and being a part of the thesis committee.

I am very grateful to Dr. Andrea Eschenlohr for sharing me with your knowledge in ultrafast magnetism and magneto-optics as well as continuous support, motivation, excellent guidance and useful advice. I especially appreciate the effort you put to make the publications possible. Thank you for reviewing my thesis with all the comments and valuable helps.

It is a pleasure to thank our collaborators: Dr. Sangeeta Sharma (Max-Born-Insitut, Berlin), Dr. Peter Elliott (Max-Born-Insitut, Berlin), Tristan Müller (Max Planck Institut, Halle) for theoretical support and fruitful discussions.

A special thanks goes to Dr. Ping Zhou for sharing a good office atmosphere, also for your experience, knowledge in ultrafast laser and nonlinear optics. I always profited from your interesting ideas and technical advices.

I would like to thank Dr. Jens Wieczorek for his experiences in the laboratory as well as setting up the molecule evaporator.

I would like to thank Dr. Shunhao Xiao for his expertise and knowledge in nonlinear optics.

I want to thank Dr. Alexander Tarasevitch for his support and advice for the laser system.

I thank Prof. Dr. Eberhard Riedle (Ludwig-Maximilians-Universität München) for his expertise and fruitful discussion of the NOPA optimization.

I want to thank Prof. Dr. Heiko Wende, David Klar and Ulrich von Hörsten for their expertise in molecule preparation and fruitful discussions.

I thank Varun Ramaprasad, Malavika Varma and Subharda Mohapatra for assistance in the nonlinear optical laboratory.

I want to thank Marius Milnikel and John Thomas for proofreading of the thesis.

I want to thank the group secretary Christina Boese for dealing with paperwork in ordering lab equipment and administrations.

I thank all the former and current members in AG Bovensiepen: Dr. Manuel Ligges, Dr. Isabella Avigo, Dr. Ishita Agarwal, Dr. Abdul Samad Seyed, Dr. Ljupka Stojcevska Malbasic, Dr. Cord Bertram, Dr. Mohammadmahdi Afshari, Frank Meyer, Andre Seyen, Jan Beckord, Fabian Brinks, Hamed Abbasi, Manuel Bridger, Oscar Naranjo, Thies Albert, Florian Kühne, Yasin Beyazit, Philipp Krumey, Mahendra Kabbinahithlu, Michael Bieske, Roland Kohn, Prof. Dr. Klaus Sokolowski-Tinten and many others.

Last but not least, I would like to thank my family and friends for their understanding, support and encouragement.

Declaration/Erklärung

Hiermit versichere ich, dass ich diese Arbeit selbständig verfasst, keine anderen als die angegebenen Quellen und Hilfsmittel benutzt sowie Zitate kenntlich gemacht habe. Diese Arbeit wurde bisher weder in gleicher noch ähnlicher Form einer anderen Prüfungskommission vorgelegt.

Duisburg, _____

_____

Jinghao Chen

DOI: 10.17185/duepublico/74308
URN: urn:nbn:de:hbz:464-20210510-143400-3